Czech Technical University in Prague
Faculty of Nuclear Sciences and Physical Engineering

Doctoral Thesis

Praha, 2015 ***Ing. Michal Vajzer***

Czech Technical University in Prague
Faculty of Nuclear Sciences and Physical Engineering

Study of hard processes in the ALICE experiment.

Doctoral Thesis

Praha, 2015 ***Ing. Michal Vajzer***

Adsiduus usus uni rei deditus et ingenium et artem saepe vincit.

-- Marcus Tullius Cicero –

Bibliografický záznam

Autor	Ing. Michal Vajzer, České vysoké učení technické v Praze, Fakulta jaderná a fyzikáně inženýrská, Katedra fyziky
Název práce	Štúdium tvrdých procesov v experimente ALICE
Studijní program	(D4CS) Aplikace přírodních věd
Studijní obor	(3901V016) Jaderné in|zenýrství
Školitel	Mgr. Jaroslav Bielčík Ph.D, České vysoké učení technické v Praze, Fakulta jaderná a fyzikáně inženýrská, Katedra fyziky
Školitel specialista	RNDr. Jana Bielčíková Ph.D, Ústav jaderné fyziky AVČR, v.v.i. Oddělení jaderné spektroskopie
Akademický rok	2014/2015
Počet stran	181
Klíčová slova	jet, anti-k_T , Bjorkenovské x, ALICE, QCD, ťažké ióny, nPDF

Bibliographic Entry

Author	Ing. Michal Vajzer, Czech Technical University in Prague, Faculty of Nuclear Sciences and Physical Engineering, Department of physics
Title of dissertation	Study of hard processes in the ALICE experiment
Degree program	(D4CS) Application of natural sciences
Field of study	(3901V016) Nuclear engineering
Supervisor	Mgr. Jaroslav Bielčík Ph.D, Czech Technical University in Prague, Faculty of Nuclear Sciences and Physical Engineering, Department of physics
Supervisor specialist	RNDr. Jana Bielčíková Ph.D, Nuclear Physics Institute of the ASCR, p.r.i. Department of Nuclear Spectroscopy
Academic Year	2014/2015
Number of Pages	181
Keywords	jet, anti-k_{T} , Bjorken's x, ALICE, QCD, heavy ions, nPDF

Study of hard processes in the ALICE experiment

Ing. Michal Vajzer

Abstract

Jets are collimated sprays of particles resulting from fragmentation of associated hard scattered partons. They are measured in different types of collisions at different energies to test perturbative quantum chromodynamic calculations and are used to study the hard scattering, fragmentation, hadronisation and other properties of partons. These properties studied in simple systems such as proton-proton collisions, serve as a baseline to investigate their modifications by hot and dense nuclear matter created in high energy heavy-ion collisions.
This thesis presents analysis of data from minimum bias proton-proton collisions at centre of mass energy of 2.76 and 7 TeV collected using the ALICE detector system at the LHC is presented with jet transverse momenta in range from 20 GeV/c to 100 GeV/c. Reconstruction of the inclusive jet cross-section from charged tracks at midrapidity is done using standard modern anti-k_T and k_T algorithms with underlying event subtraction and correction for detector effects via unfolding and its systematics study for both energies. These results are compared to Monte Carlo predictions from different PYTHIA6 tunes and results from the ATLAS collaboration, observing good agreement.
Additionally, next-to-leading order simulations of jet production are presented. They are carried out using POWHEG-Box framework, implementation of POWHEG NLO generator, with parton showering provided by PYTHIA8. These simulations are performed for proton-proton collisions at centre of mass energy of 7 TeV and proton-lead collisions at 5.02 TeV, in order to study jet production cross sections and ratio of jet spectra reconstructed using different resolution parameter, in momentum range matching that of real data analyses. Additionally, the modification of lead parton distribution functions with respect to the one of proton is investigated via extracted Bjorken x variable using the leading di-jet in the event as no significant modification is observed in differential cross section.
Parton distribution function's effect on heavy ions are implemented using nuclear parton distribution functions such as HKN07 and utilising nuclear modification factors provided in EPS09. Jet reconstruction algorithms are provided by the FastJet package.
Keywords: *jet, anti-*k_T *, Bjorken-x, ALICE, QCD, heavy ions, nPDF*

Štúdium tvrdých procesov v experimente ALICE

Ing. Michal Vajzer

Abstrakt

Jety sú kolimované spŕšky častíc pochádzajúce z fragmentácie partónu z tvrdého rozptylu. V rôznych typoch zrážok pri rôznych energiách slúžia na testovanie predpovedí poruchovej kvantovej chromodynamiky a k štúdiu tvrdých rozptylov, rozptylov s veľkou prenesenou hybnosťou, fragmentácie, hadronizácie a iných vlastností partónov. Tieto vlastnosti študované v jednoduchých systémoch ako napríklad zrážky protón-protón slúžia ako referencia pre štúdium ich zmien v horúcej a hustej jadrovej hmote vytvorenej v zrážkach vysoko-energetických ťažkých iónov.

V tejto práci je prezentovaná analýza dát z minimálne trigrovaných zrážok protón-protón s energiou 2.76 TeV a 7 TeV v ťažiskovej sústave nazbieraných pomocou detektoru ALICE na urýchľovači LHC v rozsahu hybností od 20 GeV/c do 100 GeV/c. Rekonštrukcia diferenciálnych inkluzívnych účinných prierezov z nabitých dráh v midrapidite je sprostredkovaná štandardnými modernými algoritmami anti-k_{T} a k_{T} . Tieto jety majú odčítané pozadie zo zrážky a sú opravené na efekty detektorovej rekonštrukcie prostredníctvom štatistickej dekonvolúcie. Výsledky sú porovnané s predpoveďami Monte Carlo generátoru PYTHIA6 s rôznymi ladeniami a s meraniami kolaborácie ATLAS, pozorujúc veĺmi súhlas medzi výsledkami oboch kolaborácií.

Ďalej sú prezentované simulácie druhého rádu v rozklade Taylorovej rady jetovej produkcie poruchovej kvantovej chromodynamiky. Tieto simulácie sú produkované pomocou POWHEG-Box, implementácie POWHEG generátoru, s použitím produkcie portónových spršiek pomocou Monte Carlo generátoru PYTHIA8 a zamerané na protón-protónové zrážky s energiou 7 TeV v ťažiskovej sústave a zrážky protón-olovo s 5.02 TeV, študujúc diferenciálne inkluzívne účinné prierezy jetovej produkcie a pomery jetových spektier s rôznymi rozlišovacími parametrami v rozsahu hybností pozorovaných v analýze reálnych dát. Modifikácie partónových distribučných funkcií pre jadro olova je študované prostredníctvom Bjorkenovského x extrahovaného z vedúceho di-jetu v zrážke, keďže neboli pozorované žiadne signifikantné modifikácie v diferenciálnych účinných prierezoch. Efekty partónových distribučných funkcií pre jadrá olova sú implementované prostredníctvom jadrových PDF ako HKN07 a použitím jadrových modifikačných faktorov popísaných v EPS09. Jetové rekonštrukčné algoritmi sú poskytnuté balíčkom FastJet.

Klíčová slova: $j$et, anti-k_{T} , Bjorkenovské x, ALICE, QCD, ťažké ióny, nPDF

Acknowledgement

Foremost, I would like to express my gratitude to my supervisor Dr. Jaroslav Bielčík and my consultant Dr. Jana Bielčíková for their support, guidance and all the help they have provided during all these years.

Besides them, my thanks goes to Prof. Dr. Johannes P. Wessels and Priv.Doz. Dr. Christian Klein-Bösing for their support and helpful ideas during my DAAD stay in Münster.

I would like to thank to all my colleagues for stimulating discussions and fun we had either on conferences, while supervising labs or after work.

Last but not least, I would like to thank my parents Anna and Ján, and my sisters Janka and Michaela, for their continuous support throughout my life.

Declaration:

I hereby certify that I am the sole author of this thesis. I certify that, to the best of my knowledge, my thesis does not infringe upon anyone's copyright nor violate any proprietary rights and that any ideas, techniques, quotations, or any other material from the work of other people included in my thesis, published or otherwise, are fully acknowledged in accordance with the standard referencing practices.

Ing. Michal Vajzer

Contents

List of Figures

List of Tables

List of Symbols

ALICE	A Large Ion Collider Experiment
ATLAS	A ToroidaL ApparatuS
CERN	Conseil Europen pour la Recherche Nuclaire
CMS	Compact Muon Solenoid
DIS	Deep Inelastic Scattering
EMCAL	Electro-Magnetic Calorimeter
FAIR	Facility for Antiproton and Ion Research
FSR	Final State Radiation
HIC	Heavy-Ion Collision
HMPID	High Momentum Particle Identification
ISR	Initial State Radiation
ITS	Inner Tracking System
LHC	Large Hadron Collider
LO	Leading Order
MoEDAL	Monopole and Exotics Detector At LHC
MPI	Multi-Parton Interaction
NICA	Nuclotron-based Ion Collider fAcility
NLO	Next-to-Leading Order
PDF	Parton Distribution Function
PHOS	Photon Spectromenter
PID	Particle Identification

PSB	Proton Synchrotron Booster
PS	Proton Synchrotoron
QCD	Quantum Chromodynamics
QED	Quantum Electro-Dynamics
QFT	Quantum Field Theory
QGP	Quark Gluon Plasma
SDD	Silicon Drift Detector
SPD	Silicon Pixel Detector
SPS	Super Proton Synchrotron
SSD	Silicon Strip Detector
TOF	Time of Flight
TOTEM	TOTal Elastic and diffractive cross section Measurement
TPC	Time Projection Chamber
TRD	Transition Radiation Detector
UE	Underlying Event
ZDC	Zero Degree Calorimeter

Introduction

Particle physicists have been able to describe strong interaction, an interaction between quarks and gluons, using *Quantum Chomodynamics*. Strongly interacting particles carry *colour*, new degree of freedom in theory. We observe only colourless, white particles. Hadrons are composed of two or three valence quarks.

Although observation of individual quarks and gluons is impossible due to *colour confinement*, collimated showers of particles, called *jets*, have been observed in electron-positron collisions. These jets are a result of multiple parton emissions from these quarks or gluons followed by their subsequent hadronisation, where harder partons lead to higher multiplicities of final state jets. They are used as a tool to connect final state particles on experimental level and QCD partons from hard scatterings on theoretical level. By measuring jet cross-sections, we are able to test perturbative predictions from hard-scatterings. On the other hand, by studying particle composition and momenta of individual jet constituents, we investigate fragmentation process of single hard parton into shower of collimated particles.

Heavy-ion collisions, where hot and dense QCD matter is created, showed that jets can be used to study medium, they are passing through, via collisional and radiation energy loss. Comparing di-hadron correlations from proton-proton, deuteron-gold and gold-gold collisions, it was observed that in gold-gold collision peak associated with back-to-back jet production disappears. The momentum from original hard parton is redistributed via medium induced energy loss and particles with smaller momentum are created. Results from analyses of jet fragmentation by CMS and ATLAS collaboration suggest enhancement of particle production in heavy-ion data only for small transverse momenta and large distances from jet axis. Furthermore, results from charged hadron and jet analyses in heavy-ion collisions compared to proton-proton baseline exhibit significant yield suppression down to the factor 0.6 for the largest jet momenta.

However, precise analyses involving tracks in heavy-ion collisions are problematic not only due to the large backgrounds present but also due to the relatively large volume of collision, influencing path length of the hard parton inside created medium and consequent energy lost. These analyses should enable study of *quark-gluon plasma* a state of QCD matter where quarks and gluons are deconfined and move relatively freely. It is expected that this state was naturally present few moments after the Big Bang and can be recreated by colliding highly energetic nuclei.

In order to deduce properties of this state created in final stages of the collision, original initial state effects have to be accounted for. This is done by studying proton-ion or deuteron-ion collisions. Recent results from proton-lead collisions suggest possible interesting topics for jet studies for different centralities contrary to minimum bias selection where no modification is observed. However, in case of charged hadrons enhancement at large transverse momenta from ATLAS and CMS, current lack proton-proton baseline keep a shadow of a doubt in final interpretation of these results.

Jet analysis at the energy frontier is carried out by the ATLAS and CMS collaboration. They are able to reconstruct jet energies up to 1 TeV. However, ALICE, another one of the main experiments at the LHC focused primarily on physics of colliding heavy ions, offers unique capabilities compared to the other to. Although the momentum reach is significantly limited compared to ATLAS and CMS, ALICE is distinguished by excellent tracking capabilities in central region. Not only is it possible to study tracks down to 0.15 GeV/c but for the Run 2 of the LHC there will be runs when magnetic field of L3 magnet will be reduced from 0.5 T to 0.2 T, lowering the threshold on the studied tracks. Additionally, several different detector system specialise in particle identification and particle discrimination providing unique capabilities among the LHC experiments. This enables study of identified jet fragmentations furthering knowledge about jets and also studies such as changes in strangeness content of jets in the presence of QCD medium.

This work focuses on study of jets reconstructed from charged tracks in proton-proton collisions and next-to-leading order pQCD predictions for proton-lead collisions at the LHC energies using nuclear parton distribution functions accessible in LHAPDF.

This thesis is organised in following way. Chapter 1 contains theoretical description of forces between particles and more thorough description of concepts within Quantum Chromodynamics is provided in order to properly explain subject of jets. In chapter 3 the concepts of QCD are used to illustrate jet production and their evolution. Algorithms for reconstruction of these jets are described here as well. Furthermore, areas of interest, where jets are being used, are listed, followed by chapter 2 explaining concepts and signals of heavy-ion collisions and quark-gluon plasma. An emphasis is placed on the role of jets in ion-ion and proton-ion collisions. Experimental part of the thesis starts, in chapter 4, by description of the Large Hadron Collider and the ALICE detector system, used for analysis of proton-proton collisions. Description of analysis tools including methods used for data correction is provided as well. Following chapter, chapter 5, is focused on the selected data with description of triggers used in the analysis of real data from the ALICE detector system. It deals with track and jet selection as well, describing several of their properties. Corresponding simulations to these data are described in chapter 6 where productions used for detector effect corrections and comparison are produced. Additionally, the second part of this chapter describes next-to-leading order pQCD simulations of jets studied using POWHEG-Box. Performance of the used analysis methods and estimation of systematic uncertainties for all presented results is provided in the chapter 7. Similarly to previous chapter, first part of this chapter is connected with analysis of the real data and the second part is dedicated to NLO analysis. The results of the described analyses are provided in the chapter 8, followed by chapter 9 where everything is summed up and conclusions are drawn.

STATEMENT OF AUTHOR'S CONTRIBUTION TO PRESENTED RESULTS

Besides studying at Faculty of Nuclear Sciences and Physical Engineering, I have been employed by Nuclear Physics Institute of the Academy of Sciences of Czech Republic, public research institute, since October 2010, where I have become member of Nuclear Spectroscopy group. I have become member of the ALICE collaboration at the Large Hadron Collider, where I have been analysing data and presented results at conferences.

From the beginning of my involvement in jet analysis group within the ALICE physics working groups, I was responsible for running official GRID analyses for proton-proton analyses for users analysing jets. My responsibility was setting up proper parameters of algorithms and datasets for analysis of proton-proton collisions to be used by user analyses. I was responsible for testing of all the analyses involved and support in setting up user tasks.

Additionally, during the data taking I did operator shifts as data acquisition (DAQ) shifter, as shifter for central trigger processing (CTP) and as high level trigger (HLT) shifter. Moreover, I was assigned position of shift leader in matters of safety (SLIMOS).

My analysis involved momentum correction of jets reconstructed from tracks. This resulted in fully corrected differential jet cross section with subtracted underlying event. Furthermore I studied increasing jet collimation as a function of jet's transverse momentum and difference between reconstructed jet spectra from proton-lead collisions with respect to proton-proton baseline. These studies were done using next-to-leading order simulations of hard scatterings with lead nuclear parton distribution function.

In October 2012, I have presented first proton-proton preliminary spectra for proton-proton collisions at 7 TeV with different resolution parameters at the Hot Quarks 2012 conference with first proceeding, J. Phys. Conf. Series **446** (2013) 012004, as a result. Here Figure 1 and Figure 2 are results of my analyses. In the following conference, EPS HEP 2013, I have presented fully corrected cross section for jets reconstructed with various resolution parameter for proton-proton collision at both 7 and 2.76 TeV. These jets have subtracted underlying event and study of jet collimation as a function of jet transverse momenta was presented as well. In the proceeding, PoS EPS-HEP 2013 (2013) 464, these results correspond to Figure 1, 2, 3 and 4a. Additionally, improved jet spectra and jet constituents spectra were presented. In September 2014, I have presented at the 18th Conference of Czech and Slovak Physicists results of my study of next-to-leading order pQCD simulations of proton-proton and proton-lead collisions at the LHC energies. Resulting proceeding is fully result of my analysis on local computational cluster.

As one of the analysers of jets in proton-proton collisions, I am a member of paper committee (PC) for paper, *C*harged jet cross sections and properties in proton-proton collisions at $\sqrt{s} = 7$ TeV, arXiv:1411.4969, submitted to Physics Reviews D. Here, I was responsible for Monte Carlo simulations, matrix inversion techniques of unfolding of uncorrected spectra and part of the results presented. As the paper is composed of three different analyses, I am responsible for Fig.1-6 of this paper.

List of my publications is in Appendix E.

Chapter 1. Standard Model

Basic physical properties of particles and observed processes are described using *Standard Model.* This theory was developed in the second half of 20th century and finalized in 1970s when existence of quarks was proven. It is a collaborative work of many scientists around the world and it incorporates theory of *electro-weak* interactions, which describes interactions between all particles via exchange of $\mathrm{W}^{\pm}$, Z bosons and photon, gauge bosons, particles integer spin, corresponding to this theory. On fundamental level[1], all fermions, particles with half spins, interact through electro-weak interaction. Another theory within framework of Standard Model is theory of strong interactions, which is carried by gluons and affecting fundamental particles carrying *colour charge*, i.e. quarks and gluons. Theory gravitational force, intermediated by gravitons, is not included at all in Standard Model, however all massive or energetic particles feel gravitational attraction. The theory of Standard Model was validated by discovery of new boson in 2012 that was further confirmed in the 2013 to be *Higgs boson* [1], predicted in the 1964 by Peter Higgs [2]. This particle is consequence of mechanism proposed by Anderson [3] in the 1962, and further developed independently by Brout and Englert [4], Higgs [2] and Guralnik, Hagen and Kibble [5]. It is spin-0 neutral particle with parity of +1 and mass of approximately $125\mathrm{GeV}/c^2$.

However, Standard model is not complete theory as other observations lead to problems indescribable by this theory. Therefore, physics beyond standard model is expected to explain phenomena like dark matter or dark energy, non-visible part of universe, as only 4.9% of mass–energy of universe is created by visible objects [6], i.e. particles we can describe.

Overview of fundamental particles in Standard model is listed in table Tab. 1.1, with

---

[1] fundamental based on our present knowledge

leptons in its first part. These are fermions with spin-1/2 and non-zero masses. There are three different generations of leptons, each having own quantum number that is conserved and consisting of neutral and negatively charged particle. Naming is based on charged lepton in each generation, i.e. electon, muon and tau lepton, denoted e, μ and τ respectively, giving rise to *electron neutrino*, *muon neutrino* and *tau neutrino* and electronic number, muonic number and tauonic number. This leptonic number is +1 for each lepton of given generation, -1 for their antiparticles and 0 for all other particles.

Second part of the Tab. 1.1 contains properties of gauge bosons. These are particles with spin-1 which behave according to Bose-Einstain statistics. Photon, γ, is massless neutral stable particle, responsible for electro-magnetic interaction. W-bosons, $\mathrm{W}^{\pm}$, are charged massive bosons and Z-boson, Z^0, is neutral massive boson. All three particles have lifetime of the order of $10^{-25}\,\mathrm{s}$ and are responsible for electro-weak interactions. Their mass is explained via Higgs mechanism. Gluons are massless particles responsible for strong interactions. They are neutral and carry net colour charge.

Lower part of Tab. 1.1 contains properties of quarks. These are massive particles divided into, similarly to the leptons, three generations, however all quarks have non-zero electric and colour charge. In the first generation are up and down quarks, in the second generation are charm and strange quarks and third generation contains top and bottom quarks with charge of $2/3\,e$ and $-1/3\,e$ respectively. These different quarks are distinguished according to their *flavour*, which is represented by specific non-zero quantum number they carry, i.e charm, strangeness, topness and bottomness. Furthermore, up and down quark have non-zero value of isospin and all quarks have baryon number of 1/3.

1.1 Electro-weak theory

Electro-weak theory was developed by Glashow, Salam and Weinberg in 1968, unifying weak interactions with electromagnetism. This was achieved via introduction of conserved *weak hypercharge*, Y_{W}, within theoretical framework based on Yang-Mills theory, relating electric charge, Q ,and weak isospin of particles, T_3, according to formula

$$\frac{Y_W}{2} + T_3 = Q. \tag{1.1}$$

On its own electro-magnetic force has been described throughout centuries by many scientists and mathematically summed by Maxwell in 1861. Electro-magnetic interactions occur between electrically charged objects via transfer of photons, which quantum nature was hypothesized by Albert Einstein in 1905 [7] and was validated by such experiments as Compton scattering of single photon. Range of electromagnetic interaction is infinite due to the massless nature of these particles. No conservation law is violated by electromagnetism. Quantum field theory describing electromagnetic interactions is *Quantum Electrodynamics.* It is an abelian gauge theory with symmetry group U(1). Its lagrangian is as follows

	particle		mass / MeV/c^2	Q / C	interactions	quantum number
lepton	electron	e^-	$0.511\,998\,928(11)$	$-1e$	El-Weak	+1 e-lepton
	muon	μ^-	$105.658\,371\,5(35)$	$-1e$	El-Weak	+1 μ-lepton
	tau	τ^-	$1776.82(16)$	$-1e$	El-Weak	+1 τ-lepton
	e-neutrino	ν_e	$< 0.000\,002$	0	Weak	+1 e-lepton
	μ-neutrino	ν_μ	< 0.192	0	Weak	+1 μ-lepton
	τ-neutrino	ν_τ	< 18.2	0	Weak	+1 τ-lepton
gauge boson	photon	γ	0	0	El-Mag	
	W boson	W	$80\,385 \pm 15$	$-1e$	El-Weak	
	Z boson	Z	$91\,187.6 \pm 2.1$	0	El-Weak	
	gluon	g	0	0	strong	colour
quark	up	u	$2.3^{+0.7}_{-0.5}$	$+2/3e$	all	colour, $+1/2$ I_3
	down	d	$4.8^{+0.5}_{-0.3}$	$-1/3e$	all	colour, $-1/2$ I_3
	charm	c	1275 ± 25	$+2/3e$	all	colour, +1 C
	strange	s	95 ± 5	$-1/3e$	all	colour, −1 S
	top	t	$173070 \pm 520 \pm 720$	$+2/3e$	all	colour, +1 T
	bottom	b	4180 ± 30	$-2/3e$	all	colour, −1 B'

Table 1.1: Basic properties of particles, their masses, electric charge, types of interactions and quantum numbers carried. All particles with non-zero mass undergo gravitational interactions, carried by graviton. Isospin, charm, strangeness, topness and bottomness, are denoted with I_3, C, S, T and B' respectively.

$$\mathcal{L} = \bar{\psi}\left(i\gamma^\mu D_\mu\right)\psi - \frac{1}{4}F_{\mu\nu}F^{\mu\nu} \tag{1.2a}$$

$$+ \frac{1}{2\xi}\left(\partial^\mu A_\mu\right)^2, \tag{1.2b}$$

$$D_\mu \equiv \partial_\mu - ieA_\mu + ieB_\mu, \tag{1.2c}$$

$$F_{\mu\nu} = \partial_\mu A_\nu - \partial_\nu A_\mu, \tag{1.2d}$$

where γ^μ are Dirac matrices, ψ is bi-spinor field spin-1/2 particle. Term (1.2b) represent gauge fixing term with ξ as calibration parameter, which is 1 for Feynman gauge and limiting $\xi \to 0$ for Landau gauge, which is in classical approximation equivalent to Lorentz gauge. Covariant matrix is defined using minimal substitution (1.2c) and electro-magnetic field strength tensor (1.2d). Vector A_μ is covariant four-potential of electromagnetic field of particle and B_μ is external field.

Weak interaction does violate conservation of parity and charge-parity symmetry. Moreover, it changes flavour of interacting quarks. Theory of weak interaction was proposed at first by Enrico Fermi in 1934 [8], when he attempted to explain beta decay of neutron by four-fermion interaction without range.

There are two types of weak interactions, those mediated by $\mathrm{W}^{\pm}$ boson called **charged currents**, possibly changing flavour when quarks interact, and those mediated by neutral Z boson.

Weak interactions are explained by unifying them with electromagnetic interaction. This happens at energies of the order of 10^2 GeV. Gauge theory unifying electro-weak interactions is based on $\mathrm{SU}(2) \otimes \mathrm{U}(1)$ symmetry, with massless W^+, W^-, W^0 bosons of weak isospin and B^0 boson of weak hypercharge.

Experimental observation of neutrino scattering confirmed existence of neutral currents, by Gargamelle collaboration [9]. Second major discovery establishing electro-weak theory of interactions was discovery of W and Z bosons in 1983 by UA1 and UA2 collaborations [11–14], at the SPS colliding protons and anti-protons with centre of mass energy of 540 GeV.

1.2 Theory of strong interactions

The other interaction described by Standard Model are strong interactions. On large scales strong interactions binds nucleons, protons and neutrons, inside nuclei, therefore it is responsible for stability of atoms, overcoming electro-magnetic repulsion of protons. On smaller scales, this theory describes interactions between particles carrying *colour charge*, carried only by quarks and gluons. This colour charge can attain three different states named in analogy to three different colours of RGB model, red r, green g and blue b.

Gluons carry combination of different colour and anti-colour, which yields non-zero net colour charge, therefore 8 different eigenstates

$$\mathrm{r\bar{g}}, \mathrm{r\bar{b}}, \mathrm{b\bar{g}}, \mathrm{g\bar{r}}, \mathrm{g\bar{b}}, \mathrm{b\bar{r}}, \frac{1}{\sqrt{2}}\left(\mathrm{r\bar{r}} - \mathrm{g\bar{g}}\right), \frac{1}{\sqrt{6}}\left(\mathrm{r\bar{r}} + \mathrm{g\bar{g}} - 2\mathrm{b\bar{b}}\right)$$

In contrast to massless photons that have no charge, massless gluons have colour charge and therefore interact with each other. This is characteristic feature of non-abelian gauge theory, i.e. non-commutativeness, and as a consequence limits range of interactions.

Quantum field theory describing strong interactions within the framework of Standard Model is called *Quantum Chromodynamics*. It is non-abelian gauge theory based on SU(3) symmetry group and it's lagrangian is

$$\mathcal{L} = \sum_{\text{flavors}} \bar{\psi}_i \left(i \left(\gamma^\mu D_\mu\right)_{ij} - m\delta_{ij} \right) \psi_j - \frac{1}{4} F^a_{\mu\nu} F^{\mu\nu}_a \tag{1.3a}$$

$$- \frac{1}{2\lambda} \left(\partial^\mu A^a_\mu \right)^2 \tag{1.3b}$$

$$+ \partial_\mu \bar{c^a} \partial^\mu c^a + g f^{abc} \left(\partial^\mu \bar{c^a} \right) A^b_\mu \eta^c, \tag{1.3c}$$

where ψ_i is spin-1/2 quark field and A^a_μ is massless spin-1 gluon field. Here indices i and j indicate triplet representation of colour group, therefore acquire values $1, 2, 3$. Field strength tensor is defined as

$$F^a_{\mu\nu} = \partial_\mu A^a_\nu - \partial_\nu A^a_\mu + g f^{abc} A^b_\mu A^c_\mu, \tag{1.4}$$

where a, b, c run over 8 colour degrees defined by adjoint representation of SU(3) group and f^{abc} are structure constants of SU(3) group. Covariant derivative acting on triplet classical part of lagrangian (1.3a) is defined as

$$(D_\mu)_{ij} = \partial_\mu \delta_{ij} + ig \left(t^c A^c_\mu \right)_{ij}, \tag{1.5}$$

where t^c are generators of SU(3) group. Second line (1.3b) represents gauge fixing term with gauge parameter λ and third line so-called *Faddeev-Popov ghost* field. In this term η^c is complex scalar field obeying Fermi statistics and contains both kinematic term and interaction with gluon field.

QCD, similarly as QED, joins different quark flavours via *strong hypercharge*, $\mathrm{Y_S}$, conservation implying conservation of aforementioned flavours. Denoting strangeness as S, charm C, bottomness B', topness T, and baryon number[2] as B, strong hypercharge is defines as

$$Y_S = S + C + B' + T + B, \tag{1.6}$$

and relation to isospin, $\mathrm{I_3}$ and charge is defined by Gell-Mann-Nishijima formula,

$$Q = I_3 + \frac{Y_S}{2}. \tag{1.7}$$

There are few very important topics in QCD that have to be commented on in greater detail. These include form of QCD potential, implication of self-interaction of gluons for running coupling constant. This has great consequences in so-called *asymptotic freedom* and *colour confinement* in QCD, which are responsible for extremely complex behaviour, significantly different from QED.

1.2.1 QCD potential

Behaviour at small and large distances varies significantly in QCD. At small distances behaviour between static quark – anti-quark is repulsive described by Coulomb term. On the other hand at large distances, potential is linearly rising and it is described by confinement term. Altogether, it can be summarized as (1.8), and as such is used in lattice calculations.

$$V^{\mathrm{eff}}_{\mathrm{S}}(r) = -\frac{4}{3}\frac{\alpha_{\mathrm{S}}}{r} + kr \tag{1.8}$$

The variable k is *string tension constant* and in string model represents tension of colour field between valence quarks in meson. Presence of positive string tension constants directly indicates confinement of quarks, as potential increases energy proportionally increases.

---

[2] Baryon number is defined as 1/3 of difference between number of quarks and anti-quarks in hadron. It's value is 1 for baryons, 0 for mesons and anti-mesons and -1 for anti-baryons.

Potential is tested in quarkonia, mesons composed of quark and anti-quark of the same flavour. Static potential model used in non-relativistic calculations enables to determine radius of meson, where in (1.8) distance determines size of mesons. Constants of potential are obtained by fitting quarkonia measurements.

1.2.2 Running coupling constant α_S

Strength of interactions in QCD is expressed via coupling constant[3], α_S. This is dependent on transferred momenta Q^2 between scattered partons and its evolution with momentum scale is given by renormalisation of quantum corrections. Rewriting of appropriate term of *renormalisation group equation*

$$\mu^2 \frac{\partial \alpha_\mathrm{S}}{\partial \mu^2} \equiv \beta\left(\alpha_\mathrm{S}\right), \tag{1.9}$$

where μ^2 is arbitrary parameter on which physical observables are independent and can be rewritten in form of $\ln \mu^2$, such as

$$\frac{\partial \alpha_\mathrm{S}}{\partial \ln \mu^2} = \beta\left(\alpha_\mathrm{S}\right) = -\alpha_\mathrm{S}^2\left(\mu^2\right)\left(b_0 + b_1\alpha_\mathrm{S}\left(\mu^2\right) + b_2\alpha_\mathrm{S}^2\left(\mu^2\right) + \cdots\right) \tag{1.10}$$

Substituting b_0 from (A.7a) into equation (A.6) derived from (1.9), following first approximation of running coupling constant in QCD is obtained

$$\alpha_\mathrm{S}\left(\mu^2\right) = \frac{12\pi}{\left(11n_\mathrm{c} - 2n_\mathrm{f}\right)\ln\left(\frac{\mu^2}{\Lambda^2}\right)}, \tag{1.11}$$

where n_f is number of flavours and n_c number of colours. Unless there are more than 16 different flavours, b_0 is always positive, which is opposite to QED where negative value of beta function is obtained.

Λ-parametrisation has dimension of energy and represents scale at which perturbative theory becomes meaningless. Value of Λ has to be extracted from experiment and it is approximately 200 MeV. More details can be obtained in Appendix A.

Figure 1.1 shows measured values for QCD running coupling constant dependent on exchanged momentum as obtained by CMS experiment and previous analyses done in JADE, LEP, DELPHI, ZEUS, H1 and D0 collaborations, Fig. 1.1a. Additionally, in Fig. 1.1b are shown measurements of QCD running coupling constant at mass of Z boson, with values obtained by multiple experiments and world average of 0.1184 ± 0.0007.

1.2.3 Asymptotic freedom

In QED, bare charge of particles is screened by virtual charged particle – anti-particle pairs created from virtual photons in vacuum. Vicinity of particle is, therefore, polarized by these virtual pairs diminishing field of this particle. Similarly, in QCD virtual quark – anti-quark pairs are created around colour-charged particle. However, effect of virtual

---

[3] Term coupling constant is historical remnant from era when collision energies did not allow to reliably investigate dependence of coupling on transferred momentum.

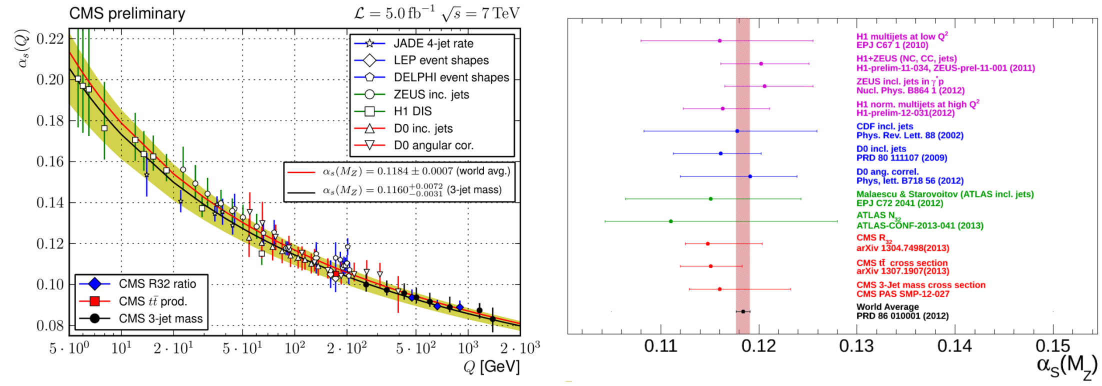

(a) Running α_S dependence on transferred momentum.

(b) Measurements of $\alpha_S\,(M_Z)$.

Figure 1.1: (Left) Dependence of α_S on transferred momentum in QCD as measured by CMS including combination of previous measurements of JADE, LEP, DELPHI, ZEUS, H1 and D0, [15]. (Right) Measurements of running coupling constant α_S at energy of M_Z, [16]. Again multiple measurements are combined and world average is $\alpha_S\,(M_Z) = 0.1184 \pm 0.0007$.

gluon polarisation of vacuum, gluon carrying both colour and anti-colour, has enhancing effect. This effect is called *anti-screening*.

Virtual quarks and gluons contributions have opposite effect, result depends on number of different quark flavours and different colours. This behaviour is characteristic for QCD and is known as *asymptotic freedom*, manifested as weakening of field between particles as energy and distance decreases. At leading order in perturbation theory, this *running coupling constant*, α_S, written as (1.11), contains first term of expansion of beta-function, (A.7a). Positive value of this coefficient expresses dominance of contribution coming from virtual gluon anti-screening.

Furthermore, dependence of coupling constant on transferred momenta, Fig. 1.1a, shows that couplings are weaker for larger transfers. This implies, that the hardest processes with the largest momentum transfers, happening over smallest time and space scales, provide the weakest binding of partons.

1.2.4 Colour confinement

Colour confinement is one of the phenomena of QCD, that no colour charged particle, colour singlet state, can be isolated and directly observed. However, no analytical proof for this phenomena exist within QCD. This phenomenon is explained by behaviour of coupling, it gets stronger with decreasing transfer momenta and increasing space-time scale, Fig. 1.1a, and form of colour potential between two quarks, (1.8).

Furthermore, this phenomena is supported by lack of experimental observation of particles with colour charge.

Based on this, several theories and models describing process of jet formation exist. These suppose, that each quark creates colour field with another anti-quark, forming meson, however quark with higher energy separates from slower companion. This results in building up potential energy and decreasing speed of hard quark, until there is enough potential energy binding these partons, that new quark–anti-quark pair can be created. This breaks bond between original quark and anti-quark, but these are now bound in mesons with newly created anti-quark and quark, as shown by the sketch in Fig. 1.2.

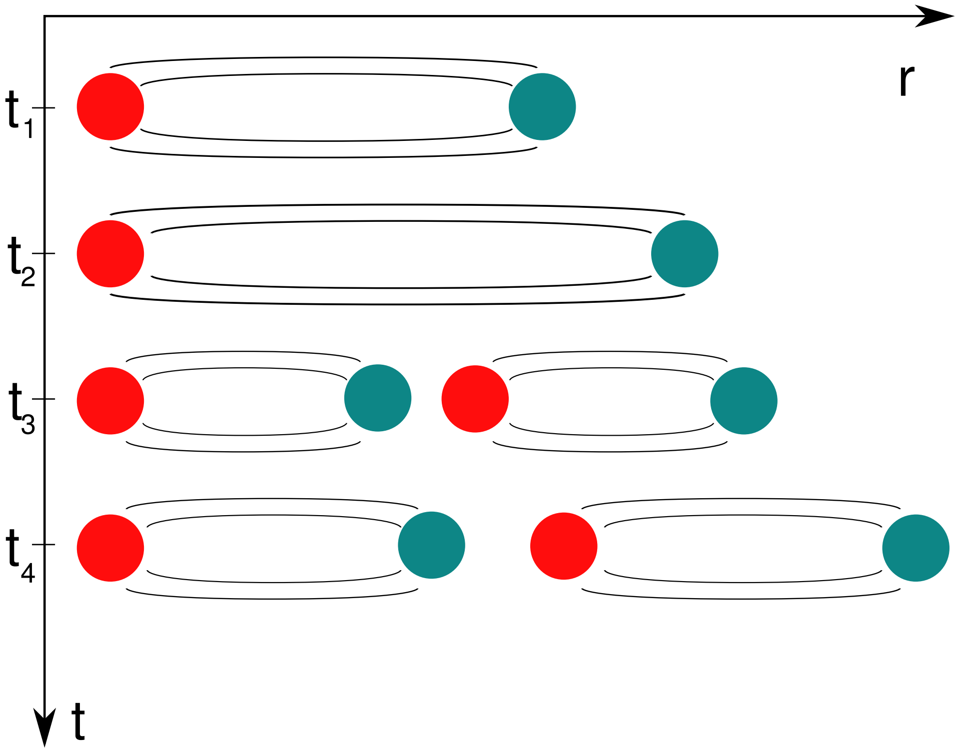

Figure 1.2: Sketch illustrates mechanism of string breaking producing large number of particles in one jet. Imagining that red and green circles represent two quarks of different colour at time t_1 have different momenta, faster moving green quark increases potential energy between them as their separations increases and its momentum appropriately decreases, as seen at t_2, when this potential energy reaches critical energy sufficient to create $q\hat{q}$ pair, denoted by another red and green quark at time t_3. These new quarks do not have to have same colour as the originals, which are now bound to these newly created quarks.

This mechanism enables transfer of kinetic energy of quark into formation of new particles. If parton has sufficient energy, several mesons can by created using this mechanism.

Chapter 2. Study of QCD medium

Jets can be used for investigation of cold and hot nuclear effects. Such studies are aimed to differentiate between effects originating in nucleus before collision and effects originating from hot and dense thermalised medium created after the collision.

2.1 Quark gluon plasma

The long time goal of studies focused on collisions of heavy ions is study of the so-called Quark Gluon Plasma. This is predicted state of matter created by dissociated quarks and gluons. It is expected that sufficiently hot and dense medium will produce free quarks, thanks to the asymptotic freedom of QCD, described in Sec. 1.2.3, where transfer of large momenta during the interactions would lead to negligible coupling constant.

This deconfined state can be represented as one phase of QCD matter, Fig. 2.1. The phase transition is expected only for baryon densities above certain threshold. This threshold density with associated temperature is called *critical point*. Below the density of critical point hadronic and quark-gluon phase form cross-over transition.

As suggested by the Fig. 2.1, several different experiments are attempting to study different parts of this phase diagram. On the energy frontier is LHC followed by RHIC. The latter named allows so-called *beam energy scan*, where different collision energies are investigated for the purpose of studying various observables as a function of collision energy, and in the long run, in order to find the critical point of phase diagram. On the side, increased baryon densities will be studied by experiments from FAIR and NICA program.

QGP is predicted to be present naturally few moments after the Big Bang. Unfortunately, the direct observation of this state is impossible, due to the expansion and associated cooling of the plasma created. However, there are several observables predicted to accompany creation of such matter. These include *collective flow*, *statistical hadronisation* and *jet quenching*.

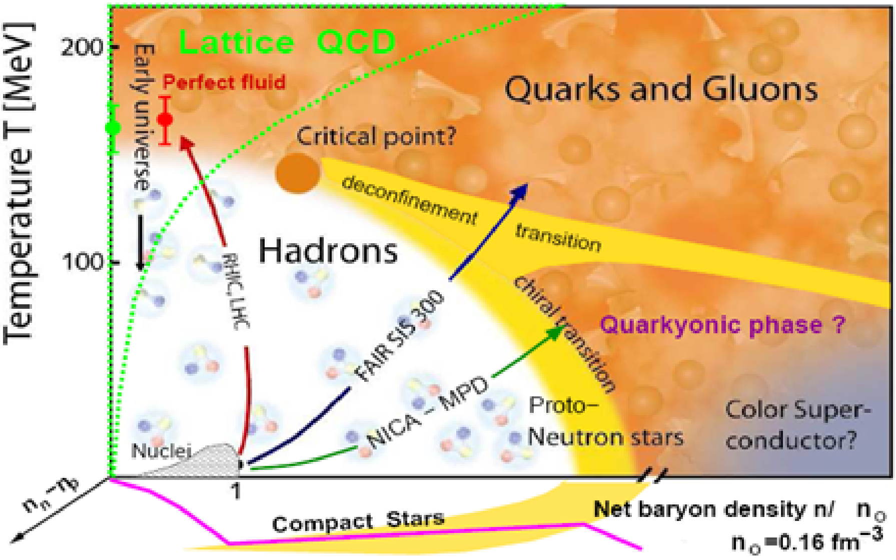

Figure 2.1: QCD phase diagram, as adapted from Ref. [24], shows several phases of QCD matter. For lowest temperatures and baryon densities, hadrons as we know them exist. Increasing temperatures, one gets QGP, deconfined state of quarks and gluons. On the other hand, by increasing baryon densities, conditions similar to neutron stars should be observed, and for even higher densities *color superconductor* phase is predicted. The figure also shows axis with dependence on difference of neutron and proton densities, indicating presence of compact stars.

2.2 Proton-ion collisions

In order to precisely differentiate effects of medium created in heavy ion collisions, the initial state of colliding particles has to be understood. Moreover, there is a difference between initial state of the heavy-ion collision and proton-proton collision, to which all the relevant comparisons are done. To get a hold of this difference collisions of heavy ions with protons or leptons are studied.

The lepton-ion deep inelastic scattering (DIS) serve mainly to study structure of ions similarly to lepton-proton collisions with nuclear parton distribution functions (nPDF) as significant contribution. These distribution describe probability of finding given quark flavour in ion with given fraction of ion's momentum. Their importance is their process independence and therefore they are used in factorised calculations of any hard process. For heavy ions, nPDFs are usually described as modification of proton PDFs, as seen in Fig. 2.2, where gluon PDFs in Pb ion are shown at two different scales using EPS09, HKN, FGS10 and nDS parametrisations.

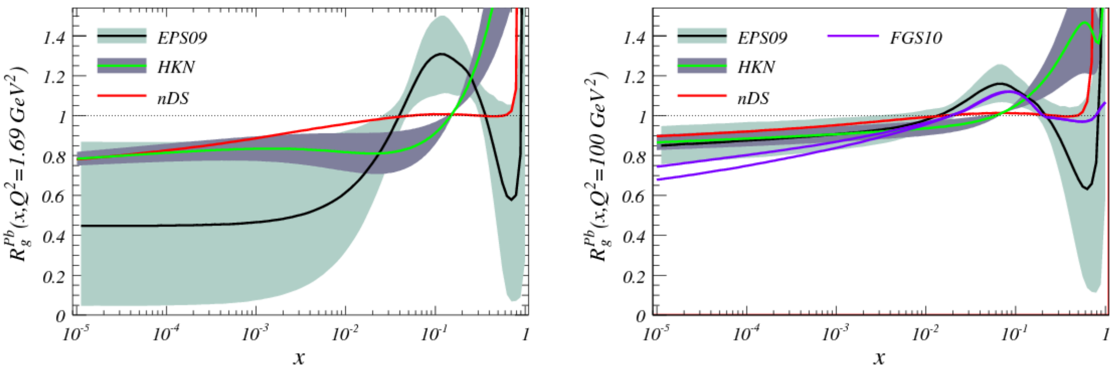

Figure 2.2: Nuclear PDFs shown for gluons in lead ion for Q^2 equal to 1.69 GeV^2 and 100 GeV^2, left and right, respectively. These nPDFs are obtained from EPS09, HKN nDS and FGS10 parametrisations. Figures are adapted from Ref. [25]

Furthermore, proton-ion collisions serve to disentangle properties of hard processes from initial state effects through observables, such as charge particle or jet R_{A+B}. This will be discussed later together with pure heavy-ion collisions at the end of the chapter.

2.3 Heavy-ion collisions

As mentioned at the beginning of this chapter, heavy-ion collisions study properties of media. The collision space-time evolution is depicted in Fig. 2.3, and undergoes several steps. In the first stage, the hardest processes take place, even before thermal equilibrium is reached, expected at 1 fm/c. The stage with thermal equilibrium is the stage when QGP is created, however due to expansion, it cools down and partons start to convert into hadrons. This hadronisation is not instantaneous in the whole fireball but spreads at the speed of sound.

After hadronisation, hadrons keep re-scattering in the fireball for a while, until the distances between them are too big , so they decouple completely. This is called *freeze-out* and one is *chemical*, when hadron abundance are not changing any more due to the small rates of inelastic processes, and the second freeze-out is *kinetic*, when kinetic energies of these hadrons stop changing. Subsequently, only decays of unstable hadrons take place.

Among the signature observables for QGP mentioned in Sec. 2.1 are included changes to chemical composition, collective behaviour of medium and changes to kinematics of hardest probes passing through the medium. Collective flow, result of collective behaviour of thermalised medium, includes *radial flow* and *elliptic flow*. By definition it describes correlation between momenta of particles and their origin. The radial flow can be observed spectra of identified particles as a function of $m_T - m_0$ variable. Due to the fact that

$$p_{\mathrm{T}}^2 = m_T^2 - m_0^2, \tag{2.1}$$

and for $p_{\mathrm{T}} \gg m_0$, p_{T} is identical with m_T, variable p_{T} is used as well. Observed spectra are fitted in order to obtain information about temperature of medium and speed of

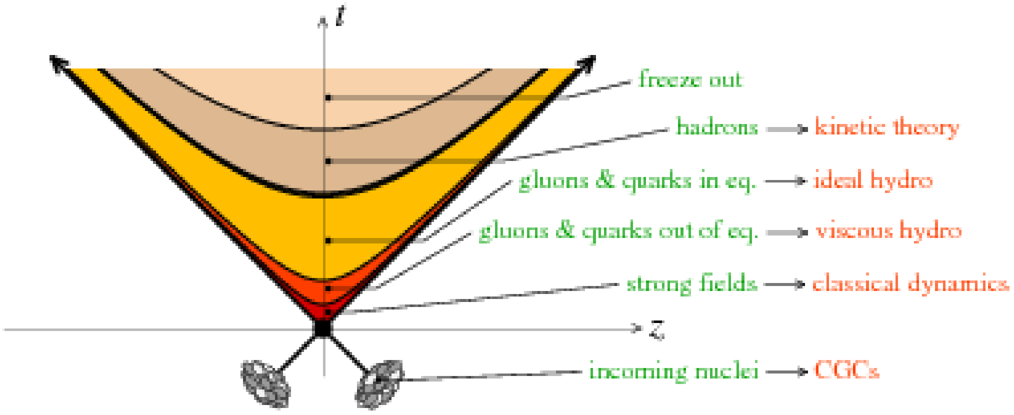

Figure 2.3: Drawing of evolution of heavy-ion collision from colliding incoming nuclei at the bottom, through classically produced strong interactions, before establishing of quarks and gluon medium. This thermalises and follows ideal hydrodynamics, followed by its freezout into hadrons. Adapted from Ref. [26].

transverse expansion. Such observation were done by PHENIX collaboration, Ref. [27], and NA49, Ref. [28].

The second type, elliptic flow, represent kinematic anisotropy that is created due to spacial deformation. In the collisions of heavy ions, centrality of collisions is important descriptor. It is a measure of how precise are the collisions in terms of distance between centre of colliding ions, so called impact parameter. This separation can be imagined as distance between centres of two overlapping circles. More central the collision greater the area of the common overlap. However, more peripheral collision leads to almond-shaped overlapping region and different pressure gradients in different directions from centre to border of the overlap region[1]. These anisotropies are observed as non-zero coefficients of the Fourier transformation of particle spectra,

$$\frac{\mathrm{d}N_i}{\mathrm{d}y p_\mathrm{T} \mathrm{d}p_\mathrm{T} \mathrm{d}\varphi} = \frac{1}{2\pi} \frac{\mathrm{d}N_i}{\mathrm{d}y p_\mathrm{T} \mathrm{d}p_\mathrm{T}} \left(1 + 2v_2^i \cos 2\left(\varphi - \varphi_p\right) + \dots\right), \tag{2.2}$$

where $\varphi - \varphi_\mathrm{p}$ represents relative angle from collision plane, defined by impact parameter and direction in which the ions are moving.

Statistical hadronisation encompasses changes in chemical composition of observed final-state particles, and includes phenomena such as *strangeness enhancement* and *suppression of J/Ψ production*. Compared to smaller systems, dramatic increase in strangeness production is observed in heavy-ion collisions. It cannot be created in hadronic rescatterings and therefore originates from rapid strangeness production mechanism from thermal gluons, predicted in Ref. [29].

Strangeness suppression in smaller system can be understood from statistical approach where strong interactions conserve strangeness without fluctuations, where conserving strangeness has to be created in the same small volume. However, for large fireballs

---

[1] This is true for spherical ions, however, non-spherical ions or deformed ions lead to non-zero higher order coefficients of the Fourier transformation.

created by heavy ions, these balancing strange particles do not have to be created nearby, but within the whole volume of the large system.

Suppression of J/Ψ production as observable was suggested in Ref. [30]. Because basic mechanism for deconfinement is via Debye screening of colour charge, quarks no longer hold together if binding radius, specific for given quarkonia, is larger than screening radius. The latter is inversely proportional to temperature of the medium.

Quarkonia melting may serve as a “thermometer” of the medium as different quarkonia states are melted away at different temperatures, due to the different binding radii, specific to each quarkonia, as suggested in Ref. [31].

However, quarkonia suppression is not only due to their melting because of medium temperature. Their production is modified via modification of PDFs. When they are created in the earliest stages of collision and therefore interact with it, by rescattering and energy loss.

Lastly, the most important observable of hot and dense medium in the scope of this work is energy loss of hard partons, i.e. jet quenching.

2.3.1 Jets in from heavy ions

Hard probes, as mentioned for the case of heavy flavours, are created in the earliest stages of the heavy-ion collision, and interact with medium as they pass through it. This was observed by STAR experiment in di-hadron azimuthal correlations, where jet-like structure is observed around trigger hadron, however, no such structure is observed on the opposite away-side, at $\Delta\phi \approx \pi$, in Au+Au collisions, Fig. 2.4. This disappearance of low p_T particles is explained by interaction if partons travelling through hot and dense medium and their rescattering at large angles with respect to original direction.

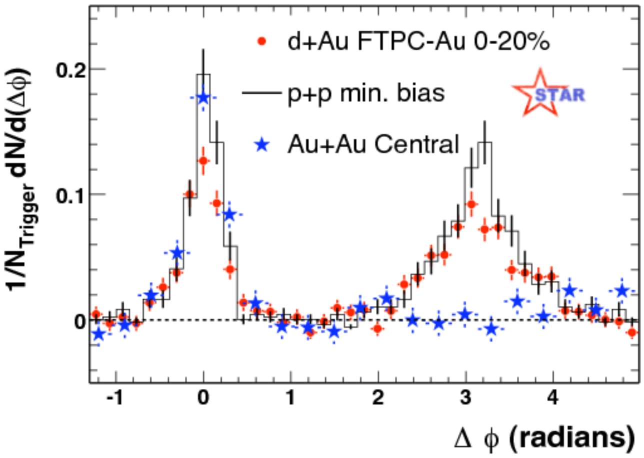

Figure 2.4: Di-hadron correlation of charged hadrons selected within defined p_T ranges in p+p, d+Au and Au+Au collisions with centre of mass energy of 200 GeV per nucleon. These correlations show disappearance of away-side peak in Au-Au collisions, explained by interactions of partons travelling through medium. Figure adapted from Ref. [32].

The most notable observable used to study energy parton energy loss is nuclear modification factor for jets and charged hadrons,

$$R_{\mathrm{A+B}} = \frac{\mathrm{d}^2 N_{\mathrm{A+B}}/\mathrm{d}y\mathrm{d}p_{\mathrm{T}}}{\langle T_{\mathrm{A+B}}\rangle\, \mathrm{d}^2\sigma_{\mathrm{pp}}/\mathrm{d}y\mathrm{d}p_{\mathrm{T}}}, \tag{2.3}$$

where yields are compared to cross sections obtained from proton-proton collisions, scaled by nuclear thickness factor dependent on number of participating nucleons and ion cross section. However, in case proton baseline is not available, comparison between central and peripheral collisions are made,

$$R_{\mathrm{CP}} = \frac{\left\langle T^{\mathrm{P}}\right\rangle \mathrm{d}^2 N^{\mathrm{C}}/\mathrm{d}y\mathrm{d}p_{\mathrm{T}}}{\langle T^{\mathrm{C}}\rangle\, \mathrm{d}^2 N^{\mathrm{P}}/\mathrm{d}y\mathrm{d}p_{\mathrm{T}}} \tag{2.4}$$

These peripheral collisions are in limit approaching results from proton-proton collisions.

In case of charged hadrons, Fig. 2.5a, their suppression in lead-lead collisions for both central and peripheral collisions, red and green markers respectively. However, for the proton-lead collisions, only low-p_{T} hadrons are suppressed indicating that the harder the particle, the smaller the effect of cold nuclear collision. Above 3 GeV/c, the result is consistent with unity[2]. Furthermore, these are consistent with CMS results, Fig. 2.5b from Ref. [34] with results from RHIC and SPS show suppression behaviour for different systems, i.e. gold-gold collisions at 200 GeV per nucleon at RHIC and lead-lead collisions at 17.3 GeV per nucleon at SPS. These results show dependence of nuclear modification factor on energy of colliding particles. As the energy decreases, the modification factor increases towards unity. Additionally, a wide range of theoretical predictions is plotted over these data.

Moving to higher transverse momenta, charged hadrons can be "substituted" by jets, which provide information about quark of gluon they originate from. This provides information about hard parton's modification in medium which reflects into nuclear modification factor. In Fig. 2.6a nuclear modification factors for charged hadrons (left) and jets (right) are shown. These two plots have "common" x-axis, however, due to the fact that jets are compound objects created from hadrons, jet region from 100-200 GeV/c and hadron region from 50-100 GeV/c sample approximately same kinematic region of parton. Keeping this fact in mind, the figure shows continuous transition from observed modification of hadrons to jets for 5% of the most central collisions. This conclusion is possible thanks to observation, [36], that fragmentation in Pb+Pb collisions are consistent within systematic uncertainties except for hadrons with the lowest transverse momenta.

Due to the unavailability of similar measurements from the ALICE collaboration, in Fig. 2.6b are shown R_{CP} modifications combining charged hadron suppression measured by the ALICE and CMS collaborations, charged jets from ALICE and calorimetric jets from ATLAS. Notable difference between high-p_{T} hadrons and low-p_{T} jets is again due to the fact that given jet interval describes hadrons from interval of smaller transverse momenta.

---

[2] However, there are no proton-proton collisions at appropriate energy, therefore the baseline is obtained by interpolating data from 2.76 TeV and 7 TeV and Monte Carlo simulations.

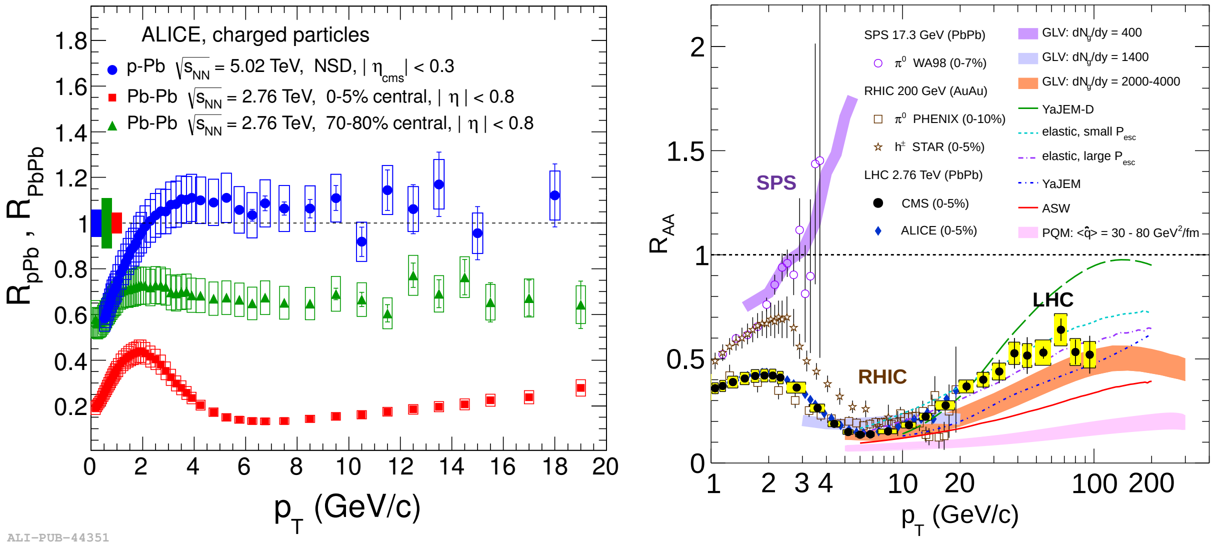

(a) ALICE $R_{\mathrm{Pb+Pb}}$ for different systems (b) charged hadron $R_{\mathrm{A+A}}$ compilation

Figure 2.5: Left plot shows dependence of charged hadron nuclear modification factor on centrality, with the most central 5% of Pb+Pb collisions producing largest suppression (red), and peripheral collisions (green) yielding suppression factor between 0.6 and 0.7. In the minimum bias p+Pb collisions (blue) the lowest p_{T} hadrons are suppressed by the factor up to 0.6 and this suppression decreases with higher p_{T} . No suppression is observed from approximately 3 GeV/c onward. The right plot shows compilation of obtained charged hadron nuclear modification factors from wide range of experiments at different collision energies. These results show consistent suppression observed by the ALICE and CMS collaborations, and decreasing suppression with decreasing collision energy, as shown by RHIC and SPS data. SPS data show opposite trend, i.e. enhancement for p_{T} above 2.5 GeV/c, however errors make this measurement inconclusive. Figures are adapted from [33] and [34], respectively.

Similarly to nuclear modification in Pb+Pb collisions, such information is obtained from p+Pb collisions. Contrary to the model predictions, charged hadron exhibits enhancement peaking at approximately 80 GeV/c observed by the ATLAS and CMS collaborations. The ALICE collaboration cannot reach such large p_{T} with current statistics available. However, nuclear modification of jet spectra show no such modification and are consistent with unity over a wide rapidity[3] and p_{T} range for minimum bias collisions. The difficulty for these type of collisions arises in non-existent proton-proton baseline at this energy and baseline used is obtain either from PYTHIA simulations or interpolation from measurements at 2.76 TeV and 7 TeV energies.

Minimum bias jets, as analysed by ATLAS [39], exhibit minimal modification in rapidity intervals spanning from -2.1 up to 2.8 units of rapidity. This is in accordance with EPS09 predictions for these energies. However, when selecting jets from specific event centralities, most central collisions, 0-10%, exhibit suppression of jet spectra for

---

[3] Rapidity and other kinematic variables will be properly defined in Sec. 3.3.1.

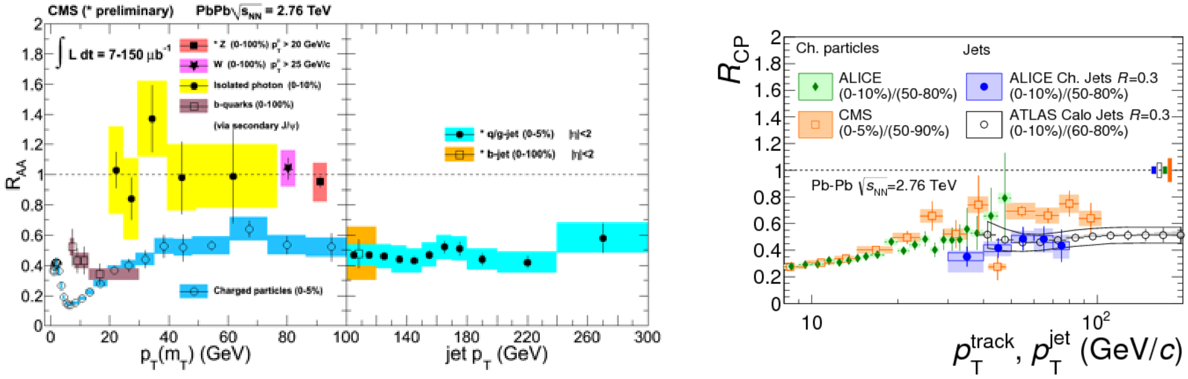

(a) Jet and charged hadron R_{Pb+Pb} in Pb+Pb.

(b) Jet and hadron R_{CP} in Pb+Pb.

Figure 2.6: Left plot shows nuclear modification factor observed in CMS using hadrons and jets and Right plot describes nuclear modification via comparison of results from central and peripheral collisions using hadrons and jets from ALICE, with additional information from ATLAS calorimetric jets and CMS hadrons. Figures adapted from Ref. [37] and Ref. [38].

high transverse momenta and the most peripheral collisions, 60-90% enhancement in the region of high transverse momenta. Moving from forward rapidity bins the suppression and enhancement is exhibited at 40 GeV/c, i.e. lower bound of bin with smallest p_T . However, in case of the most central jet bin statistically significant changes can be observed in p_T -bin at approximately 300 GeV/c. More backward rapidity regions do not have enough statistics to show significant changes.

Modification of forward rapidity bins observed via comparison of R_{CP} is found to obey scaling relation in total jet energy.

In order properly evaluate effects of cold nuclear medium and avoid using comparison between two different centralities, which pose more complicated question than in lead-lead collisions, proton-proton baseline is required. More so for the results without centrality selection where simulations or interpolations from other energies were used as a baseline.

To sum it up the LHC experiments have collected about 150 μb^{-1} of data in first two runs with lead ions involved in collisions. Estimation of centralities is done by dividing forward multiplicity into appropriate percentiles of collected events yielding good agreement with overlap geometry calculated from Glauber models. Detailed studies of identified particle yields are consistent with thermal models and strange hadrons are enhanced in these collisions.

Various scaling behaviours are observed in the measurements of collective flow. For example, in the LHC collisions, harmonics up to v_6 are observed and these measurement allow more thorough tests of hydrodynamic models.

The hard processes were calibrated using measurements of electro-weak probes like photons and W or Z bosons. These calibrations, where no modification by QCD medium is expected, required minimal modification of distributions of partons involved. This provides confidence for the results of hard probes, attributing modification in central collisions to the energy loss when travelling through QCD medium. The energy loss

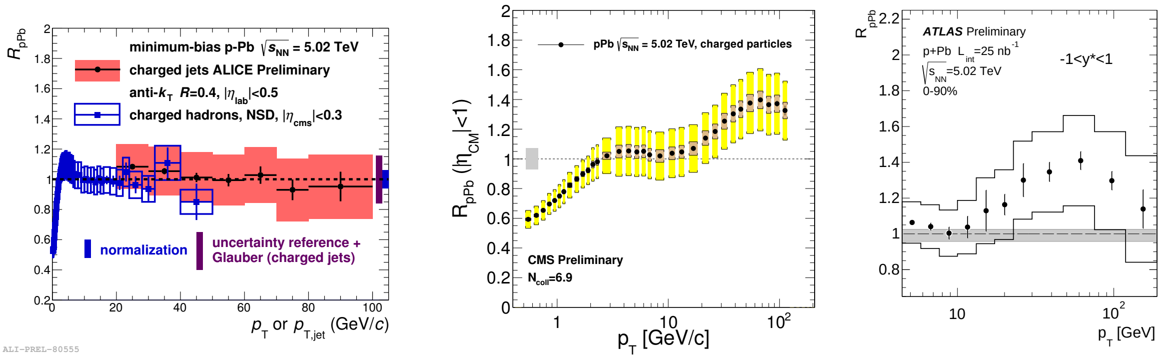

(a) charged hadrons and jets in ALICE (b) Hadrons in CMS (c) Hadrons in ATLAS

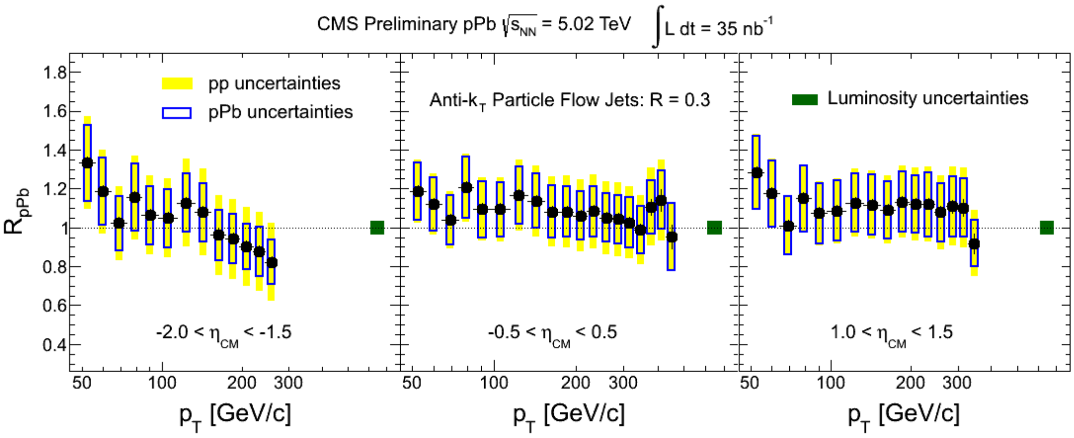

(d) Jets from CMS

Figure 2.7: Left figure shows combined measurement of charged hadron and charged jet $R_{\mathrm{p+Pb}}$ from the ALICE collaboration. These two measurements are consistent within uncertainties. However, the reach in hadron measurement is insufficient to observe similar structure as does CMS and ATLAS, center and right figures, at approximately 80 GeV/c. In the bottom figure $R_{\mathrm{p+Pb}}$ measurement from CMS for different rapidity regions with minimum bias selection show that results are consistent with unity. Figures are adapted from Ref. [40–42].

is addressed also by di-jet imbalance and inclusive and azimuthally differential single jet suppression or by jet correlations with photons. On the other hand, only mild modification around the jet axis is seen from the changes of jet shapes, i.e. transverse distribution of energy from jet axis.

The heavy flavours are produced in large numbers at the LHC and are important probe as they are expected to exhibit different behaviour than light flavours. Strong suppression is observed in case of D mesons and J/Ψ, however for low p_{T} of suppression of J/Ψ are not suppressed as in case of RHIC, suggesting presence of regeneration processes. Additionally, D mesons flow similarly as soft particles. Surprisingly, Υ are suppressed however weakly bound states are more suppressed than 1S state.

The plans for future data-taking aim to improve statistics of rare processes and observables. This requires not only improvements to delivered luminosities but also upgrades for the detectors. Furthermore, RHIC heavy ion program allows study of heavy ions collisions for smaller energies, but different heavy ion nuclei, such as copper and gold. Additionally, beam energy scan program enables investigation of observables with changing value of energy per nucleon.

The overview of knowledge obtained from collisions involving heavy ions proves without a doubt the presence of new modification of production mechanism in presence of medium. Furthermore, the collective behaviour of matter created few moments after heavy-ion collision, behaving in a way describable bby hydrodynamical models shows a large area of particle physics worth investigating. More about results from LHC can be found in Ref. [43].

Chapter 3. Jets

In chapter 1, concept of quarks and gluons and phenomenon of colour confinement, that no particle with colour charge can be observed on its own, was introduced. However, colour neutral particles, or white particles[1], are observed. In case of quarks we observe bound states, *hadrons*, which are composed of quark–anti-quark pair, *meson*, or three quarks, so called *baryon*. If separation between quarks in these bound states increases, potential energy of their bond also increases, according to formula (1.8). This increases until new pair of quark–anti-quark can be created from energy stored in this bond, as shown in Fig. 1.2. A sufficiently energetic parton can create several such pairs which result in *jet*. A simplified definition can state, that jet is final state of energetic parton, most commonly created in hard-scattering processes. It is therefore a clue on direction and magnitude of momentum carried by individual quark or gluon, as was seen in DESY experiments, where only sprays of collimated particles were observed in electron–positron collisions. TASSO detector provided picture of 3 jet event of $q\bar{q}g$ production from electron–positron annihilation without any sophisticated method for their reconstruction, [17, 18][2].

3.1 Evolution of jet

With help of factorisation of hadron production formula, Eq. 3.1, we are able to differentiate individual steps and processes that take place when jets are created.

---

[1] In analogy with optical observation when shinning red, blue and green lights over each other, observer sees white light, when particles creates colour neutral singlet state we say that it is white.

[2] These observations were used as a evidence for gluons. However, evidence for existence of gluons was provided earlier by the PLUTO collaboration from decays $\Upsilon \to ggg$, [19]. Due to the high mass of Υ, significant non-perturbative contributions had to be taken into account.

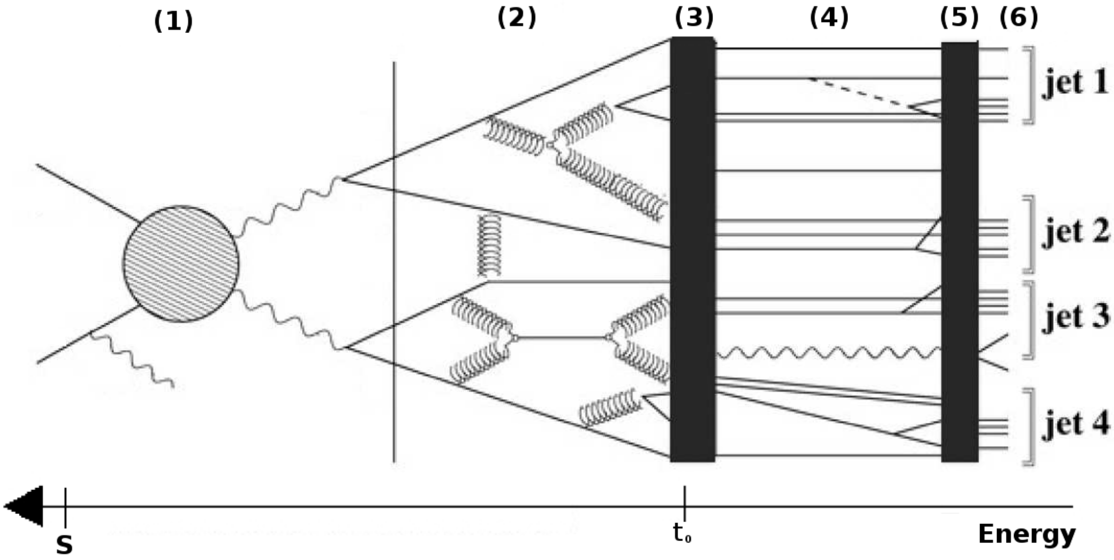

Figure 3.1: Schematic evolution of jet with individual steps corresponding to factorisation of hadron production. Energy axis represents decreasing energy scales of individual partons as they evolve from scattering (1) to final jet reconstruction (6). Step (1) represents scattering of partons within incoming colliding hadrons, with possible initial state radiation before actual hard-scattering process, shown as blob. Energy scale at this moment, S, corresponds to energy in s-channel of scattering process, which is calculated from PDFs of colliding hadrons. Step (2) represents fragmentation of original scattered partons. Theoretical calculation of this step is based on model used and may implicitly account for FSR from these scattered partons. Step (3) denotes energy scale, t_0, at which hadronisation occurs. Step (4) represents decays of unstable particles, such as 2 photon decay ofπ^0. In step (5), detector reconstruction occurs, constraining information given to jet reconstruction algorithms producing final jets, step (6). Figure adapted from Ref. [20].

$$
\begin{aligned}
E\frac{d^3\sigma}{d\vec{p}} = & \sum_{abcd}\int dx_a dx_b dz_c f_{a/p}\left(x_a,\mu_F^2\right) f_{b/p}\left(x_b,\mu_F^2\right) \otimes \\
& \otimes \left.\frac{d\sigma}{dt}\right|_{a+b\to c+d}\left(x_a, x_b, \alpha_S\left(Q^2,\mu_R^2\right), \frac{Q^2}{\mu_R^2}, \frac{Q^2}{\mu_F^2}\right) \otimes \\
& \otimes F_{h/c}\left(z_c,\mu_F^2\right).
\end{aligned}
\tag{3.1}
$$

Comparing schematic jet evolution in Fig. 3.1 and hadron factorisation formula, 3.1, we can separate whole evolution process. These are *initial stage*, dealing mainly with colliding particles, then perturbative *hard scattering stage*, marked by (1) in Fig. 3.1. *Fragmentation*, (2) and *hadronisation stage*, (3) incorporate non-perturbative aspects of QCD.

Last two stages, as marked in Fig. 3.1, before jet reconstruction using algorithms, (6), incorporate decays of unstable particles, (4), and effects of detector reconstruction, (5).

3.1.1 Initial evolution

In order to be able to calculate scattering cross-section of any process, we have to have information about incoming particles that interact. For case of leptonic collisions, this information is directly accessible from measurements of scattered colliding lepton, however when we have hadrons as beam particle we have to deal with a many unknown variables, as hadrons are composite particles. If we do not deal with specific exclusive processes, all possible particles have to be considered as an option with wide range of acceptable energies. Because incoming particles are used in head-on collisions at extremely high energies, we consider only longitudinal motion of partons, quarks or gluons, with respect of hadron they are part of. This is denoted as variable x with subscript indicating its parton type and hadron it originated from. Probability that parton i was found with momentum fraction x of hadron Y is given by *parton distribution function*, $f_{i/Y}\left(x_i, \mu_F^2\right)$ and as a probability it satisfy relation

$$\int_0^1 dx_i f_{i/Y}\left(x_i, \mu_F^2\right) = 1. \tag{3.2}$$

In order to satisfy all possible momentum fractions, integration over whole range of momenta is done for all incoming partons.

These PDFs are obtained from deep inelastic scatterings, where lepton–hadron collisions are studied. Change in momentum of incoming lepton gives exact value of transfered momentum in t-channel scattering. No change of scattered lepton indicates **neutral current** processes with photon as the most likely intermediate particle, on the other hand change in charge by $1\,e$ indicate **charged current** processes with $W^{\pm}$ bosons as mediated particle. Experiments with dedicated DIS programme are e.g. H1 and ZEUS at HERA. These measurements are analysed by different theory groups and one result of such analysis, processed into CT10 PDF datasets [21], is shown in Fig. 3.2. In Fig. 3.2a and Fig. 3.2b are shown parton distributions scaled by $3x^{5/3}$ for better lucidity at low momentum fractions, x. Theoretical expectation of these PDFs are tested in Fig. 3.2c, where cross sections are calculated as a function of transferred momenta, Q^2, for different momentum fractions, x. These calculations are in agreement with data from HERA experiment.

Effects concerning incoming particles are *initial state radiation* and represent additional radiation from interacting parton before hard scattering itself. This can result in additional modification of energies of scattered partons and modification of basic process resulting in multiple outgoing particles. With increasing energies these emission becomes more important to fragmentation.

3.1.2 Hard-scattering and final state radiation

In context of colliding beams in storage ring, majority of multipurpose detectors focuses on physics in transverse direction with respect to direction of colliding beams. Hard scattering represents set of processes, where scattered particles have high momenta at transverse directions, however hard scatterings in general are processes with large transferred momenta.

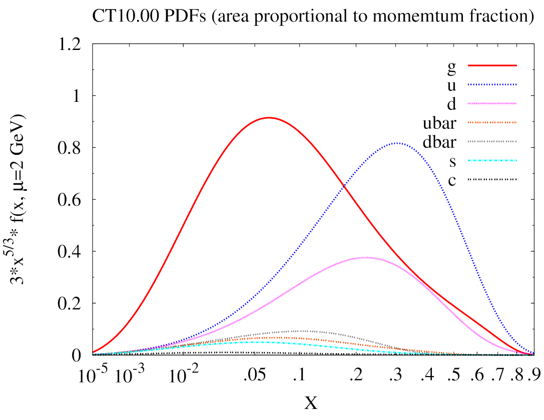

(a) Parton PDF at $\mu = 2\,\mathrm{GeV}$

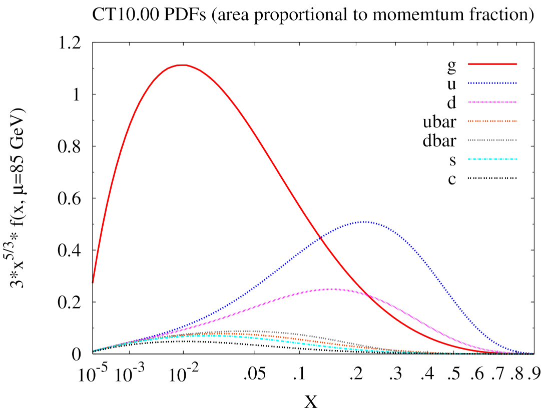

(b) Parton PDF at $\mu = 85\,\mathrm{GeV}$

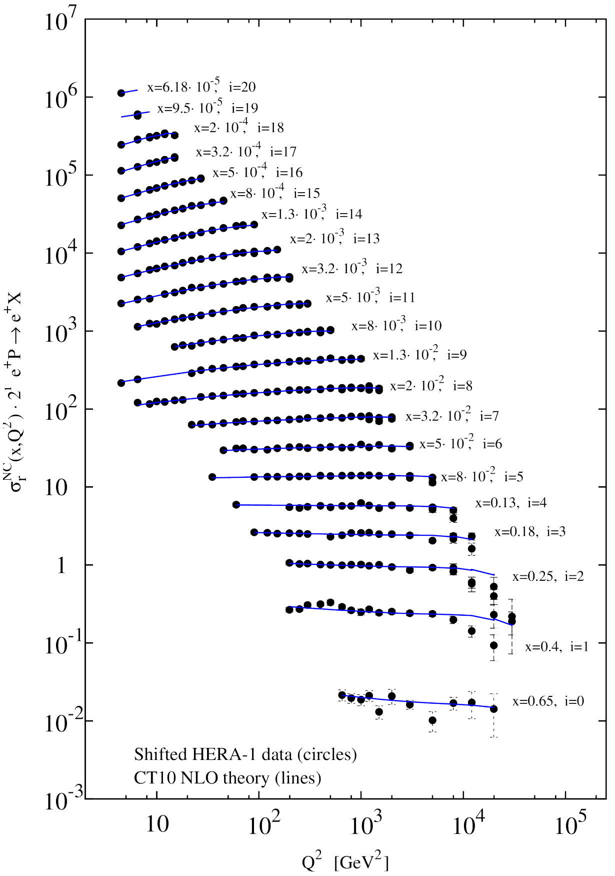

(c) Combined H1/ZEUS data provided by HERA with systematic shifts compared to predictions obtained using CT10 PDF datasets.

Figure 3.2: CT10 PDFs at $\mu = 2\,\mathrm{GeV}$, 3.2a, and $\mu = 85\,\mathrm{GeV}$, 3.2b, obtained by global fits of joint data released by H1 and ZEUS collaborations at HERA *ep* collider. These are central datasets without any error evaluation, and μ denotes factorisation scale used in calculation. In plot 3.2c are comparisons of next-to-leading order predictions using CT10 PDF datasets for reduced cross sections in $e^{+}p$ neutral-currents DIS with combined HERA data, including correlated systematic shifts. These shifts are estimated from correlation matrix provided by HERA experiments.

Leading order processes relevant for jet production are shown in Fig. 3.3, with dominant process of gluon–gluon scatterings. Additional processes include quark–gluon scattering, quark scattering and annihilation.[3]

These are main contributors to jet production cross section written in form of Mandelstam variables.These calculations are well understood because hard scattering is

---

[3] Another interesting process for jet analyses is production of jet with photon. This process can give handle on calibration of jet energy using this electromagnetic probe and could enable precise study of jet energy loss. Due to the fact that photon emission is suppressed in comparison with purely strong processes, abundance of events containing such interactions is smaller.

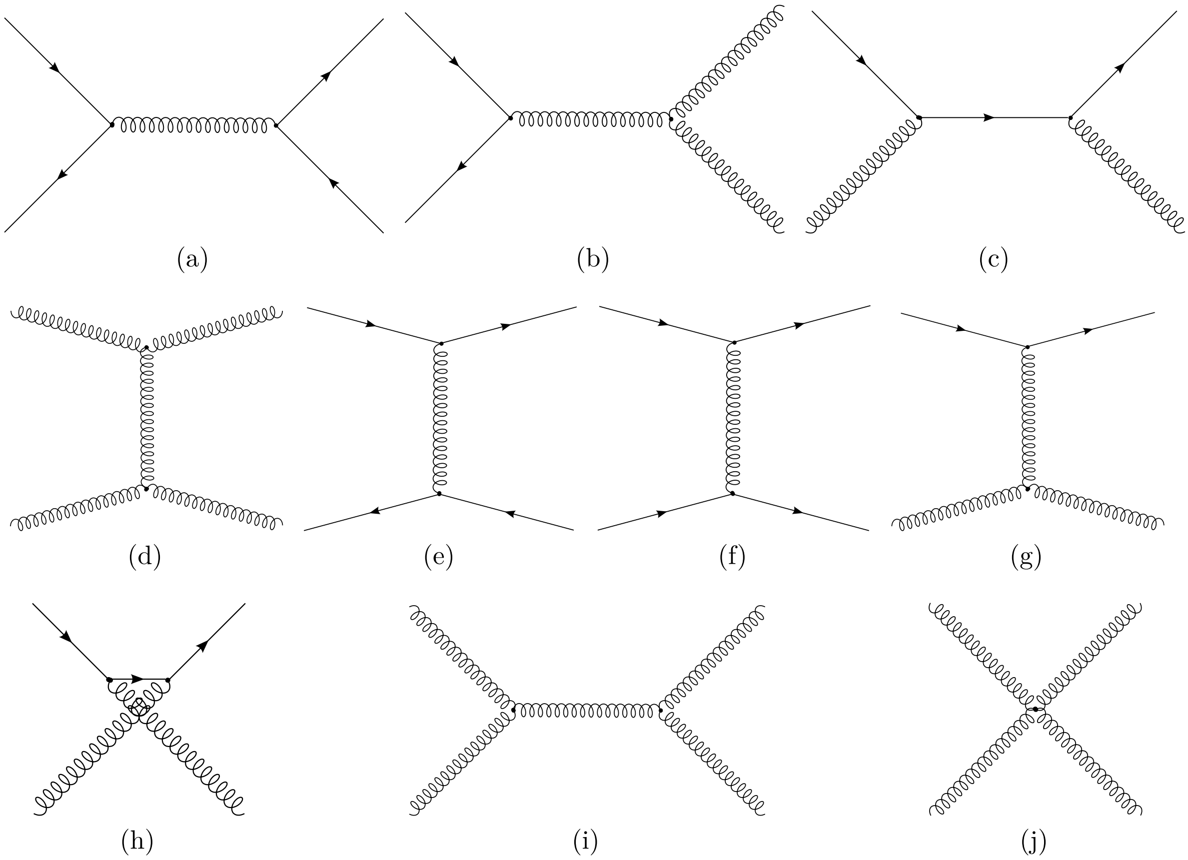

Figure 3.3: There are several leading order processes, speaking about parton scatterings, that are shown in (a)-(j). The most significant contribution for midrapidity scatterings comes from $gg \to gg$, represented by (d),(i) and (j).

calculable using perturbative QCD and this cross sections are calculated using formula

$$\left.\frac{d\hat{\sigma}}{d\hat{t}}\right|_{a+b\to c+d} = \frac{1}{16\pi\hat{s}^2}\left|\mathcal{M}\right|^2 \tag{3.3}$$

where all variables are in centre of mass system, denoted by hat above these variables, and scattering amplitudes, $\mathcal{M}$, are calculated in Tab. 3.1 for different processes.

Similarly to ISR, scattered partons may produce *final state radiation*, which changes topology of scattering and affects non-perturbative fragmentation of partons into jets.

3.1.3 Fragmentation and Hadronisation

By term fragmentation, we understand all possible processes leading to final hadron and is described by final component of (3.1), fragmentation function

$$F_{h/c}\left(z_c, \mu_F^2\right). \tag{3.4}$$

describing probability that final hadron h originating from parton c carries z_c fraction of partons momentum. Its normalisation is given by average multiplicity of hadrons coming

Subprocess	$\lvert\mathcal{M}\rvert^2/g_S^4$	$\lvert\mathcal{M}(90^o)\rvert^2/g_S^4$
$q_\alpha q_\beta \to q_\alpha q_\beta$	$\frac{4}{9}\left(\frac{\hat{s}^2+\hat{u}^2}{\hat{t}^2}+\frac{\hat{s}^2+\hat{t}^2}{\hat{u}^2}\delta_{\alpha\beta}\right)-\frac{8}{27}\frac{\hat{s}^2}{\hat{u}\hat{t}}\delta_{\alpha\beta}$	
$q_\alpha \bar{q}_\beta \to q_\alpha \bar{q}_\beta$	$\frac{4}{9}\left(\frac{\hat{s}^2+\hat{u}^2}{\hat{t}^2}+\frac{\hat{t}^2+\hat{u}^2}{\hat{s}^2}\delta_{\alpha\beta}\right)-\frac{8}{27}\frac{\hat{u}^2}{\hat{s}\hat{t}}\delta_{\alpha\beta}$	
$q\bar{q} \to gg$	$\frac{32}{27}\frac{\hat{u}^2+\hat{t}^2}{\hat{t}\hat{u}}-\frac{8}{3}\frac{\hat{t}^2+\hat{u}^2}{\hat{s}^2}$	1.0
$gg \to q\bar{q}$	$\frac{1}{6}\frac{\hat{u}^2+\hat{t}^2}{\hat{t}\hat{u}}-\frac{3}{8}\frac{\hat{t}^2+\hat{u}^2}{\hat{s}^2}$	0.1
$qg \to qg$	$\frac{\hat{s}^2+\hat{u}^2}{\hat{t}^2}-\frac{4}{9}\frac{\hat{s}^2+\hat{u}^2}{\hat{s}\hat{u}}$	6.1
$gg \to gg$	$\frac{8}{9}\left[-\frac{33}{4}-4\left(\frac{us}{t^2}+\frac{ut}{s^2}+\frac{st}{u^2}\right)\right]-\frac{9}{16}\left[45-\left(\frac{s^2}{ut}+\frac{t^2}{us}+\frac{u^2}{st}\right)\right]$	30.4

Table 3.1: Invariant amplitudes for different QCD scattering processes defined using Mandelstam variables s, t and u. Subscripts in first two rows indicate colours of scattered quarks and anti-quarks. Last column represents relative yield at the angle of 90^o in centre of mass system. However, as the first two processes depend on colour and in quark annihilation, different flavour may be created with relative yield at midrapidity of 0.2, yield are omitted. Contribution of these quarks scatterings is less than contribution from quark–gluon scattering.

from partons $\langle N_q \rangle$

$$\int_0^\infty \int_0^1 F_{h/c}\left(z_c, p_T\right) dz_c dp_T = \langle N_c \rangle. \tag{3.5}$$

4

This usually involves radiation of gluons or quark–anti-quark pair creation from original parton, calculated using DGLAP splitting functions (3.6),

$$\begin{aligned}
P_{q\to qg} &= C_F\left(\frac{1+z^2}{1-z}\right), \\
P_{g\to q\bar{q}} &= T_R\left(z^2+(1+z)^2\right), \\
P_{g\to gg} &= C_A\left(\frac{z^4+1+(1-z)^4}{z(1-z)}\right), \\
P_{q\to gq} &= C_F\left(\frac{1+(1-z)^2}{z}\right).
\end{aligned} \tag{3.6}$$

Here z is fraction of momenta split and therefore showers are dominated for values $z \to 0$ or $z \to 1$, i.e. collinear region, where no or all momenta are transferred and both particles continue in original direction.

In theoretical calculations, fragmentation processes lead to parton energy loss, until certain hadronisation scale is reached, (3) in Fig. 3.1, when final hadrons are formed. This is a result of long distance regime where perturbative theory breaks down.

---

[4] AKK

Additionally, multiple other partons are being produced, usually moving in general direction of original parton. This so-called showering process has to be specifically addressed by Monte Carlo shower generators, used for description of jets and comparison of theoretical models with experiment.

To implement hadron production into Monte Carlo, fragmentation and hadronisation have to be treated independently.

Lund string model

Lund string model is probabilistic in its nature and iterative and is described in terms of few underlying branchings. Instead of fragmenting of partons, colour string is stretched and broken between quark and anti-quark moving apart. Strings area broken into 2 colour singlet strings, as long as the invariant mass of string is greater than the on-shell mass of hadron. Pairs of particles are generated according to probability of tunnelling process, leading to flavour independent Gaussian spectrum for transverse momenta of quarks and suppression of heavy quarks due to their mass. Meson production follows idea that mesons are short pieces of string between two quark–anti-quark endpoints. On the other hand, baryon production is harder to generalize. It can be looked upon it as if quark was represented as an anti-diquark or baryon appears from successive productions of several quark–anti-quark pairs. Two free parameters must be adjusted to fit data with predictions using this model.

Cluster model

This model generates partons in branching process which tend to be arranged in confined colour-singlet clusters. Mass of these clusters is confined by infra-red cut-off in parton shower. After parton showering, clusters are split nonperturbatively into quark – anti-quark pairs. This model does not require fragmentation functions or any free parameters to describe transition. Each cluster typically decays into two hadrons depending on mass of cluster.

Independent fragmentation model

In this model, fragmentation of any system of partons is described by incoherent sum of independent fragmentation of individual partons. It is iterative process, where fragmented result is collinear with remainder of original system of partons. This remainder is just scaled version of original system. Internal inconsistencies arise within this model, therefore it is used just for special cases.

Basic comparison of these models can be seen in Tab. 3.2 and more about hadronization models can be found e.g. in Ref. [22].

3.1.4 Particle decays

Following hadronisation decay of unstable particles occurs, such as decay of top quark before forming bound meson or decay of $W^{\pm}$ and Z bosons, $\pi^0 \rightarrow \gamma\gamma$ that occur at the

	Hadronisation Model			
Feature	Cluster	Independent	String	
			Lund	UCLA
Principle	very simple	simple	complex	less complex
Lorentz invariant	yes	no	yes	
Conservation laws	automatic	ad hoc	automatic	
Mass dep. via	hadrons	quarks	quarks	hadrons
Stangeness supp.	predicted	free param.	restricted param.	predicted
Baryon supp.	predicted	free param.	restricted param.	predicted
J^P ratios.	predicted	free param.	restricted param.	predicted
Limited p_T	natural	built in	built in	natural
FF	–	Free	Restricted by L-R symmetry	
Cut-off dep.	significant	very strong	modest	
Stability problem	IR	Collinear	stable	
Limitations	Massive clusters like strings	requires large cut-off	light string as clusters	
Used in	HERWIG	ISAJET	PYTHIA	

Table 3.2: Comparison of different hadronisation models, i.e. cluster hadronisation, independent hadronisation and string hadronisation in form of it's two different approaches, Lund string model and UCLA model. Different features, such as lorentz invariance, approach to conservation laws, mass dependence etc., are listed, as well as limitations of these models and example of event generators which use these hadronization models.

distances close to interaction point of colliding partons. These decays are unavoidable and are undistinguishable from primary particles originating in collisions.

Another type of decays may be caused by interaction of particle with material without direct contribution to particle detection or identification. As an example may be photon conversion to electron-positron pair.

3.1.5 Detector effects

Detectors used in particle physics are based on measuring of transferred energy radiated by particle. This transfer is based on excitation or ionisation to the detector, however these are random processes. There are two main detector effects applicable to any experimental apparatus.

First is smearing of reconstructed energy that affects jet energy resolution. This is due to already mentioned randomness of ionisation and excitation. For charged particles, stopping power can be calculate using *Bethe formula*, determining portion of energy transferred from particle with given energy to detector volume. However number of collisions is given by value of its mean free path in given medium, therefore it is subject to fluctuations.

Second is efficiency of detector reconstruction. Total efficiency of detector is given by intrinsic efficiency, fraction of registered particles hitting detector, and geometric efficiency, given by fraction of particles going through detector with respect to all particles. Efficiency varies for different particle species, e.g. muons require special detectors due to their small interaction cross sections with materials used in detection of other particle types. These efficiencies are obtained from Monte Carlo simulations.

Furthermore, detection may be affected by pile-up. This results either from too slow detector readout of collisions, or multiple interactions happening in single triggered bunch crossing.

Additional detector effect originates in detector design. In HEP detectors, multiple observables are desired and therefore complex detectors are build. However, sometimes because of budget or construction reasons, not all detector types are used or cannot be used and therefore experiment may be suited only for analysis of charged particles and/or certain momentum ranges.

In case of jets, this can significantly constrain analyses, and only certain effects or processes can be studied.

3.1.6 Additional processes

There are, however, additional processes that may affect jet evolution and its reconstruction in collisions involving hadrons and we have to consider *milti-parton interactions*. This is due to its composite nature of hadrons. As accelerators reach higher energies, partons with same momentum fraction carry larger energy and, naturally, possibility of additional processes increases[5].

This means that additional soft processes are most likely to take place when hadrons collide and create so-called *underlying event*. This affects reconstruction of final jets, because we cannot distinguish final particles originating from soft and hard processes and needs to be studied on event-by-event basis.

Underlying event is studied by looking into transverse direction to the hardest track in event. This transverse region is located between angles $\phi_{trans} \in \left(\frac{\pi}{3}, \frac{2\pi}{3}\right)$ from this hardest track. By summing transverse momenta of all particles in this region, we are able to calculate energy density corresponding to UE. There can be restriction to rapidity or pseudo-rapidity of transverse region, depending on detector, as density depends on rapidity. For jet calculations, we have slightly modified this algorithm and it will be discussed in section 5.3.1 of this work.

In principle, UE is similar to background in heavy-ion collisions, where many nucleons from ion interact, however here the cumulative effect of UE processes is so much more pronounced, so that it produces significant correction to reconstructed jet energy. Fluctuations of this heavy ion background are induced by random Poissonian particle fluctuations, collision itself and detector effects like non-uniform efficiency of reconstruction.

---

[5] Cross section of process depends on momenta of colliding partons.

3.2 Experiment

Experimental jet picture differs from picture presented by theoreticians. We can only observe final state particles moving in one direction, because information about particle origin was lost during hadronisation phase of collision. Therefore, when speaking about *jets*, we speak about collimated sprays of particles.

Furthermore, additional effects can introduce further uncertainties and modifications requiring correction on overall jet energy scale. Among these effects are tracking efficiency, track momentum resolution and smearing and presence of underlying event. Effects connected to tracking are issue of detector reconstruction, however underlying event, as discussed in Sec 5.3.1, occurs due to the composite nature of colliding hadrons, where multiple interaction can occur simultaneously. Picture gets even less clear, when multiple particle sprays are present in given collision. Here, we must differentiate track or calorimetric towers belonging to more jets although they are close in momentum space.

As shown in Fig. 3.4, even same event can be considered as both 3-jet and 4-jet event, therefore vague definition presented at the beginning of this section has to be more specific and unambiguous. Furthermore, it has to be same for experiment and theory.

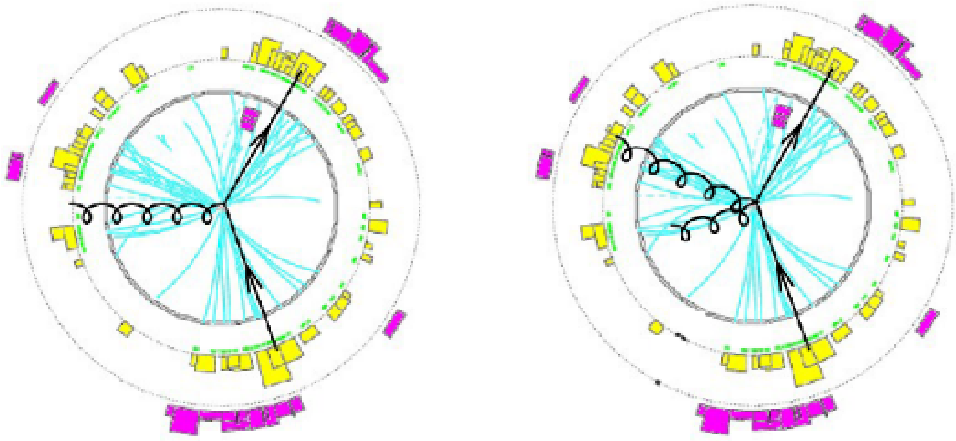

(a) 3-jet event.

(b) 4-jet event.

Figure 3.4: Same event in e^+e^- collision with different jet interpretations of produced particles. This sketch represents ambiguity of jet reconstruction, based on bias of observer analysing such events. Plots are adapted from Ref. [48].

3.3 Definition

In order to get rid of ambiguity of jet definition seen in Fig. 3.4, and for experimentalists and theoreticians to always use same reference, more thorough definition of jets is necessary. To do so, we define jets using several criteria.

First, jet is defined by *algorithm* used in reconstruction, which uses characteristic *parameters*. Most notable parameter determines resolution of algorithm, i.e. sampling area in azimuth and (pseudo-)rapidity or maximal separation between particles to be considered to be from same jet. The last defining criterion is *recombination scheme* used when combining different tracks or calorimeters into single jet.

3.3.1 Algorithms

The purpose of jet recombination algorithms is to reduce complexity of final state and connect it to QCD calculations. As mentioned before, we utilise space defined by azimuth, φ, and rapidity, y , which is determined by formula

$$y = \frac{1}{2}\left(\frac{E + p_{\mathrm{L}}}{E - p_{\mathrm{L}}}\right), \tag{3.7}$$

where p_{L} is longitudinal component of momentum with respect to beam axis[6]. When particle masses are neglected, formula 3.7 can be rewritten using polar angle, θ, introducing pseudorapidity,

$$\eta = -\ln\left[\tan\left(\frac{\theta}{2}\right)\right]. \tag{3.8}$$

Following spherical or cylindrical system of coordinates, azimuthal and polar angles are defined as

$$\varphi = \arctan\left(\frac{p_{\mathrm{y}}}{p_{\mathrm{x}}}\right), \tag{3.9a}$$

$$\theta = \arctan\left(\frac{p_{\mathrm{T}}}{p_{\mathrm{z}}}\right), \tag{3.9b}$$

respectively, where p_{T} is transverse projection of momentum.

We know two main categories of jet algorithms. These are *cone* algorithms and *sequential* algorithms. The main difference is their approach to particles [7] from point of view of clusterisation structure.

Properties of jet reconstruction algorithms

Among the main properties of jet reconstruction algorithms belongs its adaptability to hadronisation effects. When we are dealing with jet evolution as presented in section 3.1, we require that our jet algorithms reconstruct same jets at different stages of this evolution. This implies that jets reconstructed from LO or NLO partons is same as when jets are obtained from parton showers of these initial partons, as well as from hadrons.

---

[6] Beam axis is usually associated with z-axis of cylindrical coordinate system, hence use of azimuthal and polar angles.

[7] By particle in the context of reconstruction algorithms we have in mind either physical particles when used from theoretical point of view, or reconstructed tracks and calorimetric towers when used from experimental point of view and no further specification is present. These further specifications may arise from lack of tracking or calorimetric detectors.

Another important property of jet reconstruction algorithms is their *infra-red* and *collinear safety.* Infra-red safe jet algorithm is algorithm, that does not change reconstructed jets, even if soft particle is radiated between these jets. On the contrary, IR unsafe algorithm can change output of reconstruction, if such soft particle is radiated.

On the other hand, collinear safety is property of algorithm that ensures, that reconstruction is not affected when single parton radiates one or more collinear particles. Both these properties are necessary in order to calculate jets.

Cone algorithms

One of the algorithm types is *cone algorithm.* It uses partitional approach for clustering.

Algorithm starts by selecting sees, track or calorimetric tower, above some energy or momentum threshold. One seed is taken and all the other particles within distance R are added to seed. Weighted centre of this merged object is calculated and compared with with geometrical centre. If they are not same, new geometrical centre is set to be the weighted one, and this process is repeated until geometrical and weighted centre are not close enough. If they are, boundary stability can be checked, depending on algorithm.

Jet is stable at the boundary if inclusion of particles close to it does not change weighted centre of jet much. If we have stable jet candidate, before moving to another seed, we have to check whether this jet was not found in iteration with other seed.

After all seeds are processed, algorithm has to examine overlap of created jets. If energy shared by two or more jets is greater than certain fraction of jet energy, these jets are merged. On the other hand, if the shared energy is smaller, individual particles are split between individual jets according to the closeness of particle to these jets.

As a last step, jets may be rejected due to their energy not exceeding energy cut, or they may be outside geometric acceptance used in given analysis. This algorithms is described by flowchart in Fig. 3.5.

Several variations can be made to this algorithm. Boundary stability is condition that does not necessarily have to be checked. Also there can be seeded and seedless algorithms, i.e. in case of seeded energy threshold is non-zero and in case of seedless algorithm, all particles are considered to be possible seeds for jet.

This type of algorithm is easy to implement and fast. However, it is in general infra-red and collinear unsafe, making it undesirable for theoretical prediction.

SISCone

Exception is SISCone [49], Seedless Infra-red Safe Cone algorithm. The approach of adding particles to each other, in order to create cone, is much more complicated than simple adding of 4-momenta within distance of R. Other examples of cone algorithms are *Jet-Clu*, *Mid Point*, etc.

Sequential recombination algorithms

Second type are sequential recombination algorithms. These utilise hierarchical clustering, iterative procedures that try to reverse pattern of multi-gluon emission.

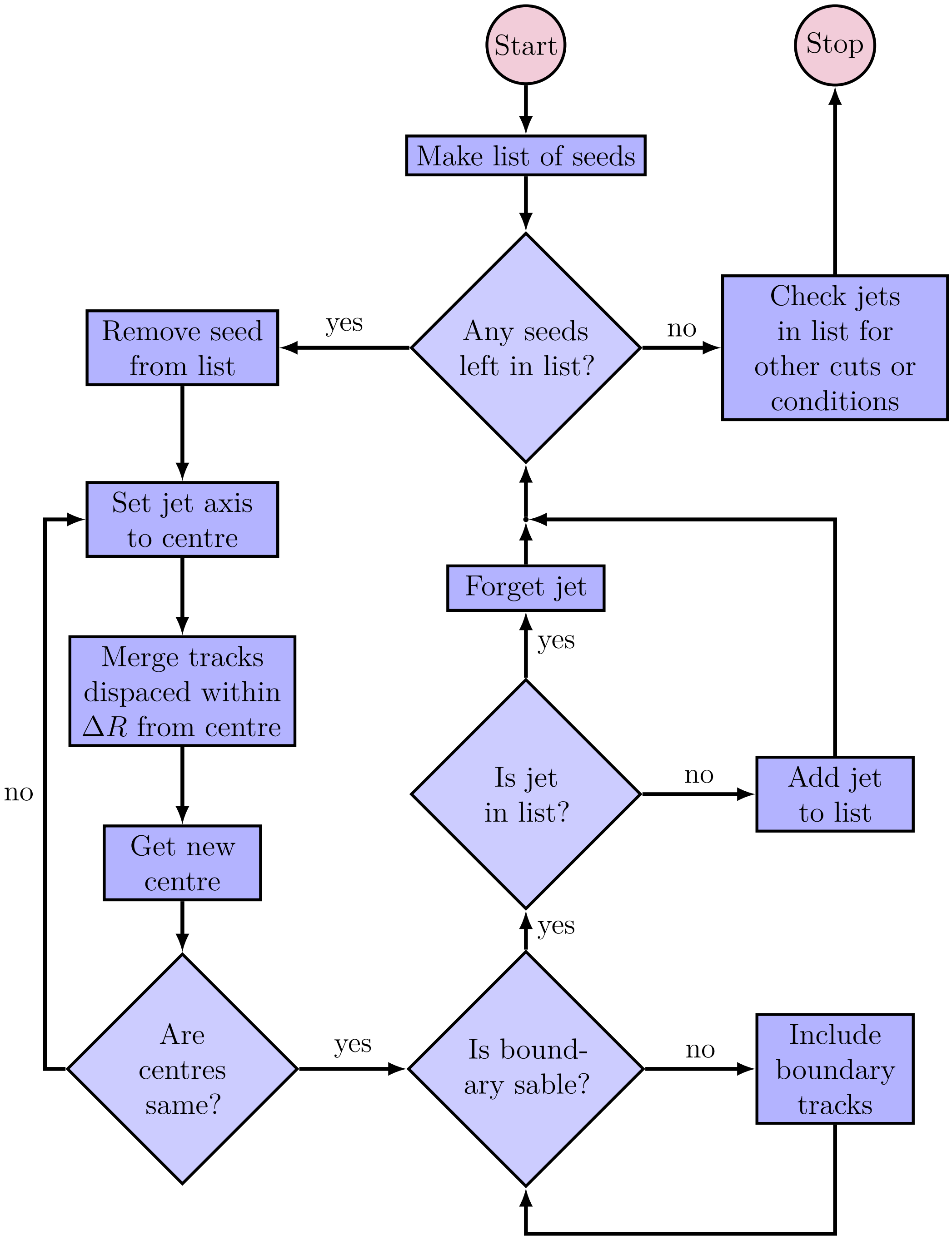

Figure 3.5: Cone algorithm.

They usually define distance between particles, that is ordered and indicates which pairs should be recombined. Distances for all particle pairs is calculated, d_{ij}, with addition of distances to beams, d_{iB}. If the smallest distance is distance between two particles, these particles are recombined according to defined recombination scheme. Afterwards, all distances have to be calculated for this new particle.

On the other hand, if shortest distance is distance of particle to beam, this particle is taken as final jet and it is taken out of list of particles that are recombined. This procedure is repeated until no particle is left in list of particles. List of final jets may contain jets created from single particles, however each particle is associated to only one final jet. This removes problem of splitting or merging of jets.

Final jets, can be rejected on the level of analysis level. Criteria may be same as in case of cone jets, i.e. jet being below energy cut, outside of analysis acceptance or leading jet particle, the most energetic particle in jet, contains significant portion of energy.

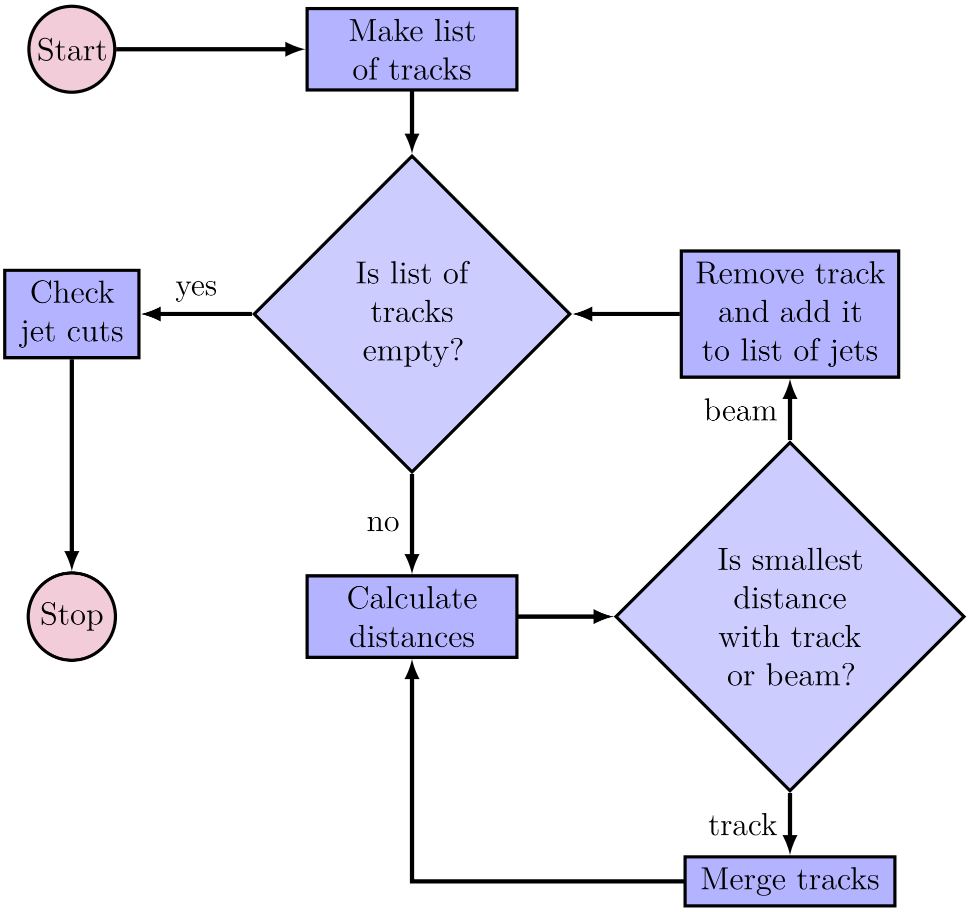

Figure 3.6: Sequential algorithm.

The distance between particles for jet reconstruction is defining for given algorithms. First algorithms were JADE and Durham, with distance definitions (3.10a) and (3.10b) respectively.

$$d_{ij} = \frac{2E_iE_j\left(1-\cos\theta_{ij}\right)}{Q^2}, \tag{3.10a}$$

$$d_{ij} = \frac{2\min\left(E_i, E_j\right)\left(1-\cos\theta_{ij}\right)}{Q^2}, \tag{3.10b}$$

where Q is relative transferred momentum of the two particles and θ_{ij} is angle between these two particles.

Another set of similar algorithms is given by distance definition (3.11).

$$d_{ij} = \min\left(k_{T,i}^{2p}, k_{T,j}^{2p}\right) \frac{\Delta\eta_{ij}^2 + \Delta\varphi_{ij}^2}{R^2}, \tag{3.11}$$

where R is distance defined in space of pseudo-rapidity and azimuth. By setting value of parameter p to zero, distance ignores transverse momenta and algorithm, *Cambridge/Aachen algorithm*, start merging of particles which are geometrically the closest. Setting $p = 1$, defines so-called k_T algorithm, which merges soft particles first and is, therefore, useful in determination of background. Setting $p = -1$ defines anti-k_T algorithm, which contrary to k_T algorithm starts merging with the hardest particles. This algorithm yields jet areas with perfect circles in space of pseudo-rapidity and azimuth and is the default algorithm of LHC experiments for signal extraction.

3.3.2 Jet area

In order to define area of reconstructed jets, several possible jet definitions can be used within the framework of *FastJet* package. These include *active area*, *passive area* and *Voronoi area*. The area can be obtained as a scalar or as an energy.

Active area

Active area is determined from filling the space with uniformly distributed extremely soft[8] particles, *ghosts*. Area of the jet is defined by number of these soft particles that the given jet contains scaled by the ratio of the area which was considered and total number of ghost that was used in the process of area determination.

Passive area

Passive area is determined from randomly generating ghost in considered area. After the jet to which this ghost belongs is determined, new ghost is randomly generated. This process is repeated many times. The final area of jet is estimated from probability of containing randomly generated ghost scaled by the total area considered for ghost generation.

Voronoi area

Voronoi area of a jet is determined as a sum of Voronoi areas of individual track constituents. Voronoi area of particle is determined from Voronoi diagram of event. For the case of k_T algorithm, the area determined from this method gives same result as passive area determination.

---

[8] Soft particle is a particle with small, insignificant amount of, energy.

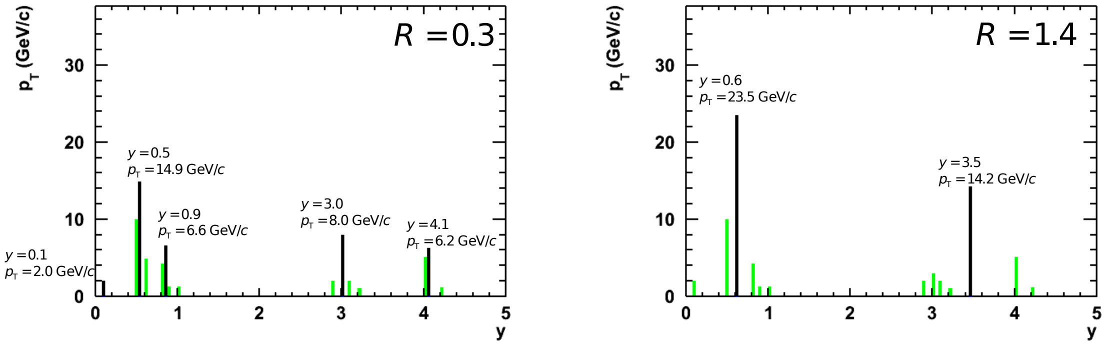

(a) (b)

Figure 3.7: Reconstruction of 1-dimensional event using 2 different resolution parameters, 0.3 and 1.4, Fig. 3.7a and Fig. 3.7b, respectively. Decreasing resolution parameter produces larger amount of jets with smaller reconstructed momenta.

3.3.3 Parameters

The most important parameter, already mentioned in text above, is *resolution parameter*. In space defined by (pseudo-)rapidity and azimuthal angle, this parameter serves as measure of area sampled by reconstruction algorithms in one jet. This parameter, keeping in mind geometrical picture in defined space, serves as a maximal distance between jet axis and it's components, i.e. jet's radius. Variation of this parameter are necessary, because higher values of resolution parameter ensure, that whole jet is contained within area sampled by algorithm. On the other hand, this increases contribution from other processes, which have to be identified and accounted for. The situation is much more complicated in collisions of heavy ions, where background processes play dominant role and only small values of resolution parameter, compared to proton–proton collisions, are used.

Effect of changing resolution parameter on jet reconstruction of simple 1-dimensional example collision is presented in Fig. 3.7, where resolution parameter, R, acquires values of 0.3, and 1.4, Fig 3.7a-3.7b respectively.

As mentioned in section discussing cone algorithms, energy fraction of jet is used for deciding, whether to split or merge overlaying jets.

3.3.4 Recombination

Last criterion defining jet is *recombination scheme*. This prescribes way in which individual particles, tracks or calorimetric towers are merged.

For most algorithms used *energy scheme* is taken as default. This scheme is based on summing 4-momenta of particles or tracks and therefore jets can acquire masses. However, for this scheme particle identification and/or assignment of energy to particle is necessary.

Another scheme, p_{T} *scheme*, is based on weighted summing of azimuthal angle and pseudo-rapidity of particles. This scheme assumes massless particles or calorimetric towers and sums transverse momenta.

Several variants of this method exist, where weighting may be based on transverse energy, for experiments where calorimetry is dominant part of detector system, or using squares of weighting variables mentioned.

Additionally, *boost invariant schemes* exist where no preprocessing occurs, which would make given particles massless.

3.4 Application of jets

The primary utilisation of jets is in testing of QCD. We are able to test both non-perturbative and perturbative aspects of this theory. Among main tests of non-perturbative QCD is study of parton fragmentation, where either identified or non-identified particle fragmentations are examined.

Fragmentation of jets, or hard partons is studied also via particle content, and shapes of jets. These shapes enable study of collimation and in case of electron-positron collisions, where there is minimal background, can be used to determine information about original parton, either if it was light quark, heavy quark or gluon. It was suggested that in order to study fragmentation via jet constituents, fragmentation moments should be used. This should reduce influence of background on obtained information.

Investigations of jet substructures are being used in searches for rare particles, most notably Higgs boson and SUSY particles. This is due to the abundance of background processes dominating expected mass regions at current production energies. Therefore substructure may be crucial in identifying these rare particles.

Jets are final states of not only rare particles, but final states of decay products of heavy particles. As an example, decay of top quark with mass of $173\,\mathrm{GeV}/c^2$ into bottom quark, 4.5 $\mathrm{GeV/c^2}$, and W boson, $91\,\mathrm{GeV}/c^2$, leaves $77\,\mathrm{GeV}$ of kinetic energy in rest frame of top quark. This energy is mainly carried by quark. Similarly when W boson decays into 2 quarks, more than $80\,\mathrm{GeV}$ of energy is distributed among these daughter quarks.

On the other hand, perturbative QCD is tested not only by obtaining jet spectra, but also by determination of strong coupling constant. This is done by comparison of 3-jet and 2-jet events, where these jets fulfil strict energy and relative spacial requirements. Because 3-jet event represents NLO process to 2-jet, LO, process, the ratio of abundances of such NLO processes with respect to LO, should be proportional to the value of coupling constant

3.5 Medium modification of jets

Similarly to other observables, jets may be used in study of influences arising from presence of medium on these observables. This medium is provided by nucleus composed of multiple nucleons, protons and neutrons. This is complementary to vacuum conditions when provided by colliding individual nucleons, i.e. protons, or leptons, which provide even cleaner probe, due to their point like nature.

Taking into account all possible observables that can be accessed by jet and jet constituent analyses, medium can be studied by investigating changes in these observables when comparing analyses in medium and in vacuum. Consequently all proton-proton based analyses serve as baseline for these comparisons.

There are 2 types of medium induced effects. First one is induced by *cold nuclear matter* and second originates in presence of *hot and dense medium*.

Effects on cold nuclear matter are investigated via study of proton-nucleus collisions. Such studies in 1970's lead to discovery of softening of low transverse momentum hadron spectra and corresponding hardening at intermediate momenta, around 3 to $6\,\mathrm{GeV}/c$, compared to scaled proton-proton result. This effect was observed by *Cronin*.

Studies of parton distribution functions within nucleus are showing differences compared to PDFs measured within protons. These differences are reflected in *nuclear modification factors*. For small values of Bjorken's scaling variable x, $x < 0.05 - 0.1$, modification factor is smaller than unity and it is called *shadowing*. In region of $x \approx 0.1 - 0.2$ ratio is larger than 1, this behaviour is called *anti-shadowing*. Region up to $x \approx 0.8$, with minimum at $x = 0.6$, so-called *EMC effect* occurs where ratio is again below unity. In the last region at the highest values of x, called *Fermi motion* region, ratio grows larger than unity again.

Another effect, affecting high-energy partons while propagating through nuclear medium, is k_{T} *broadening*. This parton experiences soft scatterings which increase transverse momentum of this parton before hard scattering.

Investigating hot and dense nuclear matter overlaps with investigation of *quark gluon plasma*, deconfined state of quarks and gluons originating in collision of heavy quarks. There are several effects originating from presence of this medium.

First of all, this medium induces energy loss of parton travelling through it, as does any medium to probe. In case of QGP, it is predicted that this energy loss would be predominantly of radiative origin, and would result in so called *jet quenching* and suppression of high-p_{T} hadrons in central nucleus–nucleus collisions with respect to proton–proton baseline. Such suppression was indeed observed in Au–Au collisions at RHIC.

Other features of heavy ion collisions that may affect jet studies are collective effects of medium. This collective behaviour is manifested as *radial flow*, an average transverse component of collective flow and *elliptic flow*, which originates from spacial asymmetry of fireball, created mainly in non-central collisions. This asymmetry generates different pressure gradients in different directions, which reflects in azimuthal asymmetry of hadron spectra.

Additionally, particle composition of jets will be affected, as formation of deconfined medium results in suppression of quarkonia production and larger interaction volume enhances production of strange–anti-strange quarks.

More thorough discussion on the role of jets in collisions of heavy ions is in Chapter 2 and topic of observables indicating creation of QGP can be found in Ref. [23].

Chapter 4. Experimental setup

4.1 Large Hadron Collider

Located at CERN, the European Organization for Nuclear Research, in Genéva, is particle physics laboratory with main goal of studying physics at the energy frontier.

Injection of particles into LHC storage rings is preceded by several preaccelerators, namely PSB, PS and SPS, in order of input beam energies. Proton synchroton boosted receives protons from LINAC 2 and lead ions from LINAC 3, with proton momenta of $0.3\,\mathrm{GeV}/c$, accelerating them up to $2.1\,\mathrm{GeV}/c$. They are transported to proton synchrotron, where they are accelerated to $26\,\mathrm{GeV}/c$ and subsequently in SPS up to $450\,\mathrm{GeV}/c$.

In LHC, proton beams are accelerated to energies up to 8 TeV [1] and lead ions reached energies of 2.76 TeV per nucleon. Total delivered integrated luminosity in proton-proton collisions by the LHC is $30\mathrm{fb}^{-1}$, combining data from year 2010, 2011 and 2012. There have been approximately $166\mu\mathrm{b}^{-1}$ of lead-lead data and $5.6\mathrm{nb}^{-1}$ integrated luminosity of proton-lead collisions.

There are four main experiments located at the LHC, ALICE, ATLAS, CMS, LHCb, and additionally TOTEM and LHCf. ATLAS and CMS are general purpose experiments designed for study of wide range of physical topics, with discovery of Higgs boson as highlight of their operation up to January 2014. LHCb is forward detector designed for study of heavy flavour physics, specifically bottom physics, covering topics like observation of CT violations via B-mesons.

Among smaller experiments belong TOTEM, LHCf and MoEDAL. TOTEM measures size of proton and its cross sections. LHCf studies neutral pions, at forward directions at

---

[1] as of January 2014

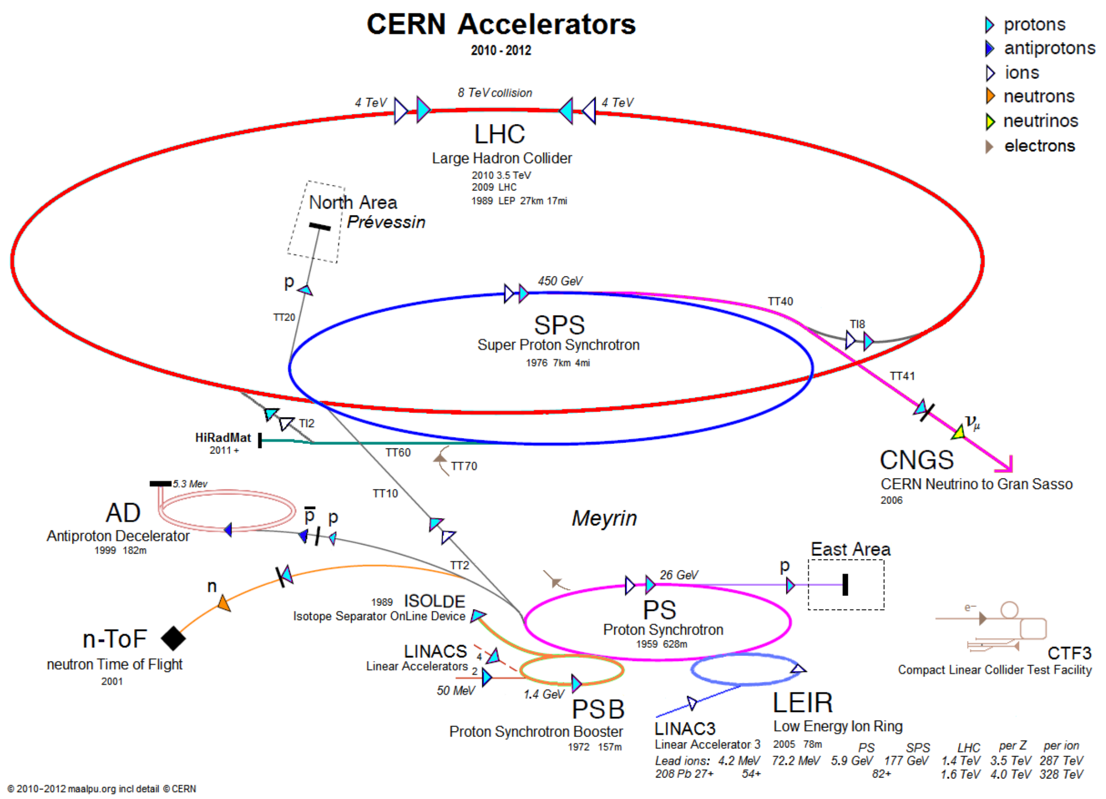

Figure 4.1: Scheme of LHC and its preaccelerators composed of linear accelerators, LINACs, BOOSTER, PS and SPS. Additionally, scheme shows preaccelerators for other CERN experiments, such as ISOLDE, AD, CNGS and n-TOF. This scheme is adapted from [44].

ATLAS and MoEDAL searches for magnetic monopole, *dyon*, and other exotic particles.

For the Run II, starting in 2015, LHC shall be colliding protons with centre-of-mass energy of 13 TeV, getting closer to the design value of 14 TeV. This should lead to significant increase in production of possible massive particles as well as increased statistical precision of Higgs measurements, with 3 times larger cross section and 5 times the amount of data.

4.2 A Large Ion Colliding Experiment

ALICE is experiment dedicated to measurement and study of mid-rapidity hadrons, leptons and photons. These tracks are reconstructed in range from 100 MeV/c up to 100 GeV/c and have to contribute to reconstruction of short lived particles. For this purpose, good resolution of vertexing detectors is needed. This has to be done in environment of lead collisions where multiplicities are over 1000 particles per unit of rapidity.

In order to measure low momenta particles and still achieve good momentum resolution and tracking efficiency, choice of magnetic field was set to maximum of L3 magnet around

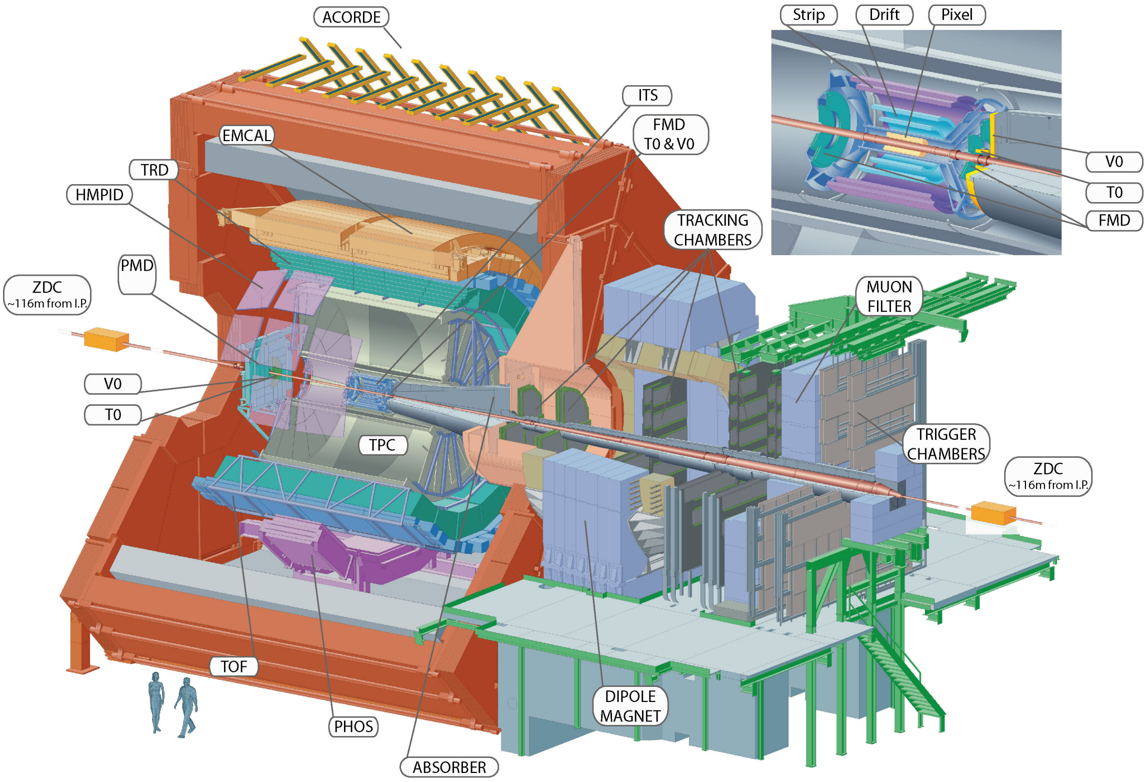

Figure 4.2: Schematic depiction of the ALICE detector systems, with labels associated to main subdetectors. In upper right corner is enlarged collision area with ITS and triggering subdetectors.

detector, which is 0.5 T. This is due to limited statistics of high momentum particles. However, a plan for detector operations with 0.2 T are planned for Run 2, in order to increase reconstruction efficiency and gain low momentum statistics mainly for di-lepton analyses.

Concerning particle identification, for low momenta particles resolving power of 3σ between π, K, p is needed for HBT, identification of hyperons, vector mesons and heavy flavour mesons. Resolving power of 2σ is sufficient for inclusive particle spectra and ratios and for high momentum particles. Detection of photons, mainly at low momenta, is necessary for reconstruction of neutral mesons such as π^0 and η, high momenta photons are important in jet physics.

Separate muon detector and spectrometer are present to measure heavy-quark resonances and quarkonia, such as $J/\psi, \psi', \Upsilon, \Upsilon', \Upsilon''$.

ALICE consists of central tracking detectors, i.e. ITS, TPC, TRD, HMPID, TOF with EMCAL and PHOS on top of them. In forward region is PMD and on the other side are muon tracking chambers with absorbers. For triggering purposes V0, T0 and FMD detectors are also part of ALICE.

Mentioned before, these subdetectors are placed inside solenoid L3 magnet, previously used in one of LEP collider's experiment, capable of producing magnetic field of 0.5 T.

Closest to interaction point of colliding particles is vacuum beam pipe, thick 0.8 mm and made out of beryllium. The outer diameter of this tube is 59.6 mm.

Inner Tracking System

The detector closest to the interaction point is ITS. It is composed of 6 cylindrical layers with radii of 4, 7, 15, 24, 39 and 44 cm, covering full azimuth and pseudo-rapidity area from -0.9 to 0.9. This coverage applies for all vertices within 10 cm along the beam direction from detector centre. Pseudo-rapidity coverage of innermost layer is $|\eta| < 1.98$ which in conjunction with FMD provides continuous coverage for measurement of charge particle multiplicities.

Each layer consists of silicon detectors, which are made for purpose of enhancement of vertexing and tracking using different detection principles. First two layers are silicon *Pixel* Detectors. Third and fourth layer are made of Silicon *Drift* Detectors. These layers ensure good resolution of primary vertex. Two outermost layers are Silicon *Strip* Detectors.

ITS ensures good resolution of primary and secondary vertices, and provides particle identification and tracking for particles with transverse momenta smaller than 100 MeV/c. Additionally, it improves resolution of track with high momenta reconstructed using TPC and partially reconstructs particles travelling through dead regions of TPC. For particle identification, at least 4 layers out of 6 possible have to have a hit from given track. ITS with it's closeness to interaction zone and resolution capabilities helps with determination of impact parameter of tracks with resolution better than 100 µm in $r - \varphi$ plane.

Momentum resolution of pions within range from 0.3 GeV/c to 3.0 GeV/c is better than 2 % and vertex reconstruction resolution in direction along beam axis is better than 0.1 mm.

Time Projection Chamber

The main tracking detector of the ALICE detector system is TPC. Furthermore, it provides identification using dE/dx measurements. It is constructed in such a way that it provides good 2 track separation and vertex detection. Thanks to 0.5 T L3 magnet, it provides transverse momentum measurement up to 100 GeV/c.

To match acceptance of other detectors such as ITS, TRD and TOF, TPC covers acceptance of $|\eta| < 0.9$ for fully reconstructed tracks. However tracks with reduced resolution and track length can be reconstructed within maximal acceptance of $|\eta_{\mathrm{max}}| \approx 1.5$.

The detector is cylindrical field cage with inner radius of 85 cm and outer radius of 250 cm. It has 5 m in beam direction. For small number of multiple scatterings, 88 m^3 mixture of Ne/CO_2, in ratio of $9:1$, was chosen as filling of TPC. However steep dependence of drift speed in this gas mixture on temperature requires excellent temperature stability, with temperature fluctuations smaller than 0.1 K.

Field cage is constructed with central electrode and end plate cathodes created by multi-wired proportional chambers in each of 18 trapezoid sectors of every end plate.

Potential gradient of 400 V/cm end high voltage of 100 kV at the central electrode ensure electron drift time approximately 90 µs.

TPC was designed energy identification resolution smaller than 10 %, momentum resolution of 5 GeV/c particle better than 5 % and track finding to be better than 90 %.

Transition Radiation Detector

TRD is detector designed for electron identification at transverse momenta greater than 1 GeV/c, where pion rejection via dE/dx is not suitable. Additionally, this detector serves as fast trigger detector for high momentum electrons, contributing to enhancement of heavy flavour analysis.

Pion rejection is necessary for J/Ψ measurement and light vector mesons reconstruction, where enhancement thanks to TRD at 3 GeV/c is by the factor of 100. As with previous detectors, TRD covers full azimuth and pseudo-rapidity region of $|\eta| < 0.9$. It is composed of 18 sectors made by 6 layers and 5-fold segmentation along z-direction, total of 540 modules. Each modules consists of 4.8 cm radiator and multi-wire proportional readout chamber. These chambers are filled with Xe/CO_2 gas mixture, 85% to 15%, with 3 cm drift region in between. Drift time is 2 µs.

Time of Flight

TOF detector is designed for particle identification and differentiation between pions, kaons and protons in momentum interval from 0.2 GeV/c to 2.5 GeV/c. Detector has full azimuthal coverage and coverage in polar angle between $\pi/4$ and $3\pi/4$. In azimuth it is divided into 18 sectors, each consisting of 5 segments of non-equal length. Outermost segments have 1.77 cm, intermediate segments are 1.57 cm long and central segment has 1.17 cm. Minimal distance from centre of detector is 370 cm and maximal distance is 399 cm. Each unit of TOF is multi-gap resistive plate chamber.

High Momentum Particle Identification

HMPID is based on ring imaging cherenkov counters. It consists of 7 modules of $1.5\,\mathrm{m}^2 \times 1.5\,\mathrm{m}^2$, composed of 1.5 cm thick layers of C_6F_{14} with index of refraction of 1.2989 for wavelengths of 175 nm, serving as radiators. Photon counters are cathode pads of multi-wire proportional chambers with CsI on top of them.

Coverage of HMPID is $|\eta| < 0.6$ and $\Delta\varphi = 57.61°$.

Muon Tracker

Design of muon tracker was motivated by measurement of heavy flavour quarkonia states, decays into di-muon state in small polar angles, i.e. with large lorentz boost. It has to withstand large multiplicities, large spacial acceptance and low momenta acceptance.

Muon tracker covers pseudo-rapidity region of $-4 \leq \eta \leq -2.5$. It consist of passive front absorber to absorb hadrons and photons from initial vertex, followed by high granularity tracking system and dipole magnet, muon filter wall and trigger chambers.

Inner part of detector is shielded from particles travelling at polar angles smaller than that of detector coverage.

Muon filter is placed after last tracking chamber and before first trigger chamber, with purpose of additional protection of these chambers. It is approximately 1 m thick iron wall and in conjunction with *front absorber* it stops muons with momenta greater than 4 GeV/c.

Dipole magnet is located outside L3 solenoid magnet, 7 m from interaction point. Its nominal field strength is 0.7 T.

Tracking chambers are constructed into 5 stations. Two stations are before, one is inside, and two are after dipole magnet. Each station is composed of 2 chamber planes and each plane is made of 2 cathode pad planes, enabling 2-dimensional hit reconstruction. Size of the pads increases as planes are further from interaction point and total number of pads is around one million.

Trigger chambers located after muon filter, are composed of resistive plate chambers, ensuring spacial resolution of muon tracks. There are 4 planes of trigger chambers in 2 stations with 1 m separation between them. Active area of these chambers is 150 m^2.

Photon Spectrometer

PHOS is detector consisting of cca. 17900 readout channels made of PWO scintillation crystals, detecting electromagnetic showers with high resolution. Detector is located 4.4 cm from interaction point covering pseudo-rapidity range from -0.12 to 0.12, with azimuthal coverage of 100°.

Purpose of this detector is to probe initial phase of heavy-ion collision via measurement of direct single photons or diphotons. Additionally, it aims to study jet-quenching as probe of deconfinement via high p_{T} photons and π^0 and signs of chiral-symmetry restoration.

Electromagnetic Calorimeter

EMCal is calorimeter with acceptance $\Delta\varphi = 110°$ and $|\eta| < 0.7$. Calorimete, made of layered lead-scintillator, is organized into *modules* of 2×2 towers. These modules are grouped by 288 into *super-modules* spanning 0.7 units in pseudo-rapidity and 20 in azimuth. There are 2 super-modules along beam direction and 5 regular super-modules in azimuth, with additional half super-module at the end.

EMCal is used for detection of photons and for reconstruction of full jet energies.. Additionally it serves as L0 and L1 triggering detector.

Relative resolution of EMCal is

$$\frac{\sigma}{E} = \frac{6.90 \pm 0.09}{\sqrt{E}} + 1/44 \pm 0.03\%, \tag{4.1}$$

for particles in range from 5 GeV/c to 100 GeV/c.

Forward Multiplicity Detector

FMD is used for obtaining offline charged-particle multiplicity information. Additionally, in conjunction with ITS, it serves for determination of multiplicity distribution in pseudo-rapidity range in the interval from -3.4 to 5.1. These multiplicity distribution can be used for determination of multiplicity fluctuations on event-by-event basis and flow analysis.

Detector is made of 51200 silicon strip channels in 5 ring counters. These are made of 20 or 40 sectors in azimuthal segmentation each sector with either 256 or 512 detector strips. Individual wafers are made of 300 µm thick and 15 cm in diameter.

Ring counters are placed -75.2, -65.8, 75.2, 83.4 and 340.0 cm from interaction point. These counters cover pseudo-rapidity ranges of -3.40 to -1.70 and 1.70 to 5.09 and these rings have inner and outer radius either 15.4 and 28.4 cm or 4.2 and 17.2 cm.

Zero Degree Calorimeter

ZDC measures number of spectator nucleons and thus number of participating nucleons.

It is located 116 m from interaction point and consist of 4 different calorimeters. Two detectors are designed for measurement of neutrons and are located approximately at zero degrees from LHC axis. This is due to the fact, that spectator protons are separated due to electromagnetic repulsion and calorimeters are located further away from beam.

Calorimeters are made of dense materials serving as absorber, and Cherenkov radiation is detected in quartz fibres, active material of detector.

Detector had to be compact due to space requirement at beam, i.e. 7 cm in transverse direction. This was satisfied by utilising dense passive material, tungsten for neutrons and brass for protons. Second constrain was radiation hardness, satisfied by utilising quartz as active material. Furthermore, advantages of utilising cherenkov radiation are fast signal and low sensitivity to radioactivation.

VZERO

V0 detector serves as triggering detector for central barrel detectors. Additionally it provides trigger for central Pb-Pb collisions and it indicates centrality of collisions itself. Furthermore, it serves as luminosity control and muon trigger validifier.

V0 is composed od 2 arrays, V0A and V0C. V0A is located 340 cm from vertex on opposite side to muon spectrometer. On the contrary, V0C is placed on the front face of front absorber, 90 cm from vertex.

Each array is composed of 32 elementary counters placed in 4 rings. These rings each occupy 0.4 to 0.6 units of pseudo-rapidity segmented into 8 sectors of $\pi/4$ in azimuth.

Each elementary counter is composed of scintilator material with wavelength shifting properties. Light is collected by photo-multipliers 3-5 m from detector.

TZERO

T0 is detector providing base signal for TOF detector. Its precision is of the order of tens ps, and it also serves as wake up signal for TRD before L0 trigger. Furthermore, it provides measurement of vertex position with precision of 1.5 cm and L0 trigger signal when this vertex is within preset values. It is used for multiplicity measurements and as minimum bias, semi–central and central trigger.

Detector system is made of 2 arrays of 12 Cherenkov counters each. One array is located 70 cm from interaction vertex, $T0_R$, with pseudo-rapidity coverage of $2.9 \leq \eta \leq 3.3$. Its position is due to restrictions made by placement of muon absorber. Second array, $T0_L$, is placed 350 cm from interaction vertex on the opposite side as is placement of muon spectrometer. Its coverage is $-5 \leq \eta \leq -4.5$.

Photon Multiplicity Detector

PMD is preshower detector measuring multiplicities and spacial distribution of photons in pseudo-rapidity and azimuthal angle. This can be done on event-by-event basis.

Designed for detection of Disoriented Chiral Condensate, it measures transverse electro-magnetic energy and reaction plane in region of $2.3 \leq \eta \leq 3.5$ thanks to its placement 360 cm from interaction point.

Detector is designed from gas proportional counter with honeycomb structure. For its insensitivity to neutrons and non-inflammability, Ar and CO_2 mixture is used.

4.2.1 Track and vertex reconstruction

For purpose of tracking in central region several different detectors are used. These include ITS, TPC, TRD, TOF and HMPID. In general, global ALICE coordinate system is used where z-axis is axis of beam pipe with direction opposite to muon arm.

Concerning nomenclature used in further in the text, *digit* is digitized signal of particle response in detector, *cluster* is set of digits adjacent in space and time, presumably generated by same particle, *reconstructed space point* is estimate of position where particle crossed sensitive element of detector and *reconstructed track* is set of 5 parameters of particle's trajectory together with corresponding covariance matrix estimate at given point in space.

Primary vertex reconstruction

Primary vertex reconstruction is done in two steps. First, primary vertex is estimated by SPD prior to tracking. Second iteration of 3D vertex determination is done using already reconstructed tracks.

Approximation of z-coordinate of primary vertex in SPD is obtained from distribution of reconstructed space-points in first pixel layer, giving cut on position along beam. Transverse plane coordinate is determined similarly from x and y distribution of these points. Then linear approximations of tracks are done using points in first and second layer of ITS omitting correlations between points whose $\Delta\varphi > 0.1°$.

Tracks reconstructed in TPC and ITS are approximated as straight line at point of the closest approach to nominal primary vertex. All tracks pairs are used to determine set of centres of closest approach for each track pair. Primary vertex is calculated as a average of these centres, and gives improved estimate on vertex position.

Vertex position is determined by minimizing track distances of closest approach to this vertex,

$$\chi^2\left(\vec{r_v}\right) = \sum_i \left(\vec{r_v} - \vec{r_i}\right)^T V_i^{-1} \left(\vec{r_v} - \vec{r_i}\right), \tag{4.2}$$

where $\vec{r_v}$ is position of vertex, $\vec{r_i}$ is point of closest approach of tracks i to vertex, V is covariance matrix for point $\vec{r_i}$. Tracks giving contribution larger than $\chi^2_{\max}$ are excluded from primary vertex determination and considered for determination of secondary vertices, kinks or decaying neutral particles.

Track reconstruction

Track parameters are determined locally using *Kalman filter*, which is advantageous in fitting and track recognition. Additionally, it has greater posibility to reject incorrect space-points on-fly, and can handle multiple scatterings and energy loss. Furthermore, it can be used to easily extrapolate tracks from one detector to another.

Clusters are found in all detectors. Starting from TPC, best tracker, reconstruction proceeds from outer to inner radius due to the minimal density of reconstructed clusters. Reconstruction of each track starts at seed. Proceeding from to inner radii, clusters are associated to existing seeds, or track candidates, refitting track parameters. When inner TPC is reached ITS clusters are processed in the same way, elongating tracks to primary vertex and improving track parameters.

Afterwards, stand-alone ITS tracking is done on clusters not associated to any track. This may recover tracks not found in TPC. Subsequently, tracking is restarted from primary vertex proceeding to outer TPC radii and extrapolating tracks to TRD, TOF, HMPID. TRD clusters improve resolution of tracks and help with particle identification. Similarly, TOF and HMPID are used to determine particle type. Refitted tracks are used in primary and secondary vertex reconstruction.

4.3 Software framework

4.3.1 ROOT and AliROOT

In order to produce analysis presented in this thesis, software `ROOT` was used. This is CERN software created for statistical data analysis. Additionally, in order to analyse data produced specifically by in the ALICE collaboration, `AliROOT` was used. It contains additional libraries for `ROOT`, which are specific for the experiment and it is framework used for official analyses within the ALICE collaboration.

4.3.2 Simulations

Additionally simulations based on several event generators were used. The main tool used in order to obtain deconvolution of true spectra and detector effects were simulations provided by `PYTHIA6.4.21` with `Perugia0` tune which provided simulated jet spectra. Detector response was obtained from reconstruction of particles in modelled detector environment, provided by `Geant3.21`. Additional `PYTHIA6` tunes used were `Perugia-2010`, `Perugia-2011` and `AMBT1` tune which was used by the ATLAS collaboration and served as a cross-check of the analyses and results. Moreover, `HERWIG` generator was used to corroborate results and provide simulations from framework different from `PYTHIA6`.

These were leading-order simulations with K-factor modification of cross section at maximum. For the purpose of next-to-leading order simulations, `POWHEG-Box` framework was used. This produced hard scatterings within colliding protons in format of Les Houches Event Files. These were used in `PYTHIA8.176` generator, which provided parton showers for each event.

4.3.3 Jet reconstruction

In order to reconstruct jets, `FastJet-v2.4.2`, [46,47] package was used. This package contains various algorithms like *SISCone* [49], k_{T} [50, 51] and *anti-*k_{T} [52]. The last algorithm named was used for reconstruction of jets in this analysis, as it is used by all the LHC experiments for jet reconstruction.

4.3.4 Unfolding

As mentioned before, reconstructed jets suffer from effects of detector reconstruction, namely reconstruction inefficiency and momentum smearing. The methods for correcting these effects are described in Sec. 4.4. For purpose of these corrections, `RooUnfold` [53,54] software framework was utilised.

4.4 Treatment of detector effects

This section is focused on correcting effects of detector in order to obtain physical result unaffected by detecting equipment used. For this purpose simulation on the level of Monte-Carlo generator is used with addition of simulation of detector itself. This level represents reconstructed data and by process of obtaining Monte-Carlo simulation level from reconstructed level, same process applied on real data shall yield physical result.

4.4.1 Bin-by-bin correction

The simplest way to correct detector effect is by using *bin-by-bin* correction method. This method is based on creating of jet spectra, or any relevant observable, from simulation on the level of generator and on the level of detector with same binning that is used in data. Then, generator level spectra, *TRUTH* spectra, are divided by detector level spectra, *RECO* spectra. This way we obtain correction factors for each bin of spectra obtained from data and the general formula is as follows

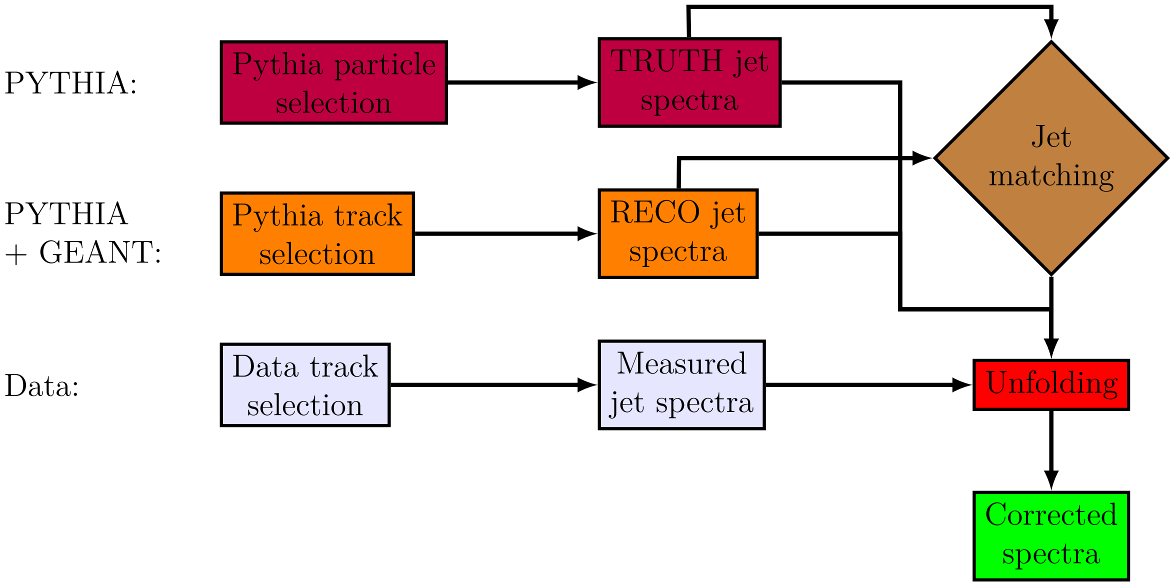

Figure 4.3: Flowchart depicting analysis of jets on 3 different levels, Monte-Carlo generator level where *truth* jet spectra are obtained, generator in conjunction with detector simulation gives *reconstructed* jet spectra and the level of real data. Spectra from both levels of simulation are used in process where jets from one level are matched to jets from another level. This provides additional information necessary for several correction methods. Corrected or physical spectra is output of the unfolding or correction process, where all the information from simulation are used.

$$\left.\frac{\mathrm{d}^2\sigma}{\mathrm{d}p_{\mathrm{T}}\mathrm{d}\eta}\right|^{\text{jets}}_{\text{corrected}}(p_{\mathrm{T}}) = \left.\frac{\mathrm{d}^2\sigma}{\mathrm{d}p_{\mathrm{T}}\mathrm{d}\eta}\right|^{\text{jets}}_{\text{raw}}(p_{\mathrm{T}})\,\frac{\left.\frac{\mathrm{d}^2\sigma}{\mathrm{d}p_{\mathrm{T}}\mathrm{d}\eta}\right|^{\text{jets}}_{\text{TRUTH}}(p_{\mathrm{T}})}{\left.\frac{\mathrm{d}^2\sigma}{\mathrm{d}p_{\mathrm{T}}\mathrm{d}\eta}\right|^{\text{jets}}_{\text{RECO}}(p_{\mathrm{T}})}, \tag{4.3}$$

where raw spectra represent uncorrected spectra obtained from real data, i.e. equivalent to RECO spectra from simulation. Similarly, corrected spectra is TRUTH spectra equivalent in for real data, and unless other corrections or effects have to be accounted for.

The only restriction of this method is that it is impossible to describe bin migration, i.e. empty bin cannot have non-zero content after correction process. Furthermore, it is required that the simulation describes data well, otherwise the result may be incorrect. Imprecise description of data may result in spectra with different slope and therefore different bin migration of jets to lower values of transverse momenta. This would reflect in incorrect correction factors.

4.4.2 Bayesian unfolding

More sophisticated way of correcting effects of detector reconstruction is by utilising *Bayesian unfolding*, a method based on Bayes' theorem about conditional probabilities from statistics

$$P(A|B)\,P(B) = P(B|A)\,P(A)\,, \tag{4.4}$$

where $P(A|B)$ is conditional probability of occurrence of event A with fulfilled condition B, $P(B)$ is probability of event B and similarly $P(A)$ is probability of A being true and $P(B|A)$ is probability of B being fulfilled with A being true as well.

The role of conditional probabilities is taken by response matrices. These are created by matching detector level jets to generator level jets and represent set of probabilities of finding jet with generated transverse momentum C_j reconstructed as jet with momentum E_i, therefore $P(E_i|C_j)$ denotes this response matrix and if we take spectra as normalised distributions we get

$$P_{\mathrm{M}}(E_i) = P(C_j|E_i)\,P(C_j)\,, \tag{4.5}$$

where $P_{\mathrm{M}}(E_i)$ is reconstructed spectrum and $P(C_j)$ is physical spectrum.

To correct reconstructed spectra, we want to multiply it with inverse of the response matrix, however this matrix is often singular and therefore imposible to invert. Taking it as a set of conditional probabilities, we want to do

$$P_{\mathrm{U}}(C_j) = P(C_j|E_i)\,P_{\mathrm{M}}(E_i)\,, \tag{4.6}$$

where $P_{\mathrm{U}}(C_j)$ is unfolded, or corrected, spectrum. This inversion is possible thanks to the Bayes' theorem, where inverted conditional probability is calculated iteratively in order to increase precision of the result, as distribution of physical spectrum is unknown at the beginning and has to be estimated at first. The process of inversion is done according to the following formula,

$$P(C_j|E_i) = \frac{P(E_i|C_j)\,P_0(C_j)}{\epsilon_j \sum_{j'} P(E_i|C_{j'})\,P_0(C_{j'})}, \tag{4.7}$$

where P_0 denotes a prior for inversion. This prior is necessary for first iteration only. The result of multiplication of jet distribution from data and inverted response matrix is used in subsequent iterations instead of this prior. The variable ϵ_j from Eq. (4.7) represents the jet reconstruction efficiency. This is probability of finding jet with energy C_j as reconstructed jet, i.e. process of jet matching found a pair to the original generator level jet. This probability is obtained in following way,

$$\epsilon_j = \sum_i P(E_i|C_j)\,. \tag{4.8}$$

Regularization of Bayesian unfolding is realised using the number of iterations used in unfolding, therefore it is necessary to determine which iterations is the last one. For purpose of this work, this was done via Pearson's coefficients, which characterize correlation between different bins of spectra. They are defined as

$$\rho_{ij} = \frac{\mathrm{cov_{i,j}}}{\sigma_i \sigma_j}, \tag{4.9}$$

where i, j are different pairs of bins of spectra and $\mathrm{cov_{i,j}}$ is element of covariance matrix. Value of Pearson's coefficient ranges from -1 to 1 , specifically,

$$\rho = \begin{cases} 1, & \text{Completely correlated} \\ 0, & \text{Uncorrelated} \\ -1. & \text{Completely anti-correlated} \end{cases} \tag{4.10}$$

For selection of number of iterations, off-diagonal elements have to be zero and diagonal elements have to be highly correlated. Consequently adjacent elements usually are uncorrelated due to bin migration and the fact, that Bayesian unfolding conserves integral of unfolded distribution.

In Ref. [55] more details about Bayesian unfolding can be found.

4.4.3 Singular Value Decomposition

Similarly to Bayesian unfolding described in Sec. 4.4.2, *singular value decomposition* unfolding method deals with the problem of inverting response matrix, which can be often singular. However, before singular value decomposition is applied several steps are applied where basic equation is normalised, rescaled and added regularisation term. In order to find physical spectrum x_j, the equation undergoes minimalisation process such that

$$\sum_{i=1}^{n_b}\left(\sum_{j=1}^{n_x}\hat{A}_{ij}x_j - b_i\right)^2 = \min, \tag{4.11a}$$

$$\sum_{i=1}^{n_b}\left(\frac{\sum_{j=1}^{n_x}\hat{A}_{ij}x_j - b_i}{\Delta b_i}\right)^2 = \min, \tag{4.11b}$$

$$\left(\hat{A}x - b\right)^T B^{-1}\left(\hat{A}x - b\right) = \min, \tag{4.11c}$$

where n_b and n_x are numbers of bins in measured and physical spectrum. $\hat{A}_{ij}$ represents elements of response matrix, b_i are bins of measured spectrum. However, Eq. (4.11a) is true for exact equations, however measured spectra come with errors Δb_i, therefore weighted least squares have to be considered, Eq. (4.11b) or in matrix notation Eq. (4.11c), with B being covariance matrix of measured spectra.

In order to minimize effects of numerical capabilities, where bins of steeply falling spectra may differ by several orders of magnitude, spectrum is normalised by x^{ini}, as described by Eq. (4.12).

$$\omega_j = x_j/x_j^{\text{ini}}, \tag{4.12a}$$

$$A_{ij}\omega_j = b_i, \tag{4.12b}$$

Well chosen initial spectrum results in transformation of problem into solving problem for ω, i.e. fractions of x^{ini}.

Eq. (4.11c) can be simplified in a way described in (4.13), due to the fact that covariance matrix of measured spectra is symmetric and a positive-definite matrix, and can be written in terms of orthogonal matrix[2] Q.

$$B = QRQ^T, \tag{4.13a}$$

$$R_{ii} = r_i^2 \neq 0, R_{ij} = 0, j \neq i, \tag{4.13b}$$

$$B^{-1} = QR^{-1}Q^T, \tag{4.13c}$$

$$\tilde{A}_{ij} = \frac{1}{r_i}\sum_m Q_{im}A_{mj}, \tilde{b}_i = \frac{1}{r_i}\sum_m Q_{im}b_m, \tag{4.13d}$$

$$\left(\tilde{A}\omega - \tilde{b}\right)^T\left(\tilde{A}\omega - \tilde{b}\right) = \min. \tag{4.13e}$$

Last step of the SVD unfolding is addition of regularisations term, with regularisation parameter τ and curvature vectors $C\omega$. This curvature is defined as $\sum_i\left[(\omega_{i+1} - \omega_i) - (\omega_i - \omega_{i-1})\right]^2$ and gives specific prescription to the curvature matrix C

$$\left(\tilde{A}\omega - \tilde{b}\right)^T\left(\tilde{A}\omega - \tilde{b}\right) + \tau\left(C\omega\right)^T\left(C\omega\right) = \min. \tag{4.14}$$

Eq. (4.14) can be rewritten in vector form as (4.15), where in order to prevent singularity of curvature matrix C, small element ξ is added to its elements on diagonal.

$$\begin{pmatrix} \tilde{A}C^{-1} \\ \sqrt{\tau}I \end{pmatrix} C\omega = \begin{pmatrix} \tilde{b} \\ 0 \end{pmatrix}. \tag{4.15}$$

Applying singular value decomposition of matrix $\tilde{A}C^{-1}$ we get (4.16a), where matrices U and V are orthogonal and S is singular matrix with non-zero elements only on diagonal. Vector d^τ can be defined as (4.16b), and this vector is necessary to determine value of regularization parameter so that components causing quick oscillations of result are omitted and only components contributing significantly to result are taken. Two different pattern are seen from values of d_i, steeply falling part that contributes to result and part oscillating close to zero. The value of i where these pattern changes determines rank, which helps to determine regularization parameter as (4.16c).

$$AC^{-1} = USV^T, \tag{4.16a}$$

$$d \equiv U^T\tilde{b}, \tag{4.16b}$$

$$\tau \equiv S_{ii}^2, \tag{4.16c}$$

$$z_i^\tau = \frac{d_i S_{ii}}{S_{ii}^2 + \tau}, \tag{4.16d}$$

$$\omega^\tau = C^{-1}Vz^\tau, \tag{4.16e}$$

$$Z_{ik} = \frac{S_{ii}^2\delta_{ik}}{S_{ii}^2 + \tau}, \tag{4.16f}$$

$$X^\tau = x^{\mathrm{iniT}}C^{-1}ZV^TC^{-1T}x^{\mathrm{ini}},. \tag{4.16g}$$

Calculating (4.16e) and (4.16f), result with corresponding covariance matrix, (4.16g) is obtained.

---

[2] For orthogonal matrix Q is valid expression $I = QQ^T$, where I is unit matrix of appropriate dimensions.

Chapter 5. Analysis of p+p collision at $\sqrt{s}$ of 2.76 TeV and 7 TeV

In this chapter, steps taken to reconstruct jets in proton-proton collisions are discussed, including event selection analysis, track selection analysis and full reconstruction of jets. Same steps are used in analysis of simulated data which are used as baseline for correction of detector effects.

Moreover, similar steps are taken in analysis of next-to-leading order simulations using *POWHEG-Box*, considering that no detector effects are present in this framework as only true jet spectra are analysed.

For purpose of this analysis, events from the year 2010 with proton-proton collisions at 7 TeV were analysed. Furthermore, also proton-proton collisions with centre of mass energy of 2.76 TeV from beginning of the year 2011 were processed.

Data-taking in ALICE is segmented into several periods within a year and they are labelled alphabetically. Periods used in this analysis are `LHC10c`, `LHC10d` and `LHC11a`.

5.1 Event selection

Event selection is done in two steps. In the first step, event has to be triggered. In second step, several cuts have to be checked in order to ensure well reconstructed and placed primary vertex.

In this analysis, minimum bias trigger was used for event selection. This trigger is defined by registering signal from V0 detector or registering a hit in SPD detector on L0[1] trigger level synchronous with 2 bunches interacting. In this analysis, the cross section of interest was MBOR, minimum bias cross section from at least one hit from SPD or hit in V0 detector. This requires passage of charged particle in region spanning 8 units of pseudo-rapidity. This information is derived from beam pick-up detector for *LHC10d* data-taking period or LHC clock and filling scheme at the CTP for period *LHC10e*. In offline analysis the signal cleaned by placing cuts on V0 timing with respect to LHC clock.

Other possible cross sections include V0AND, which requires coincidence between 2 different sides of V0 detector, to distinguish between beam-gas interaction outside of interaction region and beam-beam interactions in this region. Cross sections for proton-proton at $\sqrt{s} = 7$ TeV in May and October 2010 and for $\sqrt{s} = 2.76$ TeV in March 2011 were determined, Ref [57] from van der Meer scan[2]

These cross sections are summarised in Tab. 5.1.

$\sqrt{s}$/TeV	$\sigma^{\mathrm{MB}}_{\mathrm{OR}}$/mb	$\sigma^{\mathrm{MB}}_{\mathrm{V0AND}}$/mb
2.76	55.4 ± 1.0	47.7 ± 0.9
7.00	62.2 ± 2.2	54.3 ± 0.2

Table 5.1: Table of measured cross sections for different energies of colliding proton beams, as obtained from van der Meer scan. Two different minimum bias cross sections are shown for comparison.

Events selected by minimum bias trigger are then required to have reconstructed primary vertex within 10 cm along the beam direction from nominal interaction point, i.e. centre of the detector defining origin of global coordinate system. Complementary to this requirement, vertex could not be displaced more than 1 cm from nominal interaction point in transverse direction.

Regarding the origin of primary vertex, there has to be at least three tracks used in reconstruction of primary vertex, so called *primary tracks* or *primaries*. Moreover, primary vertex of selected event cannot be *TPCVertex*, i.e. reconstructed only from track purely from TPC but also from ITS.

List of event selection criteria

Here is summary of requirements placed on an event to be accepted for further analysis:

- minimum bias trigger,
- $|z_{\mathrm{vtx}}| \leq 10$ cm,

---

[1] L0 stands for Level zero.

[2] Van der Meer scan is method for determination of luminosity, created by Simon van der Meer, where interaction region is investigated by measuring relative interaction rates with respect to separation of beams. Usually this is done by moving beams in transverse plane step-wise, with sufficient time for collisions at each step.

- $|r_{\mathrm{vtx}}| \leq 1$ cm,
- number of contributors $N_{\mathrm{contrib}} > 2$,
- vertex cannot originate from TPC information only.

Number of events rejected by these criteria is shown in Tab. 5.2.

data-taking period	all events	fraction of all events rejected due to				accepted events
		trigger	vertex position		number of contributors	
			z-dir	xy-dir		
LHC10d	151 019 000	5.69%	7.43%	0.44%	13.54%	74.09%
LHC10e	70 166 000	24.76%	9.64%	2.25%	12.79%	59.09%
LHC11a	79 904 000	17.64%	8.33%	1.67%	22.42%	57.10%

Table 5.2: Table showing fractions of all events that do no pass individual requirements for accepted, *good*, events and fraction of accepted events.

In case of LHC10d, total number of accepted events is 111 889 980, for LHC10e period it is 41 461 090, totalling 153 362 070 for $\sqrt{s} = 7$ TeV. For events from 2011 proton-proton collisions at $\sqrt{s} = 2.76$ TeV, total number of accepted events is 45 625 000. These numbers are summarised in Tab. 5.4, with corresponding number of triggered events. This number is important for normalisation of jet production cross section, (5.1).

Complete list of runs accepted for further analysis is in Tab. 5.3.These runs were selected in such a way, that they contain sufficient number of events, they did not experience any problems concerning triggering or tracking sub-detectors during data taking and their distribution of azimuthal angle and pseudo-rapidity show expected behaviour,5.2.

5.2 Track selection

The major emphasis before jet reconstruction itself was place on track selection. Within fiducial acceptance of the ALICE detector, i.e. full azimuthal coverage and pseudo-rapidity spans from -0.9 to 0.9, we expect and require tracks to have flat distribution in azimuth.

In order to obtain such a good track distributions, several sets of tracks have been created. They originate from same set of track quality cuts. The addition of requirement for a hit in any SPD layer defines *hybrid global tracks* and exclusion of requirement of ITS track refit defines *global constrained tracks.* These sets are used as standard in analyses of jets in the ALICE Physics Working Group.

- at least 70 TPC clusters per track
- $70 + 3/2 \cdot p_{\mathrm{T}}$

Period	Runs	Events
LHC10d	122374, 125023, 125085, 125097, 125100, 125101, 125134, 125139, 125140, 125156, 125186, 125296, 125630, 125632, 125633, 125842, 125843, 125844, 125847, 125848, 125849, 125850, 125851, 125855, 126004, 126007, 126008, 126073, 126078, 126081, 126082, 126088, 126090, 126097, 126158, 126284, 126285, 126351, 126352, 126359, 126403, 126404, 126405, 126406, 126407, 126408, 126409, 126422, 126424, 126425, 126432, 126437	151.0×10^6
LHC10e	127712, 127714, 127718, 127719, 128495, 128498, 128503, 128504, 128505, 128507, 128605, 128615, 128621, 128677, 128678, 128777, 128778, 128820, 128823, 128824, 128833, 128835, 128836, 128843, 128850, 128853, 128855, 128913, 129512, 129513, 129514, 129599, 129639, 129641, 129652, 129653, 129654, 129659, 129667, 129960, 129961, 130157, 130158, 130179, 130519, 130601, 130608, 130696, 130704, 130793, 130798, 130799, 130834, 130840	70.2×10^6
LHC11a	146746, 146747, 146748, 146801, 146802, 146803, 146804, 146805, 146806, 146807, 146817, 146824, 146856, 146858, 146859, 146860	79.9×10^6

Table 5.3: Table containing complete list of data runs used with information about number of events used for each given data-taking period.

Data-taking period	Number of min. bias events	Number of accepted events
LHC10d	142.4×10^6	111.9×10^6
LHC10e	52.8×10^6	41.5×10^6
LHC10d+e	195.2×10^6	153.4×10^6
LHC11a	65.8×10^6	45.6×10^6

Table 5.4: Table summarising total number of triggered events required for jet production cross section normalisation and number of total accepted events which pass all the selection criteria.

- $\chi^2_{\mathrm{max}} = 4$ per TPC cluster
- TPC stand-alone track required
- reject daughter kinks
- require TPC refit
- at maximum share 40 % of cluster

- require ITS refit
- distance of closest approach in xy-plane smaller than 2.4 cm
- distance of closest approach in z-plane smaller than 3.2 cm
- $\chi^2_{\max} = 36$ per ITS cluster
- $\chi^2_{\max} = 36$ global constrain to TPC track
- specific requirements:
  - **Global Constrained Track Cuts**

    → refit of ITS track is not required

    → denoted by filter bit 256
  - **Hybrid Global Track Cuts**

    → require hit in any SPD layer

    → denoted by filter bit 16

These requirements define two sets of tracks that are called *global constrained tracks* and *hybrid global tracks* and in analysis they are assigned specific filter bits, 256 and 16 respectively, to differentiate them. These filter bits differentiate between different analyses track cuts. In Fig. 5.1 fraction of selected tracks as global constrained and complementary hybrid global tracks, i.e. tracks that are hybrid global but do not pass cuts for global constrained tracks. This complementarity is necessary to prevent double counting of tracks that fulfil both sets of requirements.

From azimuthal distribution in Fig. 5.1c, it is obvious, that there are segments at approximately 4 rad and 6 rad, where there are no hybrid tracks, only global constrained tracks. However, the combined distributions of number of TPC clusters and ITS points registered per track, Fig. 5.2f and Fig. 5.2e respectively, show no sign of such odd behaviour thanks to the combinations of the two sets of tracks, although later figure shows slight decrease in average number of ITS points per tracks, with significant reduction of points with 5 and 6 point per track in the azimuthal region around 4 rad and 6 rad. Also the final azimuthal distribution of tracks, Fig. 5.3c does not produce strange behaviour around these regions as the distribution is flat.

5.2.1 Quality assurance of reconstructed tracks

In order to prevent runs with inappropriate configuration of sub-detectors or with problematic part of these sub-detectors, i.e. segment of a detector was taken out of data-taking due to technical problems during the operations, that were not excluded in first process of run selection, quality of the tracks is tested per run of each period. As seen from Tab. 5.3, quite a number of runs is omitted either due to these difficulties or due to the insufficient statistics[3].

---

[3] It is noteworthy that run number is assigned even to calibration runs for each sub-detector and not only for runs with data-taking setup.

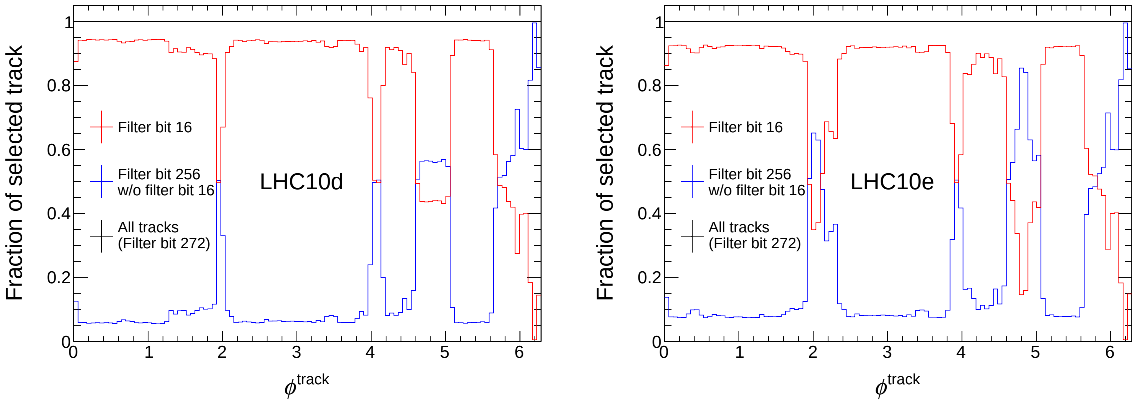

(a) LHC10d (b) LHC10e

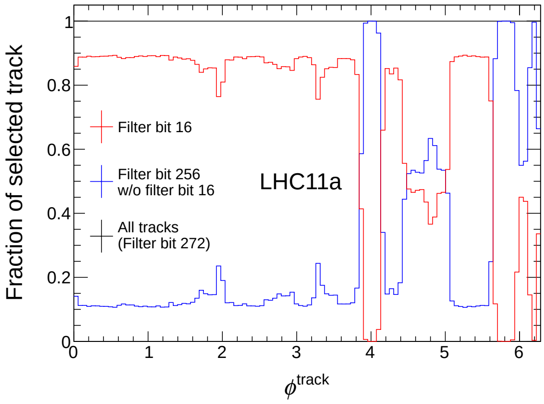

(c) LHC11a

Figure 5.1: Azimuthal distribution of fraction of tracks accepted for analysis as *hybrid global* tracks, represented by the filter bit 16 and red colour, and *global constrained* tracks that are represented by filter bit 256 and blue colour. These distributions are studied for all the analysed data-taking periods, i.e. LHC10d, 5.1a, LHC10e, 5.1b, and LHC11a, 5.1c.

Quality of the tracks is checked by looking on azimuthal distribution of tracks, specifically, number of reconstructed TPC clusters and number of ITS points obtained from track reconstruction is important. As seen in Fig. 5.2, selected tracks used in analysis have similar distribution of TPC clusters, with mean values above 130 clusters per tracks. It can be seen that segmentation of detector into 18 trapezoid sectors reflects into segmentation observed in this azimuthal distribution, as track cluster reconstruction decreases for tracks with momenta in plane where 2 sectors touch.

The reconstructed number of clusters in TPC per track does not seem to be changing in between different periods. On the other hand, number of ITS points per tracks decreases on average in LHC11a data-taking period, Fig. 5.2e, compared to periods of the year 2010. This decrease is the most pronounced at the azimuthal angle around 4 rad and 6 rad, regions that were problematic for reconstruction of hybrid global tracks, as

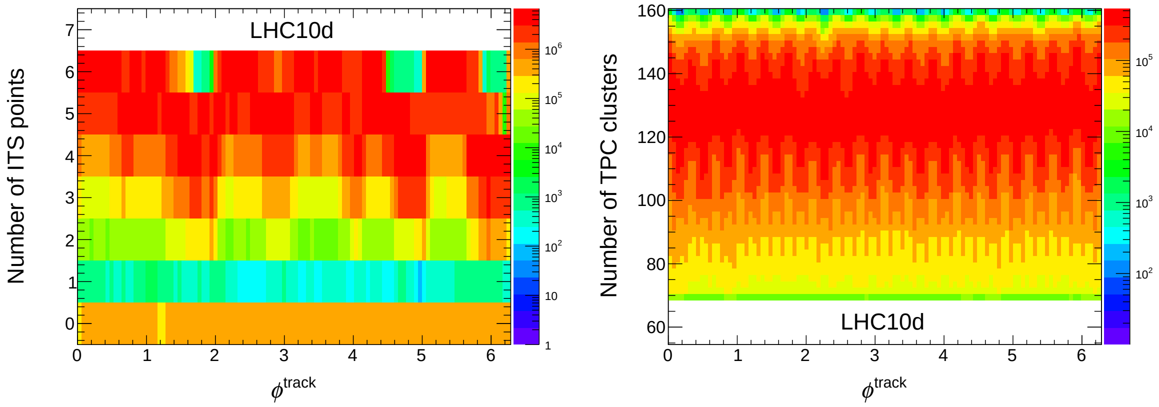

(a) ITS points in LHC10d (b) TPC clusters in LHC10d

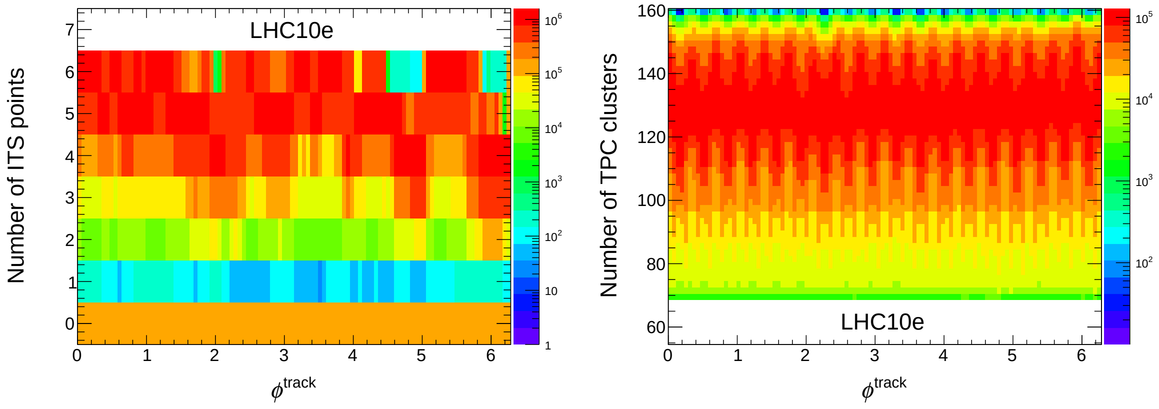

(c) ITS points in LHC10e (d) TPC clusters in LHC10e

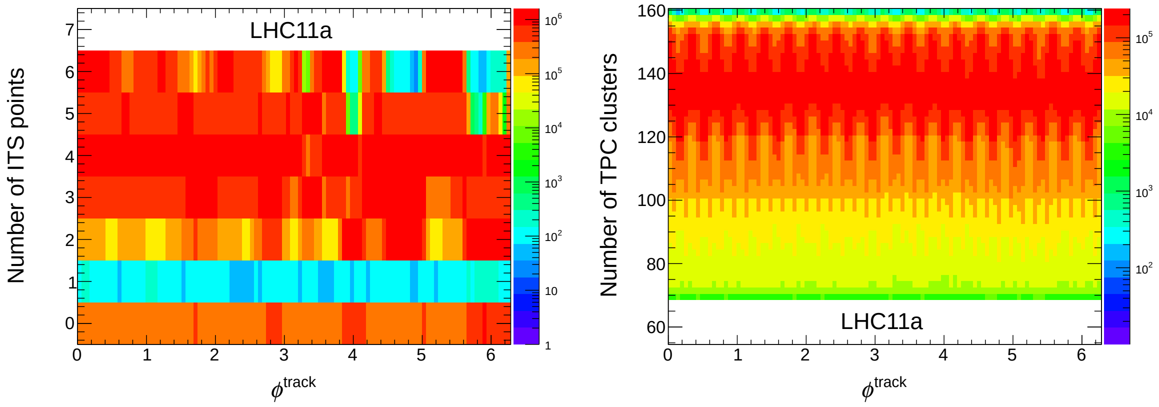

(e) ITS points in LHC11a (f) TPC clusters in LHC11a

Figure 5.2: Figure showing the number of points reconstructed in ITS used in track and number of TPC clusters per track, left and right column respectively, for individual periods, i.e. LHC10d, 5.2a 5.2b, LHC10e,5.2c 5.2d, and LHC11a 5.2e 5.2f.

mentioned earlier in the chapter.

5.2.2 Distribution of tracks

Altogether, there was 12.3×10^9 and 3.3×10^9 tracks candidates in 7 TeV and 2.76 TeV data respectively. This includes all the tracks which did not fulfil criteria on its quality. Out of these tracks over a quarter was accepted into further jet analysis. More detailed overview can be seen in Tab. 5.5.

Data-taking period	Total number of tracks	Number of accepted tracks
LHC10d	$7.676\,72 \times 10^9$	$2.092\,15 \times 10^9$
LHC10e	$4.658\,40 \times 10^9$	$1.212\,19 \times 10^9$
LHC11a	$3.322\,84 \times 10^9$	$8.746\,06 \times 10^8$

Table 5.5: Total number of tracks and number of accepted tracks in accepted events for individual analysed data-taking periods.

Furthermore, in Fig. 5.3 more detailed distributions of kinematic properties of tracks can be seen. This includes transverse momenta of selected tracks for both collision energies analysed, Fig. 5.3a. As can be seen both spectra exhibit similar behaviour. The spectra are normalised by number of events used in analysis for given collision energy and 7 TeV data exhibit enhancement over 2.76 TeV expected in collisions with increased centre-of-mass energy. It can be seen that statistics starts to be insufficient at 45 GeV/c for 2.76 TeV data. This will be reflected in the range of reconstructed jets in this type of collisions. However, these spectra are uncorrected, and same is valid for other kinematic properties of tracks discussed further in the section, and therefore no physical conclusion can be done from these observations. From the rest of the plots in Fig. 5.3, i.e. distributions of pseudo-rapidity and azimuthal angles of tracks, it is seen that both are relatively flat. In case of pseudo-rapidity, Fig. 5.3b, the first and the last bin of distribution at the edge of acceptance are significantly lower than rest of nearly flat distribution. Two effects are present here. First, this is the region where naturally pseudo-rapidity decreases with increasing absolute value of pseudo-rapidity. Second effect is from edge of detectors acceptance. The acceptance of TPC is much larger than from -0.9 to 0.9, however with higher absolute values of pseudo-rapidity the quality is lowered as smaller number of readout rows can be passed.

In case of azimuthal angle distributions, Fig. 5.3c, the distributions are relatively flat, no significant deviations are observed.

There is no difference in shape in distributions of pseudo-rapidity and azimuthal angle from the point of different energies of colliding system. This is verified because both distributions were normalised by the total number of tracks.

5.3 Jet reconstruction

Utilising several algorithms described in Sec. 3.2 with tracks selected according to requirements mentioned in Sec. 5.2 as inputs, jets are reconstructed from tracks detected by the ALICE experiment. As seen in Fig. 5.3c, tracks' acceptance spans from -0.9 to 0.9 units in pseudo-rapidity. This produces a limit on acceptance of reconstructed jets.

Furthermore, as seen in Fig. 5.4a and Fig. 5.4b, jet reconstruction produces outliers at the edge of acceptance. These jets are partially reconstructed remnants from jets that fragment also to the region outside of fiducial acceptance provided by tracking detectors. To prevent these partially reconstructed jets from influencing result, jets are counted only inside fiducial acceptance reduced by the resolution parameter, as this parameter gives roughly radius in space of pseudo-rapidity and azimuthal angle, Fig. 5.4c and Fig. 5.4d.

Moreover, these figures also account for cut on minimal transverse momenta of jets that are accepted, in order to at least partially get rid of jets that were reconstructed just because each track is considered as a proto-jet at the beginning of the reconstruction process. If this track is separated sufficiently separated from other tracks, it may end up as final jet.

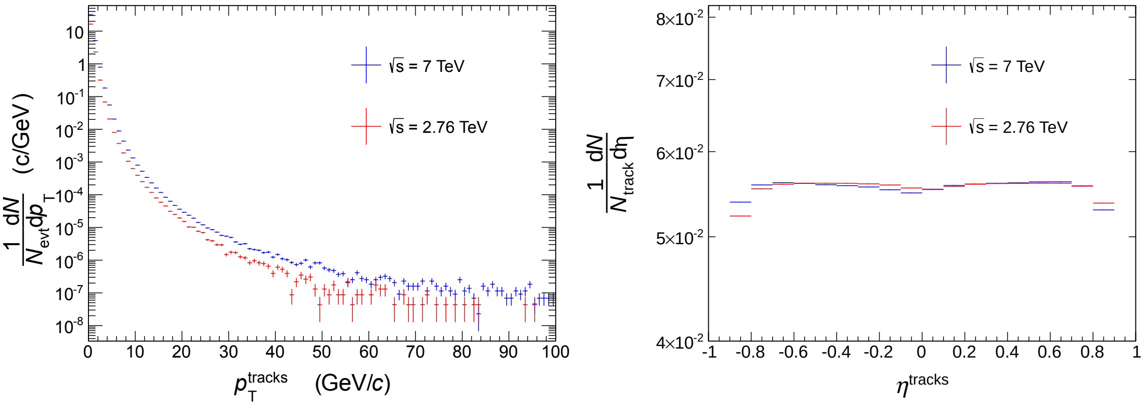

(a) transverse momenta distribution

(b) Pseudo-rapidity distribution

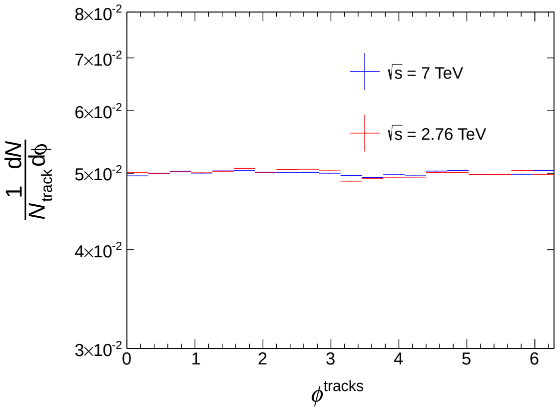

(c) Azimuthal angle distribution

Figure 5.3: Distribution of basic kinematic observables of tracks selected for jet analysis from $\sqrt{s} = 7$ TeV and $\sqrt{s} = 2.76$ TeV data are shown in blue and red, respectively. In Fig. 5.3a is shown track transverse momentum distribution, in Fig. 5.3b and Fig. 5.3c are distributions of pseudo-rapidity and azimuthal angle respectively.

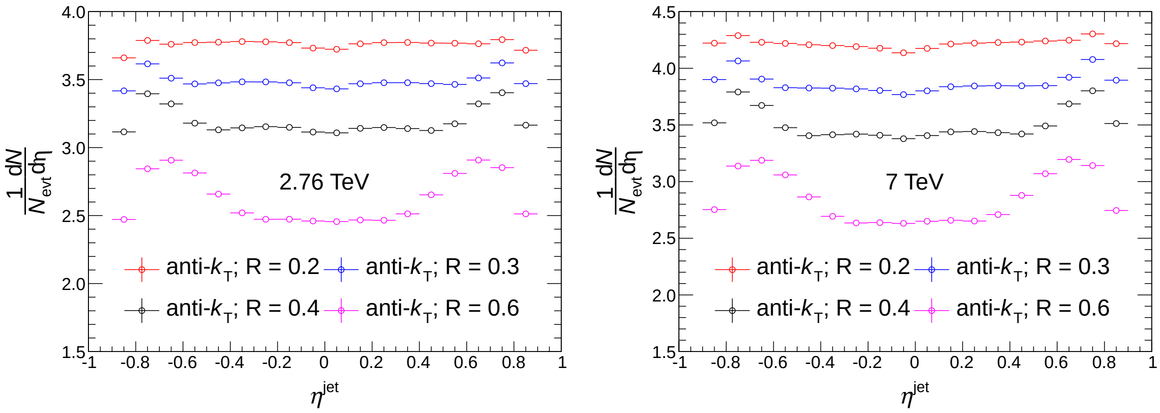

(a) Raw jet η distribution from $\sqrt{s} = 2.76$ TeV data. (b) Raw jet η distribution from $\sqrt{s} = 7$ TeV data.

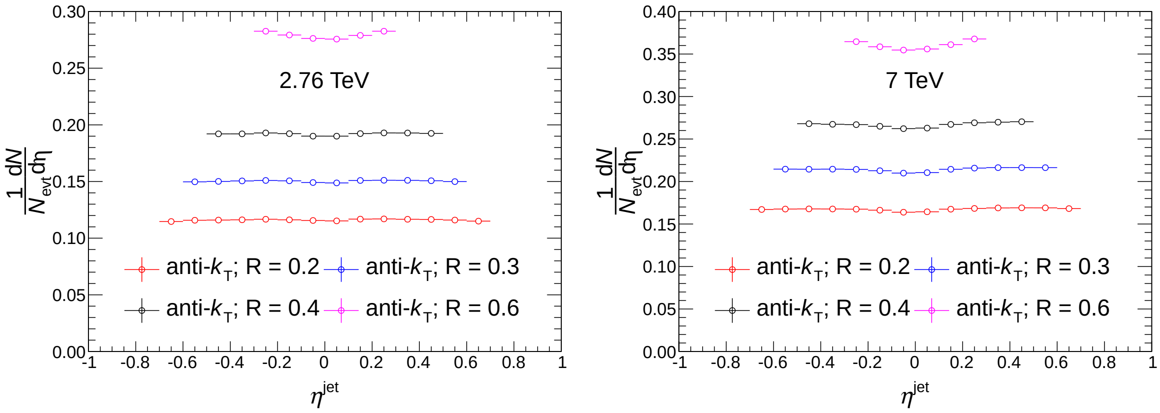

(c) Accepted jet η distribution from $\sqrt{s} = 2.76$ TeV. (d) Accepted jet η distribution from $\sqrt{s} = 7$ TeV data.

Figure 5.4: Top figures show normalised number of jets per unit of pseudo-rapidity per analysed event, in 2.76 TeV and 7 TeV data, Fig. 5.4a and Fig. 5.4b respectively. These figures clearly show outliers at the edge of acceptance which have to be rid of by reducing fiducial acceptance by value of the resolution parameter R. The result is seen in Fig. 5.4c and Fig. 5.4d, where additionally cut on minimal transverse momenta of tracks is applied. This cut reduces number of jets per event significantly.

List of jet cuts

- reconstructed from accepted hybrid global or global constrained tracks,
- acceptance $\eta^{\mathrm{jet}} \in (-0.9 + R, 0.9 - R)$,
- transverse momentum: $p_{\mathrm{T}}^{\mathrm{jet}} > 2\,\mathrm{GeV}/c$.

In order to obtain jet spectra in form of cross section, these counts have to be normalised by the number of triggered events and scaled by the cross section appropriate to the trigger used. This number has to be further corrected for the event rejection due to additional cuts such as vertex position, etc., such as in (5.1):

$$\left.\frac{\mathrm{d}^2\sigma}{\mathrm{d}p_{\mathrm{T}}\mathrm{d}\eta}\right|^{\mathrm{jets}}(p_{\mathrm{T}}) = \frac{1}{N_{\mathrm{evt}}^{\mathrm{trig}}}\sigma_{\mathrm{MBOR}}\frac{N_{\mathrm{jets}}\left(p_{\mathrm{T}}\right)}{\Delta p_{\mathrm{T}}\Delta\eta}. \tag{5.1}$$

In this formula, it is necessary to distinguish between number of triggered events and number of events accepted by analysis. The number of triggered events also reflects cases, when event does not have properly reconstructed vertex, i.e. does not pass selection criteria, however this is due to detector limitations and jets are produced in these collisions.

Additionally, as mentioned in Sec. 3.1.6, underlying event is subtracted from jets. This is done in order for reconstructed jets spectra to be directly comparable with corrected spectra from heavy-ion collisions where background subtraction has to be done. More on the subtraction is in following section, Sec. 5.3.1

5.3.1 Underlying event

Due to the composite nature of colliding hadrons, there can be multiple processes happening simultaneously during collision of two nuclei. That is why, hard-scattering processes does not have to be the only processes in the event, but rather multiple other processes can occur between *beam remnants* as sketched in Fig. 5.5. These other processes in proton-proton collisions create so-called *underlying event.* It is a small correction to

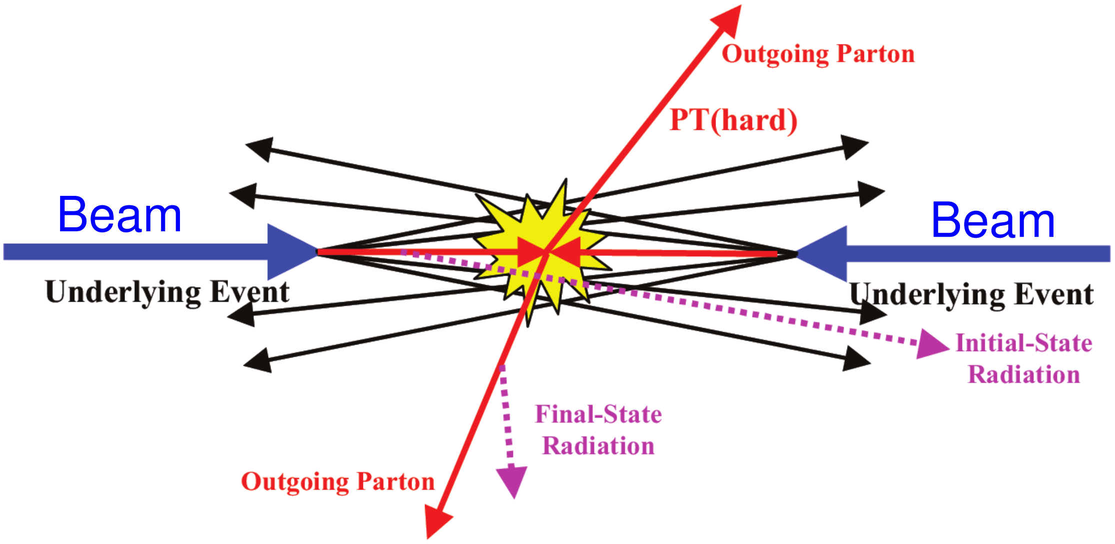

Figure 5.5: Illustration of the QCD Monte-Carlo simulation of a collision with hard scattering. The final event contains particles from the two outgoing partons with initial and final-state radiation and particles that come from the *beam remnants.* The *underlying event* is everything except the two outgoing hard scattered jets and consists of the beam-beam remnants plus initial and final-state radiation. Sketch adapted from Ref. [58].

the energy or momentum of reconstructed jet, however it does depend on collision energy and pseudo-rapidity.

On the other hand, background in collisions of heavy ions is much more significant and places restrictions on jet reconstruction. Among others is limitation on resolution parameter used in reconstruction. This is due to the fact, that larger the resolution parameter is the more background is reconstructed as a part of the jet and correcting this causes a lot of problems.

The most general way of calculating a underlying event is by finding energy density of these underlying processes outside of the jet and then subtract appropriate energy from jet, assuming that the energy density is constant in given region.

Another way for determination of underlying event, adapted from method used in Ref. [59], is by looking at particles produced transverse to the jet in question.

Taking the leading jet as point of reference, the method divides event into tree regions in azimuth, as seen in Fig. 5.6:

- **toward region** $\Delta\phi \le \pi/3$,
- **transverse region** $\pi/3 < \Delta\phi < 2\pi/3$,
- **away region** $2\pi/3 \le \Delta\phi$,

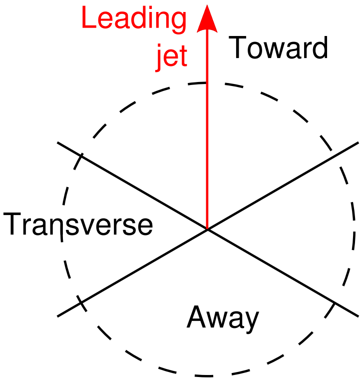

Figure 5.6: Sketch depicting division of event in azimuth to toward, transverse and away region given by the relative position to leading jet.

where $\Delta\phi$ is relative angle from leading jet. It is assumed that energy density of the underlying density is dependant on pseudo-rapidity and constant with azimuthal angle.

The toward region is occupied by signal from jet and underlying event, also away region is occupied by jet created from back-to-back hard scattering process, therefore is not appropriate for determination of underlying energy density. Such analysis yields results as shown in Fig. 5.7.

Underlying event analysis takes particles in transverse region within radius equivalent to resolution parameter from point given by pseudo-rapidity of jet and centre of this transverse region. Energy density of underlying event, ρ_{UE} is obtained by summation of transverse momenta of all the particles selected by condition above and dividing by area of πR^2. This is necessary because jet reconstruction algorithms do not give jets with areas corresponding to perfect circle, i.e. πR^2.

$$\rho_{\mathrm{UE}} = \sum_{i}^{\Delta r_i^{\mathrm{perp.cone}} \le R} \frac{p_{\mathrm{T,i}}^{\mathrm{track}}}{2\pi R^2} \tag{5.2}$$

The effect of underlying event subtraction is more dominant in low transverse momentum part of the spectra. This is caused by the definition of area of jets. It is more focused around πR^2 value for jets with higher transverse momenta. On the other hand, low momenta jets have larger spread of value of area. For purpose of this analysis, and

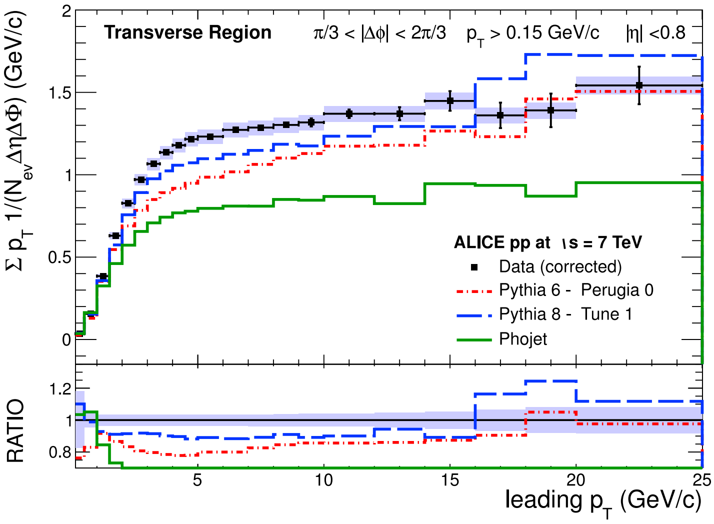

Figure 5.7: Underlying event in the ALICE collaboration obtained from reconstructed tracks. Tracks area obtained in transverse region as indicated by Fig. 5.6, by summing transverse momenta of all tracks in this region. The position of this region is estimated from reconstructed leading track in given event.

as standard for jets reconstructed in the ALICE collaboration, *active area definition* was used, and its definition is described in Sec. 3.3.2

Fig. 5.8 shows dependencies of jet area on transverse momentum of reconstructed jet, for all the resolution parameters observed in this analysis. The spread of jet areas spans from negligible to 2.2 times the area of ideal circular jet, which would obey πR^2. The dominant momentum range where areas have largest spread from this ideal value is below 10 to 20 GeV/c. These outliers are mostly caused by combinatorial jets created from randomly displaced tracks, or tracks that are moving in same general direction e.g. because they are decay products of other resonances.

Coupled with the density of underlying event, the effect of the underlying event subtraction can be seen in Fig. 5.9. Here are shown ratios of jet transverse momentum spectra after subtraction to original jet spectra. The effect increases towards the low transverse momentum region as expected from increasing spread of area of jets with transverse momentum in this range.

Figures 5.10a and 5.10b show jet transverse momentum spectra with subtracted underlying event from data-taking runs at $\sqrt{s} = 7$ TeV and $\sqrt{s} = 2.76$ TeV, respectively. This UE is subtracted as described in previous text using method of perpendicular cones.

Additionally, these plots contain binning used in final corrected spectra. It contains several underflow and overflow bins necessary for proper unfolding using both Bayesian method and SVD. For final spectra ranges only such bins were selected that contained at least 10 jets and there was no empty bin for smaller transverse momentum. These conditions are there to prevent statistically insignificant bins to enter final physical spectra.

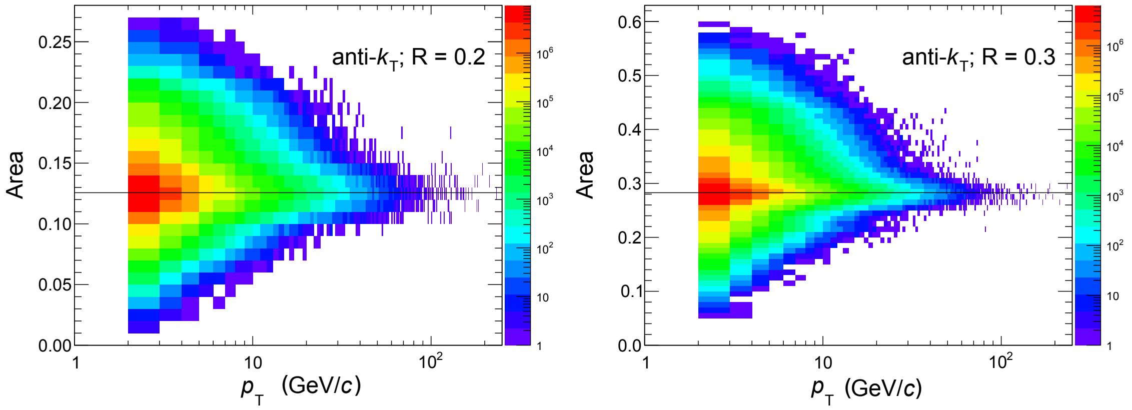

(a) $R = 0.2$ (b) $R = 0.3$

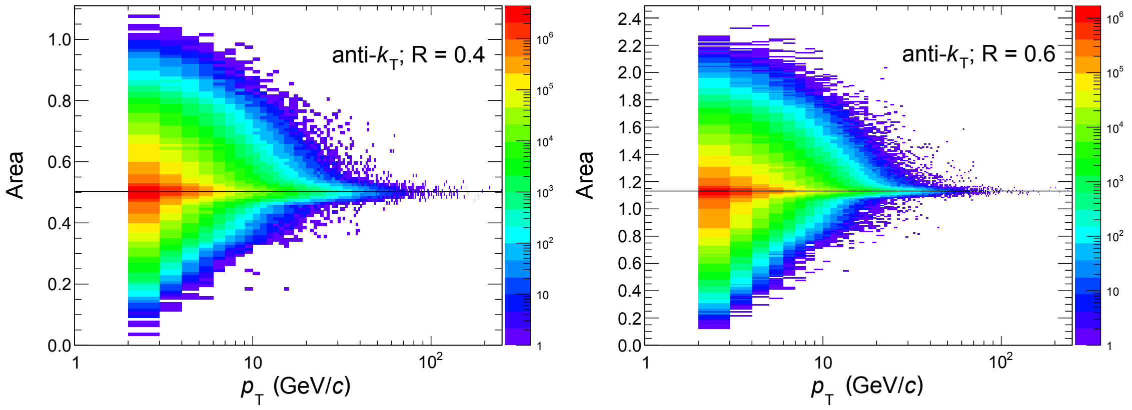

(c) $R = 0.4$ (d) $R = 0.6$

Figure 5.8: Dependence of area on transverse momentum of reconstructed jets for different resolution parameters of jets. Black line indicates ideal spherical area with radius given by resolution parameter. Scale on area axis spans from 0 to 2.2 times ideal area in each subfigure. Jets with resolution parameter equal to 0.2, 0.3, 0.4 and 0.6 are in Fig. 5.8a, Fig. 5.8b, Fig. 5.8c and Fig. 5.8d, respectively. For purpose of these plots, $\sqrt{s} = 7$ data were used.

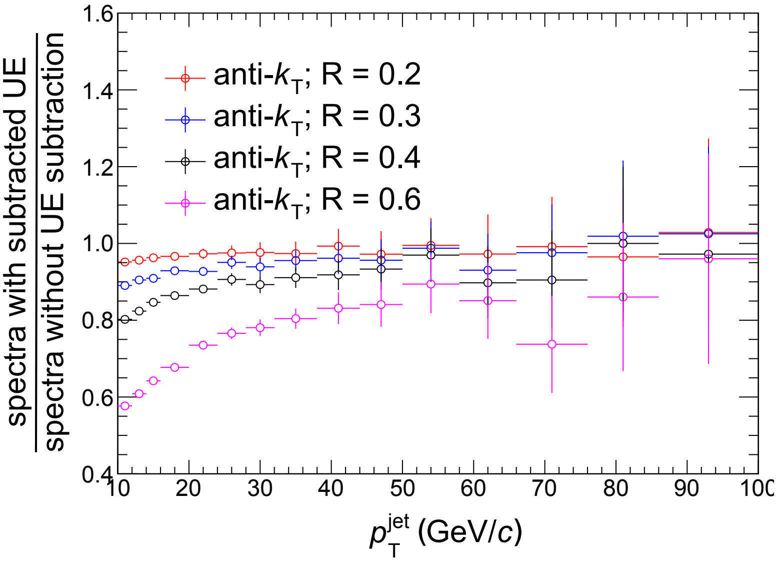

Figure 5.9: The plot shows effect of subtracting underlying event on event-by-event basis extracted from perpendicular cones method as a ratio between spectra with subtracted and without subtracted underlying event. The decrease in low transverse momentum part is caused mainly due to wider spread of jet areas in this region, compared to more defined area for larger transverse momenta.

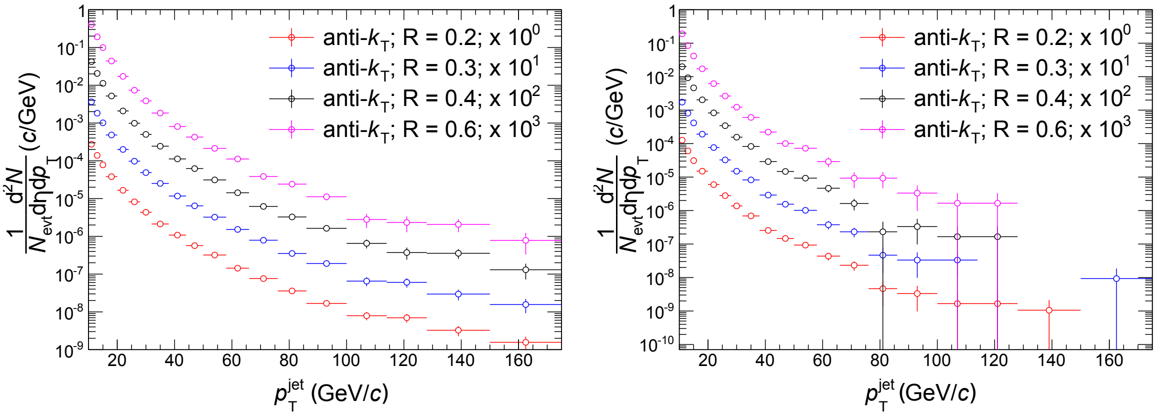

(a) 7 TeV

(b) 2.76 TeV

Figure 5.10: Uncorrected transverse momentum spectra with underlying event subtraction as described in this section. Left contains data from 7 TeV runs, Fig. 5.10a, and right from 2.76 TeV data-taking runs, Fig. 5.10b. Binning on these plots is made in accordance with the binning used for the final spectra with addition of several underflow and overflow bins used in unfolding.

Chapter 6. Analysis of simulated data

This chapter describes different simulations used in analysis of jet data from the ALICE detector system. Main focus of this description is the PYTHIA production with full detector simulation, due to the fact that these are used in unfolding of detector effects.

Additionally, simulations involving next-to-leading order jet productions are discussed in this chapter, with observables identified and further analysed.

6.1 Leading order simulations

For purpose of this analysis, `PYTHIA6.4.21` in conjunction with full detector simulation was used in order to produce response matrices of detector reconstruction of particles, which are used in jet spectra corrections. Full detector simulation was done via `Geant v3.21`. Additionally, PYTHIA6 simulations using Perugia-0, Perugia-2010, Perugia-2011 and AMBT tunes were produced without detector simulation. These tunes implement slightly different parameters in common core simulator, in order to describe different observables. Moreover, Monte-Carlo generators HERWIG and PHOJET were used as additional checks other than PYTHIA6 were used.

These simulations use leading-order processes in order to produce jet spectra. Later on, next-to-leading order processes will be discussed in Sec. 6.2.

Dataset	$p_{\mathrm{T}}^{\mathrm{hard}}$ (GeV/c)	cross-section (mb)	number of events	event weight, w_i (mb/event)
LHC11a1a	5–11	$3.754\,85 \times 10^{1}$	647 699	$5.797\,21 \times 10^{-5}$
LHC11a1b	11–21	2.440 71	730 000	$3.343\,44 \times 10^{-6}$
LHC11a1c	21–36	$2.101\,11 \times 10^{-1}$	681 627	$3.082\,49 \times 10^{-7}$
LHC11a1d	36–57	$2.355\,92 \times 10^{-2}$	808 359	$2.914\,45 \times 10^{-8}$
LHC11a1e	57–84	$3.263\,00 \times 10^{-3}$	747 200	$4.366\,97 \times 10^{-9}$
LHC11a1f	84–117	$5.610\,35 \times 10^{-4}$	737 373	$7.608\,56 \times 10^{-10}$
LHC11a1g	117–156	$1.173\,29 \times 10^{-4}$	631 722	$1.857\,29 \times 10^{-10}$
LHC11a1h	156–200	$2.780\,04 \times 10^{-5}$	548 163	$5.071\,56 \times 10^{-11}$
LHC11a1i	200–249	$7.691\,85 \times 10^{-6}$	157 920	$4.870\,73 \times 10^{-11}$
LHC11a1j	> 249	$3.583\,83 \times 10^{-6}$	408 800	$8.766\,72 \times 10^{-12}$

Table 6.1: Detailed information about simulations of jets in pp collisions at 7 TeV with simulated detector response, labelled LHC11a1. Each dataset of this simulations is generated with different range of transverse momenta of scattered hard particle, $p_{\mathrm{T}}^{\mathrm{hard}}$. This corresponds to different production cross-section that reflects in weight of each event of this simulation accounting number of simulated events in each dataset.

6.1.1 Full detector simulation

In order to provide sufficiently large sample of data for high momentum jets, simulations was carried out in different hard-p_{T} bins. These bins represent only given interval of transferred momenta in hard scattering, but together cover momentum range up to 1 TeV. To join these different simulations, each bin of hard momenta carries information about cross section, σ, used in its production and number of trials attempted, N_{trials}.

Using these values according to formula

$$w = \frac{\sigma}{N_{\mathrm{trials}}}, \tag{6.1}$$

where weights from all obtained hard bins are used in following way

$$O = \sum_{i}^{\mathrm{hard\ bins}} O_i w_i. \tag{6.2}$$

Here O is any observable from whole statistics, spanning several hard bins, and O_i are same observables in given hard p_{T} bin i. Event weights for simulation with proton-proton collisions at 7 TeV are shown in the Tab. 6.1, and for 2.76 TeV dataare in the Tab. 6.2. These tables contain momentum ranges of hard p_{T} as well as both cross sections and used trial events.

Simulation setup

Basic setup of PYTHIA6 production with full detector simulation was done using

Dataset	$p_{\mathrm{T}}^{\mathrm{hard}}$ (GeV/c)	cross-section (mb)	number of events	event weight (mb/event)
LHC11a2a	5–11	$1.190\,41 \times 10^{1}$	758 482	$1.569\,47 \times 10^{-5}$
LHC11a2b	11–21	$6.248\,74 \times 10^{-1}$	880 929	$7.093\,35 \times 10^{-7}$
LHC11a2c	21–36	$4.373\,36 \times 10^{-2}$	919 678	$4.755\,32 \times 10^{-8}$
LHC11a2d	36–57	$4.032\,61 \times 10^{-3}$	908 480	$4.438\,85 \times 10^{-9}$
LHC11a2e	57–84	$4.578\,48 \times 10^{-4}$	439 999	$1.040\,57 \times 10^{-9}$
LHC11a2f	84–117	$6.433\,05 \times 10^{-5}$	749 596	$8.582\,03 \times 10^{-11}$
LHC11a2g	117–156	$1.072\,49 \times 10^{-5}$	680 000	1.5772×10^{-11}
LHC11a2h	156–200	$2.026\,59 \times 10^{-6}$	548 277	$3.696\,29 \times 10^{-12}$
LHC11a2i	200–249	$4.330\,81 \times 10^{-7}$	452 866	$9.563\,11 \times 10^{-13}$
LHC11a2j	> 249	$1.328\,19 \times 10^{-7}$	463 270	$2.866\,99 \times 10^{-13}$

Table 6.2: Detailed information about simulations of jets in pp collisions at 2.76 TeV with simulated detector response, labelled LHC11a2. Each dataset of this simulations is generated with different range of transverse momenta of scattered hard particle, $p_{\mathrm{T}}^{\mathrm{hard}}$. This corresponds to different production cross-section that reflects in weight of each event of this simulation accounting number of simulated events in each dataset.

- CTEQ6l parton distribution function
- approximately 1×10^{6} simulated events per hard bin
- Perugia0 PYTHIA6 tune
- magnetic field of 0.5 T

Simulated hard-bins are described in Tab. 6.1 and Tab. 6.2 for 7 TeV and 2.76 TeV data, respectively. These tables show momentum range of hard p_{T} , mean cross section and number of analysed events. Additionally hard-bin weights calculated according to Eq. (6.1), are shown.

Track reconstruction

Due to the detector effects, such as momentum smearing and inefficiency in track reconstruction, not all tracks are reconstructed in the detector. Additionally, if the track is reconstructed, the energy and momentum are not necessarily precisely reconstructed, usually smeared around true value.

The efficiency of track reconstruction is shown in Fig. 6.1a, where the peak of 87% is located at values of transverse momenta at around 1.5 GeV/c. Afterwards, it starts to decrease down to 73% for tracks with the highest transverse momenta, which can be explained by decreasing efficiency of differentiating 2 close tracks with large momentum, as their negligible curvature prevents separation of one from the other.

In Fig. 6.1b, relative resolution of track reconstruction as a function of inverse of track's transverse momentum of original track. As seen, these values start at negligible values for tracks with low transverse momenta and increase linearly to 20% for 100 GeV/c tracks.

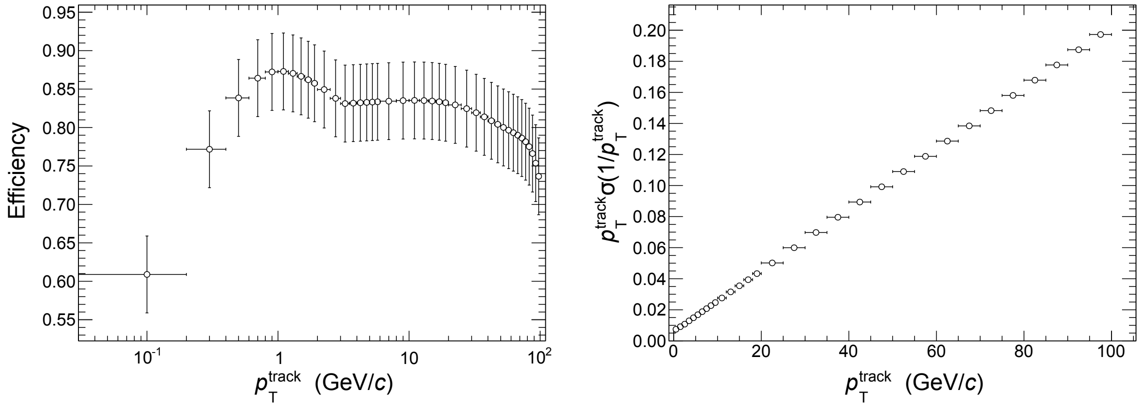

(a) Track reconstruction efficiency

(b) Track momentum resolution

Figure 6.1: Track reconstruction efficiency, (a), and relative momentum resolution, (b), are shown for hybrid track cuts.

Jet reconstruction and jet matching

For the purpose of this analysis, same jet reconstruction procedures were applied for simulated evet as to real data in order to be consistent. However, jets were reconstructed on the level of reconstructed track and in addition to this on the level of generated particles. This is necessary in order to create response matrix reflecting jet reconstruction efficiencies and momentum shifts of reconstructed jets.

In order to do so, jets are being matched on geometrical principle, which is as follows:

- all selected jets are sorted according to the value of the transverse momenta,
- to every reconstructed jet, the closest generated jet is found within $\Delta r \leq 0.1$,
- to every generated jet, the closest reconstructed jet is found within $\Delta r \leq 0.1$,
- if the generated jet that is found to be the closest one to given reconstructed jet has this reconstructed jet assigned as the closest reconstructed jet then this paired is taken as matched.

This enables definition of jet reconstruction efficiency, as it is fraction of jets that have matched pair,

$$\epsilon_{\mathrm{jet}} = \frac{\mathrm{N}_{\mathrm{gen.jet}}^{\mathrm{matched}}}{\mathrm{N}_{\mathrm{gen.jet}}}, \tag{6.3}$$

i.e. number of matched jets divided by number of all selected generated jets within acceptance. Jet reconstruction efficiencies can be seen in Fig. 6.2, where efficiencies for different resolution parameter are given as functions of transverse momenta of generated jet.

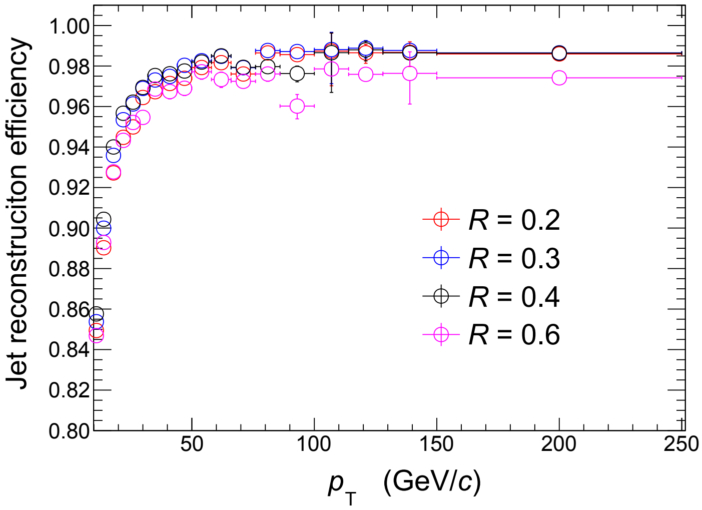

Figure 6.2: Jet reconstruction efficiency obtained from full detector simulation using Geant and PYTHIA6 for detector reconstruction . It gives information about probability of generated charged-particle jet within selected acceptance to be reconstructed within acceptance. As seen, This probability is close to 98% for higher transverse momenta of generated jets and decreases with decreasing transverse momenta. The difference between jets reconstructed using different resolution parameter encompasses the different acceptances of these different jet classes.

With defined procedure for jet matching, response matrices can be constructed. These are shown in Fig. 6.3 and Fig. 6.4, for all resolution parameters and collision energies of 7 TeV and 2.76 TeV, respectively. They are not normalised to number generated jets. First figure shows response or correlation matrices for proton-proton collisions at $\sqrt{s} = 7$ TeV and at $\sqrt{s} = 2.76$ TeV. The main difference, as can be deduced from cross section shown in Tab. 6.1 and Tab. 6.2, arose from different cross sections necessary to generate hard processes in given transverse momentum ranges. On the other hand, the shape of these response matrices is similar, as expected from the same setup of analyses. Along the line $y = x$, clear global maximum can be observed. This is a consequence of most probable value of transverse momenta of reconstructed jet being around the value of transverse momenta of generated jet. However, there are apparent tails to both sides, with dominant being for jet energy loss. This can be more clearly seen as a mean momentum shift. Both most probable value and mean momentum shift with addition of quartiles can be seen in Fig. 7.6. It is obvious that the differences between jets with different resolution parameter are minimal.

6.1.2 Pure simulation without detector effects

In case of the fast simulations, simulations that did not account for detector effects, several different tunes were used. These simulations were mainly used for result com-

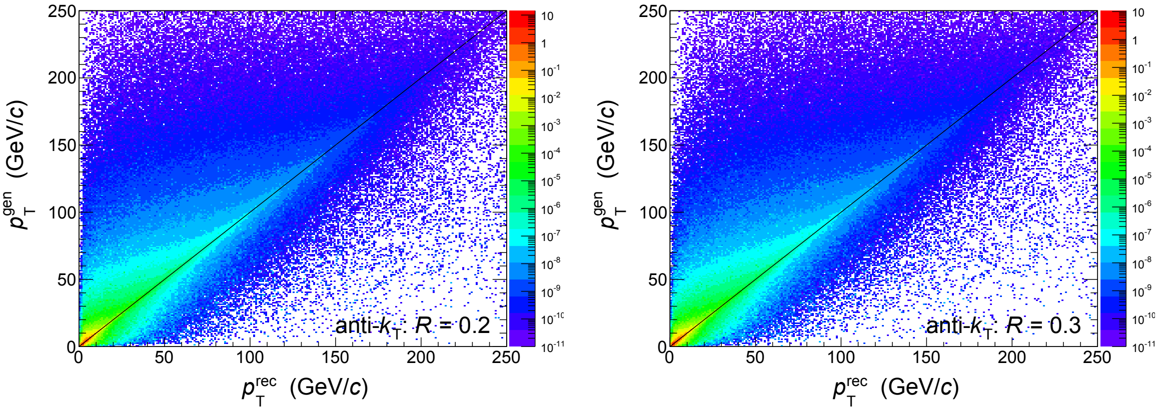

(a) $\sqrt{s} = 7$ TeV; $R = 0.2$ (b) $\sqrt{s} = 7$ TeV; $R = 0.3$

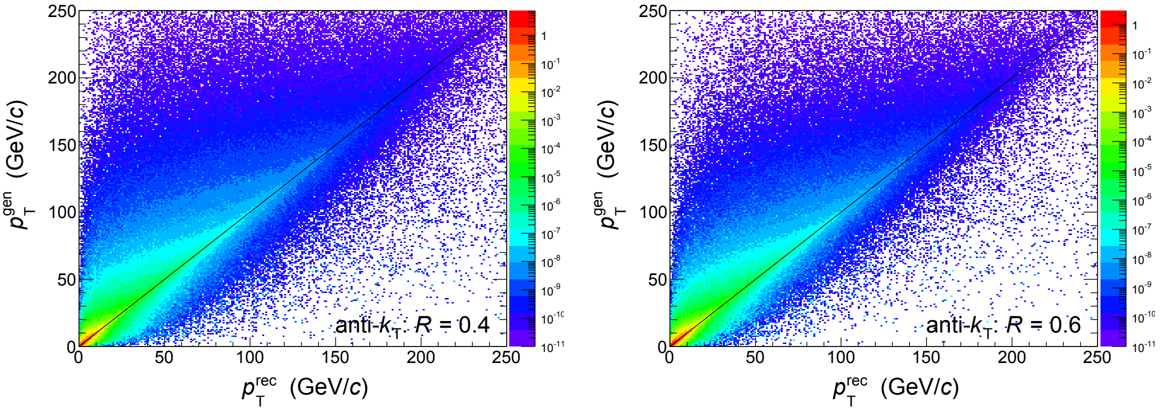

(c) $\sqrt{s} = 7$ TeV; $R = 0.4$ (d) $\sqrt{s} = 7$ TeV; $R = 0.6$

Figure 6.3: Response matrices used for determination and correction of detector effects on jet reconstruction from proton-proton collisions at $\sqrt{s} = 7$ TeV. On x-axis, reconstructed jet transverse momenta are shown opposite to the generated jet transverse momenta. Obvious shift to the upper left triangle of these matrices corresponds to energy loss during track reconstruction, however non-negligible portion of elements is present in lower right triangle of these matrices representing jets reconstructed with larger transverse momenta than the originally generated one.

parison and as such, they serve on as reference. In the text below, a brief description of different PYTHIA tunes is made. Further details can be found in Ref. [60]. These simulations are done with smeared primary vertex and CTEQ5L parton distribution function as a default.

- **PYTHIA6 Perugia 0**
  This tune by default uses CTEQ5L parton distribution functions and produces excellent agreement for Drell-Yan p_T spectrum. Combination of increased MPI cut off and slightly increased beam remnant break up and decreased colour reconection in comparison with previous tune S0(A), improves agreement of prediction in average p_T and high-p_T tail of charged particle p_T spectra.

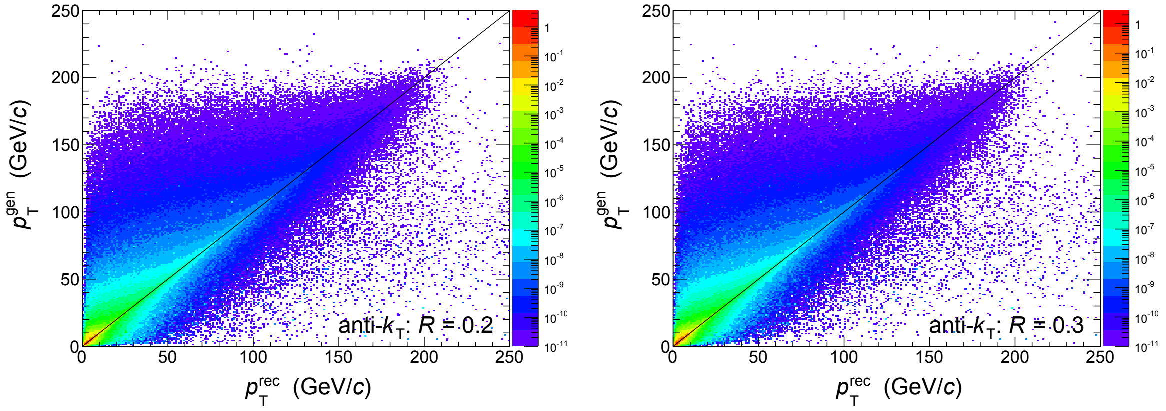

(a) $\sqrt{s} = 2.76$ TeV; $R = 0.2$

(b) $\sqrt{s} = 2.76$ TeV; $R = 0.3$

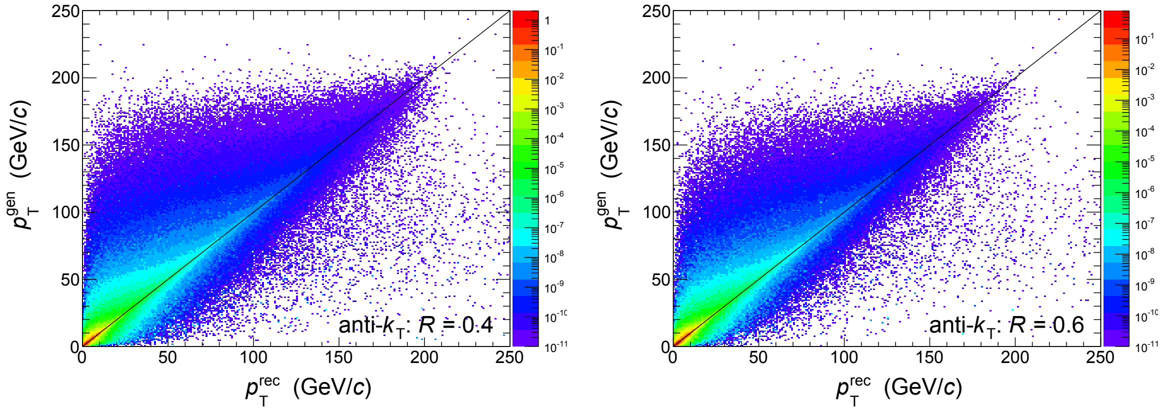

(c) $\sqrt{s} = 2.76$ TeV; $R = 0.4$

(d) $\sqrt{s} = 2.76$ TeV; $R = 0.6$

Figure 6.4: Response matrices used for determination and correction of detector effects on jet reconstruction reconstructed in proton-proton collisions at $\sqrt{s} = 2.76$ TeV. On x-axis, reconstructed jet transverse momenta are shown opposite to the generated jet transverse momenta.

- **PYTHIA6 Perugia 2010**
  This is a variant of tune Perugia 0, with increased amount of final state radiation outside of resonance decays, in order to improve hardronic event shape in comparison to Perugia 0 and improve jet shape description. Modification were done to overall strangeness, which has been increased, as well as infrared cutoff in high-z fragmentation and baryon number transport.

- **PYTHIA6 Perugia 2011**
  This tune takes into account first results from the LHC detectors, mainly minimum-bias and underlying-event data from 7 TeV and 900 GeV, such as charged-particle multiplicities from ATLAS [61] and ALICE [62], ATLAS UE measurement [63], increased baryon transport for beam remnants, slightly softer fragmentation function and slightly larger K*/K ration than in Perugia 2010 tune. Furthermore, same value of Λ_{QCD} was used for all processes.

Bin	$p_{\mathrm{T}}^{\mathrm{hard}}$ (GeV/c)	number of events
1	5−10	5×10^6
2	10−20	5×10^6
3	20−30	5×10^6
4	30−50	5×10^6
5	50−80	5×10^6
6	80−1000	5×10^6

Table 6.3: Size of simulated event sample without detector effects, with ranges of hard transverse momenta of the process and number of simulated events associated to given production bin.

- **PYTHIA6 AMBT1** This tune uses MRST2007LO* parton distribution function and was obtained from measured properties of minimum-bias events. Based on ATLAS MC09c tune, MPI cutoff and colour reconnection parameters were tuned to accommodate first results from LHC. Additionally, ISR cutoff parameter and cut-off parameter for initial momentum smearing were used. More about this tune can be found in Ref. [61].

- **HERWIG** `6.510`
  HERWIG is Monte Carlo package for simulating Hadron Emission Reactions With Interfering Gluons. No modifications were made for purpose of these simulations. More details can be obtained in Ref. [64, 65].

- **PHOJET** `1.12.1.35`
  PHOJET is pomeron/reggeon based model for production of both soft and hard particles only for leading order particles. It is suited for minimum bias studies without heavy quark production, as it works in the massless scheme. No modifications were made for purpose of these simulations.

6.2 Next-to-leading order simulations

In order to obtain better description of data than that of LO described in Sec. 6.1 with pQCD predictions, NLO simulations were carried out using POWHEG-Box [66–68] framework, where the focus was placed on jet production [69]. This framework is based on POsitive Weight Hardest Emission Generator, or POWHEG. In this analysis, NLO hard scatterings were produced in order to be able to compare these simulations with results of jet analyses from the ALICE collaboration.

6.2.1 Observables

For purpose of this analysis, we wanted to study proton-lead system via reconstruction of jets. Observing differences between data and leading-order predictions from PYTHIA, as seen in Fig. 8.3 and 8.5, observations for proton-proton collisions at 2.76 TeV and 7 TeV centre-of-mass energies. Subsequently, utilisation of *HKN07 NLO nPDFs* [72] and modification of POWHEG-Box framework to utilise modification factors to PDFs in order to describe probability of finding parton with given momentum fraction in ion. This enabled of study of proton-lead collisions with centre-of-mass energies of 5.02 TeV. Main result was R_{pPb}, nuclear modification factor for jets, i.e. comparison between jet spectra produced in proton-lead collisions and in proton-proton collisions. This variable should point out to possible enhancement or suppression in jet production, leading to effects of cold nuclear medium, which are indistinguishable from hot matter effects in pure lead-lead collisions.

Another studied effect was modification of jet cross-section as function of Bjorken's x_1 and x_2. Describing colliding partons, x_1 and x_2 denote fraction of particle's momenta carried by given parton. For sufficiently high energies of colliding particles[1] it may be assumed that

$$p_{\mathrm{beam}} \approx E_{\mathrm{beam}} = \frac{\sqrt{s}}{2}, \tag{6.4}$$

where p_{beam} is momentum of the beam particle and E_{beam} its energy. However, as partons carry only fraction of energy we can write it as (6.5a) and (6.5b). Furthermore, in 2 on 2 processes, we can write momenta of final-state particles using transverse momentum, p_{T}, azimuthal angle, φ and their rapidities, (6.5c) and (6.5d).

$$\hat{P}_1 = x_1 P_1 = x_1 \left(\sqrt{s}/2, 0, 0, \sqrt{s}/2\right), \tag{6.5a}$$

$$\hat{P}_2 = x_2 P_2 = x_2 \left(\sqrt{s}/2, 0, 0, -\sqrt{s}/2\right), \tag{6.5b}$$

$$\hat{P}_3 = p_{\mathrm{T}} \left(\cosh y_3, \cos\varphi, \sin\varphi, \sinh y_3\right), \tag{6.5c}$$

$$\hat{P}_4 = p_{\mathrm{T}} \left(\cosh y_4, -\cos\varphi, -\sin\varphi, \sinh y_4\right). \tag{6.5d}$$

Energy of the collision in a centre-of-mass frame of colliding partons, not beam particles, is defined as

$$\hat{s} = \left(\hat{P}_1 + \hat{P}_2\right)^2 = x_1 x_2 s. \tag{6.6}$$

---

[1] As $E = \sqrt{m^2 + p^2}$, we are speaking about cases when $m \ll p$.

The equation (6.6) shows relation between 2 different frames of reference via use of momentum fractions x_1 and x_2.

Invoking conservation of energy and momenta from equations (6.5), we see that component of momenta in x- and y-directions cancels directly from equations (6.5c) and (6.5d), as these relations are equivalent except for the sign for these two components.

For conservation of energy, equation (6.7) is obtained.

$$\frac{\sqrt{s}}{2}\left(x_1 + x_2\right) = p_{\mathrm{T}}\left(\cosh y_3 + \cosh y_4\right). \tag{6.7}$$

Similarly, we obtain difference of x_1 and x_2 from conservation of momenta.

$$\frac{\sqrt{s}}{2}\left(x_1 - x_2\right) = p_{\mathrm{T}}\left(\sinh y_3 + \sinh y_4\right). \tag{6.8}$$

Furthermore, we can substitute x_{T} instead of fraction of transverse momenta and collision energy, (6.9). This relation is used mainly for estimation of Bjorken's variables at midrapidity from single hadron spectra.

$$x_{\mathrm{T}} = \frac{2p_{\mathrm{T}}}{\sqrt{s}} \tag{6.9}$$

Solving 2 equations, (6.7) (6.8), with only 2 additional parameters y_3 and y_4, i.e. rapidities of final state partons in 2 on 2 process, we obtain expressions for x_1, (6.10a) and (6.10b).

$$x_1 = \frac{x_{\mathrm{T}}}{2}\left(\mathrm{e}^{\mathrm{y}_3} + \mathrm{e}^{\mathrm{y}_4}\right), \tag{6.10a}$$

$$x_2 = \frac{x_{\mathrm{T}}}{2}\left(\mathrm{e}^{-\mathrm{y}_3} + \mathrm{e}^{-\mathrm{y}_4}\right). \tag{6.10b}$$

6.2.2 Simulation setup

The simulations were set up in such a way so that direct comparison with data was possible. This implies that in order to describe jet transverse momentum region at the least up to 100 GeV/c, simulations had to calculate with 5 quark flavours due to the fact that top quark would be required if momentum region of the order of mass of the top quark[2] was reached.

Next was to select collision energies. In case of symmetric proton-proton collision, this trivially set according centre-of-mass energies of studied systems, i.e. colliding proton energies of 3500 GeV for $\sqrt{s}$ of 7 TeV and 1.380 GeV for $\sqrt{s} = 2.76$ TeV. However, in order to describe proton-lead collisions with $\sqrt{s} = 5.02$ TeV, proton with energy of 4000 GeV and Pb ion with energy of 1.580 GeV, collisions had to be calculated in reference frame, where both colliding particles had same energy, 2510 GeV, and produced hard scatterings were subsequently boosted by $\Delta y = 0.4x$. This was necessary because POWHEG-Box framework was not tested for collisions of particles with asymmetric energies.

---

[2] See Tab 1.1, for value of top quark mass.

Following parameter of simulation that was set up was PDF used for description of colliding protons. For our analysis CTEQ6.6 [70] was used for all the simulations. CTEQ6.6, obtained from LHAPDF v5.9 contains 1+44 parametrisations of protons' PDFs. This means that except for one central PDF, there are 44 error PDFs that correspond the variation of 22 parameters that are used in fit of data to produce the central PDF parametrisation. This variation is by 1σ obtained from fit in both positive and negative direction, resulting in 44 error parametrisations. In order to obtain uncertainty resulting from these variations, it is assumed that each parameter is independent, yielding uncorrelated uncertainties. These are than calculated independently for upper and lower variations according to (6.11a) and (6.11b), respectively.

$$\left[\Delta X^{+}\left(p_{\mathrm{T}}\right)\right]^{2}=\sum_{i=1}^{i_{\max}} \max\left[0, X\left(p_{\mathrm{T}}, f_{2i-1}\right)-X\left(p_{\mathrm{T}}, f_{0}\right), X\left(p_{\mathrm{T}}, f_{2i}\right)-X\left(p_{\mathrm{T}}, f_{0}\right)\right]^{2}, \tag{6.11a}$$

$$\left[\Delta X^{-}\left(p_{\mathrm{T}}\right)\right]^{2}=\sum_{i=1}^{i_{\max}} \max\left[0, X\left(p_{\mathrm{T}}, f_{0}\right)-X\left(p_{\mathrm{T}}, f_{2i-1}\right), X\left(p_{\mathrm{T}}, f_{0}\right)-X\left(p_{\mathrm{T}}, f_{2i}\right)\right]^{2}. \tag{6.11b}$$

Here, in these equations, $X\left(p_{\mathrm{T}}, f_{j}\right)$ represents studied observable in given bin of transverse momenta produced with PDF parametrisation set f_j. In case of f_0, central PDF parametrisation set was used. Equation (6.11a), (6.11b), show that only positive, negative, variations from central PDF are taken as an independent contribution to total positive, negative, systematic uncertainty in given bin of transverse momenta, respectively. These are standard equations and they represent an ideal case, as possible correlations between different bins of transverse momenta are not accounted for. $i_{\max}$ is the number of parameters of fit varied in order to obtain $2i_{\max}$ error parametrisations.

6.2.3 nPDF modification

In order to utilise nuclear modifications to PDFs provided by *EPS09* [71] parametrisations, POWHEG-Box framework had to be modified. This was done by creating clone of subroutine `genericpdf(ndns,ih,xmu2,x,fx)` in `lhapdfif.f` file. This clone,`genericpdfA`, was modified it in such a way, that it substitutes calling of the subroutine `evolvePDF` defined by *LHAPDF* framework. This subroutine fills for given PDF, scale and Bjorken's x array *fx* with momentum fraction multiplied by this x. It is substituted by calling subroutine `setlhaparm('EPS09NLO,n')` and `evolvePDFa` which additionally gets information about number of nucleons in nucleus. In the *setlhaparm* subroutine, n stands for parametrisation subset, where 1 denotes central set and all the others error parametrisation sets. *evolvePDFa* takes modification by *EPS09NLO*'s n-th parametrisation, and modifies obtained variable *fx*.

Furthermore, normalisations for u-quark and d-quark have to be taken care, as different number of neutrons and protons is in nucleus. These neutrons and protons have different composition of valence quarks and therefore have different total number of u-quarks and d-quarks. This is taken care of by applying normalisation (6.12).

$$f^{\mathrm{u}}_{\mathrm{s+v}}(x) = \frac{Z}{A}\left[R^{\mathrm{u}}_{\mathrm{s}}(x)\, f^{\mathrm{u}}_{\mathrm{s}}(x) + R^{\mathrm{u}}_{\mathrm{v}}(x)\, f^{\mathrm{u}}_{\mathrm{v}}(x)\right] + \frac{A-Z}{A}\left[R^{\mathrm{d}}_{\mathrm{s}}(x)\, f^{\mathrm{d}}_{\mathrm{s}}(x) + R^{\mathrm{d}}_{\mathrm{v}}(x)\, f^{\mathrm{d}}_{\mathrm{v}}(x)\right], \tag{6.12a}$$

$$f^{\mathrm{d}}_{\mathrm{s+v}}(x) = \frac{A-Z}{A}\left[R^{\mathrm{u}}_{\mathrm{s}}(x)\, f^{\mathrm{u}}_{\mathrm{s}}(x) + R^{\mathrm{u}}_{\mathrm{v}}(x)\, f^{\mathrm{u}}_{\mathrm{v}}(x)\right] + \frac{Z}{A}\left[R^{\mathrm{d}}_{\mathrm{s}}(x)\, f^{\mathrm{d}}_{\mathrm{s}}(x) + R^{\mathrm{d}}_{\mathrm{v}}(x)\, f^{\mathrm{d}}_{\mathrm{v}}(x)\right]. \tag{6.12b}$$

Here $R^{\mathrm{u/d}}_{\mathrm{s/v}}$ represent modification from parametrisation of modification of PDF, subscripts s and v represent *see* and *valence*, f are PDFs either before, right-hand side of equations, or after modification, left-hand side of equations. Furthermore superscripts d and u denote quark flavour and Z and A represent number of protons and nucleons in nucleus, respectively.

It is noteworthy, that *see* u-quark's and d-quark's PDFs[3] are taken to be same as PDFs of their anti-quarks.

6.2.4 Simulation production

The simulations present in this section of analysis cannot be presented in the same way as the leading order PYTHIA6 simulations, due to the fact that maximal produced hard momentum was not bound, and events were not produced with the same cross section. These simulations were produced with varying weight in order to cover statistics of events with harder transverse momentum generated. The minimum born k_{T} for simulated processes was $1\,\mathrm{GeV}/c$, and suppression factor used in simulations was $90\,\mathrm{GeV}/c$. This suppression factor in form of

$$\mathcal{S}(k_{\mathrm{T}}) = \left(\frac{k_{\mathrm{T}}^2}{k_{\mathrm{T}}^2 + k_{\mathrm{T,supp}}^2}\right)^3, \tag{6.13}$$

is multiplied to differential cross section for purpose of production of hard processes. The size of simulated samples is filled in Tab. 6.4, with majority of production focused on simulations with central PDFs and nPDFs.

---

[3] There are no *valence* s-,c-,b-,t-quarks.

Simulation	Number of events
7 TeV	39 527 906
5.02 TeV	18 799 933
5.02 TeV⊕EPSnlo(1)	38 599 856
5.02 TeV⊕EPSnlo(2 − 31)	5 999 975
5.02 TeV⊕HKN07nlo	15 395 137

Table 6.4: Size of sample of events produced in simulations for different data.

Chapter 7. Sources of uncertainties

This chapter discusses performance aspects of presented analysis, including systematic cross checks and variations leading to final results presented in Chapter 8. Firstly, uncertainties originating in track reconstruction are discussed with their effect on transverse-monentum spectrum of charged jets. This includes track reconstruction efficiency and reconstructed track momentum resolution. Furthermore, uncertainties originating from correction itself are reflected in final systematic uncertainties of spectra are described here.

Additional discussion in this part of chapter includes normalisation uncertainty, influenced by cross-section measurements, possible problem with pile-up rejection efficiency, and uncertainty from strangeness scaling.

Moreover, the performance of unfolding procedures are discussed.

7.1 Unfolding

In this section the performance of unfolding is discussed. As described in Sec. 4.4, the three different correction methods are used and these are bin-by-bin correction, Bayesian unfolding, and singular value decomposition. In case of bin-by-bin method, there is no need to regularize the procedure and leads straight to correction factors as seen in Fig. 7.1a and Fig. 7.1b.

The regularization of SVD unfolding method is defined by authors of this method by calculation of parameter vector $\vec{d}$, defined as (4.16b), using singular values of the response matrix. The behaviour of this parameter is well described. When exponential behaviour is inferior to behaviour where values of elements of vector $\vec{d}$ fluctuate around certain value, corresponding element of diagonal singular matrix is taken as value of

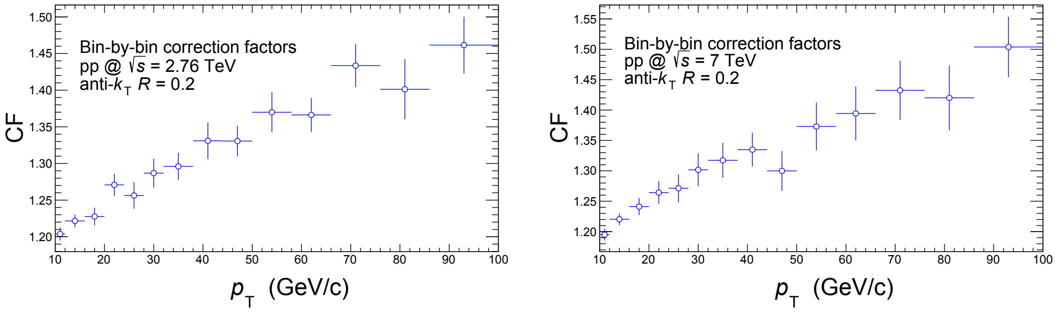

(a) $\sqrt{s} = 2.76$ TeV (b) $\sqrt{s} = 7$ TeV

Figure 7.1: Example of correction factors obtained using bin-by-bin method for anti-k_T algorithm using R equal to 0.2. Values are obtained for 2.76 TeV and 7 TeV proton-proton collisions, 7.1a and 7.1b respectively.

regularisation parameter τ according to (4.16c).

In Fig. 7.2 are shown examples of the obtained values of d_i, obtained from response matrices reconstructed for different resolution parameters.

For the case of Bayesian unfolding, regularisation parameter is number of consecutive iterations of used for final spectra. This number of iterations is small as too many iteration cause "contamination“ of unfolded spectra by fluctuations. The determining factor for selection of the number of iterations is by studying of matrix of Pearson's coefficients obtained from covariance matrix associated with unfolded spectra. These coefficients are calculated according to formula (4.9). In Fig. 7.3 shown matrices with these coefficients for selected response matrices.

The difference between jet cross sections unfolded using these different methods is small, at maximum few per cents for the largest bin of transverse momentum as seen in the Fig. 7.4.

For the purpose of correcting differential charged jet cross section, Bayesian method

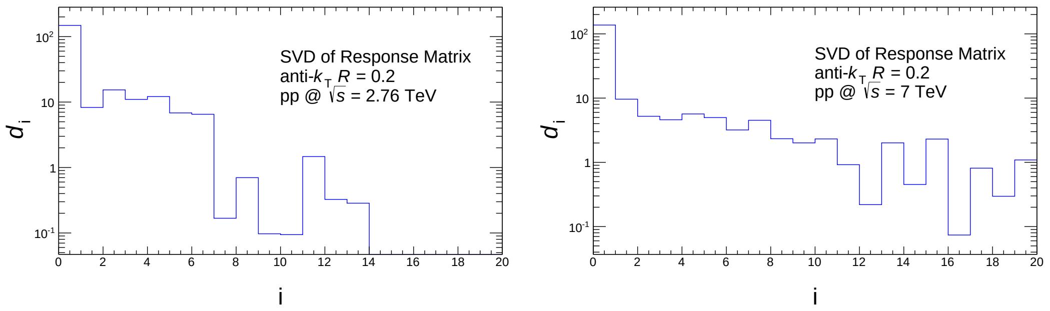

(a) $\sqrt{s} = 2.76$ TeV (b) $\sqrt{s} = 7$ TeV

Figure 7.2: Values of elements of vector $\vec{d}$ shown for anti-k_T algorithm reconstructed using resolution parameter 0.2. Values are obtained for 2.76 TeV and 7 TeV proton-proton collisions, 7.2a and 7.2b respectively.

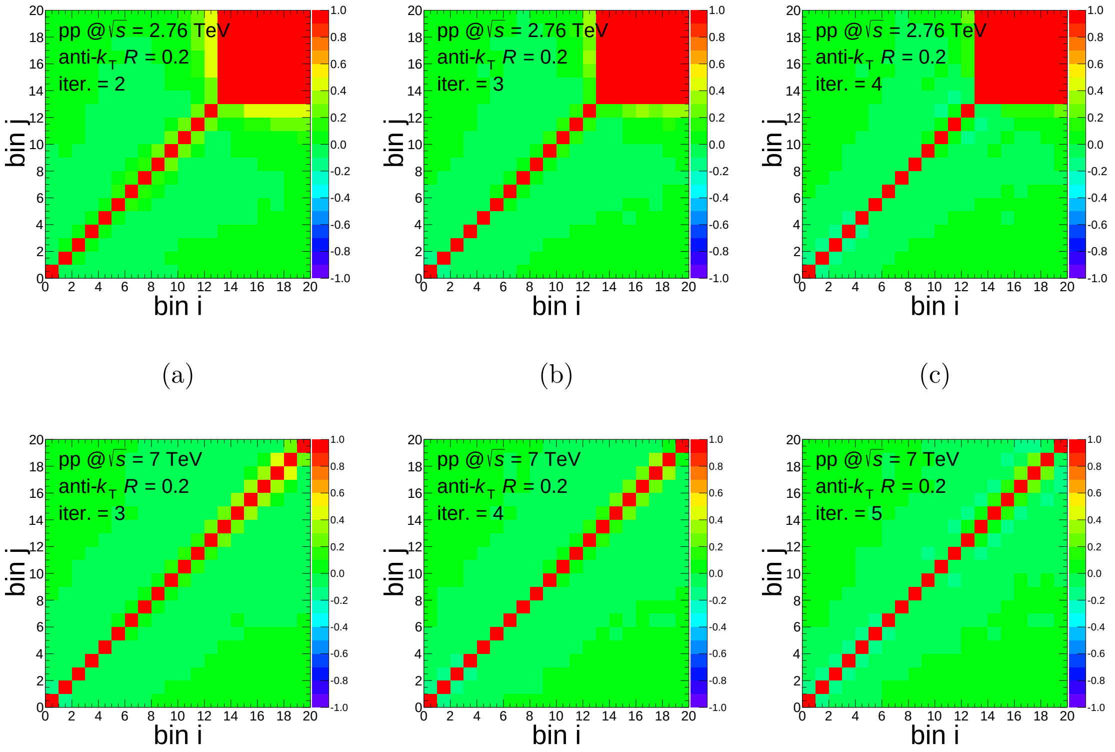

(a) (b) (c)

(d) (e) (f)

Figure 7.3: Matrices with Pearson's coefficients determined from covariant matrices corresponding to unfolded charged jet cross section for anti-k_T algorithm using R value of 0.2. Different numbers of iterations are shown for $\sqrt{s} = 2.76$ TeV and $\sqrt{s} = 7$ TeV, 7.3a-7.3c and 7.3d-7.3f respectively.

was chosen for these final corrections. The only difference is case of charged jet cross section reconstructed using different algorithms the bin-by-bin method was used. In order to account for correlated errors when making ratios to anti-k_T cross section, jet matching for two methods used in ratios was used to separate correlated and uncorrelated part of spectra.

7.2 Uncertainties due to the detector effects

The simulations used in order to describe effects of detector reconstruction utilise Geant simulations of the ALICE detector system. As a by-product, track reconstruction efficiency, Fig. 6.1a, and track transverse momentum resolution, Fig. 6.1b, are obtained from these simulations as well. Uncertainty on the description of the ALICE detectors can be evaluated by varying these efficiencies and resolutions and comparing jet spectra unfolded with response matrices obtained by these modified simulations to the spectra obtained from unfolding by original response matrices.

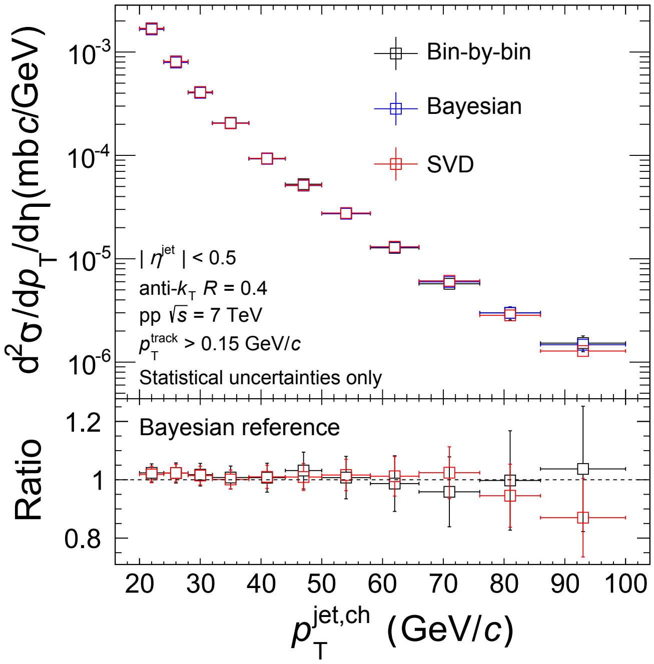

Figure 7.4: Comparison of jet cross section, obtained using anti-k_T algorithm with R equal to 0.4, unfolded using different methods. These methods include bin-by-bin (black squares) correction, SVD unfolding (red squares) and Bayesian iterative method (blue squares), which is used as a baseline for their comparison, in the bottom panel.

7.2.1 Track momentum resolution

First main contribution to the systematic uncertainty of fully corrected charged jet cross section is momentum resolution of reconstructed tracks. This resolution is obtained from full detector simulation and can be seen in Fig. 6.1b where this relative uncertainty can be described as linearly increasing with transverse momenta of reconstructed tracks. This resolution goes from approximately 0% up to 20% values for 100 GeV.

These values have been used in PYTHIA6 event generator as a basis for fast detector simulation. When track was reconstructed, normal distribution of random numbers was used with mean given by original track momentum and standard deviation obtained from relative uncertainty in Fig. 6.1b for given transverse momentum. This procedure was repeated with standard deviation of normal distribution increased and decreased by additional 20% of the original value. Such variation yielded set of additional response matrices which were used in order to correct charged jet cross section obtained without variation of standard deviation, and therefore describe uncertainty in our detector description originating in uncertainty of the momentum smearing by detector. Ratio between corrected spectra from modified and unmodified cases fluctuates around zero and maximal deviation from spectra corrected by unmodified response matrix is shown in Fig.7.5. This “envelope” takes into account also statistical errors. As can be seen the correction is small, between 3-4%, and does not differ much for spectra reconstructed using different resolution parameters. Value of 4% was taken as a final uncertainty

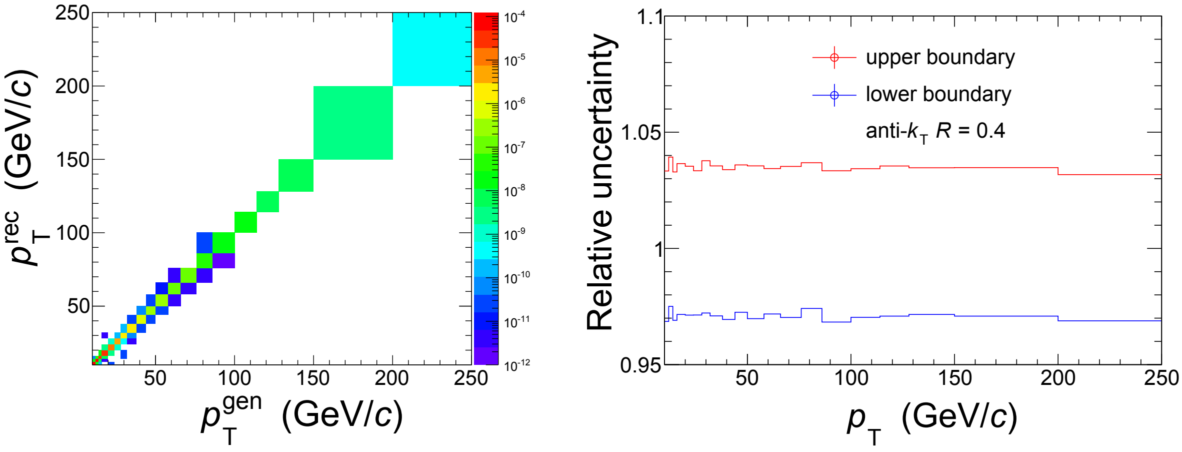

(a) Smearing response matrix

(b) Systematic uncertainty

Figure 7.5: Example of maximal relative difference between unfolded jet cross sections obtained by using response matrix with changed momentum smearing with respect to response matrix with default momentum smearing, Fig. 7.5a, Fig. 7.5b. For this case, anti-k_T jet algorithm was used with resolution parameter of 0.4 in simulated data with centre-of-mass energy 7 TeV.

originating from uncertainty in momentum smearing.

As seen in Fig. 7.5, the effect of correcting jet cross sections with response matrices obtained with modified smearing parameters has effect of few per cents on the final cross section. As these corrections are fluctuating a lot only the 4% “envelope” of the these corrected spectra is taken as final value for the systematic uncertainties.

7.2.2 Track reconstruction efficiency

Second, and the largest contribution to the systematic uncertainty in general, is the uncertainty originating from track reconstruction efficiency. The efficiency of tracks selected according to different selection criteria, defined in Sec. 5.2, are in general different, however, these two track classes are not exclusively complementary. Overall track reconstruction efficiency can be seen in the Fig. 6.1a, where efficiency increases to approximately 87% and then decreases due to differentiating of the tracks with high transverse momentum.

To correct for the inefficiency fast detector simulation with PYTHIA6 event generator was utilised in similar way, as in the case of track momentum resolution. However, in this case track’s detector reconstruction is based on generating random number between 0 to 1. If this number is smaller than efficiency, the track is accepted. However, in order to evaluate uncertainty originating from reconstruction inefficiency, value of the efficiency is increased and decreased by the value of 5%. After obtaining new set of response matrices, charged jet cross sections obtained in unmodified case is corrected by using response matrices from modified cases. Ratio between corrected spectra from modified and unmodified cases serves as final systematic uncertainty.

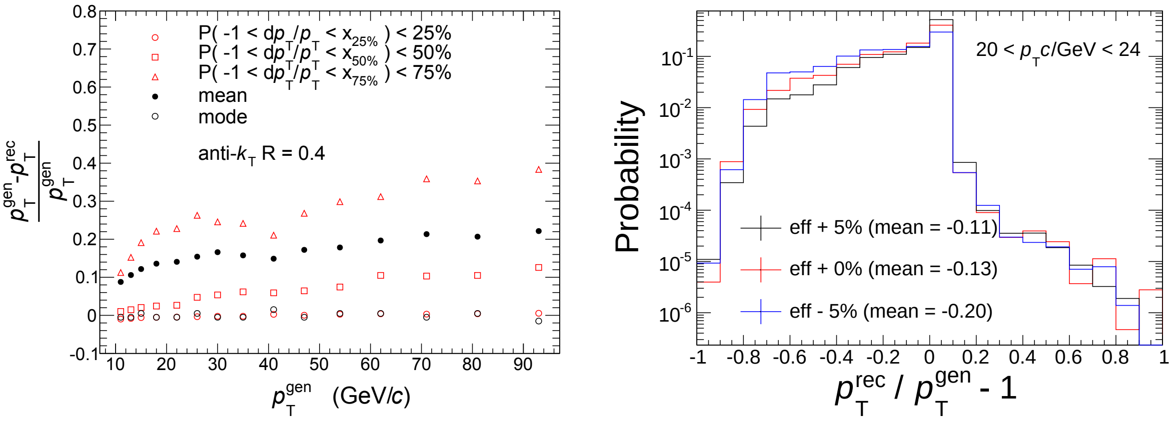

(a) Response matrix properties

(b) Probability of jet loosing energy

Figure 7.6: (a) Properties of response matrix for anti-k_T algorithm with resolution parameter of 0.4 as a function of generated transverse momentum. (b) For momentum bin from 20 to 24 GeV/c, probabilities of generated jets with transverse momenta in this momentum bin loosing momentum fraction and mean value of lost transverse momentum from response matrices from modified and unmodified track reconstruction efficiencies are shown.

Fig. 7.6a shows various properties of response matrix with mean, mode and interquartile ranges for probabilities of loosing fraction of generated momentum, for jets reconstructed using anti-k_T algorithm with resolution parameter 0.4. In the Fig. 7.6b are shown probabilities of charged jet losing or gaining given relative fraction of generated jets' transverse momentum as simulated for response matrices with modified and unmodified track reconstruction efficiencies. Also mean lost fraction of momentum is shown for these different simulations.

The Fig. 7.7 shows ratios of unfolded charged jet spectrum using response matrices obtained with ±5% variations in tracking efficiencies with respect to spectrum obtained using unmodified response matrix. This ratios are taken as contribution to systematic uncertainty from track reconstruction inefficiency.

7.3 Normalisation

The normalisation uncertainty come from determination of cross section as described in Ref. [57]. As shown in Tab. 5.1, the normalisation uncertainty for data from proton-proton collisions at $\sqrt{s}$ = 2.76 TeV is 1.8%. On the other hand, for proton-proton collisions at $\sqrt{s}$ = 7 TeV this uncertainty is 3.5%.

7.4 Contamination from secondary particles

In this analysis, only primary particles were considered as constituents of jets, and this selection is achieved in data by selecting on distance of the closest approach of the

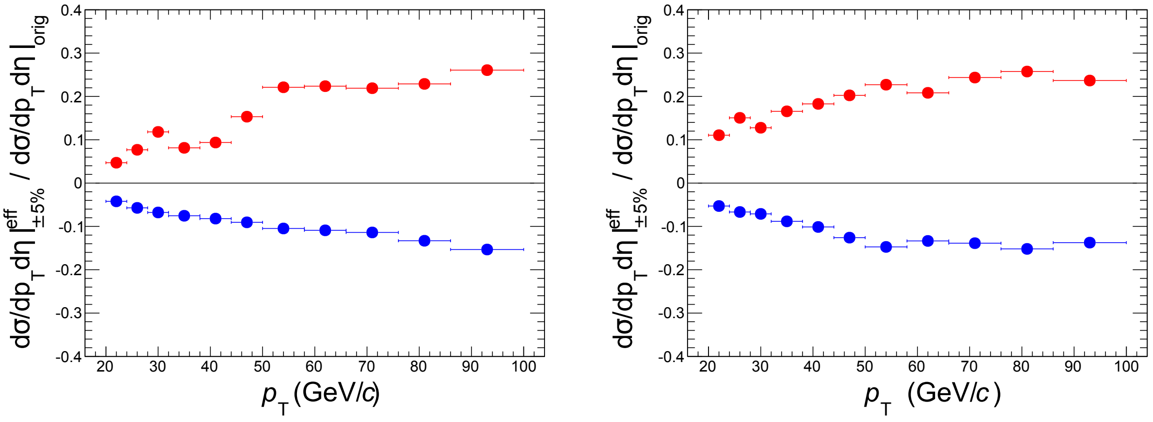

(a) $R = 0.2$ (b) $R = 0.6$

Figure 7.7: Systematic uncertainty due to the track efficiency uncertainty, obtained as ratio of spectra unfolded using response matrices with modified efficiencies as described in the text and spectra from unfolding with unmodified response matrix. The examples shown are for proton-proton collisions at $\sqrt{s} = 7$ TeV, for jets reconstructed using anti-k_T algorithm are resolution parameters 0.2 and 0.6, Fig. 7.7a and Fig. 7.7b, respectively.

track to the primary vertex, as defined in Sec. 5.2. However, charged secondary particles are produced predominantly by decays of strange particles, decays of charged pions and photon conversions.

These secondary particles introduce ambiguities to jet spectra and jet shapes, and although this contributions are implicitly corrected the independent analysis [76, 77] found that contamination by these secondary particles amount to less than 1%.

This is reflected by studying 0.5% variations of reconstructed transverse momenta using fits of jet spectra.

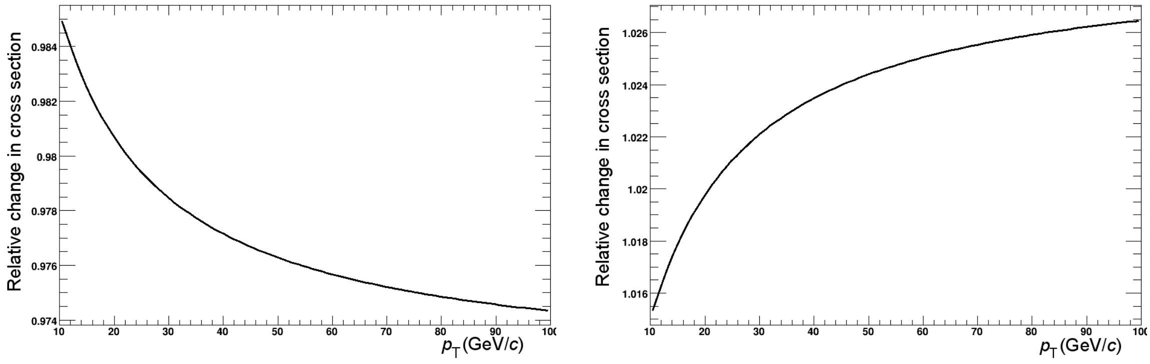

(a) Positive momentum scaling (b) Negative momentum scaling

Figure 7.8: Effect of secondary scaling on jet spectra obtained by variation of transverse momentum scale by ±0.5% in fit of jet spectra. Fig. 7.8a represent positive variation and Fig. 7.8b negative variation of momentum scale.

However, no study of secondary particle scaling is done for proton-proton collisions at centre-of-mass energy of 2.76 TeV. Therefore results of the scaling study done for collisions at centre-of-mass energy of 7 TeV are taken estimated for systematic uncertainty for collisions at 2.76 TeV. The reasoning behind this is based on the fact that production of secondary particles from strange particles is not higher than in 7 TeV collisions because production of strange particles decreases with decreasing centre-of-mass energies for the same system. Firstly, smaller energies of available for hard scatterings suppresses production of strange particles accordingly. Additionally, with increasing centre-of-mass energy, also Q^2 increases and therefore PDF for given x effectively increases as well.

7.5 Pile up

Due to the fact that two similar data-taking periods were used in analysis of charged-jet transverse-momentum spectra in proton-proton collisions at $\sqrt{s} = 7$ TeV, small differences of the data-taking setup occur.

One such difference is in probability of pile-up tracks occurring which increases in LHC10e period compared to LHC10d, as greater luminosity was increased in this period by decreasing bunch spacing in bunch trains, 50–100 ns. ALICE Physics framework implemented rejection due to the track pile-up in events by SPD system. Introducing this check has reflected on efficiency of event selection as seen in Fig. 7.9. Here, effect of additional pile-up event-selection criteria is seen as ratio of jet spectra with new additional trigger to the spectra without this trigger. The differences between periods and effect of track pile-up rejection are negligible, of the order of few percent altogether, with respect to the overall systematic uncertainties, therefore, this trigger is not included in event selection criteria of the final jet analysis.

Figure 7.9: Effect of including track pile-up event rejection on jet spectra shown as ratio of jet spectra with pile-up rejection (PUR) and without this rejection for different datasets, LHC10d, LHC10e, and both altogether, left, centre and right panel of plot respectively. The errors in these plots are overestimated due to the fact that same data are analysed, however, errors are calculated as if they were uncorrelated. The overall effect of additional pile-up rejection leads to negligible change in jet spectra with respect to the systematic uncertainties.

$\sqrt{s}$	R	p_{T} intervalGeV/c	Effic./%	Resol.	Normal.	Unfold.	Seco.	Total / %
2.76 TeV	0.2	20 - 24	$^{+8.1}_{-7.1}$	4%	1.8%	3.0%	2.2%	$^{+9.9}_{-9.1}$
		50 - 58	$^{+20.7}_{-14.0}$	4%	1.8%	1.6%	2.3%	$^{+21.3}_{-15.0}$
	0.3	20 - 24	$^{+7.1}_{-6.6}$	4%	1.8%	3.0%	2.4%	$^{+9.1}_{-8.7}$
		50 - 58	$^{+20.5}_{-15.0}$	4%	1.8%	1.6%	2.4%	$^{+21.2}_{-15.9}$
	0.4	20 - 24	$^{+5.9}_{-5.3}$	4%	1.8%	3.0%	2.6%	$^{+8.2}_{-7.8}$
		50 - 58	$^{+20.0}_{-16.9}$	4%	1.8%	1.4%	2.4%	$^{+20.7}_{-17.7}$
	0.6	20 - 24	$^{+7.5}_{-6.3}$	4%	1.8%	6.6%	2.4%	$^{+11.2}_{-10.4}$
		50 - 58	$^{+21.3}_{-14.7}$	4%	1.8%	1.9%	2.5%	$^{+22.0}_{-15.6}$

$\sqrt{s}$	R	p_{T} intervalGeV/c	Effic./%	Resol.	Normal.	Unfold.	Seco.	Total / %
7.00 TeV	0.2	20 - 24	$^{+4.6}_{-4.2}$	4%	3.5%	3.0%	1.9%	$^{+7.8}_{-7.6}$
		50 - 58	$^{+22.1}_{-10.5}$	4%	3.5%	1.6%	2.5%	$^{+23.0}_{-12.2}$
		86 - 100	$^{+26.0}_{-15.3}$	4%	3.5%	5.2%	2.8%	$^{+27.1}_{-17.2}$
	0.3	20 - 24	$^{+5.6}_{-4.3}$	4%	3.5%	3.0%	2.0%	$^{-8.5}_{-7.7}$
		50 - 58	$^{+22.5}_{-10.5}$	4%	3.5%	1.6%	2.5%	$^{+23.3}_{-12.1}$
		86 - 100	$^{+25.6}_{-15.2}$	4%	3.5%	5.4%	2.8%	$^{+26.8}_{-17.2}$
	0.4	20 - 24	$^{+7.5}_{-4.5}$	4%	3.5%	3.0%	2.1%	$^{+9.9}_{-7.9}$
		50 - 58	$^{+23.2}_{-10.6}$	4%	3.5%	1.4%	2.5%	$^{+24.0}_{-12.2}$
		86 - 100	$^{+24.9}_{-15.0}$	4%	3.5%	5.6%	2.7%	$^{+26.2}_{-17.2}$
	0.6	20 - 24	$^{+11.1}_{-5.3}$	4%	3.5%	6.6%	2.3%	$^{+14.2}_{-10.3}$
		50 - 58	$^{+22.6}_{-14.3}$	4%	3.5%	1.9%	2.5%	$^{+23.4}_{-15.6}$
		86 - 100	$^{+23.7}_{-13.7}$	4%	3.5%	6.0%	2.6%	$^{+25.1}_{-16.1}$

Table 7.1: Summary of systematic uncertainties for charged jet cross sections obtained from real data. Individual contributions are track reconstruction efficiency, *Effic.*, track momentum resolution, *Resol.*, normalisation uncertainty, *Normal.*, uncertainty from selected unfolding method, *Unfold.*, and uncertainty from corrected secondary scaling, *Seco.*. Sum of all these uncertainties, *Total*, is in quadratures.

In the Tab. 7.1 are summed up contributions to systematic uncertainty described in previous sections for all resolution parameters of anti-k_{T} jets reconstructed in for both centre-of-mass energies analysed. For purpose of table lucidity, only 3 bins of transverse momenta are shown. These are bins 20-24 GeV/c, 50-58 GeV/c and 86-100 GeV/c.

7.6 POWHEG-Box simulation cross-checks

As listed in Tab. D.1, POWHEG-Box simulations require several parameters for their setup. Several parameters, such as grid sampling used for calculation of cross section and newly introduced mechanism for suppression of emission of harder particle than the emitter is were left unchanged. Other parameters such as minimum born k_{T} and born suppression factor are expected to have strange behaviour in certain regions. This includes introduction of spikes in spectra when using suppressed cross section and not reliable results in region close to the minimum born k_{T}, when utilising this suppressed production. The effects of these choices has to be checked.

In Fig. 7.10 are plotted spectra from 2 000 000 events from unsuppressed (red) charged-jet spectra and same spectra from simulations with suppression factor equal to 10 GeV/c (blue), 40 GeV/c (black) and 150 GeV/c (magenta). It is obvious that unsuppressed simulation lacks in reach of jet momentum and statistics statistics starting from 20 GeV/c. With increasing suppression factor, reach of the jet spectra significantly improves for the same amount of simulated events, moreover, for k_{T} of 150 GeV/c statistics is sufficient to describe jet spectra in transverse-momentum range of insterest, i.e. up to 200 GeV/c.

7.7 POWHEG-Box systematic uncertainties

As mentioned in section 6.2, the main sources of systematic uncertainties for NLO simulations are firstly maximal deviation of varied renormalisation and factorisation scales. These systematic uncertainty arises from finite order in perturbative calculations. Additionally, if applicable, error parametrisations originating from variations in parame-

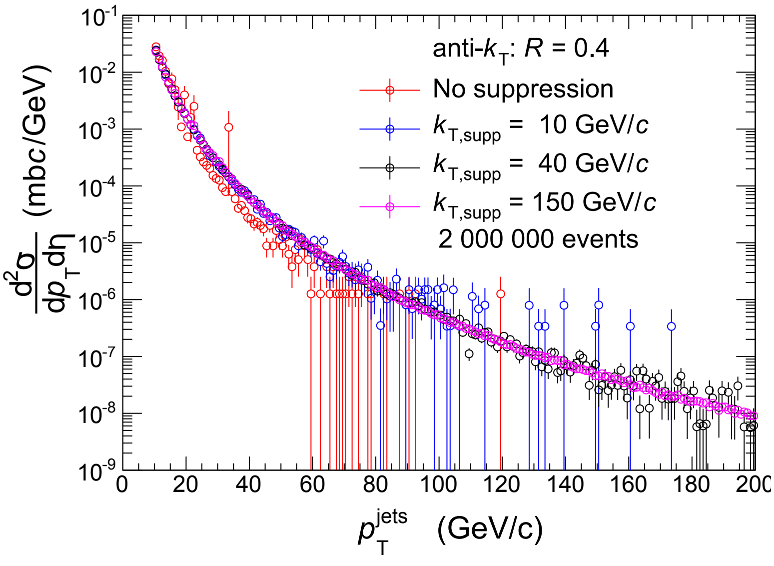

Figure 7.10: Comparison of jet spectra produced with 2 000 000 events with no born suppression factor, red points, and suppression factor of 10 GeV/c, 40 GeV/c and 150 GeV/c, blue, black and magenta points respectively.

ters of PDF fits are taken as uncorrelated sources of systematic uncertainties for both PDFs and nuclear modifications to PDF. These errors, as mentioned previously, originate from uncertainties of original deep inelastic scatterings, where structure of hadrons is investigated. Last main contribution is from different PYTHIA8 tunes.

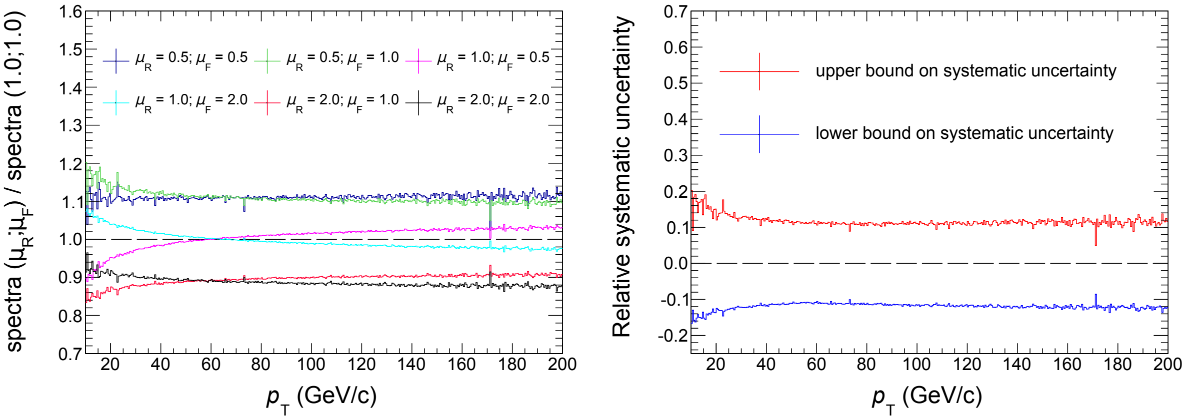

(a) Ratio of transverse momentum spectra of charged jets with modified renormalisation and/or factorisation scalesby factor the μ_{R} and μ_{F} with respect to unmodified spectra.

(b) Relative systematic uncertainty of charged jet spectra from variation of renormalisation and/or factorisation scales by the factor μ_{R} and μ_{F}.

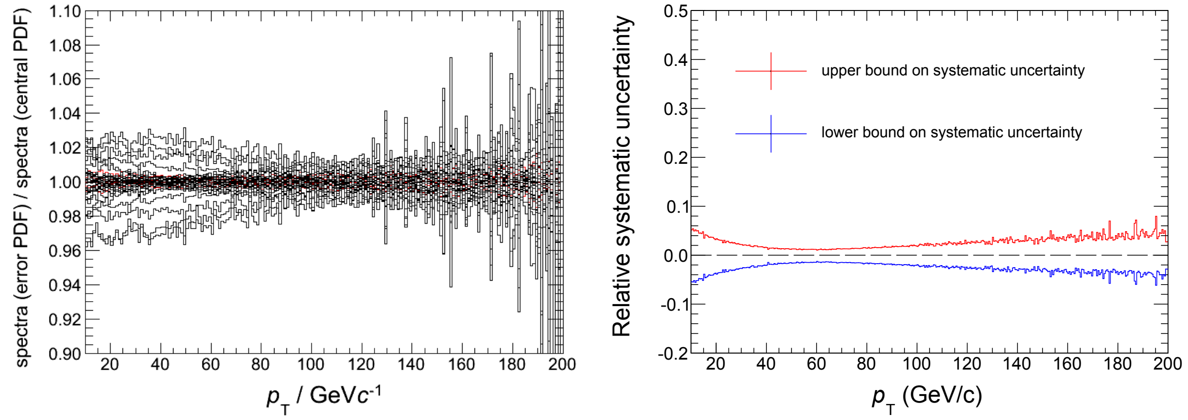

(c) Ratio of transverse momentum spectra of charged jets with error PDF parametrisations with respect to spectra produced with central PDF parametrisation.

(d) Relative systematic uncertainty of charged jet transverse momentum spectra originating from simulations using error PDF parametrisations according to the Eq. (6.11).

Figure 7.11: Systematic uncertainties for charged jet transverse momentum spectra. Two main sources are scale variations,7.11a, resulting in final systematic uncertainty taken as maximal deviation from unmodified case 7.11b. Second source are recalculations of spectra using error PDF parametrisations, 7.11c, resulting in relative systematic uncertainty 7.11d.

7.7.1 Charged jet transverse momentum spectra

In Fig.7.11 are shown systematic variations of anti-k_T spectrum reconstructed using resolution parameter $R = 0.4$ from charged tracks only. These systematic variations were carried out as is described in sec. 6.2. Fig. 7.11a and Fig. 7.11b show individual variation of pair of renormalisation and factorisation scale and final relative systematic uncertainty corresponding to envelope obtained from maximal scale variation respectively. On the other hand, Fig. 7.11c and Fig. 7.11d represent individual variations of error PDFs with respect to central PDF and final relative systematic uncertainty obtained from differences of individual error and central PDFs, according to prescriptions (6.11).

Differences between charged jet spectra reconstructed using different resolution parameters are negligible.

7.7.2 Full jet transverse momentum spectra

Similarly to Fig. 7.11, the Fig. 7.12 contains systematic study for the case of the full jet cross section. In Fig. 7.12a are shown relative changes in cross section for appropriate change in renormalisation and/or factorisation scale. Final systematic uncertainty is of the order of approximately 13%, as show in Fig. 7.12b where final uncertainty is taken as envelop of all the possible combinations of scale modifications. For the case of the variations of PDF parametrisations, individual variations yield difference from central parametrisation of the order of few percent at maximum, as seen in Fig. 7.12c. Adding these differences in quadrature, as they originate from variations of uncorrelated parameters of PDF parametrisation, systematic uncertainty, Fig. 7.12d, of the order of approximately 5% is obtained. The uncertainty is relatively symmetrical with only a small differences. The largest uncertainties are obtained for the lowest regions of transverse momenta and minimum is reached between 70 and 80 GeV/c for both, upper and lower, bounds. Afterwards, uncertainty slowly increases reaching 4% at 200 GeV/c.

As for charged jets, differences between cross sections reconstructed using different resolution parameters are negligible.

7.7.3 Transition to boosted frame

In order to be able to compare results from p+Pb collisions at the LHC, simulation has to account for different energies of colliding particles. In this case, colliding proton had 4 TeV in the reference frame of the detectors and colliding lead ions had energy of 1.58 TeV. However, POWHEG-Box framework is unable to produce collisions of particles with different energies[1].

First, the difference in reconstructed jet cross sections from collisions with symmetric and asymmetric energies of colliding protons. As seen in Fig. 7.13, where the effect on anti-k_T algorithm with resolution parameter of 0.4 reconstructed in acceptance from -0.5 to 0.5 units of pseudo-rapidity, the effect is of the order of few percent. The figure shows

---

[1] After attempting to do such simulations, produced events were rejected due to momentum conservation problems during PYTHIA8 reconstruction. Such POWHEG-Box simulations with asymmetric particle energies have not been tested for all processes [78].

production with 3 different minimal hard transverse momentum generated in collisions in order to reach high transverse momenta of jets. These different production show slightly different behaviour in transverse momentum range approximately below the value of jet transverse momenta equal to hard p_{T} threshold.

In order to avoid this systematic overestimation of jet cross-section in comparisons with real data, events in the produced LHE files from POWHEG-Box simulations of

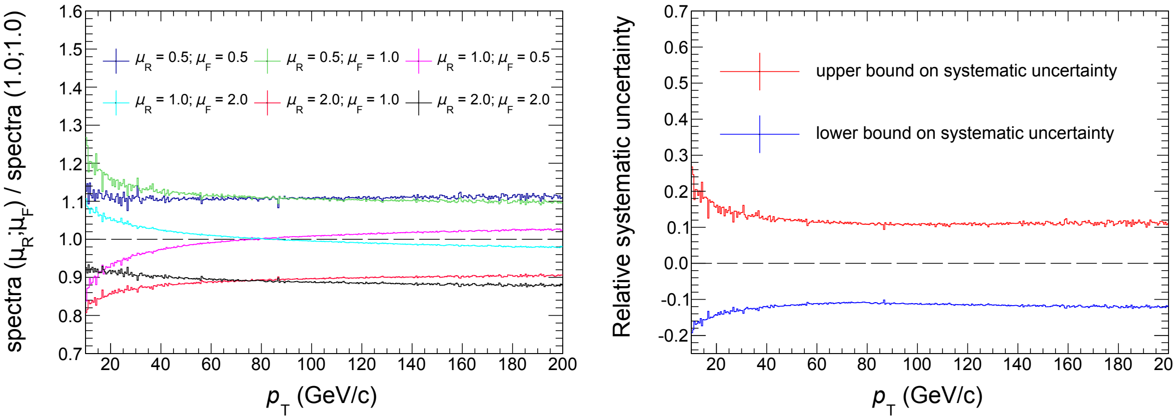

(a) Ratio of transverse momentum spectra of full jets with modified renormalisation and/or factorisation scalesby factor the μ_{R} and μ_{F} with respect to unmodified spectra.

(b) Relative systematic uncertainty of full jet transverse momentum spectra originating from variation of renormalisation and/or factorisation scales by the factor μ_{R} and μ_{F}.

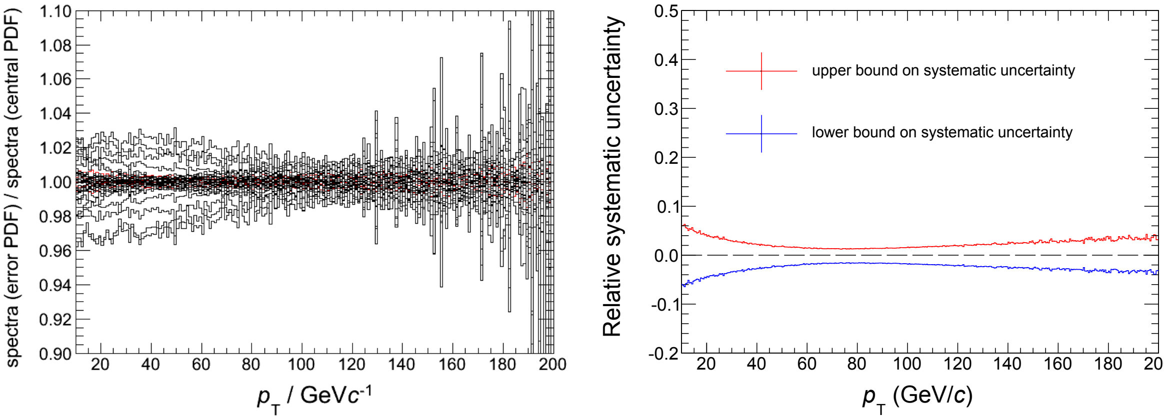

(c) Ratio of transverse momentum spectra of full jets with error PDF parametrisations with respect to spectra produced with central PDF parametrisation.

(d) Relative systematic uncertainty of full jet transverse momentum spectra originating from simulations using error PDF parametrisations according to the Eq. (6.11).

Figure 7.12: Systematic uncertainties for full jet transverse momentum spectra. Two main sources are scale variations,7.12a, resulting in final systematic uncertainty taken as maximal deviation from unmodified case 7.12b. Second source are recalculations of spectra using error PDF parametrisations, 7.12c, resulting in relative systematic uncertainty 7.12d.

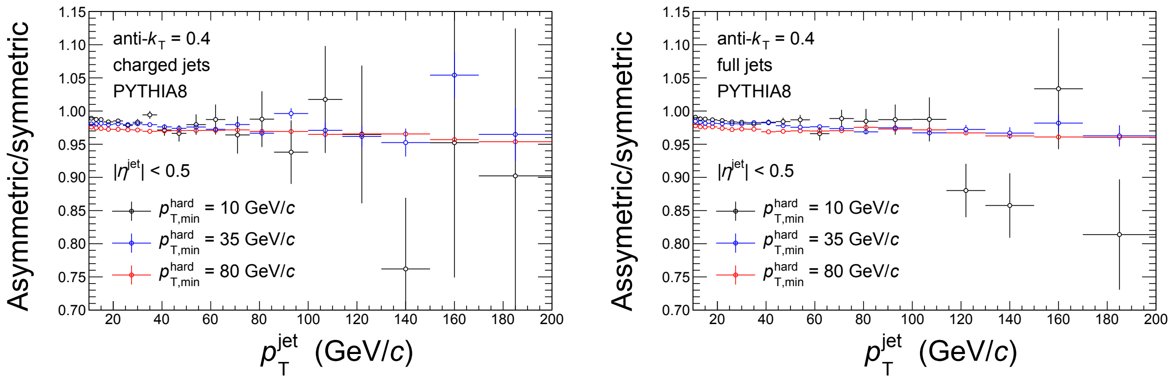

(a) Charged jets

(b) Full jets

Figure 7.13: Effect of boosting p+p collisions in PYTHIA8 simulation by rapidity value of -0.465 on anti-k_T jet spectra reconstructed using resolution parameter 0.4 in pseudo-rapidity region from -0.5 to 0.5. Three different minimum hard p_T , 10 GeV/c, 35 GeV/c and 80 GeV/c, black, blue and red, respectively, were used for description of large values of jet transverse momenta.

symmetric p+p and p+Pb-like collisions have been boosted by rapidity

$$\Delta y = -0.465. \tag{7.1}$$

This boost ensured that the first colliding particle had energy 4000 GeV and second had 1580 GeV and appropriate gain/loss of energy and momenta along z direction occurred to all the particles in hard scattering.

7.8 EPS09 variations

Utilisation of central modification to PDF with additional 30 error modifications of proton PDF enabled these PDFs to serves as a source for another systematic uncertainty. This is contrary to HKN07 nuclear PDFs, which do not have any associated error nPDFs.

7.8.1 Spectra

The studies involving EPS09 modification involve jet spectra, this uncertainty is transported to ratios with baseline spectra and modification of ratio between jet cross sections reconstructed using different resolution parameters. These systematic uncertainties have been obtained using Eq. 6.11a and Eq. 6.11b and are plotted in the Fig. 7.14. For purpose of simplicity, only cross section plots for anti-k_T with resolution parameter of 0.4 are shown, as different values of resolution parameters yield consistent results.

General feature of these uncertainties is large values at low transverse momenta, i.e. below 20 GeV. These originate from simulation parameters, where in order to produce sufficient momentum reach of the cross section, simulations had to use non-zero suppression factor, Eq. 6.13, which significantly decreases number of events at low transverse momenta and produces weight fluctuations for these values. As there are 30 different sets of modification factors used for the determination of systematic uncertainty, fluctuation in at least one of them causes large increase in final systematic uncertainty. Such fluctuation occurs practically for every set and therefore large corresponding uncertainty does not have to have physical origin, but is simulation driven.

The relevant transverse momentum region, in this case from 20 GeV/c and above, shows relatively symmetric behaviour up to cca. 120 GeV/c, for all variables listed above. The behaviours starts to be asymmetric for charged-jet cross sections and ratios of cross sections reconstructed using different resolution parameter, however, partial responsibility for these increases may be due to the limited statistics used for study.

Altogether, relative systematic uncertainty for charged-jet and full-jet cross section originating from EPS09nlo parametrised description of modified parton distribution

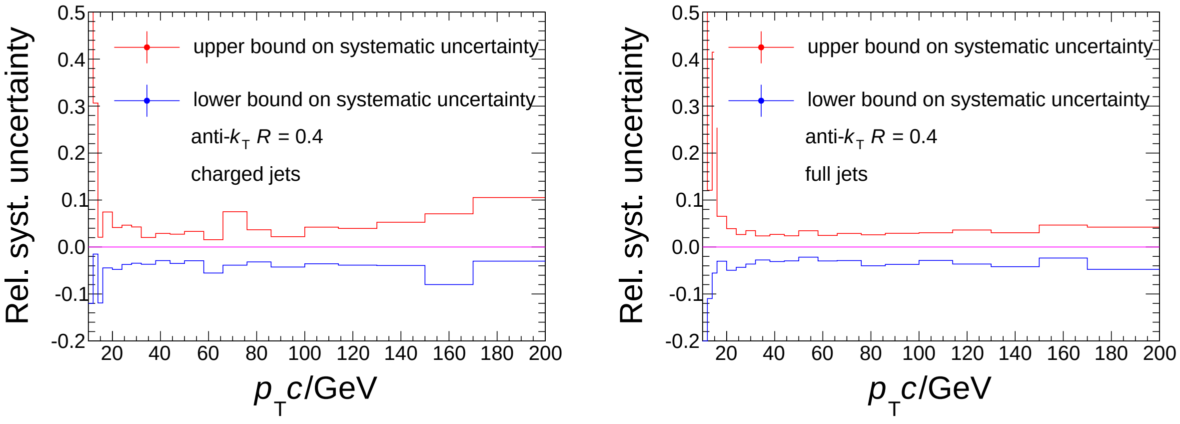

(a) Charged jet cross section

(b) Full jet cross section

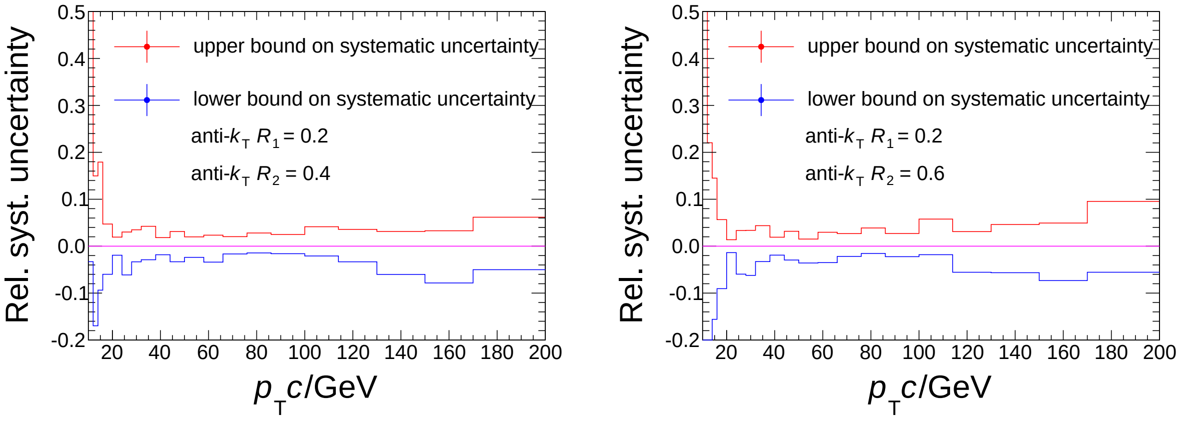

(c) Cross section ratio for $R_2 = 0.4$

(d) Cross section ratio for $R_2 = 0.6$

Figure 7.14: Systematic uncertainty on jet cross section observables, charged-jet and full-jet cross sections, 7.14a and 7.14b , respectively, and ratio between charged-jet cross section reconstructed using resolution parameter 0.2 and 0.4 (0.6), 7.14c(7.14d), originating from EPS09 error datasets describing modification of proton PDF.

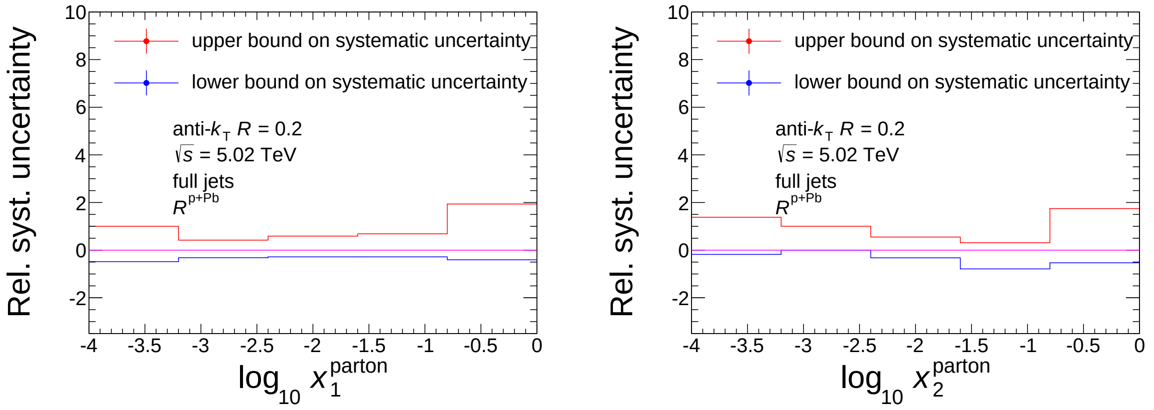

(a) parton x_1 from proton (b) parton x_2 from lead-like ion

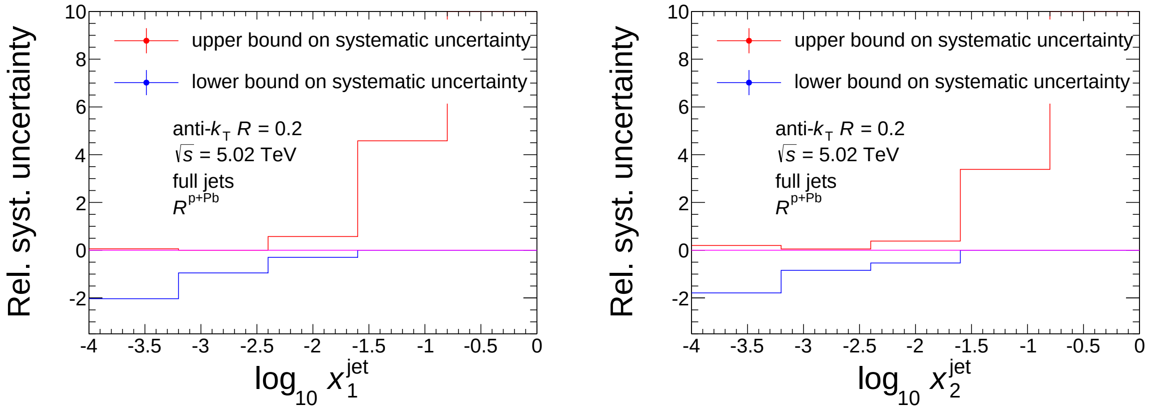

(c) jet x_1 from proton (d) jet x_2 from lead-like ion

Figure 7.15: Systematic uncertainty on distribution of Bjorken's x variable modification in proton-lead like collisions obtained by modifying PDFs by EPS09nlo modification factors with respect to proton-proton baseline. Cases of 7.15a and 7.15b are obtained directly from information about the hard scattering. Bjorken's x in 7.15c and 7.15d originate from reconstructed leading di-jet.

functions compared to proton case is of the order of approximately 4% with occasional fluctuation for charged-jet case in relevant region of transverse momenta. For the case of ratio of charged-jet cross sections reconstructed with different resolution parameters, relative systematic uncertainty is approximately 3% for relevant transverse momenta region.

7.8.2 Distribution modifications

For the case of modifications of partons' distributions as a function of their fraction of original energy with respect to the energy of incoming colliding proton or ion, even wide rapidity range and small binning in $\log(x)$ did not prevent large statistical uncertainties. Even the systematic uncertainty for modification of x_1 and x_2 distributions obtained directly from hard-scattering information, Fig. 7.15a and Fig. 7.15b, is around 100% and for edge bins suffering mostly due to the small size of simulated sample produces double the uncertainty.

For the case of x reconstructed from jets using Eq. 6.10 the lower values of x_1 and x_2 have uncertainty up the the double of the value of modification for lower bound of systematic uncertainty, however upper bound is negligible in comparison. For large-x systematic uncertainties, the situation is opposite. Lower bound of uncertainty is negligible and upper bound exceeds quadruple of the value of the modification.

The systematic uncertainties for modification of x_1 and x_2 distributions exhibit similar behaviour for case of reconstruction from di-jets and similar behaviour for the case of study of direct information from simulated hard scattering. However, the case of jet reconstruction is strongly affected by small size of sample for most energetic colliding partons.

Observed behaviour for studied systematic uncertainties did not show dependence on selected resolution parameter. Uncertainty from scale variations is in majority of investigated momentum interval below 15%. This is valid for all the observables. On the other hand uncertainties from taking into account uncertainties from PDF and nPDF parametrisations are below 5% with minimum observed at the transverse momenta of approximately $70\,\mathrm{GeV}/c$.

Event if there was no boosting of the frame of reference due to asymmetric energies of colliding particles, this would have minimal effect, as the spectrum would still lie within uncertainties, obtained from other sources.

On the other hand, systematic uncertainties for parton distributions as a function of $\log x_{1,2}$ are large for cases with lacking size of the sample.

Chapter 8. Results

In this chapter, results of previously described analyses are presented. Firstly, individual corrected charged jet spectra reconstructed from data collected by the ALICE detector system. Subsequently, comparison with several Monte-Carlo generators and their tunes, and additionally comparison with the results of ATLAS experiment. Following these comparisons are ratios of jet spectra reconstructed using different resolution parameter and therefore probing different areas.

In the second part of this chapter, results of the study of NLO simulations using POWHEG-Box framework are presented. These results provide complementary comparison with previous results from the ALICE data. Furthermore, jet modification is extracted for case of collisions of protons and lead ions with respect to available results.

8.1 Jet spectra

In following section fully corrected inclusive charged jet cross sections measured in proton-proton collisions with anti-k_{T} algorithm using various values for resolution parameters R are presented.

8.1.1 Jet reconstruction using different algorithms

In order to reconstruct jets, an algorithm has to be used. However, various algorithms can exist with different approach to the reconstruction. From a physical point of view, these algorithms have to produce consistent results.Situation may differ in collisions of heavy ions, where different approach are more sensitive to different physics. As an example may serve anti-k_{T} and k_{T} algorithms, where first starts with most energetic

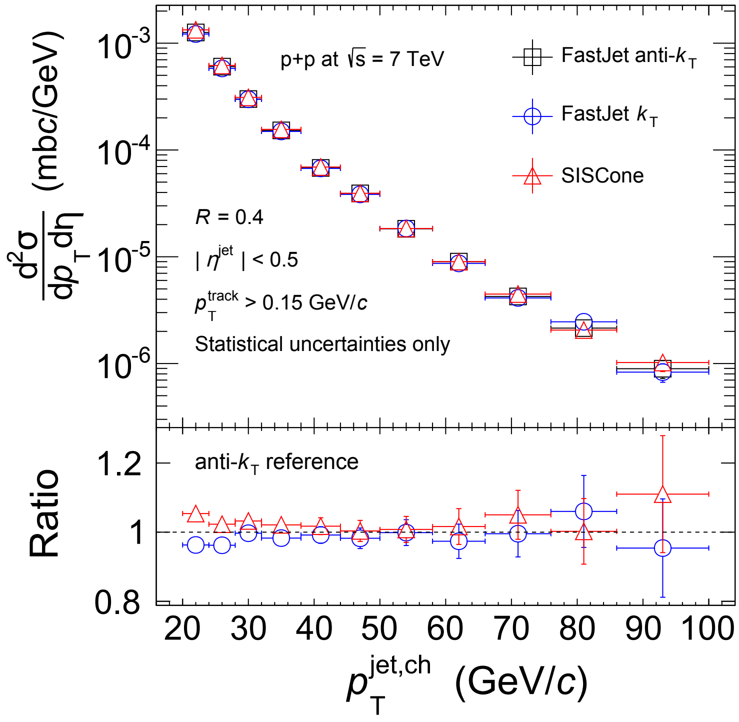

Figure 8.1: Comparison of inclusive charged jet cross section corrected using bin-by-bin correction factors.

particles and second with least energetic particles and therefore anti-k_T is used for signal, i.e. jets, and k_T for background.

For validation purposes, jet spectra produced with anti-k_T algorithm is compared with k_T and SISCone algorithm, Fig. 8.1. Jet spectra shown in this plot are reconstructed using resolution parameter $R = 0.4$ in pseudo-rapidity acceptance from -0.5 to 0.5, with underlying event subtraction. These spectra are consistent within statistical uncertainty as seen in bottom part of the figure, where ratios of these spectra are made with respect to the anti-k_T jet cross section. The difference of up to 5% for the small transverse charged jet momenta is caused by the different reconstructed jet areas caused by different reconstruction algorithm used.

8.1.2 Proton-proton collisions with centre-of-mass energy 2.76 TeV

In Fig. 8.2 are shown fully corrected inclusive differential jet cross sections reconstructed for various resolution parameters using anti-k_T algorithm and resolution parameters R values of 0.2, 0.3, 0.4 and 0.6 depicted by blue, red, black and magenta points, respectively. These spectra are corrected for underlying event using method of perpendicular cones.

Jet cross sections in 2.76 TeV proton-proton collisions span from 20 GeV/c up to 76 GeV/c. This range is driven by rather small size of sample of taken data at this

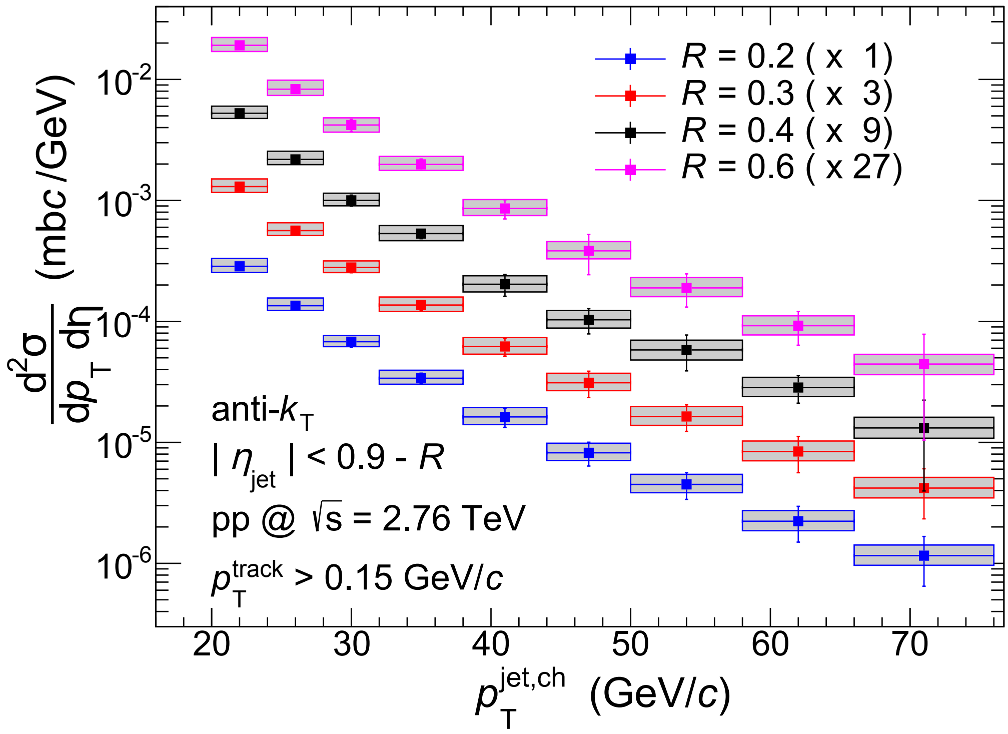

Figure 8.2: Fully corrected inclusive charged jet cross section reconstructed as a function of transverse momentum from proton-proton collision at $\sqrt{s} = 2.76$ TeV reconstructed using FastJet anti-k_T algorithm with various resolution parameters R, ranging from 0.2 to 0.6. Reconstructed jets are corrected for underlying event by method of perpendicular cones. Tracks used in reconstruction had at least 0.15 GeV/c and were reconstructed within pseudo-rapidity range of -0.9 to 0.9 and in full azimuthal coverage. Individual spectra reconstructed with resolution parameters of 0.2, 0.3, 0.4 and 0.6 are scaled by the factor 1, 3, 9 and 27, respectively, in order to increase readability of the plot.

collision energy, i.e. only one data-taking period in year 2011, meant as a reference sample for heavy-ion collisions, which are taken at $\sqrt{s_{NN}} = 2.76$ TeV.

In order to validate reconstructed cross-section, data reconstructed from the ALICE experiment are compared to several predictions obtained from PYTHIA and HERWIG generators. Several different tunes, described in Sec. 6.1, are used for the case of PYTHIA Monte-Carlo event generator. These include AMBT1, which was used mainly for purpose of consistency check for 7 TeV data with the ATLAS experiment. Additionally, Perugia-0, Perugia-2010 and Perugia-2011 are used.

In general neither of used monte-carlo predictions describes data well. As can be seen from Fig. 8.3, in general HERWIG underestimates jet energy scale. On the other hand, description provided by AMBT1 significantly overestimates jet cross section at low transverse momenta, however, going to higher values the description gets better. The best descriptions are provided by Perugia tunes, which provide relatively consistent prediction nearly in whole transverse momentum range, with exception of Perugia-0 tune for low transverse momentum case of jet spectrum reconstructed with resolution

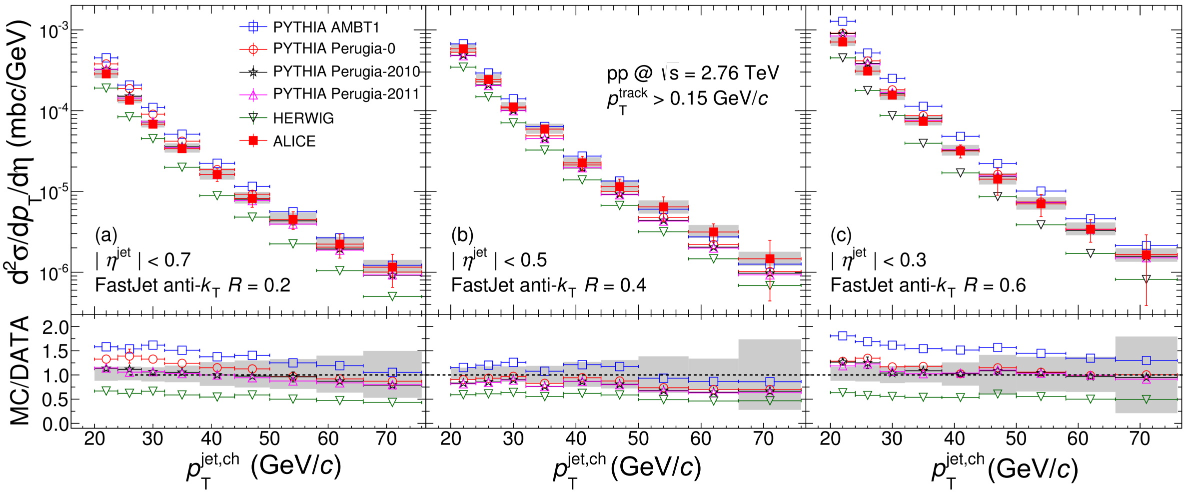

Figure 8.3: Comparison of jet spectrum from proton-proton collision at $\sqrt{s}$ = 2.76 TeV with Monte-Carlo predictions produced by PYTHIA tune AMBT1 (blue squares), Perugia-0 (red circles), Perugia-2010 (black stars), Perugia-2011 (magenta up-triangles) and HERWIG (green down-triangles).

parameter of 0.2, where it overestimated data by approximately 30%. However, even Perugia tunes fail to describe properly spectrum reconstructed using resolution parameter of 0.4, where from 50 GeV/c, these tunes underestimate data by 30-40%.

There are problem to describe both jet energy scale and jet energy shape. On the other hand with increasing transverse momentum of charged jets cross section, the systematic uncertainty significantly increases and taking into consideration 1σ , Perugia-2010 and Perugia-2011 provide consistent description within these uncertainties.

8.1.3 Proton-proton collisions with centre-of-mass energy 7 TeV

Figure 8.4 shows fully corrected inclusive differential charged jet cross sections as a function of transverse momentum reconstructed from proton-proton collisions at $\sqrt{s} = 7$ TeV, reconstructed by anti-k_T algorithm with resolution parameters of 0.2, 0.3, 0.4 and 0.6. These cross sections range from 20 to 100 GeV/c, thanks to increased number of taken data. Also increased collision energy provides with higher values of cross sections compared to measurements taken at $\sqrt{s} = 2.76$ TeV.

Similarly to the Fig. 8.3, in the Fig. 8.5 are comparisons of several Monte-Carlo event generators with the ALICE measurement at $\sqrt{s} = 7$ TeV. Majority of predictions has problem for low transverse momenta. From approximately 30 GeV/c PYTHIA tune Perugia-2011 provides the best description of data for all resolution parameters. Due to the fact that PYTHIA tune Perugia-2010 provided very similar results as Perugia-2011 tune, this tune was substituted by PHOJET. Both PHOJET and HERWIG underestimate data by 20% at maximum.

Furthermore, AMBT1 overestimates cross section by approximately 50%, which is the largest value from set of used generators. This generator was included due to the fact that the ATLAS collaboration did comparison with it [73]. They made a similar

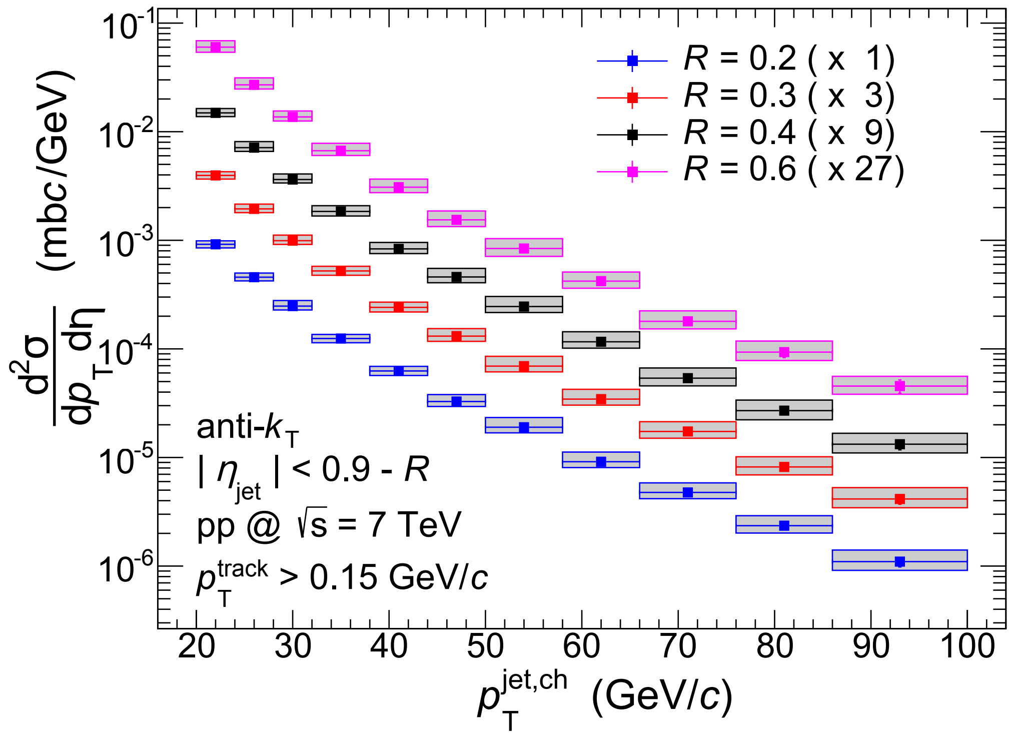

Figure 8.4: Fully corrected inclusive charged jet cross section reconstructed as a function of transverse momentum from proton-proton collision at $\sqrt{s} = 7$ TeV reconstructed using FastJet anti-k_T algorithm with various resolution parameters R, ranging from 0.2 to 0.6. Reconstructed jets are corrected for underlying event by method of perpendicular cones. Tracks used in reconstruction had at least 0.15 GeV/c and were reconstructed within pseudo-rapidity range of -0.9 to 0.9 and in full azimuthal coverage. Individual spectra reconstructed with resolution parameters of 0.2, 0.3, 0.4 and 0.6 are scaled by the factor 1, 3, 9 and 27, respectively, in order to increase readability of the plot..

observation, that PYTHIA AMBT1 overestimated spectra they reconstructed by 30% to 60% for both resolution parameters used, i.e. 0.4 and 0.6.

However, there are several differences are between this analysis and one produced by the ATLAS experiment. First of all, they have used reconstructed tracks with transverse momenta of at least 0.3 GeV/c. Furthermore, no underlying event subtraction was done in case of the ATLAS results. Lastly, the ATLAS spectra have slightly different acceptance range, instead of pseudo-rapidity, they have used rapidity. This difference plays insignificant role, due to the fact that boost-invariant p_T scheme used in this analysis does not take track masses into consideration when reconstructing jets. However, the ATLAS collaboration used default E-scheme that does take this into consideration. Final difference between jet spectra reconstructed in range defined by pseudo-rapidity and rapidity plays insignificant role. Similarly, the difference in jet spectra reconstructed using 0.3 GeV/c and 0.15 GeV/c is minimal.

However, to account for difference in spectra due to underlying event subtraction, the data were re-analysed also using track threshold defined by the ATLAS analysis. These

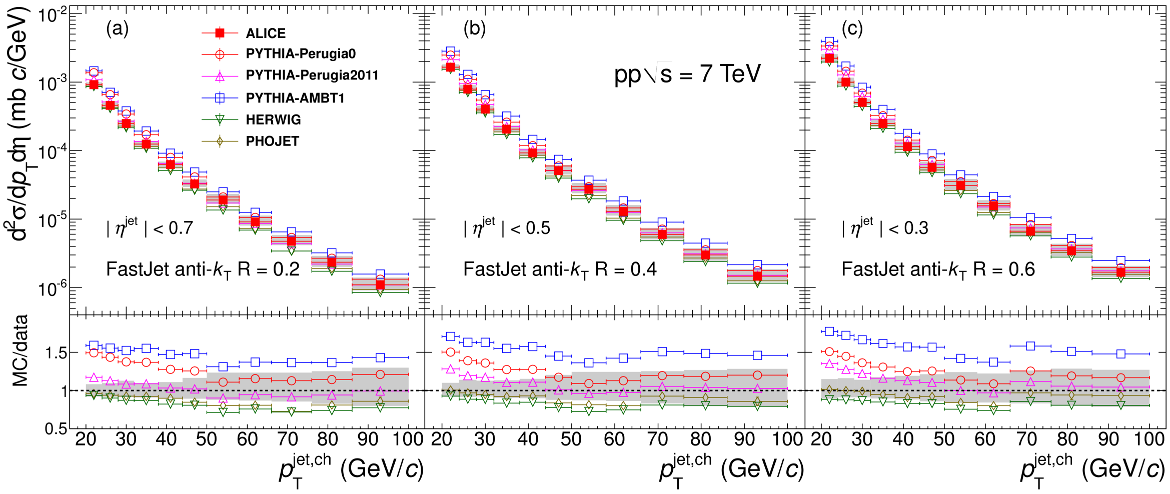

Figure 8.5: Comparison of jet spectrum from proton-proton collision at $\sqrt{s} = 7$ TeV with Monte-Carlo predictions produced by PYTHIA tune AMBT1 (blue squares), Perugia-0 (red circles), Perugia-2011 (magenta up-triangles), HERWIG (green down-triangles) and PHOJET (brown diamonds).

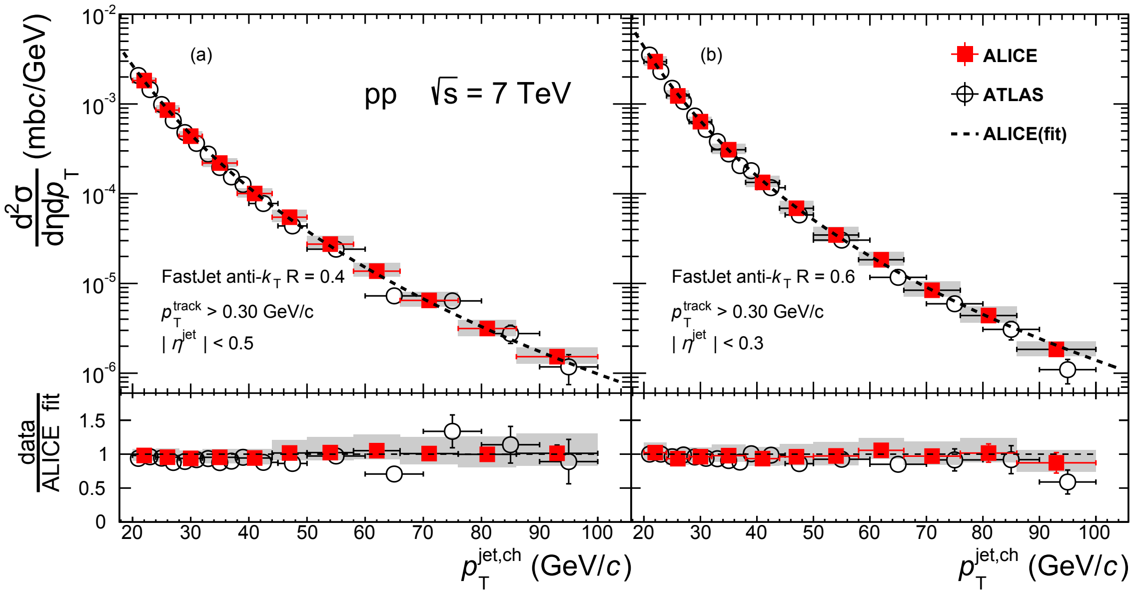

Figure 8.6: Comparison of fully corrected differential charged jet cross section from proton-proton collision at $\sqrt{s} = 7$ TeVreconstructed from tracks with at least $0.3\,\mathrm{GeV}/c$ without underlying event subtraction. Open squares represent data produced by the ATLAS collaboration with same requirements. Dotted line represents Tsallis' fit of the ALICE data. Bottom panels show ratio between data points and the ALICE fit. Gray bands represent systematic uncertainties on the ALICE data. Systematic uncertainties of the ALTAS data have been added in quadrature to statistical errors.

cross sections are shown in Fig. 8.6, however, due to the different binning used in these two analyses, the ALICE cross section are fitted using Tsallis' function and used as a reference for comparisons. Bottom panels of Fig. 8.6 show ratio of data and averaged integral of fit for given bin.

These ratios show good agreement in whole used range with exception of fluctuations in case of the ATLAS data around 75 GeV/c for resolution parameter 0.4 and last bin, 95 GeV/c, for resolution parameter 0.6.

8.2 Jet ratios

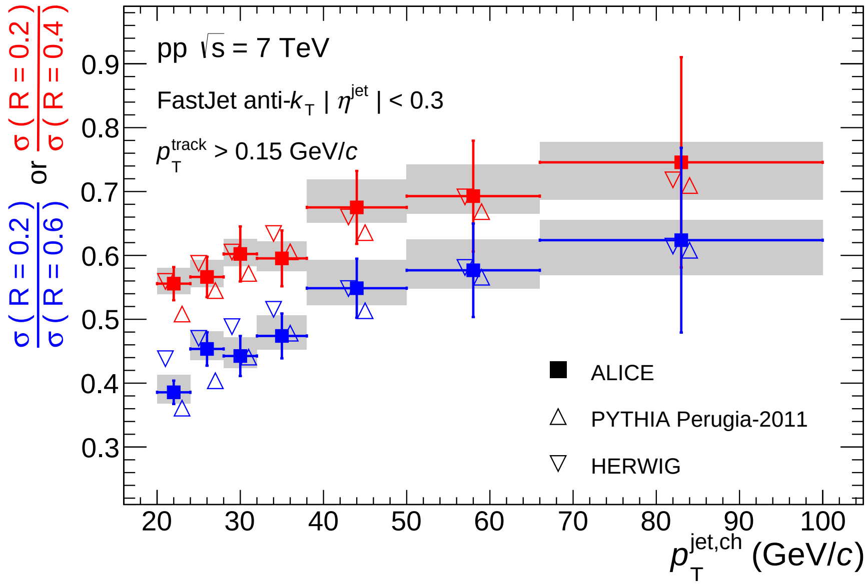

Figure 8.7: Ratios of fully corrected differential charged jet cross section reconstructed as a function of transverse momenta with different resolution parameter R in jet acceptance of $-0.3 < \eta^{\text{jet}} < 0.3$. Red squares represent ratio between cross section reconstructed using resolution parameter 0.2 and 0.4, blue squares represent case of 0.2 and 0.6. Same analysis was used to obtain predictions by PYTHIA tune Perugia-2011 (upward triangles) and HERWIG (downward triangles) with colours consistent with data points.

By studying ratio of fully corrected differential cross sections of jets reconstructed using anti-k_{T} algorithm with different resolution parameters changes of jet fragmentation with the increasing transverse momenta is observed. This change in jet fragmentation is represented via increased jet collimation. As jet energy increases, more and more of the tracks reconstructed inside jet are located closer to the jet axis representation of which is indicated by increased fraction of inclusive jets' cross section reconstructed with smaller resolution parameter with respect to bigger resolution parameter. If this fraction would reach value of 1, simplified representation would indicate that the same number of jets is reconstructed with different resolution parameters and thanks to the fact that resolution parameter is measure of the average area reconstructed by the jet algorithm. Concept of the increasing collimation can be imagined as decreasing variance of normal distribution with increasing jet energy where mean representing jet center.

Although this observable does not directly measure jet fragmentation like other observables, such as fragmentation functions[1] and jet shapes[2], it has an advantage that fully corrected jet cross section with subtracted underlying event can be used in any type of colliding system, even heavy-ion collisions where discrimination between signal and background tracks is impossible.

In order to prevent cross sections used in production of these ratios to be correlated, whole data-sample was split in halves with each half used to obtain jets reconstructed with different resolution parameter. Furthermore, in order to prevent to prevent any inconsistencies, jets reconstructed with different resolution parameters are still accepted in same region defined by the smallest possible acceptance, i.e. $-0.3 < \eta < 0.3$. This prevents possible influence caused by pseudo-rapidity dependence of jet production. However, statistical uncertainties were too big for last momentum bins, therefore, new binning is introduced. This binning is based on the original binning. Even this was not enough to produce sensible results in proton-proton collisions at $\sqrt{s} = 2.76$ TeV , therefore, only results from proton-proton collisions at $\sqrt{s} = 7$ TeV are presented. These results are in the Fig. 8.7.

---

[1] $\frac{\mathrm{d}N}{\mathrm{d}p_{\mathrm{T}}\mathrm{track}}$ in jet pt bin

[2] jet shapes

8.3 Comparison of jet spectra with NLO calculations

The obtained cross section from PYTHIA6 predictions, Fig. 8.5, show discrepancy with reconstructed jets for the low transverse momentum regions. However, comparison of cross section with the ATLAS experiment, Fig. 8.6, where jets are reconstructed as closely to the jet selection done by ATLAS as possible, shows quite good agreement between these two experiments although different binnings were used. Due to this inconsistency between simulations and experiments predictions from higher orders were investigated. This was done using POWHEG-Box framework with particle showers implemented in PYTHIA8 Monte-Carlo event generator.

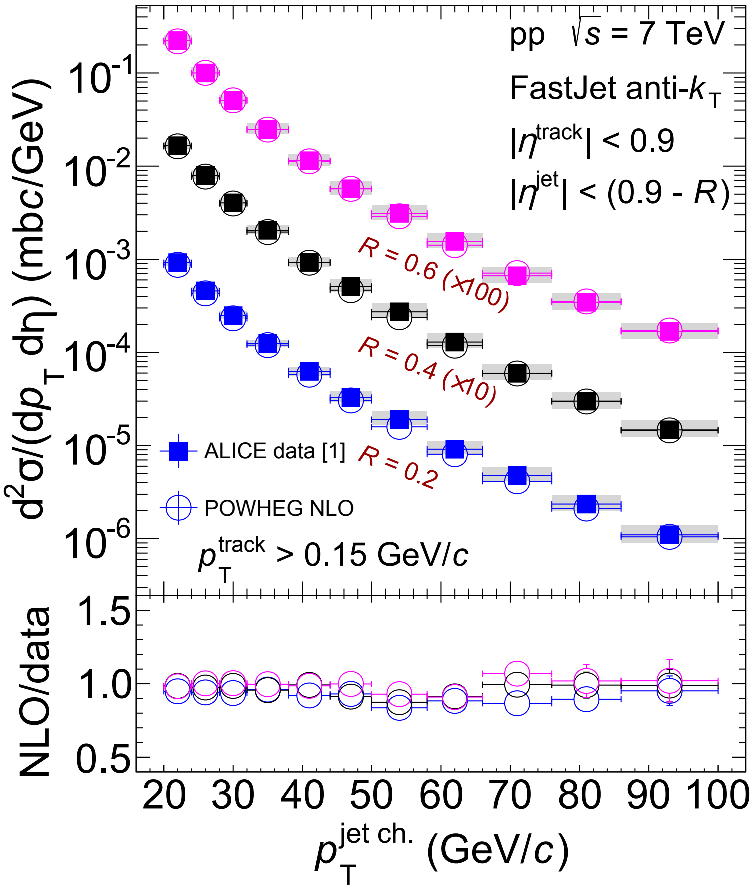

Figure 8.8: Comparison of fully corrected differential jet cross section obtained from real data with the NLO calculations for p+p at $\sqrt{s} = 7$ TeV. Both analyses follow same track and jet constrains and cuts. In bottom panel, ratio between data and NLO predictions without systematic uncetainties.

In the case of NLO calculations exactly same jet reconstruction steps were used as in the analysis of real data from proton-proton collisions at $\sqrt{s} = 7$ TeV. In Fig. 8.8, comparison between the ALICE measurement and NLO POWHEG-Box simulation with

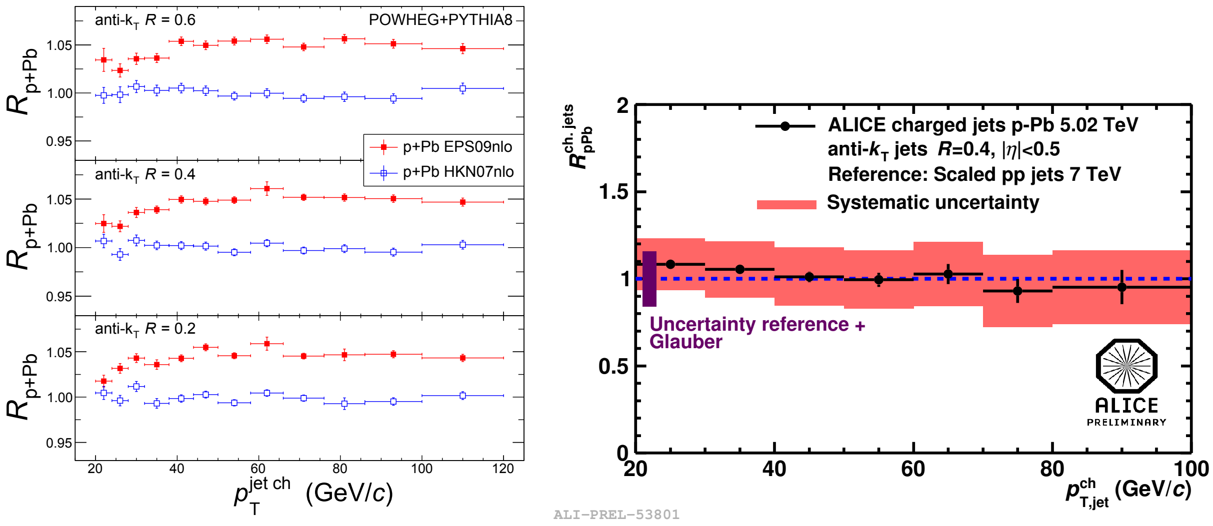

(a) NLO prediction for charged jet nuclear modification.

(b) ALICE charged jet nuclear modification.

Figure 8.9: (a) Nuclear modification function for charged jets, $R_{\rm p+Pb}$, as a function of jet transverse momenta shown for resolution parameters 0.2, 0.4, 0.6 in top, middle and bottom panel, respectively. Red full squares show modification when EPS09nlo nuclear modification factors of proton PDFs were used and open blue squares are result of HKN07nlo nPDFs. (b) Results of analysis of proton-lead collisions at centre-of-mass energy of 5.02 TeV in the ALICE experiment, compared with the interpolated spectrum corresponding to proton-proton collisions at the same energy.

parton showering provided by PYTHIA8 is shown. The bottom panel of this figure shows ratio between data and NLO. Very good agreement is obtained with differences up to 10-15%. For purpose of readability no systematic uncertainties are shown in this panel, however, both the ALICE data and NLO simulations have uncertainty of 15% on average.

8.4 Calculations for proton-lead collisions at $\sqrt{s_{\rm NN}} =$ 5.02 TeV

Although comparison between real data and NLO predictions from Sec. 8.3 showing very good agreement improves our descriptive capabilities for jets, they also serve as validation of simulation setup for further analyses. This includes simulations of jet cross section for proton-proton and proton-lead collisions at $\sqrt{s_{\rm NN}} = 5.02$ TeV. The p+Pb collision are obtained using HKN07 nPDFs and by applying EPS09 nuclear modification factors to proton PDFs provided by CTEQ6.6.

For simplicity, nuclear modification of charged jet cross sections are shown. These modifications are calculated as

$$R^{\mathrm{jets}}_{\mathrm{A+B}} = \left. \frac{\dfrac{\mathrm{d}N^2_{\mathrm{A+B}}}{\mathrm{d}p_{\mathrm{T}}\mathrm{d}\eta}}{\langle T_{A+B}\rangle \dfrac{\mathrm{d}\sigma^2_{\mathrm{p+p}}}{\mathrm{d}p_{\mathrm{T}}\mathrm{d}\eta}} \right|_{\mathrm{jets}}, \tag{8.1}$$

where $T_{\mathrm{A+B}}$ is nuclear overlap function, [74], which defines average number of nucleon collisions per nucleon cross section. It is calculated in framework of Glauber model from nuclear thickness functions, or nuclear profiles of nuclei. This formula is used for the case of real data, however, in case of simulations final spectra are produced as differential cross section as a function of transverse momenta, therefore no correction for number of nucleon-like collisions is necessary and nuclear modification can be calculated as a ratio of obtained cross sections.

In Fig. 8.9a are shown these nuclear modifications factors for charged jets as a function of jet transverse momenta. The predictions produced from HKN07nlo nPDFs show no modification along the whole analysed range of jet transverse momenta, however, nuclear modifications obtained using EPS09nlo are systematically above unity, showing approximately 5% enhancement.

In the Fig. 8.9b are for comparison charged jet nuclear modification factors obtained by the ALICE collaboration, [75]. These results are consistent with no modification of jet production cross section and, therefore, are within systematic uncertainty also consistent with prediction obtained by analysis described in this work.

8.5 Modification of jet shape

Similarly to the Sec. 8.2, study of ratios of charged jets cross sections reconstructed using different resolution parameters was done. Here, changes in composition of scattered hard partons was investigated, as this change could lead to changes ratio of quark and gluon jets. As these two different types of jets have slightly different fragmentation this should may reflect in slightly different jet shape and, therefore, different ratio of spectra reconstructed using different resolution parameters.

However, as seen in Fig. 8.10, no apparent modification of these ratios can be observed. This is shown using ratio of anti-k_{T} jets cross section with resolution parameter 0.2 with respect to jet reconstructed using resolution parameter 0.4 or 0.6. In both cases, pseudorapidity range from -0.3 to 0.3 as determined by acceptance of jets reconstructed with the largest resolution parameter, 0.6. This is done so that both ratios are comparing jets from the same acceptance region. However, as seen from figure, prediction for p+Pb collisions using EPS09nlo and HKN07nlo, red and blue circles respectively, are consistent with p+p reference, black circles, within statistical uncertainty and no apparent modification is observed.

Other observable had to be chosen for investigation of changes in PDFs.

8.6 Modification of PDFs

For the purpose of studying modification of PDFs in the presence of cold nuclear medium, this can be done in lepton-ion collisions. The attempt was made to extract information about energy fraction carried by parton from ion undergoing hard scattering. This extraction was done using leading di-jet in the event reconstructed using anti-k_{T} algorithm with resolution parameter 0.2 using all the final state particles, in order to contain full jet energy. The jets were accepted in full azimuthal range and in rapidity range from -4 to 4. Final state particles used in the Fastjet reconstruction were within acceptance of -4.5 to 4.5 units of rapidity and full azimuthal coverage. Utilising Eq. 6.10a and 6.10b, taking transverse momenta from leading jet, energy of the collision in the centre of mass, and rapidities of reconstructed jets, x_1 and x_2 were reconstructed in both proton-proton and proton-lead-like collision. These results were used in order to extract information about modification of these distributions, as seen in the Fig. 8.11, where this modification is shown for both x_1 and x_2. Additionally, direct information about x_1 and x_2 obtained from simulated partons in hard scattering is shown as red empty squares for purpose of method evaluation. Taking into account systematic uncertainties from variation of EPS09 parametrisation, Fig. 7.15, the case of direct observation of Bjorken's x-variable is well within expectations for $R^{x_1}_{\mathrm{p+Pb}}$, i.e. without modification at all and $R^{x_2}_{\mathrm{p+Pb}}$ modified considerably in case of p+Pb with respect to p+p baseline. In case

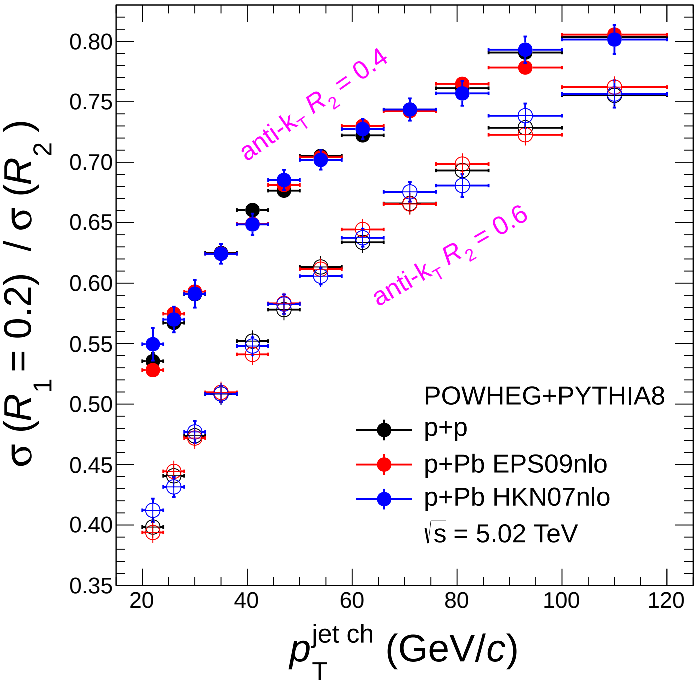

Figure 8.10: Ratio of jet cross section reconstructed using resolution parameter 0.2 with respect to resolution jets reconstructed using resolution parameter 0.4 or 0.6, full and open circles respectively. Red and blue circles show p+Pb collisions at 5.02 TeV prediction using EPS09nlo and HKN07nlo, respectively.

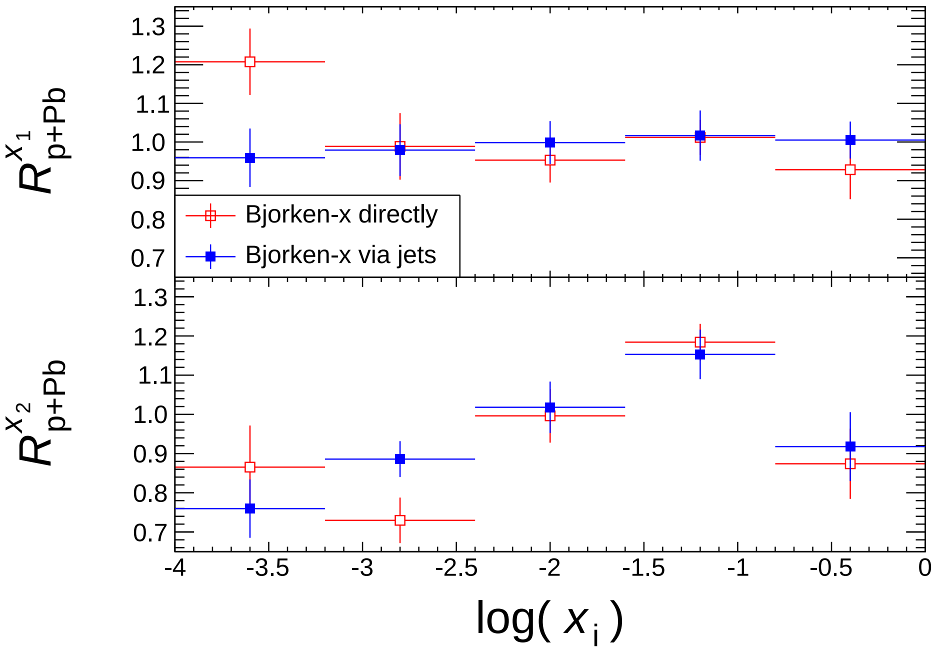

Figure 8.11: Modification of x_1 and x_2 distributions, top and bottom panel respectively, shown as ratio between distribution from p+Pb collisions with respect to p+p baseline distribution. These distributions are obtained directly from hard-scattering information (red) and from leading di-jet information (blue).

of indirect observation of these variables via measurement of leading dijet, consistent behaviour with direct observation is extracted. However, systematic uncertainties for distributions obtained from jet kinematics decrease impact of these results.

The value of uncertainties is caused by several reasons such as consequence of small sample, however, differences in nPDF parametrisation itself between different parton types or Q^2 scales, as seen in Fig. 2.2, may lead to considerable systematic variations. This is due to the fact, that this type of measurement did not differentiate between transferred momenta in hard scattering, and it was unable to discriminate different types of colliding partons although having considerable role.

Chapter 9. Discussion

Jets are used to test pQCD calculations and description of fragmentation processes. The first is achieved by direct comparison of cross section of jet production and calculated cross sections. The latter is obtained by comparing properties like constituent spectra and their distribution from jet axis, i.e. jet shapes, with predictions from different fragmentation models implemented in different Monte Carlo event generators or different tunes of these generators.

In this work the first measurements of the charged jet spectra with subtracted underlying events are presented. These cross sections are reconstructed using resolution parameters 0.2, 0.3,0.4 and 0.6 from proton-proton collisions with centre of mass energy 2.76 TeV and 7 TeV measured by ALICE experiment. The first set of reconstructed jets, for 2.76 TeV, is in range of $20\,\mathrm{GeV}/c$ to $76\,\mathrm{GeV}/c$ and spans from 10^{-6} to 10^{-3} mb$c$/GeV. However, comparing these spectra to different Monte Carlo generators shows that calculations differ from measured spectra at low p_{T} . Overall, for HERWIG generator, energy scale is off by the factor 2 and for AMBT1 tune of PYTHIA6 generator, for the largest resolution parameter, there is double the yield predicted relative to measured data.These spectra are most important for the comparison with results obtained from lead-lead collisions in order to provide direct measurement of $R_{\mathrm{Pb+Pb}}$ of jets, as these lead collisions are obtained at the same $\sqrt{s_{\mathrm{NN}}}$. Furthermore, the underlying event subtraction ensures clean jet signal necessary for comparison with results in lead-lead collisions where background is significantly different from proton-proton collisions. However, the smaller size of sample compared to ATLAS, prevents from increasing momentum reach of any analysis involving jets.

The second set of cross sections obtained from proton-proton collisions at 7 TeV cover transverse momentum range from $20\,\mathrm{GeV}/c$ up to $100\,\mathrm{GeV}/c$, spanning from 10^{-6} to 2×10^{-3} mb$c$/GeV. These spectra differ from Monte Carlo generator mainly in the low

p_{T} region up to 50 GeV/c, otherwise the result from proton-proton collisions are within systematic uncertainty. The maximal difference between these Monte Carlo spectra and data is 30% for HERWIG which underestimates jet productions and approximately about 60% difference between measured data and calculated spectra using AMBT1 tune of PYTHIA6, overestimating data. Both these generators overestimate or underestimate data in case of both collision energies. The problem seems to be mainly with energy scale, however for the case of AMBT1 and Perugia0 tunes this difference varies relatively significantly.

In order to validate procedure and previously obtained data, same procedure was applied with modification of threshold momenta of tracks accepted for the reconstruction in order to produce comparable spectra with results from the ATLAS collaboration. However underlying event subtraction was omitted as well, in order to be fully compatible. The comparison with fit of the ALICE data shows quite good agreement between the two collaborations in the whole range accessible by the ALICE collaboration. The changes to account different analysis did not have significant influence on the final systematic uncertainties.

Due to the fact that neither Monte Carlo generator properly describes whole transverse momenta range, the next-to-leading simulations, instead of leading order QCD simulations provided by PYTHIA6, PHOJET and HERWIG generators, are used for comparison. This is done using POWHEG-Box event generator via calculated NLO hard scatterings. Parton showers of scattered partons and creation of underlying event is provided by PYTHIA8 Monte Carlo generator. The results show good agreement with data, indicating that next-to-leading order calculations should be used for jet production at the LHC energies. However, heavy ion analysis of hadron-jet correlations shown that better description of the results is provided by leading order simulations. On the other hand, these processes have to threat parton interaction with QCD medium created in these heavy-ion collisions. These reconstructed spectra have already used for interpolation of jet spectra to the collisions energy of $\sqrt{s} = 5.02$ TeV. It is the collision energy corresponding to energy of proton-lead collisions present in LHC in the beginning of the year 2013, but where there is no proton-proton baseline present from data.

Lastly, as mentioned before, fragmentation can be investigated by studying jet composition. This is usually achieved by jet shape analysis and jet constituents spectra. However, in order to study heavy-ion collisions, such approach is problematic. To distinguish jet signal particles and particles that are background only becomes much more difficult with increasing complexity of colliding systems and with increasing collision energies. Therefore even proton-proton with extreme energies will produce significant underlying event. A simple method for estimation of rough jet structure is by producing ratio of jets with different resolution parameters in same acceptance. Such analysis shows, that at 20 GeV/c only approximately 55% of jets are reconstructed with resolution parameter 0.2 with respect to resolution parameter 0.4. This number increases and at 100 GeV/c, it is approximately 75%. When comparing jets with resolution parameters 0.2 and 0.6 only 40% of jets with parameter of 0.6 are reconstructed with algorithm using parameter of 0.2. Although this number rises to 65% at 100 GeV/c, the statistical uncertainties are around 25%. This is even after merging several of the bins of the original spectra, producing overwhelming uncertainties. These results clearly show that with increasing energy the fraction of jets reconstructed with algorithm using smaller resolution parameter, i.e. producing smaller areas of the jet, increases with respect to one using larger resolution. If such behaviour would continue for higher energies, the reconstruction algorithms with larger resolution parameters would serve just as cross checks of data produced with the smallest resolution parameter. This however is impossible in the collisions where underlying processes are present, as in case of hadron-hadron collisions.

In the second part of this thesis, next-to-leading order simulations using POWHEG-Box framework were studied implementing nuclear modification to parton distribution functions. While the functionality of the framework was tested on proton-proton collisions where quite good agreement was achieved, the test of proton-lead behaviour is much more complicated. Therefore, nPDFs were used as well as EPS09 nuclear modification factors. The behaviour of data obtained from proton-lead simulation compared with proton-proton baseline, $R_{\mathrm{p+Pb}}$ shows that compared to baseline, the change in proton-lead collisions is insignificant, few per cents at maximum in the studied region of jet transverse momenta. This is however at midrapidity. The observation is consistent with measurements.

Studying changes in composition of jets may indicate changes in parton distribution function, however, observed difference between data and simulations were insufficient to draw any conclusions. Taking into account minimal change in jet spectra indicates that such observation is not feasible.

Therefore, studying directly changes in Bjorken's x variables could be the only option. By utilising leading di-jet in order to obtain values of x_1 and x_2 for both proton-proton and proton-lead simulations with cross-check from the values obtained directly from information about hard scattering, change in between these two systems were observed. The changes were observed for the second particle, i.e. proton PDF modified into lead PDF. The other one was mainly unchanged, except for lowest values of x. Enhancement in distribution of partons containing 0.05-0.1 of nuclide energy is at the level of 20%. The distributions show suppression for the values of x lower than 0.004. Data obtained from direct information is fairly consistent with the di-jet information. However, the drawback of this method is lack of information about momentum scale and the fact that using this method distinguishing origin of scattered particles is practically impossible, therefore results represent integration over all the flavours available.

Furthermore, the LHC experiments attempt to reconstruct jets within different collision centralities. This yielded results in form of different behaviours of the reconstructed spectra, possibly obtaining information about interaction with cold nuclear matter. However, such analysis is impossible within the framework of simulations used for proton-lead collisions, as no geometry can be accounted for, and information about passing through medium would require parton treatment such as in case of models describing parton energy loss in hot and dense medium. Additionally, structure of colliding ions for initial processes is accounted by LHAPDFs.

Future program for collisions at the Large Hadron Collider will provide insight to the properties of hot and dense medium by increasing statistics of lead-lead collisions and improved understanding of cold medium of accelerated lead ions studied by their collisions with protons. Possible changes to detector and magnet configuration of the ALICE experiment will provide increased capabilities for data taking, further increasing statistical precision of provided data and allowing study of processes involving charged tracks with transverse momentum below 150 MeV/c. Implementation of full TRD detector will provide discrimination capabilities do differentiate between pion and electron and installation of DCal calorimeter will increase possible observables in jet ALICE physics programme by observables such as di-jet studies, where the imbalance between back-to-back jets travelling through medium should provide useful information.

Appendices

A. Renormalisation of running coupling constant

For renormalisation invariance, physical observable must not depend on chosen scheme in theoretical calculations.

Lets us consider scale μ, point at which UV divergencies are removed, and observable R. In general, R is a function of momentum q, coupling α and mass m of particles,

$$R = R\left(q, \alpha, m\right). \tag{A.1}$$

Independence of R can be expressed via *renormalisation group equation*,

$$\mu^2 \frac{d}{d\mu^2} R = 0, \tag{A.2a}$$

$$\left[\mu^2 \frac{\partial}{\partial \mu^2} + \frac{\partial \alpha}{\partial \mu^2}\frac{\partial}{\partial \alpha} + \frac{\partial m}{\partial \mu^2}\frac{\partial}{\partial m}\right] R = 0. \tag{A.2b}$$

Using beta function series from (1.10) and focusing only on first term of this series

$$\frac{\partial \alpha_S}{\partial \ln \mu^2} = -\alpha_S^2\left(\mu^2\right) b_0 \tag{A.3}$$

$$-\frac{\partial \alpha_S}{\alpha_S^2} = b_0 \partial \ln \mu^2, \tag{A.4a}$$

$$\frac{1}{\alpha_S\left(\mu^2\right)} - \frac{1}{\alpha_S\left(\mu_0^2\right)} = b_0 \ln\left(\frac{\mu^2}{\mu_0^2}\right), \tag{A.4b}$$

$$\frac{1}{\alpha_S\left(\mu^2\right)} = \frac{1 + \alpha_S\left(\mu_0^2\right) b_0 \ln\left(\frac{\mu^2}{\mu_0^2}\right)}{\alpha_S\left(\mu_0^2\right)}, \tag{A.4c}$$

$$\alpha_S\left(\mu^2\right) = \frac{1}{b_0\left[\frac{1}{b_0 \alpha_S\left(\mu_0^2\right)} + \ln\left(\frac{\mu^2}{\mu_0^2}\right)\right]}. \tag{A.4d}$$

Introducing momentum scale, Λ, or so called QCD scale parameter using dimensional transmutation,

$$\Lambda^2 \equiv \mu_0^2 \exp\left[-\frac{1}{b_0}\frac{1}{\alpha_S\left(\mu_0^2\right)}\right], \tag{A.5a}$$

$$\ln\frac{\mu_0^2}{\Lambda^2} = \frac{1}{b_0}\frac{1}{\alpha_S\left(\mu_0^2\right)}. \tag{A.5b}$$

This scale parameter is the only adjustable parameter except for quark masses and is determined from data. Substituting $\alpha_S\left(\mu_0^2\right)$ in (A.4d),

$$\alpha_S\left(\mu^2\right) = \frac{1}{b_0 \ln\left(\frac{\mu^2}{\Lambda^2}\right)}, \tag{A.6}$$

obtaining expression for coupling constant dependant only on transferred momenta and QCD scale Λ. Value of this scale is around 200 MeV, and is dependant on

Values of the few following coefficients in the series from the beta function are as follows,

$$b_0 = \left(\frac{1}{4\pi}\right)\left[11 - \frac{2}{3}n_f\right], \tag{A.7a}$$

$$b_1 = \left(\frac{1}{4\pi}\right)^2\left[102 - \frac{38}{3}n_f\right], \tag{A.7b}$$

$$b_2 = \left(\frac{1}{4\pi}\right)^3\left[\frac{2857}{2} - \frac{5033}{18}n_f + \frac{325}{54}n_f^2\right]. \tag{A.7c}$$

Coefficients of beta function are dependent on renormalisation scheme, however first two coefficients are universal among the massless schemes.

More can be found in Ref. [22, 45].

B. Fitting charged jet cross section

In the analysis two different distributions were used in order to fit jet cross sections. First, used mainly on real data, is Tsallis distribution [79, 80],

$$f\left(p_{\mathrm{T}}\right)=a\left(1+\frac{p_{\mathrm{T}}}{b}\right)^{-c}, \tag{B.1}$$

or mostly in NLO simulations, modified Hagedorn function was used

$$f'\left(p_{\mathrm{T}}\right)=a'\left(\frac{1}{p_{\mathrm{T}}+b'}\right)^{c'}, \tag{B.2}$$

where a,b and c are fitted parameters. These two distributions are equivalent when fitted parameters are set as follows

$$c=-c', \tag{B.3a}$$

$$b=b', \tag{B.3b}$$

$$a=a'\left(b'^{-c'}\right). \tag{B.3c}$$

C. PYTHIA6 tune Perugia0

Parameter	Value	Definition
PARP(64)	1.0000	ISR renormalization scale prefactor
MSTP(67)	2	ISR coherence option for 1st emission
PARP(67)	1.0000	ISR Q2max factor
MSTP(68)	3	ISR phase space choice & ME corrections
MSTP(70)	2	ISR IR regularization scheme
MSTP(72)	1	ISR scheme for FSR off ISR
PARP(71)	2.0000	FSR Q2max factor for non-s-channel procs
PARJ(81)	0.2570	FSR Lambda_QCD scale
PARJ(82)	0.8000	FSR IR cutoff
MSTP(81)	21	Comment: pp→jet + jet at 7000 TeV
PARP(82)	2.0000	UE IR cutoff at reference ecm
PARP(89)	1800.0000	UE IR cutoff reference ecm
PARP(90)	0.2600	UE IR cutoff ecm scaling power
MSTP(82)	5	UE hadron transverse mass distribution
PARP(83)	1.7000	UE mass distribution parameter
PARP(79)	2.0000	BR composite x enhancement
PARP(80)	0.0500	BR breakup suppression
MSTP(91)	1	BR primordial kT distribution
PARP(91)	2.0000	BR primordial kT width <|kT|>
PARP(93)	10.0000	BR primordial kT UV cutoff
MSTP(95)	6	FSI colour (re-)connection model
PARP(78)	0.3300	FSI colour reconnection strength
PARP(77)	0.9000	FSI colour reco high-pT dampening streng
MSTJ(11)	5	HAD choice of fragmentation function(s)
PARJ(21)	0.3130	HAD fragmentation pT
PARJ(41)	0.4900	HAD string parameter a
PARJ(42)	1.2000	HAD string parameter b

Table C.1: Pythia tune Perugia-0 parameters.

D. POWHEG-Box parameters

parameter	value	description
numevts	100 000	number of events per simulation
ih1 and ih2	1	type of colliding particles (protons)
ebeam1, ebeam2	2510 GeV 3500 GeV	beam energy
bornktmin	1	minimum hard k_T considered
bornsuppfactor	90	suppression factor
storeinfo_rwgt	1	stores information for reweighting
compute_rwgt	0 or 1	reweights events with new scale or PDF
lhans1lhans2		PDF id number from LHA
	10550	CTEQ6.6 proton PDF
	100151	HKN07 proton PDF
	100168	HKN07 lead PDF
renscfact	0.5, 1.0, 2.0	factor changing renormalisation scale
facscfact	0.5, 1.0, 2.0	factor changing factorisation scale
manyseeds	1	enables parallel production
doublefsr	1	parameter introducing new production mechanism to reduce spikes in showered output, by preventing emitted particle to be harder than emitter
par_diexp par_dijexp par_2gsupp	4 4 4	Set of parameters introduced in order to increase separation of generated regions. This helps to reduce spikes when producing weighted events.

Table D.1: General setup of different parameters of POWHEG-Box simulations as found in powheg.input.

E. Publications

- "Jet measurements in proton-proton collisions with the ALICE experiment at LHC," J. Phys. Conf. Ser. **446** (2013) 012004, arXiv:1212.6890 [hep-ex].
- "Charged jet spectra in proton-proton collisions with the ALICE experiment at the LHC," PoS EPS **-HEP2013** (2013) 464,arXiv:1311.0148 [hep-ex].
- "Study of jet properties in p+p collisions at $\sqrt{s} = 7$ TeV and p+Pb collisions at $\sqrt{s} = 2.76$ TeV using POWHEG-Box framework," Proceedings from 18th CCSP in Olomouc.
- "Charged jet cross sections and properties in proton-proton collisions at $\sqrt{s} = 7$ TeV," arXiv:1411.4969 [nucl-ex], submitted to Physical Review D.

Jet measurements in proton-proton collisions with the ALICE experiment at LHC

2013 J. Phys.: Conf. Ser. 446 012004

(http://iopscience.iop.org/1742-6596/446/1/012004)

Hot Quarks 2012 IOP Publishing
Journal of Physics: Conference Series **446** (2013) 012004 doi:10.1088/1742-6596/446/1/012004

Jet measurements in proton-proton collisions with the ALICE experiment at LHC

Michal Vajzer[1,2] **on behalf of the ALICE collaboration**
[1]Nuclear Physics Institute – Prague, Czech Republic
[2]Faculty of Nuclear Sciences and Physical Engineering, CTU – Prague, Czech Republic

E-mail: `michal.vajzer@cern.ch`

Abstract. The study of jets, collimated sprays of particles associated with hard partons, is an important tool in testing perturbative quantum chromodynamics (pQCD) and probing hot and dense nuclear matter created in high energy heavy-ion collisions. Jets enable the study of hard scatterings, fragmentation and hadronisation and their modification in the presence of a nuclear medium with respect to baseline vacuum measurements, which is acquired from jet measurements in proton-proton collisions.

We have analysed data from proton-proton collisions at $\sqrt{s}$= 7 TeV measured by the ALICE experiment at the LHC and reconstructed the inclusive spectra of charged particle jets at mid-rapidity using anti-k_{T} clustering algorithm. We present the jet spectra corrected for detector effects using several unfolding methods. Furthermore, we examine various properties of jets, such as their charged particle multiplicity and jet shapes.

1. Introduction

Jets are collimated sprays of particles created from an energetic parton (quark or gluon), which is produced in the initial stage of the collision. They are an excellent tool to test pQCD and study fragmentation and hadronisation in proton-proton collisions and their modification in collisions of heavy ions. Here, they also serve as probe of hot and dense nuclear matter with an aim of exploring quark-gluon plasma (QGP), which is a challenging task due to an elusive characteristics that requires a combination of various signatures. A Large Ion Colliding Experiment (ALICE) has excellent tracking capabilities and can reconstruct and identify charged particles with transverse momenta down to 150 MeV/c. We report measurements of the charged jet spectra and jet shape observables, such as charged track multiplicities and radial momentum density distributions [1]. These observables are studied at centre of mass energy $\sqrt{s}$= 7 TeV and compared to predictions obtained from Monte-Carlo generators.

2. Data analysis

The results presented in this paper are based on an analysis of the data from proton-proton collisions at the LHC taken in 2010 by the ALICE. The online event selection is done using the V-ZERO (V0) detector and Inner Tracking System (ITS), selecting 160M minimum bias events. From these events, only those with reconstructed primary vertex within 10 cm from the nominal interaction point are further analysed.

For charged jet reconstruction, tracks from the ITS and Time Projection Chamber (TPC) are used. These tracks are selected to be within pseudorapidity $|\eta| \leq 0.9$ and transverse momenta

(p_{T}) greater than 0.15 GeV/c. They are used as input for FastJet [2] to reconstruct jets using anti-k_{T} algorithm. It belongs to sequential recombination jet algorithms. Anti-k_{T} merges hard particles first while k_{T} starts with soft particles and is therefore more suitable for determination of background. Resolution parameters $R = \sqrt{\Delta\eta^2 + \Delta\varphi^2}$, used in this analysis are 0.2, 0.4 and 0.6. For further analysis, jets had to have p_{T} of at least 5 GeV/c and be within $|\eta_{jet}| \le 0.9 - R$.

In order to obtain jet shape observables and charged jet spectra at particle level we have to correct effects of detector reconstruction. We are using PYTHIA [3] (Perugia0 tune) simulated data to acquire spectra on a particle level and a full GEANT simulation of detector to extract detector response matrices linking generator level jet spectra with recontructed spectra. We use 3 different correction procedures.

As PYTHIA reproduces the measured jet observables such as spectra and jet shapes, reasonably well, as seen in [1], we adopted a bin-by-bin correction procedure using simulated events as first method. In this technique, the correction factors (CF) are computed for each jet p_{T} bin as the ratio between the observable at particle level and the same observable at a detector level in the same p_{T} bin,

$$\mathrm{CF}\,(p_{\mathrm{T}}) = \left.\frac{\mathrm{d}\sigma^{\mathrm{ch}}_{\mathrm{jet}}}{\mathrm{d}p_{\mathrm{T}}\mathrm{d}\eta}\right|^{\mathrm{part}}_{\mathrm{MC}} \Bigg/ \left.\frac{\mathrm{d}\sigma^{\mathrm{ch}}_{\mathrm{jet}}}{\mathrm{d}p_{\mathrm{T}}\mathrm{d}\eta}\right|^{\mathrm{det}}_{\mathrm{MC}}. \tag{1}$$

This correction is subsequently applied to a raw jet spectrum.

Second method, we used to find an inverse matrix to the response matrix, is Bayesian unfolding [4]. This is possible because the response matrix is composed of a probability distribution of finding given a cause – generated jet of given $p^{\mathrm{ch,MC-gen}}_{\mathrm{T,jet}}$ – as an effect – reconstructed jet with any value $p^{\mathrm{ch,MC-rec}}_{\mathrm{T,jet}}$.

Third method and another regularized unfolding procedure used as a cross-check in jet spectrum analysis is the Singular Value Decomposition of the response matrix [5]. This method decomposes the response matrix into two square orthogonal matrices and a diagonal singular matrix. Subsequently it converts the problem to a system of linear equations and solves it.

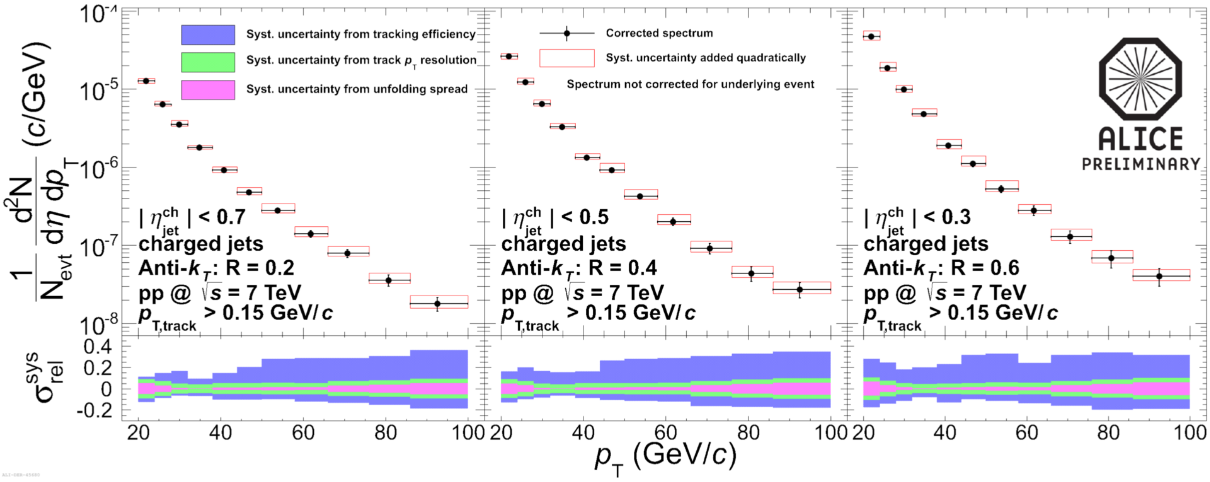

Figure 1. (Color online) Charged jet spectra corrected for detector effects reconstructed using anti-k_{T} algorithm with resolution parameter R (left) 0.2; and (middle) 0.4; and (right) 0.6; from pp collisions at $\sqrt{s}$= 7 TeV. Error bars indicate statistical uncertainties. In bottom part are relative systematic uncertainties obtained from different sources for the anti-k_{T} algorithm with corresponding R.

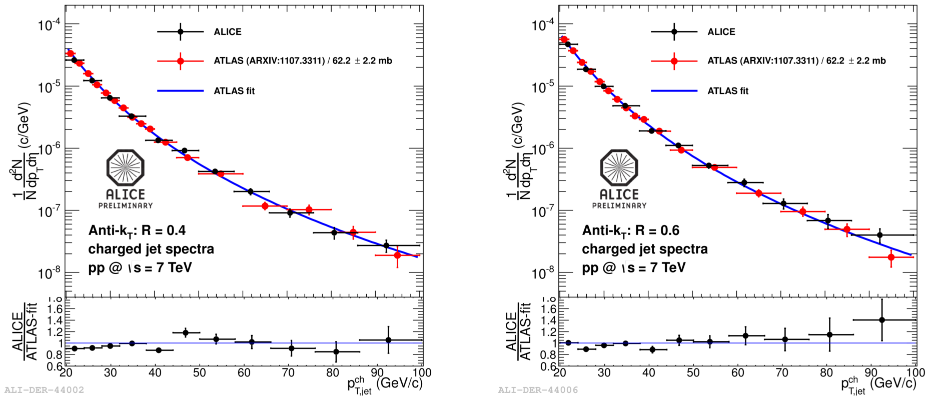

(a) Anti-k_{T}; R = 0.4 (b) Anti-k_{T}; R = 0.6

Figure 2. (Color online) Charged jet spectra from anti-k_{T} algorithm with resolution parameter R of (a) 0.4; and (b) 0.6; from pp collisions at $\sqrt{s}$= 7 TeV measured by the ALICE (black points) and the ATLAS (red points) collaborations. The line is a Tsallis fit of the ATLAS results. Error bars indicate statistical uncertainties. In bottom part is ratio of the ALICE charged jet spectrum to the ATLAS results.

3. Results

In Fig. 1 we present the unfolded charged jet spectra for anti-k_{T} algorithm with resolution parameters R of 0.2, 0.4 and 0.6 in top panel, with the relative systematic uncertainties in the bottom panel of each plot, reconstructed from proton-proton collisions at $\sqrt{s}$= 7 TeV using the ALICE detector system. The most significant uncertainties are obtained from varying track reconstruction effiency, track p_{T} resolution and simulation with parametrised detector response. The final systematic uncertainties are obtained by adding above mentioned uncertainties in quadrature.

The results presented here are consistent with results obtained by the ATLAS collaboration [6], as shown in the Fig 2, obtained from charged tracks in $|\eta| \leq 0.5$ with $p_{\mathrm{T}} \geq 0.3$ GeV/c.

Fig. 3 shows jet shape variables. The charged track multiplicity of a jet, defined as a mean number of charged tracks in the leading jet, i.e. one with the largest transverse momentum in the event, belonging to given $p_{\mathrm{T,jet}}^{\mathrm{ch}}$ bin, is obtained from charged tracks used for the jet reconstruction within a jet cone. The mean track multiplicity in such jets obtained from the analysed data is shown in Fig 3(a), with respect to a charged jets' transverse momentum bin. Increasing value of average number of tracks is observed with increasing jet p_{T} bin, as previously measured by the CDF collaboration [8]. Also, predictions obtained from the PYTHIA (Perugia0 tune), PYTHIA (Perugia11 tune) and PHOJET [7] are shown here. Results from data differ by 10% from values obtained from Monte-Carlo predictions.

The radial momentum density is defined for jets of given $p_{\mathrm{T,jet}}^{\mathrm{ch}}$ bin as a sum of momenta of charged tracks $p_{\mathrm{T,track}}^{\mathrm{ch}}$ belonging to the leading jet with respect to their distance from the jet axis in $\eta - \varphi$ plane, normalized by number of jets,

$$\frac{\mathrm{d}p_{\mathrm{T}}^{\mathrm{sum}}}{\mathrm{d}r}(r) = \frac{1}{2\Delta r}\frac{1}{\mathrm{N_{jet}}}\sum_{\mathrm{jets}} p_{\mathrm{T,jet}}^{\mathrm{ch}}\left(r \text{ - } \Delta r,\ r + \Delta r\right), \tag{2}$$

where $p_{\mathrm{T,jet}}^{\mathrm{ch}}$ (r -Δ r , r +Δ r) denotes the sum of $p_{\mathrm{T,track}}^{\mathrm{ch}}$ of all charged tracks which are displaced from jet axis by $r \pm \Delta r$ of given jet. N_{jet} is number of leading jets in analysis.

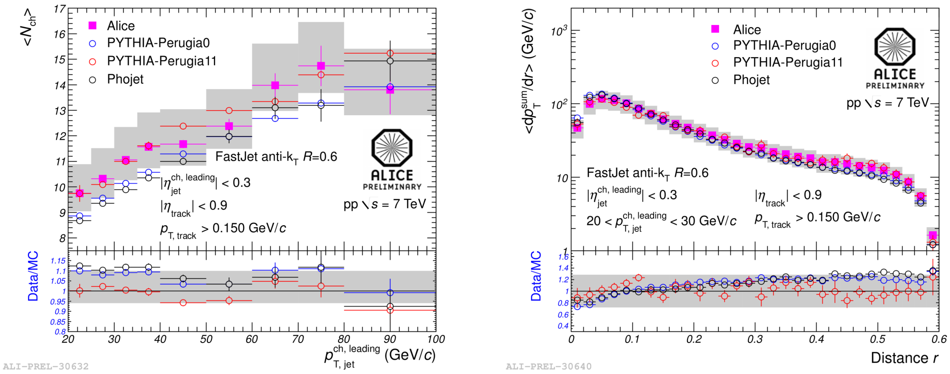

(a) Charged track multiplicity (b) Radial momentum distribution

Figure 3. (Color online) (a) Mean charged track multiplicities of leading jet as a function of $p_{\mathrm{T,jet}}^{\mathrm{ch}}$. (b) The radial momentum distribution from a jet axis in leading charged jets in $20 \leq p_{\mathrm{T,jet}}^{\mathrm{ch}} \leq 30$ GeV/c momentum bin. Results from pp collision at $\sqrt{s}$= 7 TeV using the ALICE (magenta squares) and predictions from PYTHIA (Perugia0 tune) (blue circles), PYTHIA (Perugia11 tune) (red circles) and PHOJET (black circles) are shown with thes ratio of data and predictions from Monte-Carlo simulations in the bottom part. Error bars indicate statistical uncertainties and gray bands systematic uncertainties.

In the Fig 3(b) we observe a decreasing radial momentum density with decreasing distance from a jet axis. This suggests that most of the jet energy is concentrated around a jet axis. Comparison of the slopes of two different jet p_{T} bins at a small distances from jet axis indicate that high energy jets are more collimated than jets with smaller energy.

4. Conclusions

We reported measurements of inclusive charged jet spectra in pp collisions at midrapidity, charged track multiplicities within leading jet and the radial momentum density for jets reconstructed using anti-k_{T} algorithm. The reconstructed jet spectra are consistent with results obtained from the ATLAS collaboration and jet shape observables follow the trend expected from previous results of the CDF collaboration and are in reasonable agreement with predictions from PYTHIA and PHOJET calculations.

Acknowledgements

This work was supported by the Grant Agency of the Czech Technical University in Prague, grant No. SGS10/292/OHK4/3T/14 and by Ministry of education, youth and sports of Czech Republic, grant No. LA08015.

References

[1] S. K. Prasad [ALICE Collaboration], J. Phys. Conf. Ser. **389**, 012005 (2012).
[2] M. Cacciari, G. P. Salam and G. Soyez, Eur. Phys. J. C **72** (2012) 1896.
[3] T. Sjstrand, S. Mrenna and P. Skands, JHEP05 (2006) 026.
[4] G. D'Agostini,NIM A 362 (1995) 487.
[5] A. Höcker and V. Kartvelishvili, NIM A 372 (1996) 469.
[6] G. Aad *et al.* [ATLAS Collaboration], Phys. Rev. D **84** (2011) 054001
[7] S. Roesler, R. Engel and J. Ranft, hep-ph/0012252.
[8] T. Affolder *et al.* [CDF Collaboration], Phys. Rev. D 65, 092002 (2001).

PROCEEDINGS OF SCIENCE

Charged jet spectra in proton-proton collisions with the ALICE experiment at the LHC

Michal VAJZER[*]
for the ALICE Collaboration.

Nuclear Physics Institute, The Academy of Sciences of the Czech Republic
Řež, Czech Republic
Faculty of Nuclear Sciences and Physical Engineering, Czech Technical University in Prague
Prague, Czech Republic

E-mail: `michal.vajzer@cern.ch`

Jets are collimated sprays of particles resulting from fragmentation of hard scattered partons. They are measured in different types of collisions at different energies to test perturbative Quantum Chromodynamic calculations and are used to study the hard scattering, fragmentation and hadronisation of partons. These phenomena, measured in simple systems such as proton–proton collisions, serve as a baseline to investigate their modifications by hot and dense nuclear matter created in high energy heavy-ion collisions.

We have analysed data from minimum bias proton–proton collisions at centre of mass energy of 2.76 and 7 TeV collected using the ALICE detector system at the LHC and reconstructed the inclusive jet cross section from charged tracks at midrapidity. We present jet spectra reconstructed using the infrared and colinear safe anti-k_T algorithm with underlying event subtraction, corrected for detector effects via unfolding for both collision energies. Furthermore, results from analyses of fragmentation distributions and jet shape observables are shown. All results are compared with measurements of other LHC experiments and with Monte Carlo generators.

The European Physical Society Conference on High Energy Physics
18-24 July, 2013
Stockholm, Sweden

---

[*] Speaker.

1. Introduction

Jets are observable final states of hard scattered partons. They serve as a tool for testing of both perturbative and non-perturbative aspects of Quantum Chromodynamics (QCD), namely cross sections of scattering production and parton shower evolution. In collisions of heavy ions, due to the short formation time of hard partons, they are used as an important probe in the study of produced nuclear medium. For these studies, proton–proton collisions are an important baseline.

We present production cross sections for the charged part of jets using reconstructed charged tracks, further denoted as “charged jets”, in proton–proton collisions with centre of mass energies of 2.76 TeV and 7 TeV, as reconstructed with the ALICE detector system. Furthermore, we show properties of these jets derived from analysis of individual jet constituents, namely average charged particle multiplicity, summed track transverse momentum in radial slices from jet axis and the momentum distribution of individual jet constituents.

2. Data analysis

2.1 Event selection

We have analysed 7 TeV proton–proton collisions from the year 2010 and 2.76 TeV proton–proton collisions from 2011, recorded using A Large Ion Collider Experiment[1] (ALICE) at the Large Hadron Collider (LHC). We select minimally biased events triggered with the VZERO detector which consist of two forward triggering scintillator counters. In offline analysis, the reconstructed primary vertex was required to be within 10 cm along the beam axis from the nominal interaction point. At least 2 tracks had to be associated with this primary vertex.

2.2 Jet reconstruction

Jets are the final state of hard partons, but experimentally observed only as collimated sprays of particles. In our analysis, we focus on charged particles reconstructed as tracks in the central tracking detectors, namely the Time Projection Chamber (TPC) and silicon Inner Tracking System (ITS), consisting of 2 layers of pixel, drift and strip detectors each. We obtain track distributions in full azimuth and pseudo-rapidity interval $|\eta| < 0.9$. Tracks are selected with reconstructed transverse momenta of at least 150 MeV/c.

In order to reconstruct jets, we utilize reconstructed tracks as input for FastJet’s [2] anti-k_T [3] algorithm, sequentially merging particles into proto-jets according to their transverse momenta and distance from each other. The anti-k_T algorithm starts merging with particles with the highest transverse momenta. We reconstruct jets with various resolution parameters R, a measure of the size of the jet in the space of pseudo-rapidity (η) and azimuthal angle (φ) [1], ranging from 0.2 to 0.6. The jet *eta* acceptance was reduced by the value of this parameter in order to exclude partially reconstructed jets from the analysis.

---

[1] R is measure of distance in space of pseudo-rapidity and azimuthal angle and distance is calculated as $r = \sqrt{(\eta_i - \eta_j)^2 - (\varphi_i - \varphi_j)^2}$

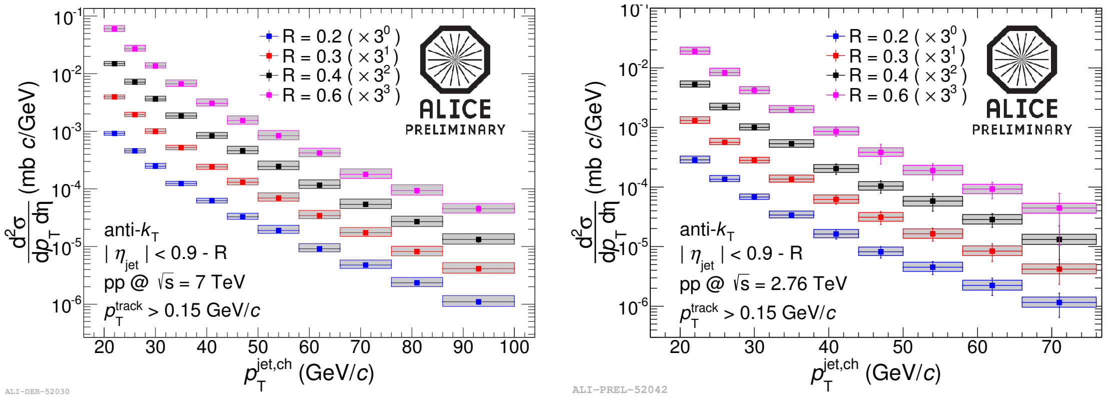

(a) $\sqrt{s} = 7$ TeV (b) $\sqrt{s} = 2.76$ TeV

Figure 1: Charged anti-k$_T$ jet spectra measured in 7 TeV and 2.76 TeV collisions, Fig. 1(a) and Fig. 1(b) respectively. The error bars represent statistical uncertainties and boxes represent systematic uncertainties coming mainly from track reconstruction efficiency. Spectra are scaled by factors of 1, 3, 9 and 27 for resolution parameter 0.2, 0.3, 0.4 and 0.6 respectively.

2.3 Corrections

Due to the composite nature of colliding protons, more simultaneous (mostly soft) processes may occur in one collision, the so called *underlying event*. After jet reconstruction, we have to subtract effects of these simultaneous processes. This was obtained on event by event basis from tracks in cones perpendicular to the jet axis in azimuth and at the same pseudo-rapidity. Then, the jet spectra are corrected for effects of detector reconstruction, namely track momentum resolution and efficiency of particle reconstruction. This efficiency is the main source of systematic uncertainties of the jet spectra, increasing with the jet transverse momentum. Other sources of uncertainty

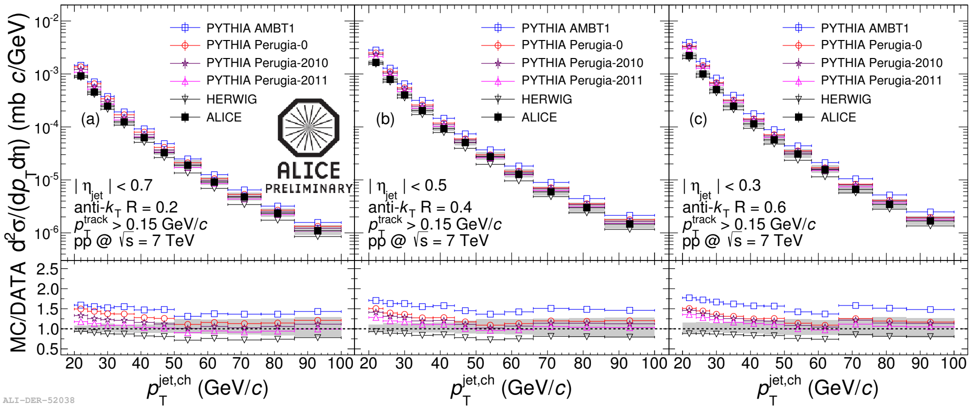

Figure 2: Jet cross section (full black squares) measurement in proton–proton collisions at 7 TeV compared to Monte Carlo predictions obtained from PYTHIA Perugia-0 (open red circles), PYTHIA Perugia-2010 (open purple stars), PYTHIA Perugia-2011 (open magenta triangles), PYTHIA AMBT1 (open blue squares) and HERWIG (open black triangles). Lower panel of each plot shows ratios of Monte Carlo predictions to data.

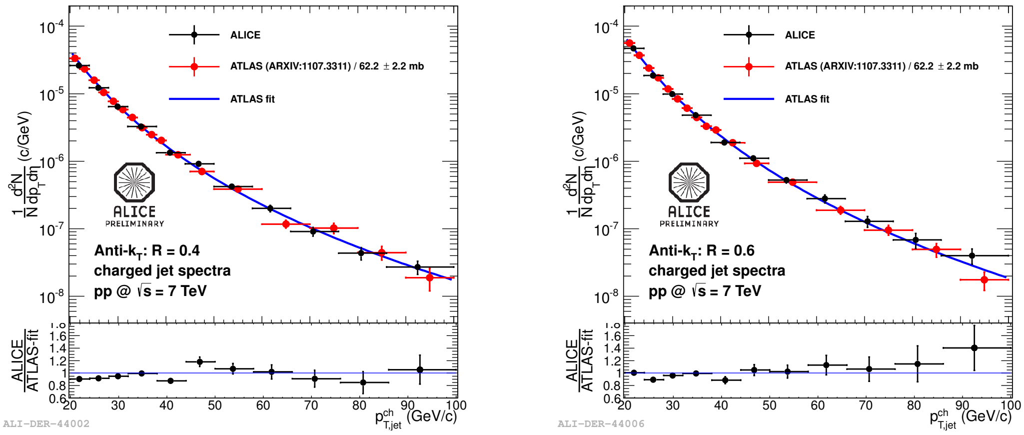

(a) anti-k$_T$, R = 0.4

(b) anti-k$_T$, R = 0.6

Figure 3: Charged jet spectra measured by the ALICE and ATLAS experiments (black and red points respectively), with minimum transverse momentum of 150 MeV/*c* and 300 MeV/*c*, respectively, without underlying event subtraction. The blue line represents Tsallis' fit of ATLAS data. The lower panels show comparisons of the ALICE datapoints to the ATLAS data fit. Fig. 3(a) shows anti-k$_T$ jet spectra reconstructed with resolution parameter of 0.4 and in Fig. 3(b) jet spectra with resolution parameter value of 0.6.

are the track momentum resolution and the unfolding method, with contribution of few per cents. Moreover, in case of jet shapes and fragmentation observables, non-negligible uncertainties and corrections are due to the presence and subtraction of underlying event and contamination from secondary decays. For the correction of jet spectra a Bayesian unfolding method [4, 5] was used and cross checked with results from Singular Value Decomposition of the response matrix [6]. Jet shapes and fragmentation observables are corrected using a bin-by-bin method, where data are corrected with factors obtained from Monte Carlo simulations by reconstructing the same observable at generator and detector level.

3. Results

3.1 Jet spectra

Jet spectra were reconstructed from 1.9×10^8 minimum bias collisions with centre of mass energy of 7 TeV and 7×10^7 minimum bias collisions at 2.76 TeV. These spectra are shown in Fig. 1, with statistical uncertainties represented with error bars and systematic uncertainties shown as gray boxes.

We compare our results with predictions from Monte-Carlo generators, Fig. 2. Considering several different tunes of the PYTHIA [7, 8] generator, Perugia-0, Perugia-2010, Perugia-2011 and AMBT1 [9], and the HERWIG [10, 11] generator. None of the generators provides a satisfactory description. However, these improve with increasing transverse momentum. For 7 TeV data, the best description is provided with the HERWIG for low and the PYTHIA Perugia-2011 for high transverse momenta.

A comparison of the measurements with results obtained by the ATLAS experiment [12] is shown in Fig. 3. No underlying event subtraction was done for those results, therefore we produced

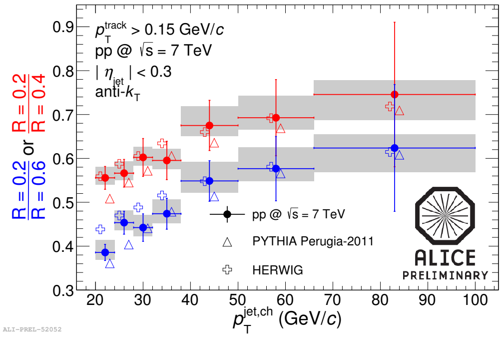

(a) ratios of jet cross sections

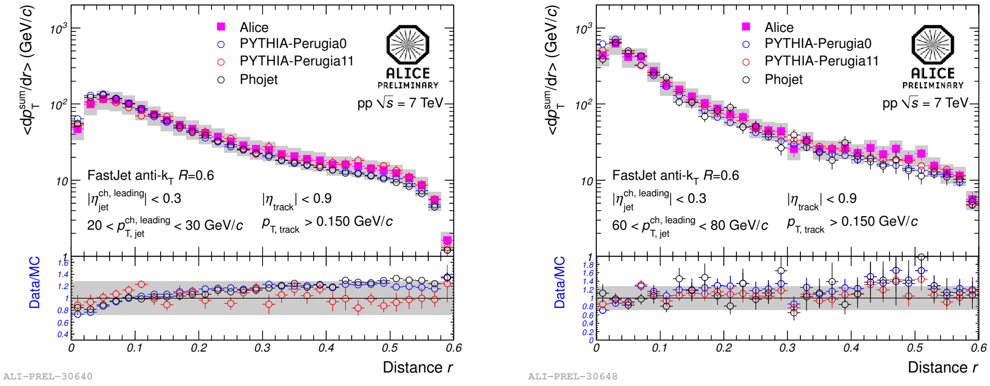

(b) p_T^{sum} density for $20 < p_T^{ch,jet} < 30$ GeV/c (c) p_T^{sum} density for $60 < p_T^{ch,jet} < 80$ GeV/c

Figure 4: Fig. 4(a) shows ratios of jet spectra reconstructed with resolution parameter 0.2 and 0.4 (full red circles), and between spectra with resolution parameters 0.2 and 0.6 (full blue circles). Comparison to Monte Carlo simulations is made using HERWIG and PYTHIA Perugia-2011 (open crosses and triangles, respectively). Fig. 4(b) and Fig. 4(c) show summed transverse momentum distribution inside jets as a function of distance r from jet axis, for jets in 20-30 GeV/c and 60-80 GeV/c p_T bins, respectively. In lower panel comparison between data (full magenta squares) and predictions from PYTHIA tunes Perugia-0 and Perugia-2011 and PHOJET (open blue, red and black circles respectively) are shown.

spectra without subtracted underlying event as well. Moreover, the ATLAS analysis uses tracks with transverse momenta of at least 300 MeV/c. Although no correction for this difference was done, we observe a good consistency of the ALICE and ATLAS measurements. This is due to a small influence of different track cuts on final spectra.

3.2 Jet properties

Jet fragmentation was studied using various observables that address transverse and longitudinal momentum distributions with respect to the jet axis.

To the first category belongs the ratio of jet spectra with different resolution parameters and transverse momentum distribution around the jet axis. The comparison of jet spectra reconstructed using different resolution parameters shows, Fig. 4(a), increasing ratio with increasing transverse momentum and a similar behaviour is observed in predictions from Monte Carlo simulations.

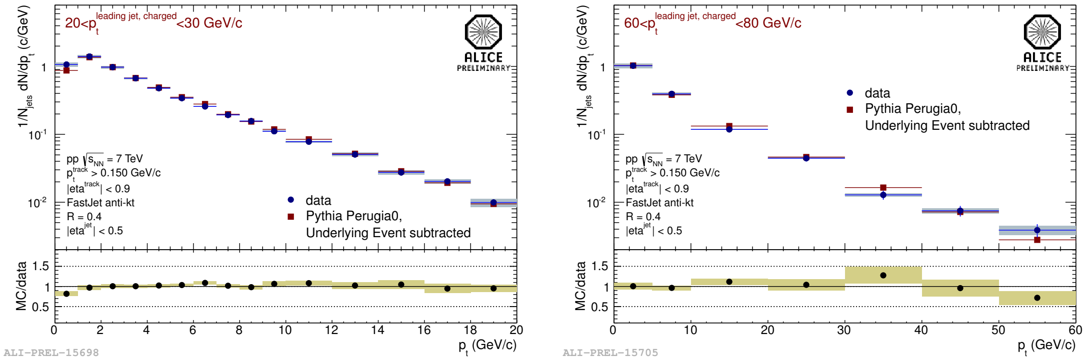

(a) track p_T in jets with $20 < p_T < 30$ GeV/c (b) track p_T in jets with $60 < p_T < 80$ GeV/c

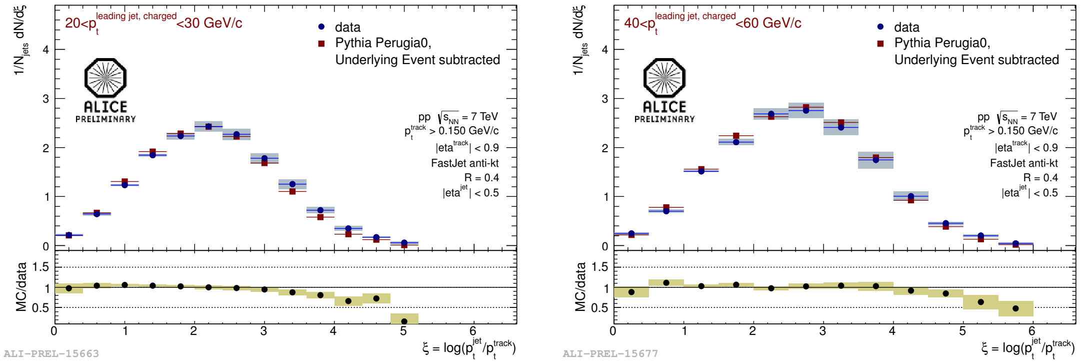

(c) ξ for jets with $20 < p_T < 30$ GeV/c (d) ξ for jets with $40 < p_T < 60$ GeV/c

Figure 5: Transverse momentum distributions of jet constituents, Fig 5(a) and Fig. 5(b), and transverse momentum distribution scaled to transverse momentum of jets, Fig. 5(c) and Fig. 5(d), for two jet transverse momentum bins of anti-k$_T$ jets with resolution parameter of 0.4.

Increasing ratio indicates a stronger collimation of jets as larger fraction of jet momentum is reconstructed by jetfinder with smaller resolution parameter. Ratio of 1 would indicate, that jets reconstructed with different resolution are completely contained within area defined by smaller resolution, and no additional energy is reconstructed with jetfinder with larger resolution. Although this is an indirect observation of jet collimation, same observable can be obtained from studies of heavy ions collisions.

The transverse momentum density of charged tracks is other observable quantifying increased collimation of particles within the jet. In Fig. 4(b) and Fig. 4(c) we show a comparison between transverse momentum distributions of jets as a function of distance from jet in two different jet p_T bins, 20-30 GeV/c and 60-80 GeV/c. From these distributions, increased transverse momentum density of jets at small r for higher jet p_T bin is observed. This is consistent with predictions from Monte Carlo simulations.

Concerning the longitudinal properties of jets, we focus on transverse momentum distributions of jet particles in two jet p_T bins, Fig. 5(a) and Fig. 5(b), show a small dependence on jet energy. In Fig. 5(c) and Fig. 5(d) scaled transverse momenta distributions of these tracks with respect to the transverse momentum of the jet they belong to, $\xi = \log\left(p_T^{\text{ch,jet}}/p_T^{\text{ch,track}}\right)$. Here, the distribution of

ξ is shown for two different jet p_T bins, 20-30 GeV/c and 40-60 GeV/c. The characteristic shape of distribution, "hump-backed" plateau, is observed, which is a result of QCD coherence [13]. The position of this plateau moves to higher values of ξ and the area under the distribution increases, with increasing transverse momentum of jets, as expected from QCD calculations based on Modified Leading Logarithmic Approximation [14]. Our observations are quantitatively consistent with predictions from Monte Carlo simulations obtained with the PYTHIA.

4. Summary and Conclusions

We have analysed jet spectra from proton–proton collisions at centre-of-mass energies of 2.76 TeV and 7 TeV with the anti-k_T algorithm using several different jet resolution parameters. Large variations in descriptions of cross sections provided by various tunes of Monte Carlo generators are observed. On the other hand, Monte Carlo predictions are consistent with our measurement of jet shape observables and fragmentation distributions from proton–proton collisions at centre of mass energy of 7 TeV. The *hump-backed plateau* is observed in the ξ distribution as predicted by QCD coherence and its behaviour is in a qualitative agreement with theoretical calculations. Our observation of momentum dependence of jet collimation is consistent with Monte Carlo predictions within uncertainties for both direct and indirect measurements.

Acknowledgement

This work was supported by Grant Agency of the Czech Technical University in Prague, grant SGS13/215/OHK4/3T/14, and by Ministry of Education of the Czech Republic, grant LG 13031.

References

[1] The ALICE Collaboration et al 2008 JINST 3 S08002.

[2] M. Cacciari, G. P. Salam, Phys. Lett. B **641**, 57 (2006).

[3] M. Cacciari, G. P. Salam, G. Soyez, JHEP **04**, 63 (2008).

[4] G. D'Agostini, Nucl. Inst. Meth. A **362**, 487 (1995).

[5] T. Adye, arXiv:1105.1160 [physics.data-an].

[6] A. Höcker, V. Kartvelishvili, Nucl. Inst. Meth. A **372**, 469 (1996).

[7] T. Sjostrand, S. Mrenna, P.Z. Skands, JHEP **05**, 026 (2006).

[8] P. Z. Skands, Phys. Rev. D **82**, 074018 (2010).

[9] ATLAS Collaboration, ATLAS-CONF-2010-031 (2010).

[10] G. Marchesini et al., Computer Physics Communications **67**, 465 (1992).

[11] G. Corcella et al., JHEP **0101**, 010 (2001).

[12] G. Aad *et al.* (ATLAS Collaboration), Phys. Rev. D **84**, 054001 (2011).

[13] B. I. Ermolayev, V. S. Fadin, JETP Lett. **33**, 285 (1981);
A. H. Mueller, Phys. Lett. B **104**, 161 (1981).

[14] Y. L. Dokshitzer, S. Troyan, Proc. XOX winter School of the LNPI, 1984, Vol. I, p. 144.

Study of jet properties in p+p collisions at $\sqrt{s} = 7$ TeV and p+Pb collisions at $\sqrt{s} = 5.02$ TeV using POWHEG-Box framework

Michal Vajzer[1,2]

[1] *michal.vajzer@cern.ch, Nuclear Physics Institute ASCR, Na Truhlarce 39/64, 180 86 Praha 8, Czech Republic*
[2] *michal.vajzer@fjfi.cvut.cz, FNSPE CTU in Prague, Břehová 7, 115 19 Praha 1, Czech Republic*

Abstract. In this contribution, next-to-leading order (NLO) simulations of jet production are presented. These simulations are carried out using POWHEG-Box framework [1], implementation of POWHEG next-to-leading-order generator, with parton showering provided by PYTHIA8 [2]. We focus on p+p collisions with centre of mass energy of 7 TeV and p+Pb collisions at 5.02 TeV, where we study jet production cross sections and ratio of jet spectra reconstructed in different collisions systems. Parton distributions considering effects of heavy ions are implemented using nuclear parton distribution functions (nPDFs) such as HKN07 [3] and using nuclear modification factors provided in EPS09 [4]. Jet reconstruction is done using anti-k_T algorithm included in FastJet package [5].

1 Introduction to jets

When a parton, a quark of gluon, is created with sufficient energy, it undergoes a complex evolution that produces a lot of final state particles. In theory jet is this final state of such parton, however, in experiment there is no information about the origin of particles, only spray of collinear particles are observed. The jet algorithm is then applied to reconstruct the jet and it has to produce consistent results.

The jet evolution can be theoretically described using to hadron production factorisation. Individual stages of evolution happen at different energy scales and therefore can be calculated separately and combined.

2 Analysis overview

In the analysis presented here, POWHEG-Box framework was used. It is based on a next-to-leading order momentum ordered processes. As an input, it uses PDF parametrisation described by CTEQ6.6 [6]. The output of POWHEG-Box are only particles involved in hard scatterings and these have to undergo further parton shower evolution. For this purpose PYTHIA8, monte-carlo event generator, has been used. It produces final state particles for given hard processes, which are subsequently analysed by anti-k_T jet algorithm, standard algorithm used by the LHC experiments, from FastJet package.

Main sources of systematic uncertainties in jet production in the described setup originate from variation of renormalisation and factorisation scales in the process generation itself, 13% uncertainty and from parametrisations of PDFs and nPDFs, approx. 6%.

3 Jet spectra in p+p at 7 TeV collisions

Figure 1 shows comparison between fully corrected jet cross section reconstructed from charged tracks only by the ALICE collaboration [7] and results of simulation with analysis setup described in Sec. 2 with cuts following those used in real data analysis for several values of resolution parameter, R, which describes area of the jet. Good agreement between data and simulation is observed. This serves as a baseline for further analyses.

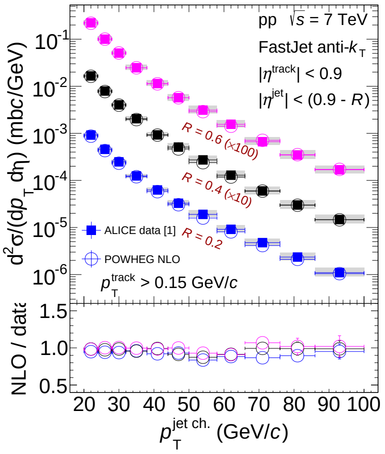

Figure 1. Jet spectra reconstructed using anti-k_T algorithm as obtained by ALICE (full squares) and by NLO simulations (open circles).

4 Jets in p+Pb at 5.02 TeV collisions

The study of p+Pb collisions provides information about cold nuclear effects or initial state effects that can be further used to improve understanding of medium before collisions and differentiate effects due to cold and hot media in heavy-ion collisions. To account for lead nuclei in the simulation framework, the PDF of second colliding proton has to be changed. This can be either directly to nuclear PDF, such as HKN07, or by using modification factors on already existing proton PDFs as in case of EPS09, both options are considered.

In order to observe changes in jet spectra with respect to the changed type of colliding particles, variable $R_{\mathrm{p+Pb}}$ is defined as a ratio of jet cross section in p+Pb collisions with respect to baseline of p+p collision at same centre of mass energies scaled by number of binary collisions. Figure 2 are R_{pPb} for different resolution parameters of reconstructed anti-k_{T} jets for both HKN07 and EPS09 nPDFs. The second one is systematically above 1, however, all results plotted are consistent with observation made by the ALICE collaboration [8].

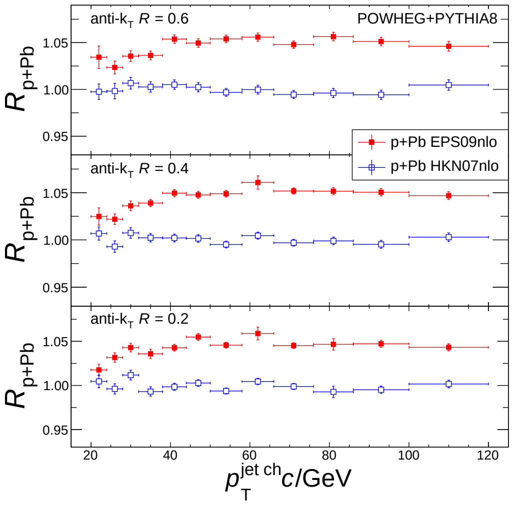

Figure 2. Ratio of jet spectra in p+Pb collisions with respect to p+p baseline for various resolution parameters.

5 Measrements using Bjorken's x

Variables x_1 and x_2 describe fraction of energy carried by partons in colliding nuclei with respect to the energy of these ions. They can be obtained directly from hard scattering simulation information. Additionally, they can be obtained from information of scattered hadronized partons in leading order processes. However, in the NLO processes the leading jets reconstructed in acceptance range of $-4.5 < y < 4.5$ are used with resolution parameter of 0.2. In order to calculate x_1 and x_2, formulae

$$x_1 = \frac{p_{\mathrm{T}}}{\sqrt{s}}\left(e^{y_3} + e^{y_4}\right), x_2 = \frac{p_{\mathrm{T}}}{\sqrt{s}}\left(e^{-y_3} + e^{-y_4}\right),$$

are used, where y_3 and y_4 represents rapidity of leading and subleading jet, respectively and p_{T} is transverse momentum of leading jet.

As seen in Figure 3, where ratio of extracted differential spectra as a function of x_1 or x_2 in p+Pb collisions with respect to p+p case, similarly to the Sec. 3, information obtained from jets is consistent with direct information from simulation in wide range of x and there is no apparent modification of PDF as function of x_1, which is trued as this represents unchanged distributions function of proton.

In case of ion modified to account for lead, enhanced probability is observed at values of $x_2 \approx 0.1$ and followed by suppression of probability for smaller values of x_2. This is consistent with overall picture presented in [9].

6 Summary

Presented results show very good agreement between data and simulation in p+p collisions at $\sqrt{s} = 7$ TeV. Modification of analysis to account for p+Pb collisions has shown that there is no apparent modification of jet cross section which is validated by results from the LHC experiments. Study of jets with respect to extracted values of x_1 and x_2 have shown that these jets can be used to observe changes in PDFs of heavy ions with respect to protons, however, these changes are integrated over all the parton types and over the whole range of Q^2 in hard scattering. Additionally, wide rapidity range had to be used to investigate big values of $x_{1,2}$ as possible.

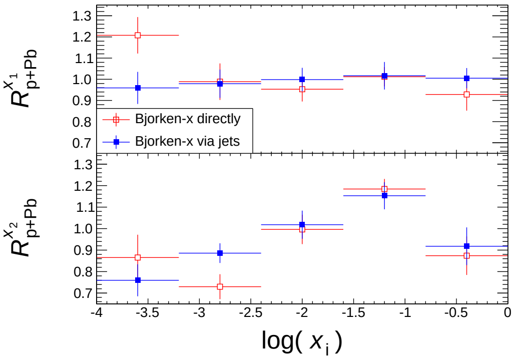

Figure 3. Modification of obtained PDFs in p+Pb collisions with respect to p+p case as a function of $x_{1,2}$.

7 Acknowledgement

This work was supported by the MEYS grant CZ.1.07/2.3.00/20.0207 of the European Social Fund in the Czech Republic: Education for Competitiveness Operational Programme, by the German Academic Exchange Service by the grant A/13/91563, by the grant LG 13031 of the Ministry of Education of the Czech Republic and by the Grant Agency of the CTU in Prague, grant SGS13/215/OHK4/3T/14.

References

[1] S. Alioli, *et al.*, JHEP **1104** (2011) 081.
[2] T. Sjostrand, *et al.*, Comp. Phys. Com. **178** (2008) 852.
[3] M. Hirai, *et al.*, Phys. Rev. C **76** (2007) 065207.
[4] K. J. Eskola, *et al.*, JHEP **0904** (2009) 065.
[5] M. Cacciari, *et al.*, Eur. Phys. J. C **72** (2012) 1896.
[6] P. M. Nadolsky, *et al.*, Phys. Rev. D **78** (2008) 013004.
[7] M. Vajzer (ALICE collab.), PoS EPS-HEP 2013 (2013) 464.
[8] J. F. Grosse-Oetringhaus (ALICE collab.), arXiv:1408.0414.
[9] C. A. Salgado, *et al.*, J. Phys. G **39** (2012) 015010.

EUROPEAN ORGANIZATION FOR NUCLEAR RESEARCH

CERN-PH-EP-2014-254
08 October 2014

Charged jet cross sections and properties in proton-proton collisions at $\sqrt{s}$ = 7 TeV

ALICE Collaboration*

Abstract

The differential charged jet cross sections, jet fragmentation distributions, and jet shapes are measured in minimum bias proton-proton collisions at centre-of-mass energy $\sqrt{s} = 7$ TeV using the ALICE detector at the LHC. Jets are reconstructed from charged particle momenta in the mid-rapidity region using the sequential recombination k_{T} and anti-k_{T} as well as the SISCone jet finding algorithms with several resolution parameters in the range $R = 0.2 - 0.6$. Differential jet production cross sections measured with the three jet finders are in agreement in the transverse momentum (p_{T}) interval $20 < p_{\mathrm{T}}^{\mathrm{jet,ch}} < 100$ GeV/c. They are also consistent with prior measurements carried out at the LHC by the ATLAS collaboration. The jet charged particle multiplicity rises monotonically with increasing jet p_{T}, in qualitative agreement with prior observations at lower energies. The transverse profiles of leading jets are investigated using radial momentum density distributions as well as distributions of the average radius containing 80% ($\langle R_{80}\rangle$) of the reconstructed jet p_{T}. The fragmentation of leading jets with $R = 0.4$ using scaled p_{T} spectra of the jet constituents is studied. The measurements are compared to model calculations from event generators (PYTHIA, PHOJET, HERWIG). The measured radial density distributions and $\langle R_{80}\rangle$ distributions are well described by the PYTHIA model (tune Perugia-2011). The fragmentation distributions are better described by HERWIG.

---

*See Appendix A for the list of collaboration members

1 Introduction

Jets consist of collimated showers of particles resulting from the fragmentation of hard (high momentum transfer Q) partons (quarks and gluons) produced in high energy collisions. The production cross sections of jets were measured in detail in proton-antiproton (p$\bar{\text{p}}$) collisions at the Tevatron ($\sqrt{s}$ = 540 GeV, 630 GeV, 1.8 TeV and 1.96 TeV) [1–8]. Measurements were also carried out recently at the CERN LHC at higher energies ($\sqrt{s}$ = 2.76, 7 and 8 TeV) in proton-proton (pp) collisions [9–13]. Jet shape observables were previously measured by the CDF [14–16], and D0 [17] collaborations in p$\bar{\text{p}}$ collisions and more recently by the ATLAS and CMS collaborations in pp collisions [18–20]. The fragmentation functions of jets produced in p$\bar{\text{p}}$ collisions were reported by the CDF collaboration [21]. Jet fragmentation in pp and Pb–Pb collisions at the LHC were reported by the ATLAS [9, 22, 23] and CMS [24] collaborations. Jet production in e^+e^-, ep, p$\bar{\text{p}}$, and pp collisions is well described by perturbative Quantum Chromodynamics (pQCD) calculations. The measured jet properties are typically well reproduced by Monte Carlo (MC) generators such as PYTHIA [25], HERWIG [26, 27], and PHOJET [28]. The unprecedented beam energy achieved at the Large Hadron Collider (LHC) in pp collisions enables an extension of jet production cross section and property measurements carried out at lower energies. Such measurements enable further tests of QCD and help in tuning of MC event generators.

In this paper, we present measurements of the jet production cross sections, jet fragmentation distributions, and transverse jet shape observables in pp collisions at $\sqrt{s}$ = 7 TeV. The analysis is restricted to charged particle jets, i.e. jets reconstructed solely from charged particle momenta, hereafter called charged jets. ALICE has already reported measurements of charged jet production in Pb–Pb collisions at 2.76 TeV [29]. Charged jets are reconstructed with particles having p_T down to values as low as 0.15 GeV/c, thereby allowing to test perturbative and non-perturbative aspects of jet production and fragmentation as implemented in MC generators. The measured particle spectra in jets reflect the jet fragmentation function, as summarized in [30] (Sec. 19). The jet shape distributions are related to the details of the parton shower process.

Jets also constitute an important probe for the study of the hot and dense QCD matter created in high energy collisions of heavy nuclei. In such collisions, large p_T partons penetrate the colored medium and lose energy via induced gluon radiation and elastic scattering (see [31] and references therein). The measurements in pp collisions thus provide a baseline for similar measurements in nucleus–nucleus (A–A) and proton-nucleus (p–A) collisions.

Medium modifications of the parton shower may change the fragmentation pattern relative to the vacuum [32]. There are empirical indications [33] that the scale relevant to these effects is given by the medium temperature of the order of few hundred MeV rather than the hard scattering scale. At such small particle momenta, the jets measured experimentally in pp and A–A collisions also contain contributions from the underlying event (UE). In pp collisions [15], the UE includes gluon radiation in the initial state, the fragmentation of beam remnants and multiple parton interactions. In this study, we subtract the UE from the distributions measured in pp collisions, to allow for a meaningful comparison to models, because theoretical modeling of the underlying event is very complex. To disentangle UE and hard parton fragmentation into low momentum particles, we correct our measurements using a technique similar to that applied in [21], described in Sec. 6.4. This approach will also help to make eventually a comparison with data from A–A collisions, where the UE in addition includes hadrons from an expanding fireball.

This paper is organized as follows. Section 2 describes the experiment and detectors used for the measurements reported in this work. Details of the jet reconstruction algorithms and parameters are presented in Sec. 3, while jet observables are defined and discussed in Sec. 4. Section 5 discusses the MC simulations carried out for comparisons of measured data to models, data corrections for instrumental effects, and systematic error studies. The procedures applied to correct for instrumental effects are presented in Sec. 6. The methods used to evaluate systematic uncertainties of the measurements are discussed in Sec. 7. Results are presented and discussed in comparison with MC Event Generator simulations in Sec. 8. Section 9 summarizes the results and conclusions of this work.

2 Experimental setup and data sample

The data used in this analysis were collected during the 2010 LHC run with the ALICE detector [34]. This analysis relies primarily on the Time Projection Chamber (TPC) [35], the Inner Tracking System (ITS) [36], and the V0 [37] sub-detectors. The V0 and ITS are used for event selection. A minimum bias trigger is achieved by requiring at least one hit in either the V0 forward scintillators or in the two innermost Silicon Pixel Detector layers (SPD) of the ITS, in coincidence with an LHC bunch crossing. The efficiency for detecting inelastic events is about 85% [38]. The TPC and ITS are used for primary vertex and track reconstruction. Only events with a primary vertex within ±10 cm along the beam direction from the nominal interaction point are analyzed to minimize dependencies of the TPC acceptance on the vertex position. The results reported in this paper are based on 177×10^6 minimum bias events corresponding to an integrated luminosity [38] of (2.9 ± 0.1) nb^{-1}.

The ALICE solenoidal magnet is operated with a magnetic field of 0.5 T that provides a good compromise between momentum resolution at high p_{T} and detection of low p_{T} particles. Charged tracks are reconstructed using the combined information from the TPC and the ITS utilizing a hybrid reconstruction technique described in [13] to assure uniform φ distribution. The acceptance for charged tracks is $|\eta| <0.9$ over the full azimuth. This hybrid technique combines two distinct track classes: (i) tracks containing at least three hits (of up to six) in the ITS, including at least one hit in the SPD, and (ii) tracks containing fewer than three hits in the ITS, or no hit in the SPD. The momentum of tracks of class (i) is determined without a vertex constraint. The vertex constraint is however added for tracks of class (ii) to improve the determination of their transverse momentum. The track momentum resolution $\delta p_{\mathrm{T}}/p_{\mathrm{T}}$ is approximately 1% at p_{T} = 1 GeV/c for all reconstructed tracks, and 4% at p_{T} = 40 GeV/c for 95% of all tracks. For tracks without a hit in the ITS (5% of the track sample) the resolution is 7% at p_{T} = 40 GeV/c. The analysis is restricted to tracks with a Distance of Closest Approach (DCA) to the primary vertex smaller than 2.4 cm and 3.2 cm in the plane transverse to the beam and the beam direction, respectively, in order to suppress contributions from secondary particles produced by weak decays and interactions of primary particles with detector materials and beam pipe.

Tracks in the TPC are selected by requiring a p_{T} dependent minimum number of space points ranging from 70 (of up to 159) for p_{T} = 0.15 GeV/c to 100 at $p_{\mathrm{T}} > 20$ GeV/c. A χ^2 cut on the track fit is applied. Secondary particles which are not produced at the primary vertex may acquire a wrong momentum when constrained to the vertex. Therefore, a χ^2 cut on the difference between the parameters of the track fit using all the space points in the ITS and TPC and using only the TPC space points with the primary vertex position as an additional constraint is applied. The track reconstruction efficiency for primary charged particles is approximately 60% at p_{T} = 0.15 GeV/c and rises to a value of about 87% at 1 GeV/c and is approximately uniform up to 10 GeV/c beyond which it decreases slightly. The efficiency is uniform in azimuth and within the pseudorapidity range $|\eta| < 0.9$. Further details on the track selection procedure and tracking performance can be found in [13].

3 Jet reconstruction

The charged jet reconstruction is carried out using the infrared-safe and collinear-safe sequential recombination algorithms anti-k_{T} [39] and k_{T} [40, 41] from the FastJet package [42] and a seedless infrared safe iterative cone based algorithm, named SISCone [43] to obtain the jet cross sections. The three jet finders are found to be in good agreement within the uncertainties as discussed in Sec. 8.1. All other observables (as discussed in Sec. 4) are analyzed with anti-k_{T} only. Charged tracks with $p_{\mathrm{T}} > 0.15$ GeV/c and within

$|\eta| < 0.9$ are the inputs to the jet reconstruction algorithms. A boost invariant p_{T} recombination scheme is used to determine the transverse momenta of jets by adding the charged particle transverse momenta. Jets are reconstructed with resolution parameters R = 0.2, 0.3, 0.4, and 0.6 to enable a systematic study of the production cross section and shape properties, as well as to provide a suite of references for measurements performed in p–A and A–A collisions. The analyses reported in this work are restricted to jets detected within the range $|\eta| <$ (0.9 - R) in order to minimize edge effects in the reconstruction of jets and biases on jet transverse profile and fragmentation functions. The inclusive jet cross sections are reported as a function of p_{T} in the interval $20 < p_{\mathrm{T}}^{\mathrm{jet,ch}} < 100$ GeV/c. The properties of the charged jet with the highest p_{T} in the event, the so called *leading jet*, are presented in the same p_{T} interval.

4 Jet observables

The results are reported for a suite of charged jet properties including inclusive differential jet cross section, charged particle multiplicity in leading jets ($\langle N_{\mathrm{ch}}\rangle$), leading jet size ($\langle R_{80}\rangle$), radial distribution of p_{T} within the leading jet ($\langle \mathrm{d}p_{\mathrm{T}}^{\mathrm{sum}}/\mathrm{d}r\rangle$), and jet fragmentation distributions ($F^{p_{\mathrm{T}}}$, F^{z}, F^{ξ}). The definition of these observables and the methods used to measure them are presented in this section. Correction techniques applied to measured raw distributions to account for instrumental effects (including the detector acceptance and resolution), as well as the UE, are discussed in Sec. 6. All observables reported in this work are corrected to particle level as defined in Sec. 5.

The differential jet cross section is evaluated using the following relation:

$$\frac{\mathrm{d}^2\sigma^{\mathrm{jet,ch}}}{\mathrm{d}p_{\mathrm{T}}\mathrm{d}\eta}(p_{\mathrm{T}}^{\mathrm{jet,ch}}) = \frac{1}{\mathscr{L}^{\mathrm{int}}}\frac{\Delta N_{\mathrm{jets}}}{\Delta p_{\mathrm{T}}\Delta\eta}(p_{\mathrm{T}}^{\mathrm{jet,ch}}), \tag{1}$$

where $\mathscr{L}^{\mathrm{int}}$ is the integrated luminosity and ΔN_{jets} the number of jets in the selected intervals of Δp_{T} and $\Delta\eta$.

The charged particle multiplicity in leading jets, N_{ch}, is defined as the number of charged particles found within the leading jet cone. Results for the mean charged particle multiplicity, $\langle N_{\mathrm{ch}}\rangle$, computed in bins of jet p_{T} are presented for resolution parameter values R = 0.2, 0.4, and 0.6.

The size of the leading jet, R_{80}, is defined as the radius in the $\Delta\eta$ – $\Delta\varphi$ space that contains 80% of the total p_{T} found in the jet cone. Results for the mean value, $\langle R_{80}\rangle$, are presented as a function of jet p_{T} for resolution parameter values R = 0.2, 0.4, and 0.6.

The distribution of p_{T} density, $\mathrm{d}p_{\mathrm{T}}^{\mathrm{sum}}/\mathrm{d}r$, within a leading jet is measured as a function of the distance $r = \sqrt{(\Delta\eta)^2 + (\Delta\varphi)^2}$ from the jet direction. The momentum density is calculated jet by jet as a scalar sum of the transverse momenta, $p_{\mathrm{T}}^{\mathrm{sum}}$, of all charged particles produced in annular regions of width Δr at radius r centered on the jet direction. The mean value of the momentum density, $\langle \mathrm{d}p_{\mathrm{T}}^{\mathrm{sum}}/\mathrm{d}r\rangle$, is evaluated as a function of r using the following relation:

$$\langle\frac{\mathrm{d}p_{\mathrm{T}}^{\mathrm{sum}}}{\mathrm{d}r}\rangle(r) = \frac{1}{\Delta r}\frac{1}{N_{\mathrm{jets}}}\sum_{\mathrm{i}=1}^{N_{\mathrm{jets}}} p_{\mathrm{T}}^{\mathrm{i}}(r-\Delta r/2, r+\Delta r/2) \tag{2}$$

where $p_{\mathrm{T}}^{\mathrm{i}}(r-\Delta r/2,\mathrm{r}+\Delta r/2)$ denotes the summed p_{T} of all tracks of jet i, inside the annular ring between $r-\Delta r/2$ and $r+\Delta r/2$. The mean value is reported in bins of jet p_{T} for resolution parameter values R = 0.2, 0.4, and 0.6. N_{jets} denotes the number of jets per bin.

The fragmentation of the leading jet is reported based on the distributions

$$F^{p_{\mathrm{T}}}(p_{\mathrm{T}}, p_{\mathrm{T}}^{\mathrm{jet,ch}}) = \frac{1}{N_{\mathrm{jets}}}\frac{\mathrm{d}N}{\mathrm{d}p_{\mathrm{T}}}, \tag{3}$$

$$F^z(z^{\mathrm{ch}}, p_{\mathrm{T}}^{\mathrm{jet,ch}}) = \frac{1}{N_{\mathrm{jets}}}\frac{\mathrm{d}N}{\mathrm{d}z^{\mathrm{ch}}}, \tag{4}$$

$$F^{\xi}(\xi^{\mathrm{ch}}, p_{\mathrm{T}}^{\mathrm{jet,ch}}) = \frac{1}{N_{\mathrm{jets}}}\frac{\mathrm{d}N}{\mathrm{d}\xi^{\mathrm{ch}}}, \tag{5}$$

where N is the number of charged particles. The scaled p_{T} variables $z^{\mathrm{ch}} = p_{\mathrm{T}}^{\mathrm{particle}}/p_{\mathrm{T}}^{\mathrm{jet,ch}}$ and $\xi^{\mathrm{ch}} = \log(1/z^{\mathrm{ch}})$ are calculated jet by jet for each track. In contrast to the definition in [30], the energy carried by neutral particles is not contained in the jet momentum. The (scaled) p_{T} spectra of the jet constituents are normalized per jet and presented in bins of jet p_{T}. $F^{p_{\mathrm{T}}}$, F^z and F^{ξ} are complementary representations: the particle p_{T} spectra $F^{p_{\mathrm{T}}}$ are less sensitive to uncertainties in the jet energy scale and may be more suitable as a reference for future measurements in nuclear collisions than the standard representation F^z, whereas the F^{ξ} distributions emphasize fragmentation into low momentum constituents and are particularly suited to demonstrate QCD coherence effects [44, 45].

In this work, the averages $\langle N_{\mathrm{ch}}\rangle$, $\langle R_{80}\rangle$, and $\langle \mathrm{d}p_{\mathrm{T}}^{\mathrm{sum}}/\mathrm{d}r\rangle$ are referred to as jet shape observables (jet shapes) and $F^{p_{\mathrm{T}}}$, F^z and F^{ξ} as fragmentation distributions.

5 Monte Carlo simulations

Instrumental effects, such as the limited particle detection efficiency and the finite track momentum resolution, induce momentum dependent particle losses and impact the jet energy scale and structures of the observables reported in this work. The effect of the detector response is studied using the simulation of the ALICE detector performance for particle detection and jet reconstruction. Simulated events are generated with PYTHIA 6.425 [25] (tune Perugia-0 [46]) and the produced particles are transported with GEANT3 [47]. The simulated and real data are analyzed with the same reconstruction algorithms. Jets reconstructed based directly on the charged particle momenta produced by MC generators are hereafter referred to as *particle level* jets whereas those obtained after processing the generator outputs through GEANT and the ALICE reconstruction software are referred to as *detector level* jets. As the data are corrected for instrumental effects, their comparison with simulation is done at particle level only.

The detector response to simulated charged jets with $R = 0.4$ is illustrated in Fig. 1, showing on a jet-by-jet basis the probability distribution of the relative difference between the charged jet p_{T} at the particle level ($p_{\mathrm{T}}^{\mathrm{jet,particle}}$) and at the detector level ($p_{\mathrm{T}}^{\mathrm{jet,detector}}$). The probability distribution is shown for three different

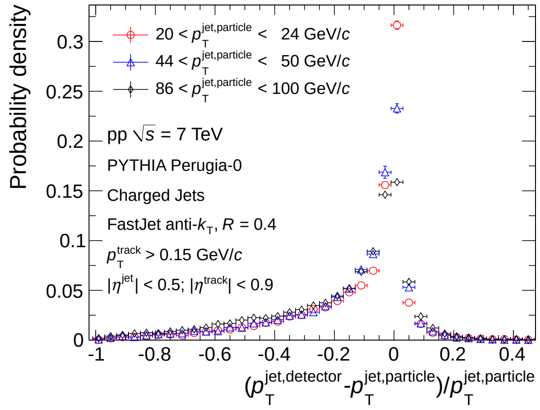

Fig. 1: (Color online) Probability distribution of the relative momentum difference of simulated ALICE detector response to charged jets in pp collisions at $\sqrt{s}$ = 7 TeV for three different $p_{\mathrm{T}}^{\mathrm{jet,particle}}$ intervals. Charged jets are simulated using PYTHIA Perugia-0 and reconstructed with the anti-k_{T} jet finding algorithm with $R = 0.4$.

$p_{\mathrm{T}}^{\mathrm{jet,particle}}$ intervals. The distributions have a pronounced maximum at zero ($p_{\mathrm{T}}^{\mathrm{jet,detector}} = p_{\mathrm{T}}^{\mathrm{jet,particle}}$). The tracking p_{T} resolution induces upward and downward fluctuations with equal probability, whereas the finite detection efficiency of charged particles results in an asymmetric response. The probability that $p_{\mathrm{T}}^{\mathrm{jet,detector}}$ is smaller than $p_{\mathrm{T}}^{\mathrm{jet,particle}}$ varies between 88 and 92% as function of $p_{\mathrm{T}}^{\mathrm{jet,particle}}$.

The event generators PHOJET 1.12.1.35 [28], HERWIG 6.510 [26, 27], and several PYTHIA tunes are used for comparisons to data and for systematic investigations of the sensitivity of the MC correction factors to variations of the detector response as well as to jet fragmentation and hadronization patterns. PYTHIA, PHOJET, and HERWIG utilize different approaches to describe the parton shower and hadronization process. HERWIG makes of angular ordering a direct part of the evolution process and thereby takes correctly into account coherence effects in the emission of soft gluons. PYTHIA 6.4 is instead based on transverse-momentum-ordered showers [48] in which angular ordering is imposed by an additional veto. Phojet generates angular ordered initial-state radiation, whereas for final state radiation the mass-ordered PYTHIA shower algorithm is used. Hadronization in PYTHIA and PHOJET proceeds via string breaking as described by the Lund model [49], whereas HERWIG uses cluster fragmentation. The PYTHIA Perugia tune variations, beginning with the central tune Perugia-0 [46], are based on LEP, Tevatron, and SPS data. The Perugia-2011 family of tunes [46] and the ATLAS Minimum Bias tune AMBT1 [50] belong to the first generation of tunes that also use LHC pp data at $\sqrt{s} = 0.9$ and 7 TeV with slight variations of the parameters controlling the modeling of the UE and fragmentation. Compared to the central Perugia-2011 tune, AMBT1 uses a lower value of the infrared regularization scale for multiple partonic interactions resulting in higher UE activity. It also uses a probability density of sum of two Gaussians for the matter distribution inside the proton and a higher non-perturbative color-reconnection strength for string fragmentation. The HERWIG generator version and PYTHIA tunes used in this work utilize the CTEQ5L parton distributions [51], except for PYTHIA tune AMBT1 which uses MRST 2007LO* [52]. PHOJET uses GRV94 [53].

6 Corrections

Two classes of correction techniques are used to account for instrumental effects in the measurements reported in this work. The techniques are known as bin-by-bin correction and Bayesian unfolding [54]. A third technique based on Singular Value Decomposition (SVD) [55] is also used as a cross check. The techniques and their comparative merits are presented in the following subsections. Corrections for contamination from secondary particles and UE are discussed in Secs. 6.3 and 6.4 respectively.

The jet shapes and fragmentation distributions are corrected using the bin-by-bin method, while the cross sections are corrected with the Bayesian unfolding technique. All observables are corrected for secondaries contamination. All observables, except $\langle R_{80} \rangle$, are also corrected for UE contamination.

6.1 Bin-by-bin correction method

The bin-by-bin correction method is used to correct the jet shape observables and fragmentation functions. To validate the method, it is also applied to the jet cross sections. It utilizes MC simulations as described in Sec. 5 and is based on ratios of values for observables obtained at particle (generator) level and detector level as a function of variable $\mathbf{x}$. In this work, $\mathbf{x}$ can be 1-dimensional (e.g. jet p_{T} in case of the jet spectra) or 2-dimensional (e.g. jet p_{T} and particle p_{T} in case of the fragmentation distributions). Let $O_{\mathrm{mc}}^{\mathrm{part}}(\mathbf{x})$ be the observable value at the particle level, and $O_{\mathrm{mc}}^{\mathrm{det}}(\mathbf{x})$ the value obtained at the detector level. The correction factors are defined as the ratio of the particle and detector level values of $O_{\mathrm{mc}}^{\mathrm{part}}(\mathbf{x})$ and $O_{\mathrm{mc}}^{\mathrm{det}}(\mathbf{x})$ in bins of $\mathbf{x}$. The corrected measurements, $O_{\mathrm{data}}^{\mathrm{corrected}}$, are obtained bin-by-bin by multiplying the raw (uncorrected) values, $O_{\mathrm{data}}^{\mathrm{uncorrected}}$, as follows,

$$O_{\mathrm{data}}^{\mathrm{corrected}}(\mathbf{x}) = O_{\mathrm{data}}^{\mathrm{uncorrected}}(\mathbf{x}) \frac{O_{\mathrm{mc}}^{\mathrm{part}}(\mathbf{x})}{O_{\mathrm{mc}}^{\mathrm{det}}(\mathbf{x})}. \tag{6}$$

The correction factors depend on the shape of the simulated jet spectrum and fragmentation distributions. Systematic uncertainties related to the accuracy with which data are reproduced by the simulations are discussed in Sec. 7.2.

Correction factors obtained for the jet p_{T} spectra range from 25% to 50% and reach a maximum at 100 GeV/c. The bin-by-bin corrections applied to jet shape observables include subtraction of contamination associated with the production of secondary particles within the detector. Correction factors obtained for $\langle N_{\mathrm{ch}} \rangle$ at $R = 0.2$ (0.4, 0.6) are of the order of 2-6% (3-5%, 4-6%) while for $\langle R_{80} \rangle$ at $R = 0.2$ (0.4, 0.6) they are found in the range 5-7% (2-10%, 4-9%). Correction factors applied on radial momentum densities have a maximum value of 12%(15%, 19%) at $R = 0.2$ (0.4, 0.6). In contrast, for the fragmentation distributions, the bin-by-bin correction and the correction for the contamination from secondaries, discussed in Sec. 6.3, are carried out in separate steps. The typical value of the corrections at the maximum of the F^{ξ} distribution is of the order of few percent only. The correction factors for $F^{p_{\mathrm{T}}}$ and F^{z} are largest at low particle p_{T} (up to 50%), where the tracking efficiency is smallest, and at the highest z^{ch} (up to 40%) where the impact of the track momentum resolution is strong and detector effects at the track level strongly influence the reconstructed jet momentum.

6.2 Unfolding using response matrix inversion techniques

Instrumental effects associated with acceptance, particle losses due to limited efficiency, and finite momentum resolution are modeled using a detection response matrix, which is used to correct observables for these effects. The jet p_{T} response matrix is determined by processing MC events through a full ALICE detector simulation as described in Sec. 5. The particle level (true), $T(t)$, and detector level (measured), $M(m)$, p_{T} spectra of the leading jet are both subdivided in 11 bins in the interval $20 < p_{\mathrm{T}}^{\mathrm{jet,ch}} < 100$ GeV/c. The matrix elements R_{mt} express the conditional probability of measuring a jet p_{T} in bin, m given a true value in bin, t. The measured distribution, M, can thus be estimated by multiplying the true distribution, T, by the response matrix,

$$M = RT. \tag{7}$$

Experimentally, the unfolding problem involves the determination of T given M. This is symbolically written as

$$T = R^{-1}M. \tag{8}$$

However the matrix R may be singular and can not always be inverted analytically. Consequently, other numerical techniques are needed to obtain the true, physically meaningful, distribution T given a measured distribution M. Furthermore, the exact solution, even if it exists, is usually unstable against small variations in the initial estimates of the measured distribution, and oscillating due to finite statistics in the measured distribution. This problem can be overcome using a regularization condition based on a priori information about the solution.

The Bayesian unfolding technique [54] is an iterative method based on Bayes' theorem. Given an initial hypothesis (a prior), P_t, with $t = 1, ..., n$, for the true momentum and reconstruction efficiency, ε_t, Bayes' theorem provides an estimator of the inverse response matrix elements, $\tilde{R}_{tm}$,

$$\tilde{R}_{tm} = \frac{R_{mt} P_t}{\varepsilon_t \sum_{t'} R_{mt'} P_{t'}}. \tag{9}$$

The measured distribution, M_m, is thus unfolded as follows

$$P'_t = \sum_m \tilde{R}_{tm} M_m, \tag{10}$$

to obtain a posterior estimator, P'_t, of the true distribution. The inversion is improved iteratively by recursively using posterior estimators to update and recalculate the inversion matrix. The number of iterations serves as a regularization parameter in the unfolding procedure. For jet spectra studies, the measured spectra are used as prior and convergence is obtained typically after three iterations.

As an additional cross check, the analysis of charged jet cross sections is also carried out with the RooUnfold implementation of the Singular Value Decomposition (SVD) unfolding technique [55, 56] using raw measured spectra as prior distributions. The performance of the Bayesian unfolding, SVD unfolding, and bin-by-bin correction methods are compared based on PYTHIA Perugia-0 simulated jets. The three methods produce results that are found to be within 4% of the truth distribution. The cross sections reported in this work are obtained with the Bayesian unfolding method.

6.3 Contamination from secondary particles

Charged secondary particles are predominantly produced by weak decays of strange particles (e.g. K^0_S and Λ), decays of charged pions, conversions of photons from neutral pion decays and hadronic interactions in the detector material. The charged jet transverse momentum, jet shapes and fragmentation distributions include by definition only primary charged jet constituents. Secondary particles introduce ambiguities in the jet energy scale and contribute to the raw reconstructed multiplicity, momentum density, and fragmentation distributions. Although their contribution is minimized by the analysis cuts described in Sec. 2, the measured distributions nonetheless must be corrected for a small residual contamination. The subtraction of the secondary particle contamination is implicitly included in the bin-by-bin correction applied for measurements of jet shape observables. It is however carried out separately and explicitly in the measurements of the fragmentation function. The contribution of secondaries is estimated from MC simulations, separately for each bin in jet p_{T} and particle p_{T}, z^{ch} and ξ^{ch}. The correction applied to the measured fragmentation functions is highest, up to 35%, at small p_{T} and large ξ^{ch}. It amounts to few percent only when averaged over all jet constituents. To enhance the low strangeness yield in the PYTHIA Perugia-0 simulations to the level observed in data, the contamination estimate is multiplied by a data-driven correction factor based on measurements [57] of strange particle production in non-single-diffractive events by the CMS collaboration and simulations from [58]. The contamination of secondaries from strange particle decays is small, and the effect of the strangeness scaling on the final result is less than 1%. No scaling is applied on the correction to the jet spectrum and jet shape observables.

6.4 Underlying event subtraction

There is no strict definition of the Underlying Event. Operationally, it corresponds to all particles produced in an event that are not an integral part of a jet or produced directly by hard scattering of partons. The ATLAS [59, 60], CMS [61] and ALICE [62] collaborations have already published studies of UE in pp collisions at $\sqrt{s}$ = 7 TeV. In this work, a similar method is adopted to determine the UE yield and correct the measured jet observables for this source of contamination.

The UE particle yield is estimated event-by-event based on circular regions perpendicular to the measured jet cones as in [21]. The circular regions have the same size as the jet resolution parameter and are placed at the same pseudorapidity as the leading jet but offset at an azimuthal angle $\Delta\varphi = \pi/2$ relative to the jet axis.

For the jet cross section measurements, the UE is subtracted on a jet-by-jet basis prior to unfolding and the same treatment is applied to jets obtained from simulations before jet response matrix is created.

In the case of the fragmentation and jet shape observables, no correction for the UE contribution to the reconstructed jet energy is applied, but the UE contribution to the measured distributions in each bin of jet p_{T} is subtracted. The p_{T} spectra of particles in the perpendicular cone are accumulated and averaged over many events. To account for variations of the cone size of the anti-k_{T} jets, the spectra are weighted jet by jet with the ratio of the cone size, determined by FastJet, to the nominal aperture of πR^2 for a jet with resolution parameter R. The difference between the weighted and unweighted UE distributions is at the level of 1%. The $\xi^{\rm ch}$ variable is computed jet-by-jet for each particle using the transverse momentum of the leading jet. The radial $p_{\rm T}$ sum distributions are obtained relative to the axis of the perpendicular cone.

The algorithms used for jet reconstruction are sensitive to statistical fluctuations of the particle density which are possibly enhanced by local variations of the detection efficiency and secondary particle production. This reconstruction bias may differ for the jet region and the UE region. Hence, the UE distributions are corrected first for tracking efficiency, resolution and contamination from secondary particles. The fully corrected distributions are then subtracted in bins of the leading jet transverse momentum. The correction is smaller than 2.5% of the charged jet energy, but it is considerable for the fragmentation distributions at the lowest track momentum and highest $\xi^{\rm ch}$, where the ratio of UE background to fragmentation signal takes values up to 2.5. No self-consistent technique exists to subtract the UE in the $\langle R_{80}\rangle$ measurements, these measurements are therefore reported without correction for UE contamination. However, comparing the radial $\langle {\rm d}p_{\rm T}^{\rm sum}/{\rm d}r\rangle$ distributions before and after UE subtraction, the increase in jet size $\langle R_{80}\rangle$ due to the UE is estimated to be of the order of few percent only. The systematic uncertainties for not performing the UE subtraction are thus found negligible compared to other sources of errors in the measurements of $\langle R_{80}\rangle$.

7 Estimation of systematic uncertainties

A summary of all systematic uncertainties for selected bins is given in Table 1 for the cross section measurements, and in Table 2 for the $\langle N_{\rm ch}\rangle$, $\langle R_{80}\rangle$, $\langle {\rm d}p_{\rm T}^{\rm sum}/{\rm d}r\rangle$, $F^{p_{\rm T}}$, $F^{p_{\rm T}}$ and F^{z} distributions. The uncertainties given in each column of the table are described in this section.

7.1 Tracking efficiency and resolution

Uncertainties associated with the momentum resolution and charged track reconstruction efficiency lead to systematic uncertainties in measurements of the jet cross section, jet shapes, and jet fragmentation functions.

The relative systematic uncertainty on tracking efficiency is estimated to be 5% based on several variations of cuts used in the track selection introduced earlier. The relative systematic uncertainty on the track momentum resolution amounts to 20% [63].

In order to evaluate the effect of these uncertainties on the measured jet cross sections, the corresponding rescaled response matrix is used to unfold the spectra. For the jet shape and fragmentation observables, the impact of the finite detector efficiency and momentum resolution on the bin-by-bin correction factors is estimated by applying parametrized detector response to PYTHIA events clustered with FastJet, and varying the efficiency and resolution independently. Systematic uncertainties for the jet particle multiplicity and jet shape observables are given in Table 2 for a resolution parameter $R = 0.4$. For larger (smaller) R, a moderate increase (decrease) of the uncertainties is observed related to tracking efficiency. For the fragmentation distributions, variations of the momentum resolution induce the most significant changes at high track $p_{\rm T}$. The systematic uncertainties due to the efficiency variations are largest at the highest $z^{\rm ch}$ and smallest at intermediate values.

7.2 Bin-by-bin correction

The data correction methods used in this work are largely based on tune Perugia-0 of the PYTHIA event generator. The particular structure of jets produced by PYTHIA might however conceivably affect the magnitude, and dependencies of the correction factors on the jet momentum, particle momentum, or radial dependence r. The possible impact of such event generator dependencies is examined by comparing the amplitude of the bin-by-bin corrections obtained with PYTHIA tunes Perugia-0 and Perugia-2011, with those obtained with the HERWIG generator. This is accomplished with a parametrized detector response and the anti-k_{T} jet finder. In addition, the impact of modifications of the jet fragmentation is studied by artificially duplicating and removing jet particles with a momentum dependent probability. The variations are constrained to be at a similar level as the differences observed between simulations and data reaching up to a factor of 2.5 for values of z^{ch} close to 1 in the fragmentation distributions. The charged particle multiplicity is affected by $\sim$30%. The resulting systematic uncertainties are largest for high values of z^{ch} and track p_{T} and small values of ξ^{ch}.

As an independent check, a closure test with a 2-dimensional folding technique is carried out on the fragmentation distributions from an inclusive jet sample (comprising leading and sub-leading jets). A response matrix in bins of generated and reconstructed jet p_{T} and particle (scaled) transverse momentum is used to fold the corrected results back to the uncorrected level. Since the folding method has negligible dependence on the event generator, the comparison of the folded to the original distributions reveals possible biases of the bin-by-bin correction. The observed non-closure at the level of few percent is consistent with the systematic uncertainty assigned to the bin-by-bin correction from modifications of the fragmentation pattern.

7.3 Response unfolding

The unfolding techniques used in this work correct the measured jet spectra for the detector response. The limited measurement resolution, discussed in Sec. 5, results in a small, but finite, probability for bin migration of the reconstructed jet momentum relative to the true value. Consequently, the unfolding introduces a correlation between neighbouring bins of the corrected spectrum, and statistical fluctuations in the measured data result in a spectral shape systematic uncertainty. To assess this uncertainty, the raw jet spectra are smeared by a Gaussian function with a width given by the statistical uncertainty in the given momentum bin. The resulting spectra are then unfolded and the systematic uncertainty is evaluated as a spread of the corrected spectra. The value of this systematic uncertainty increases roughly linearly with $p_{\mathrm{T}}^{\mathrm{jet,ch}}$, reaching a maximum value of $\sim$7% at $p_{\mathrm{T}}^{\mathrm{jet,ch}} \approx 100$ GeV/c.

7.4 Underlying event subtraction

In this work, we use perpendicular cones to measure and subtract the UE as described in Sec. 6.4. However, there is no unique prescription on how to determine the UE. In a prior, trigger hadron based, UE analysis by the ALICE collaboration [62], a geometrically different definition of the transverse region was used. The charged particle transverse momentum densities obtained in our analysis are consistent with the saturation values in the transverse region measured in [62]. In [64], the UE was estimated from dijet events and imposing an additional veto on a third jet. An alternative simulation to estimate and subtract the UE in a similar way is performed using particle level output from a MC event generator. The UE is measured from events with a dijet in the detector acceptance, to understand if and how the non-leading jet affects the UE estimate, rejecting events with additional charged jets with a p_{T} exceeding 8 GeV/c. The resulting difference on the fragmentation distributions is used to assign a 5% systematic uncertainty to the estimated UE. The resulting systematic uncertainty on the fragmentation distributions is highest at low transverse momenta. Systematic uncertainties on $\langle \mathrm{d}p_{\mathrm{T}}^{\mathrm{sum}}/\mathrm{d}r \rangle$ are largest at large distances r in the jet p_{T} interval 20 - 30 GeV/c. The uncertainty increases for higher values of the resolution parameter R. Systematic uncertainties on the measured charged jet cross sections are smaller than 1% and considered negligible.

The anti-k_{T} jet finder typically produces circular jet cones, and the UE contribution to the jet shapes and fragmentation distributions is evaluated consistently in circular cones. In individual jets, particles may however be added at a distance $r \geq R$ thereby giving rise to a convex deformation of the cone. Concave deformations might also occur. The dependence of the fragmentation distributions on the cone shape is checked by repeating the analysis using only tracks in an ideal cone around the jet axis. In this case no jet area scaling of the UE is applied. The low momentum particle yield is most affected: at high jet radii, low z^{ch} fragmentation dominates over high z^{ch} fragmentation. In addition, the probability to collect a soft particle from the UE is comparatively higher than at small r. The observed effect is negligibly small: a maximum depletion of 4% of the particle yield at the highest ξ^{ch} in the smallest jet momentum bin is observed. Considerably smaller variations are found for all other jet momenta and ξ^{ch} bins. The effect is reproduced in MC simulations, and no systematic uncertainty is associated to the jet cone shape.

7.5 Cross section normalization

The determination of luminosity and related systematic uncertainties are discussed in [65, 66]. A normalization uncertainty of 3.5% is assigned to the cross section measurement.

7.6 Contamination from secondary particles

The reconstructed primary particles originate from the main interaction vertex and have a non-zero distance of closest approach DCA because of finite resolution effects. The DCA of secondaries however spans a much broader range of values. Reducing the maximum allowed DCA value reduces contaminations from secondaries but also reduces the detection efficiency of primary particles. In this analysis, primary particles are selected requiring a small DCA as discussed in Sec. 2, and a correction for the residual contribution of secondary particles is applied, as explained in Sec. 6.3. The systematic uncertainty associated to the correction is estimated by reducing the maximum allowed DCA used in the selection of primary tracks by more than a factor of 9 using a p_{T} dependent cut. The resulting fragmentation distributions are corrected consistently for contamination and cut efficiency and residual differences in the fully corrected spectra are assigned as systematic uncertainty. The highest uncertainty is found for large values of ξ^{ch}.

The dependence of the correction on the strange particle yield in the PYTHIA Perugia-0 simulations is estimated from comparison to data as explained in Sec. 6.3. The effect on the jet cross sections is less than 3% and is assigned as systematic uncertainty. For the jet shape observables it is negligible.

Distribution	Bin (GeV/c)	Track eff. (%)	Track p_{T} res. (%)	Unfolding (%)	Normalization (%)	Sec. (%)	Total (%)
$\frac{d^2\sigma^{\mathrm{jet,ch}}}{dp_{\mathrm{T}}d\eta}$ ($R = 0.2$)	20-24	$^{+4.6}_{-4.2}$	4.0	3.0	3.5	1.9	$^{+7.8}_{-7.6}$
	50-58	$^{+22.1}_{-10.5}$	4.0	1.6	3.5	2.5	$^{+23.0}_{-12.2}$
	86-100	$^{+26.0}_{-15.3}$	4.0	5.2	3.5	2.8	$^{+27.1}_{-17.2}$
$\frac{d^2\sigma^{\mathrm{jet,ch}}}{dp_{\mathrm{T}}d\eta}$ ($R = 0.4$)	20-24	$^{+7.5}_{-4.5}$	4.0	3.0	3.5	2.1	$^{+9.9}_{-7.9}$
	50-58	$^{+23.2}_{-10.6}$	4.0	1.4	3.5	2.5	$^{+24.0}_{-12.2}$
	86-100	$^{+24.9}_{-15.0}$	4.0	5.6	3.5	2.7	$^{+26.2}_{-17.2}$
$\frac{d^2\sigma^{\mathrm{jet,ch}}}{dp_{\mathrm{T}}d\eta}$ ($R = 0.6$)	20-24	$^{+11.1}_{-5.3}$	4.0	6.6	3.5	2.3	$^{+14.2}_{-10.3}$
	50-58	$^{+22.6}_{-14.3}$	4.0	1.9	3.5	2.6	$^{+23.4}_{-15.6}$
	86-100	$^{+23.7}_{-13.7}$	4.0	6.0	3.5	2.7	$^{+25.1}_{-16.1}$

Table 1: Summary of systematic uncertainties for selected bins in selected cross section distributions

Distribution	Bin	Track eff. (%)	Track p_T res. (%)	Bin-by-bin corr. (%)	UE (%)	Sec. (%)	Total (%)
$\langle N_\mathrm{ch} \rangle$	20-25 GeV/c	$^{+5.8}_{-5.0}$	$^{+4.0}_{-3.5}$	$^{+0.7}_{-0.9}$	0.8	negligible	$^{+7.1}_{-6.2}$
	80-100 GeV/c	$^{+5.8}_{-5.0}$	$^{+4.0}_{-3.5}$	$^{+0.7}_{-0.9}$	0.5	negligible	$^{+7.1}_{-6.2}$
$\langle R_{80} \rangle$	20-25 GeV/c	$^{+6.1}_{-5.5}$	$^{+3.6}_{-4.3}$	$^{+1.7}_{-1.7}$	–	–	$^{+7.2}_{-7.2}$
	80-100 GeV/c	$^{+6.1}_{-5.5}$	$^{+3.6}_{-4.3}$	$^{+1.7}_{-1.7}$	–	–	$^{+7.2}_{-7.2}$
$\langle \frac{\mathrm{d}p_\mathrm{T}^\mathrm{sum}}{\mathrm{d}r} \rangle$ 20< $p_T^\mathrm{jet,ch}$ <30 GeV/c	0.00 - 0.04	$^{+8.1}_{-6.5}$	$^{+5.9}_{-2.4}$	$^{+2.9}_{-3.1}$	negligible	negligible	$^{+10.4}_{-7.5}$
	0.20 - 0.24	$^{+8.1}_{-6.5}$	$^{+5.9}_{-2.4}$	$^{+2.9}_{-3.1}$	0.3	negligible	$^{+10.5}_{-7.6}$
	0.36 - 0.40	$^{+8.1}_{-12.0}$	$^{+5.9}_{-2.4}$	$^{+2.9}_{-3.1}$	15.0	negligible	$^{+18.3}_{-19.6}$
$\langle \frac{\mathrm{d}p_\mathrm{T}^\mathrm{sum}}{\mathrm{d}r} \rangle$ 60< $p_T^\mathrm{jet,ch}$ <80 GeV/c	0.00 - 0.04	$^{+10.6}_{-5.1}$	$^{+5.6}_{-6.5}$	$^{+3.7}_{-3.4}$	negligible	negligible	$^{+12.6}_{-8.9}$
	0.20 - 0.24	$^{+10.6}_{-5.1}$	$^{+5.6}_{-6.5}$	$^{+3.7}_{-3.4}$	0.4	negligible	$^{+12.6}_{-9.0}$
	0.36 - 0.40	$^{+10.6}_{-5.1}$	$^{+5.6}_{-6.5}$	$^{+3.7}_{-3.4}$	1.6	negligible	$^{+12.7}_{-9.1}$
F^{p_T} 20< $p_T^\mathrm{jet,ch}$ <30 GeV/c	0 - 1 GeV/c	5.0	0.1	0.7	3.3	3.2	6.8
	6 - 7 GeV/c	0.8	negligible	2.3	negligible	0.5	2.4
	18 -20 GeV/c	9.9	0.5	6.0	negligible	0.4	11.6
F^{p_T} 60< $p_T^\mathrm{jet,ch}$ <80 GeV/c	0 - 5 GeV/c	5.2	0.3	0.2	0.8	2.1	5.7
	20 - 30 GeV/c	1.4	negligible	3.7	negligible	0.6	4.0
	50 - 60 GeV/c	10.5	3.5	9.6	negligible	0.6	14.6
F^{z} 20< $p_T^\mathrm{jet,ch}$ <30 GeV/c	0 - 0.1	4.7	1.6	0.2	1.6	1.4	5.2
	0.3 - 0.4	0.4	negligible	2.7	negligible	0.3	2.8
	0.9 - 1.0	15.5	1.1	4.8	negligible	0.6	16.3
F^{z} 60< $p_T^\mathrm{jet,ch}$ <80 GeV/c	0 - 0.1	5.0	0.3	0.3	0.7	1.3	5.3
	0.3 - 0.4	1.2	0.2	3.7	negligible	0.4	3.9
	0.8 - 1.0	13.8	3.1	6.1	negligible	1.2	15.4
F^{ξ} 20< $p_T^\mathrm{jet,ch}$ <30 GeV/c	0 - 0.4	9.9	0.5	4.6	negligible	0.7	10.9
	0.8 - 1.2	0.6	negligible	3.0	negligible	0.5	3.1
	4.8 - 5.3	5.1	0.7	0.9	15.3	7.8	17.9
F^{ξ} 60< $p_T^\mathrm{jet,ch}$ <80 GeV/c	0 - 1.0	5.0	0.5	3.9	negligible	0.7	6.4
	1.0 - 2.0	1.3	0.4	3.4	negligible	0.6	3.8
	5.0 - 6.2	5.7	0.2	0.7	6.5	6.2	10.6

Table 2: Summary of systematic uncertainties for selected bins in selected jet shape and fragmentation distributions for $R = 0.4$.

8 Results

8.1 Comparison of jet finding algorithms

Figure 2 (top panel) shows the differential cross sections of charged jet production measured in pp collisions at $\sqrt{s}$ = 7 TeV using the k_{T}, anti-k_{T}, and SISCone jet finding algorithms. The distributions are obtained with a resolution parameter, R = 0.4, for jets in the pseudorapidity range $|\eta^{\mathrm{jet}}| < 0.5$, and transverse momenta from 20 to 100 GeV/c. The bottom panel of the figure displays the ratios between the cross sections obtained with the k_{T}, and SISCone algorithms to those obtained with the anti-k_{T} as a function of the jet transverse momentum. For a correct treatment of statistical correlations between the numerator and denominator, the data were divided into fully correlated and uncorrelated subsets. The distributions are corrected using the bin-by-bin correction procedure described in Sec. 6.1. The ratios of the jet cross sections are consistent with unity over nearly the entire range of jet transverse momenta spanned by this analysis. A significant deviation of 5% is observed only in the lowest p_{T} bin ($p_{\mathrm{T}}^{\mathrm{jet,ch}}$ = 20-24 GeV/c) between the SISCone and anti-k_{T} algorithms. For larger $p_{\mathrm{T}}^{\mathrm{jet,ch}}$ SISCone and k_{T} algorithms agree within errors with the anti-k_{T} algorithm.

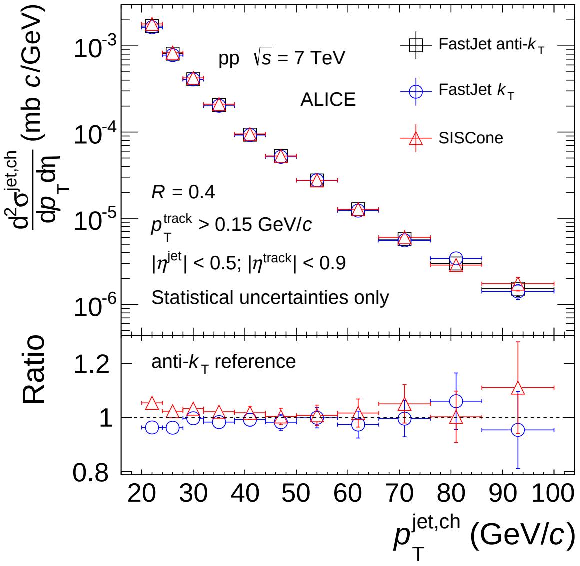

Fig. 2: (Color online) Top panel: Charged jet cross sections in pp collisions at $\sqrt{s}$ = 7 TeV. Symbols correspond to different algorithms used for jet reconstruction. Bottom panel: Ratios between jet cross sections obtained by k_{T}, and SISCone to that obtained by anti-k_{T}.

The anti-k_{T} algorithm initiates particle clustering around the highest p_{T} particles of an event. In contrast, the k_{T} algorithm initiates jet finding by clustering particles with the lowest momenta. It is thus rather sensitive to events with a large, fluctuating density of low momentum particles as produced in A–A collisions. The anti-k_{T} algorithm does not exhibit such sensitivity and is thus favored for studies of jet production in A–A collisions. Since there are no large differences observed between the spectra obtained with the three jet finders discussed above, and considering the fact that the results of this work will be used as a reference for similar measurements in A–A and p–A collisions, the remainder of the analyses presented in this work are performed with the anti-k_{T} algorithm exclusively.

8.2 Charged jet cross section

Figure 3 presents the fully corrected inclusive charged jet cross section measured in pp collisions at $\sqrt{s}$ = 7 TeV using the anti-k_{T} jet finder. Corrections for the detector response and instrumental effects are carried out using the Bayesian unfolding method presented in Sec. 6.2. The distributions are also cor-

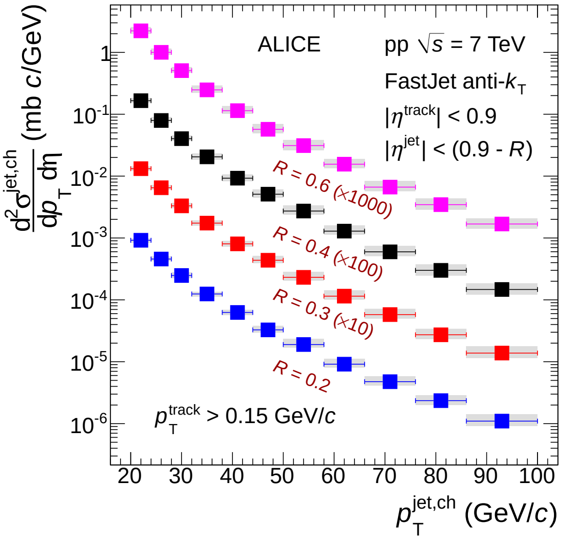

Fig. 3: (Color online) Inclusive charged jet cross sections in pp collisions at $\sqrt{s} = 7$ TeV using the anti-k_T algorithm with $R = 0.2$ (0.3, 0.4, and 0.6) within $\left|\eta^{jet}\right| \leq 0.7$ ($\left|\eta^{jet}\right| \leq 0.6$, $\left|\eta^{jet}\right| \leq 0.5$, and $\left|\eta^{jet}\right| \leq 0.3$).

rected for UE contamination on an event-by-event basis according to the method described in Sec. 6.4. Inclusive charged jet cross sections are reported for resolution parameter values $R = 0.2$, 0.3, 0.4 and 0.6, and limited to pseudorapidity ranges $|\eta| < (0.9 - R)$ in order to avoid losses due to partially reconstructed jets at the edge of the pseudorapidity acceptance. Statistical uncertainties are displayed as vertical error bars. Individual sources of systematic uncertainties are p_T dependent. In Fig. 3 as well as in all other figures the data points are placed at the bin centre along the abscissa and the horizontal error bars indicate the bin width while the vertical error bars indicate the statistical uncertainties. The total systematic uncertainties are obtained as a quadratic sum of individual systematic uncertainties, as described in Sec. 7, and are shown as shaded bands around the data points in Fig. 3 as well as in all other figures.

The measured charged jet cross sections are compared to those reported by the ATLAS experiment [9] at $R = 0.4$ and 0.6 in Fig. 4. The ATLAS charged jets are measured in the rapidity $|y| \leq 0.5$ at both $R = 0.4$ and 0.6, using charged tracks with $p_T \geq 0.3$ GeV/c without underlying event subtraction. The ALICE therefore also uses the same track p_T selection without underlying event subtraction unlike Fig. 3. To quantify the level of agreement between the ALICE and ATLAS jet cross section measurements, the ALICE data are fitted with a modified Tsallis [67, 68] distribution ($f(p_T) = a \cdot \left(1 + \frac{p_T}{b}\right)^{-c}$). The Tsallis fits are shown as dotted black curves in the top panels of Fig. 4. The χ^2/dof of the fits are 2.97/8 and 4.27/8 for $R = 0.4$ and 0.6 respectively. The bottom panels of Fig. 4 show the ratios of the ALICE and ATLAS data points to the fit function. The gray bands represent the systematic uncertainties on ALICE data points. Despite fluctuations in the high p_T range of the ATLAS data, both datasets are in excellent agreement.

In the top panels of Fig. 5, the measured charged jet cross sections are compared to predictions from PYTHIA (tunes Perugia-0, Perugia-2011, and AMBT1), PHOJET, and HERWIG for $R = 0.2$, 0.4 and 0.6. The ratios of the MC simulations to measured data are shown in the bottom panels of Fig. 5. In the high p_T range, PYTHIA Perugia-2011 describes the data best, while in the low p_T range data is best described by HERWIG and PHOJET. All PYTHIA tunes systematically overestimate the measured data in the low transverse momentum range and the discrepancy increases with increasing cone size. The worst discrepancy with the data is observed for the PYTHIA tune AMBT1, which overestimates the data by factors ranging from 25% to 75% over the studied p_T range for $R = 0.2$. The disagreement grows with increasing resolution parameter, and is worst for $R = 0.6$.

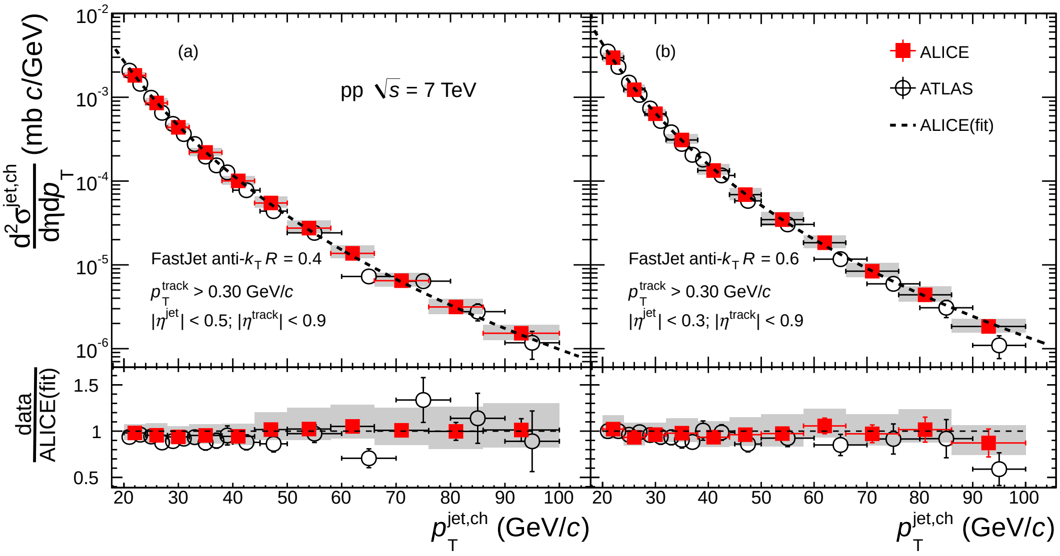

Fig. 4: (Color online) Top panels: Comparison of the charged jet cross section in the ALICE and the ATLAS [9] experiments in pp collisions at $\sqrt{s} = 7$ TeV. Statistical and systematic uncertainties are shown separately for ALICE data points, the gray bands indicating the systematic uncertainties, while for the ATLAS data points, the error bars show the statistical and systematic uncertainties summed in quadrature. The dotted line represents a Tsallis fit used to parametrize the ALICE data. Bottom panels: The ratio of the ALICE and ATLAS charged jet spectrum to the parametrized ALICE data. Note that the labels in the figures correspond to the ALICE measurements (see text for details).

Figure 6 shows the ratios of cross sections for jets with resolution parameters R = 0.2, R = 0.4 and R = 0.2, R = 0.6. The ratio of jet spectra [13] is sensitive to the collimation of particles around the jet axis and serves as an indirect measure of the jet structure used particularly in A–A collisions [69], where large background fluctuations greatly complicate jet shape studies. In order to compare the ratios within the same jet pseudorapidity range, the ratios are studied within $|\eta| < 0.3$, which coincides with the fiducial jet acceptance for the largest resolution parameter studied (R = 0.6). To avoid statistical correlations between the numerator and denominator, disjoint subsets ot the data are used. The measured ratios are also compared to those from PYTHIA Perugia-2011 and HERWIG simulations. The measured ratios confirm the expected trend of increased collimation with increasing transverse momentum of jets, corroborated also by the simulation results. At high p_T (> 30 GeV/c), both PYTHIA and HERWIG are in good agreement with the data within uncertainties. However at low p_T (< 30 GeV/c) PYTHIA tends to underpredict the data for both the ratios whereas HERWIG tends to overpredict the data for the ratio $\sigma^{jet,ch}(R = 0.2)$ / $\sigma^{jet,ch}$ (R = 0.6).

8.3 Charged particle multiplicity in the leading jet

The corrected mean charged particle multiplicity distributions $\langle N_{ch} \rangle$ in the leading jet are shown in Fig. 7 (left panel) as a function of jet p_T for R = 0.2, 0.4, and 0.6. The $\langle N_{ch} \rangle$ rises monotonically with increasing jet p_T as well as with increasing R. These results are in qualitative agreement with those reported by the CDF [15] collaboration and more recently by the CMS [19] collaboration based on slightly different kinematic track cuts.

In the left panel of Fig. 7, the measurements are compared to predictions by the MC models PYTHIA (tunes Perugia-0, Perugia-2011, AMBT1), PHOJET, and HERWIG. Ratios of the predictions to the data are displayed in the right panel. The model predictions are well within 10% of the measured data with largest deviations of ∼15% at R = 0.6 and 0.2 towards large jet p_T. The PYTHIA tune Perugia-0 tends to

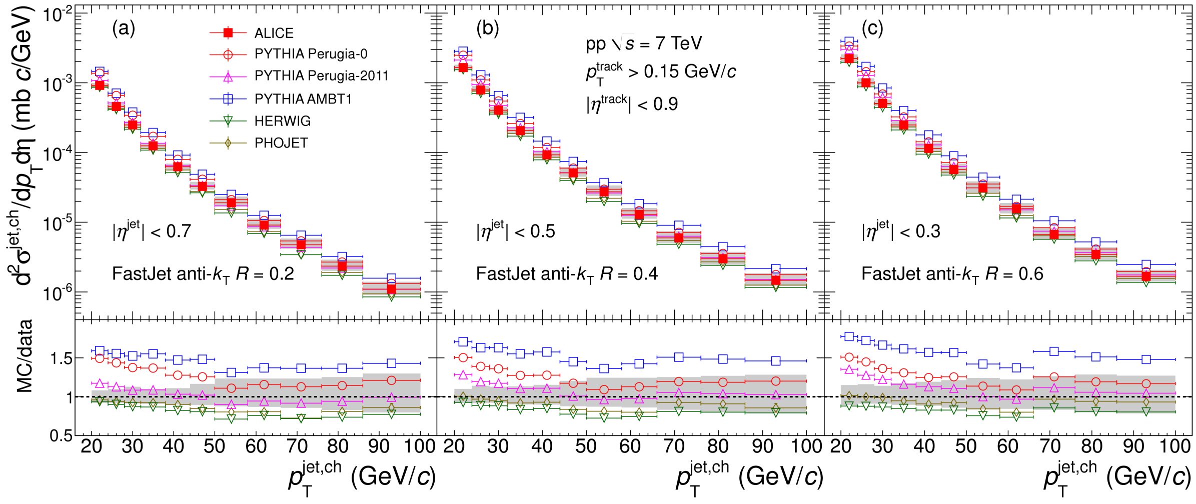

Fig. 5: (Color online) Top panels: Charged jet cross sections measured in the ALICE experiment in pp collisions at $\sqrt{s}$ = 7 TeV compared to several MC generators: PYTHIA AMBT1, PYTHIA Perugia-0 tune, PYTHIA Perugia-2011 tune, HERWIG, and PHOJET. Bottom panels: Ratios MC/Data. Shaded bands show quadratic sum of statistical and systematic uncertainties on the data drawn at unity.

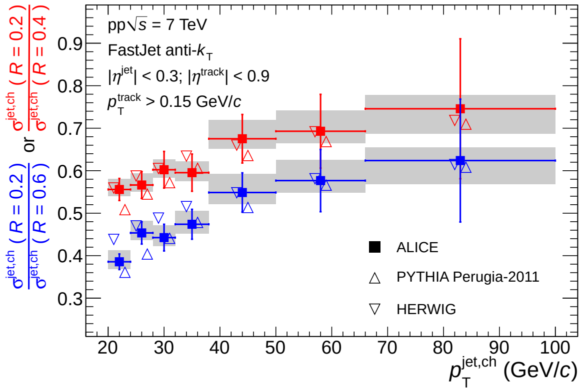

Fig. 6: (Color online) Ratios of jet cross sections for charged jets reconstructed using anti-k_T algorithm with resolution parameters 0.2 and 0.4 and 0.2 and 0.6. The jet acceptance is restricted to $|\eta^{jet}| \leq 0.3$. The ratios in data are compared to PYTHIA Perugia-2011 and HERWIG simulations.

systematically underestimate the measured particle multiplicities particularly at the largest R for smaller jet momentum, whereas HERWIG tends to overpredict the data at smaller R. An overall agreement between the data and MC predictions is found to be best with the Perugia-2011 tune and PHOJET.

8.4 Transverse momentum density distributions within the leading jet

The left panels of Figs. 8, 9, and 10 show leading jets average p_T density radial distributions $\langle dp_T^{sum}/dr \rangle$ measured with resolution parameters R = 0.2, 0.4, and 0.6, respectively. The distributions are plotted separately for jets in the p_T intervals 20 - 30, 30 - 40, 40 - 60, and 60 to 80 GeV/c. The latter three distributions are scaled by factors of 10, 100, and 1000 respectively for clarity. The transverse momentum density is largest near the jet axis and decreases approximately exponentially with increasing r. Densities are largest at the highest jet p_T where they are also found to have the steepest dependence on r. This indicates that high p_T jets are on average more collimated than low p_T jets as already hinted in Fig. 6.

The measured distributions are compared to predictions with MC models. The right panels of Figs. 8, 9,

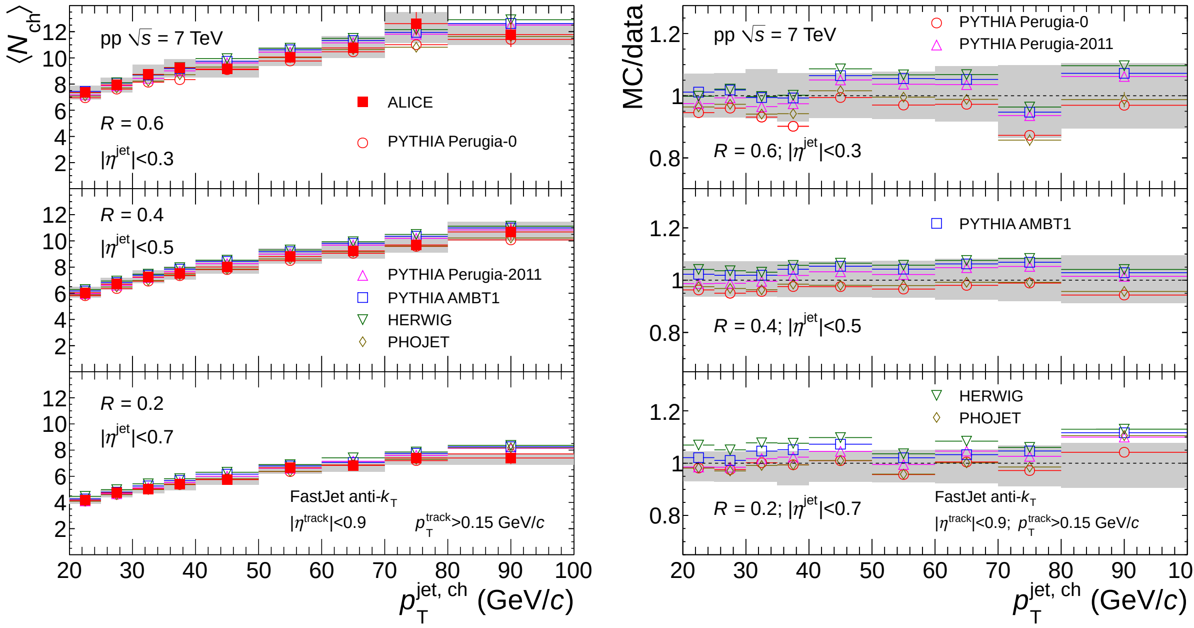

Fig. 7: (Color online) Left panel: Mean charged particle multiplicity in the leading charged jet as a function of jet p_{T} compared to MC models for pp collisions at $\sqrt{s}$ = 7 TeV for various jet resolution parameters (R = 0.6 (left top), R = 0.4 (left middle) and R = 0.2 (left bottom)). UE contributions are subtracted from both data and MC. Right panel: Ratios MC/data. Shaded bands show the quadratic sum of statistical and systematic uncertainties on the data drawn at unity.

and 10 display ratios of the model calculations to measured data. The MC models qualitatively reproduce the magnitude of the measured densities as well as their radial dependence. The agreement between the MC model calculations and data is better at smaller R (= 0.2). At R = 0.4 and 0.6 HERWIG and Perugia-0 tune of PYTHIA tend to underpredict the measured transverse momentum density except at small r for the two lowest jet p_{T} bins. The excess over the data for the smallest r and the slope of the ratio of simulations to data observed for R = 0.6 indicates stronger jet collimation for low p_{T} jets than observed in the data. This observation is consistent with the discrepancy of the Herwig model to the measured cross section ratio discussed in Sec. 8.2 (see also Fig. 6). In the last bin of Figs. 9, and 10 (right panel), large deviations of MC models (PHOJET and HERWIG) from the data are found, whereas good agreement is observed when data and simulations are not corrected for the UE contribution (not shown). This indicates that the UE is underestimated by these models, as reported in [62] for PHOJET and in [60] for HERWIG simulations of the UE density of charged and neutral particles with $p_{\mathrm{T}} > 0.5$ GeV/c.

8.5 Leading charged jet size

The left panel of Fig. 11 displays measured distributions of the average radius, $\langle R_{80} \rangle$, containing 80% of the total jet p_{T} observed in jet cones with R = 0.2, 0.4, and 0.6. The distributions are corrected using the bin-by-bin method described in Sec. 6.1 to account for instrumental effects. No corrections are applied for UE contributions, which are estimated to have a negligible effects on measured $\langle R_{80} \rangle$ values. Jet widths are largest at the lowest measured p_{T} and decrease monotonically with increasing p_{T}, indicating that high p_{T} jets are more collimated than low p_{T} jets (as observed in Figs. 6, 8, 9, and 10) in a similar way as predicted by various MC models and in qualitative agreement with prior measurement by the CDF [15] collaboration.

Figure 11 also displays $\langle R_{80} \rangle$ distributions predicted by PYTHIA (tunes Perugia-0, Perugia-2011, AMBT1), PHOJET, and HERWIG. All five models qualitatively reproduce the observed magnitude and p_{T} dependence of $\langle R_{80} \rangle$ at R = 0.2 and 0.4. However, at R = 0.6, HERWIG, PHOJET, and PYTHIA Perugia-0

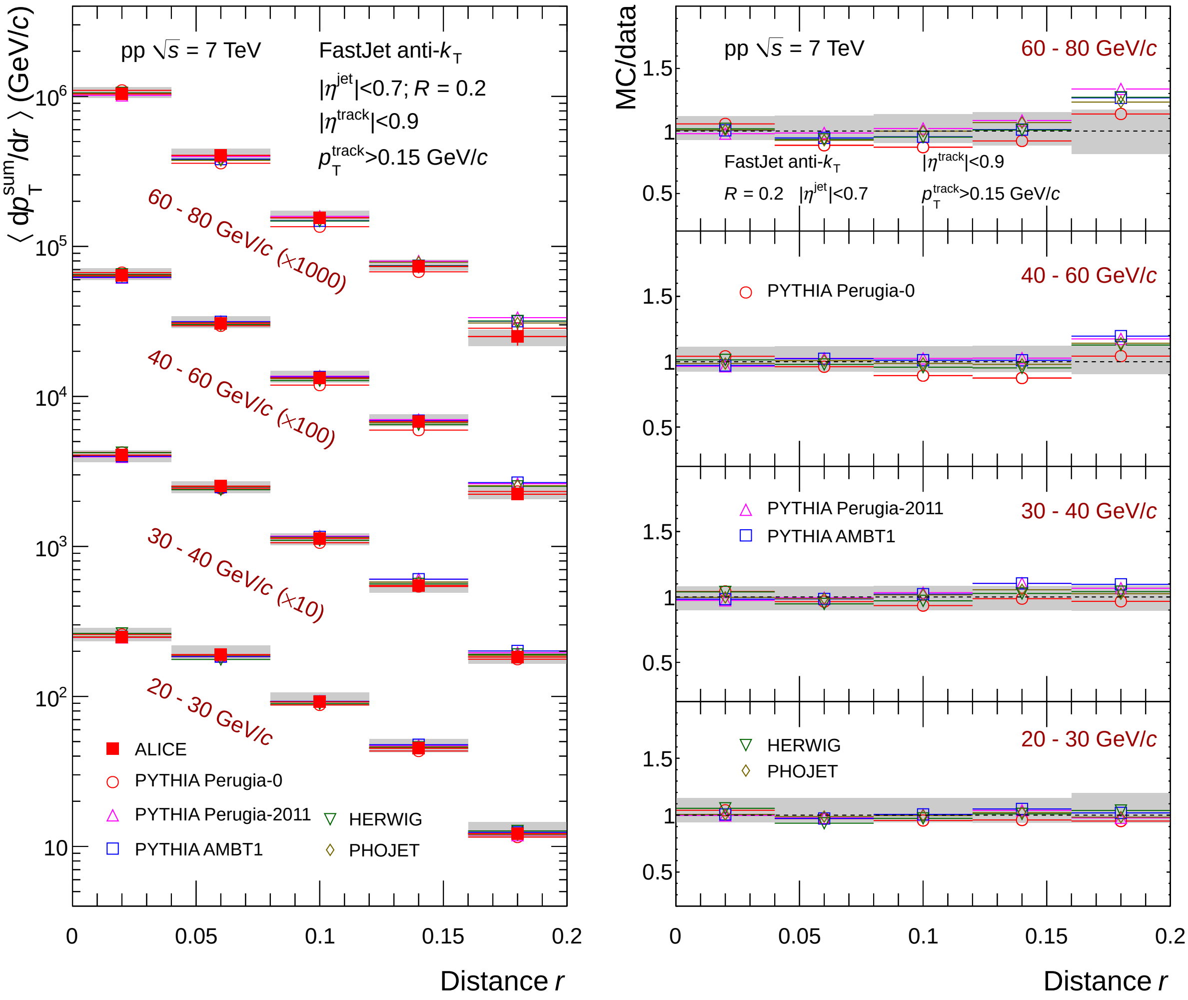

Fig. 8: (Color online) Left panel: Radial distributions of p_T density as a function radial distance 'r' from the jet direction for leading charged jets reconstructed with resolution parameter $R = 0.2$ for selected jet p_T ranges in pp collisions at $\sqrt{s} = 7$ TeV. Measured distributions are compared to MC model calculations. UE contributions are subtracted from both data and MC. Right panel: Ratios MC/data. Shaded bands show the quadratic sum of statistical and systematic uncertainties of the data drawn at unity.

tune systematically underpredict the data at low p_T. The PYTHIA tunes Perugia-2011 and AMBT1 are in best agreement with the measured values.

8.6 Jet fragmentation

The left panels of Figs. 12, 13, and 14 present the measured p_T spectra F^{p_T} and scaled p_T spectra F^z and F^ξ of charged particles in leading charged jets reconstructed with a resolution parameter $R = 0.4$. The data are corrected for instrumental effects, UE background, and contamination from secondary particles. Systematic uncertainties, indicated by the shaded bands, include the detector response, UE subtraction, correction for secondaries and event generator dependence.

The particle momentum distributions F^{p_T} are shown for four bins in jet transverse momentum: 20 - 30, 30 - 40, 40 - 60, and 60 - 80 GeV/c. The latter three are scaled by factors of 10, 100, and 1000 respectively for clarity. The p_T spectra of the jet constituents span 2 - 3 orders of magnitude. The slopes are steepest for the lowest p_T jets and progressively flatter with increasing jet p_T. This dependence is essentially driven by the jet energy scale, as illustrated in Fig. 13, which displays fragmentation distributions F^z for

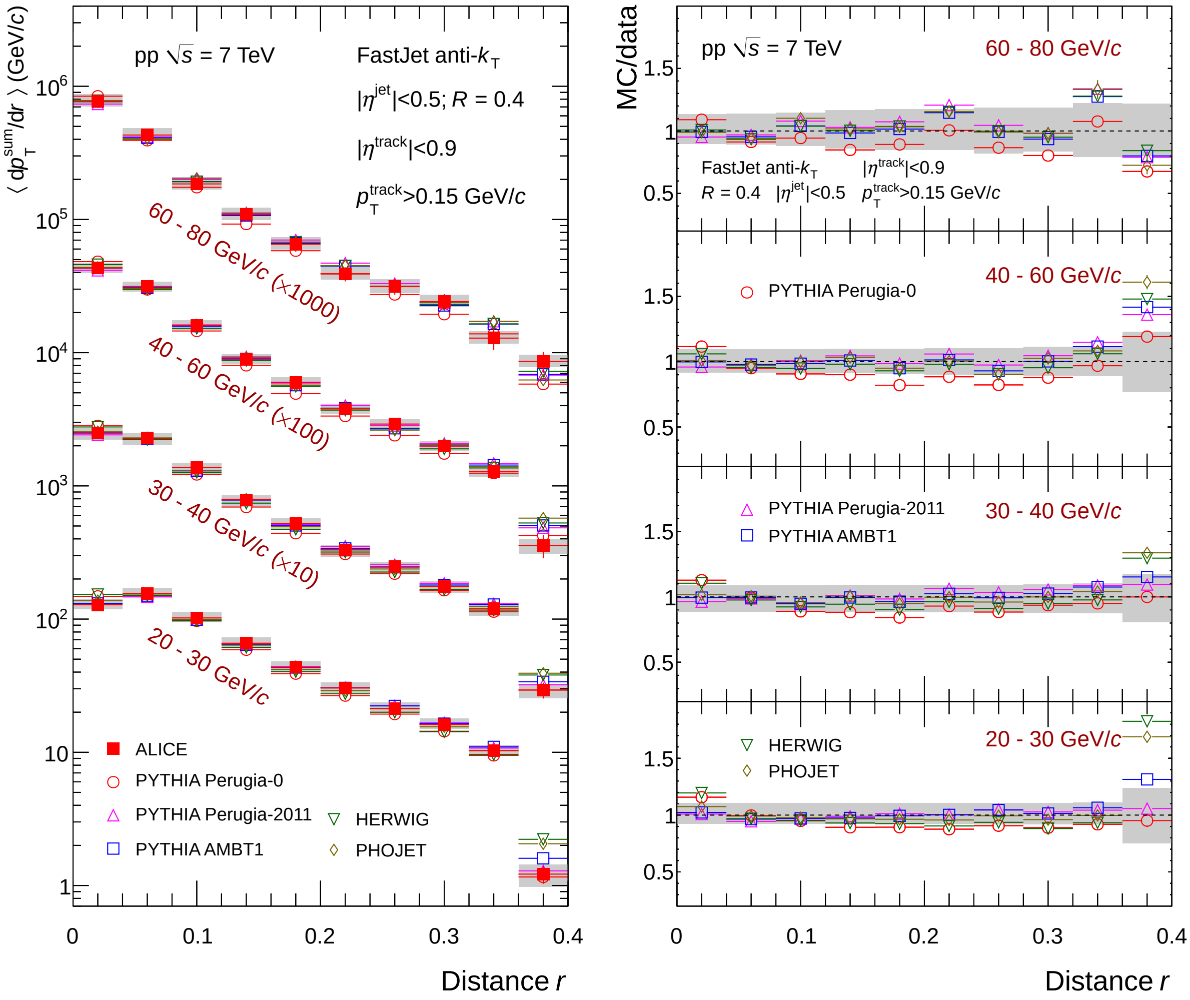

Fig. 9: (Color online) Same as Fig. 8 for a resolution parameter $R = 0.4$.

jets in the same four jet momentum ranges. For $z^{\mathrm{ch}} > 0.1$ all measured distributions are consistent within uncertainties, indicating a scaling of charged jet fragmentation with charged jet transverse momentum.

The fragmentation distributions F^{ξ}, shown in Fig. 14, resolve in more detail the differences observed for small values of z^{ch}. For small values of $\xi^{\mathrm{ch}} \lesssim 2$, the distributions exhibit the approximate scaling already seen for F^{z}, whereas at higher ξ^{ch}, corresponding to small z^{ch}, a pronounced maximum ('hump-backed plateau') is observed, indicating the suppression of low momentum particle production by QCD coherence [44, 45]. With increasing jet transverse momentum, the area of the distributions increases, showing the rise of particle multiplicity in jets (as observed in Fig. 7), and the maximum shifts to higher values of ξ^{ch}. This observation is in qualitative agreement with full di-jet fragmentation functions measured in p$\bar{\mathrm{p}}$ collisions at $\sqrt{s} = 1.8$ TeV [21] and with expectations from QCD calculations based on the Modified Leading Logarithmic Approximation (MLLA) [70].

The measured fragmentation distributions are compared to calculations obtained from the HERWIG [26, 27], PHOJET [28] and PYTHIA [25] event generators and the ratios of the calculated MC distributions to measured distributions are shown in the right panels of Figs. 12, 13, and 14. The UE contributions to MC events are estimated and subtracted using perpendicular cones pointing into the event transverse region as described in Sec. 6.4. At high particle transverse momenta and high z^{ch}, the data and simulations agree within uncertainties, except for the two lowest jet p_{T} bins, where the measured yield seems to be systematically higher than the simulations with PYTHIA tunes Perugia-2011 and AMBT1 for $z^{\mathrm{ch}} > 0.6$.

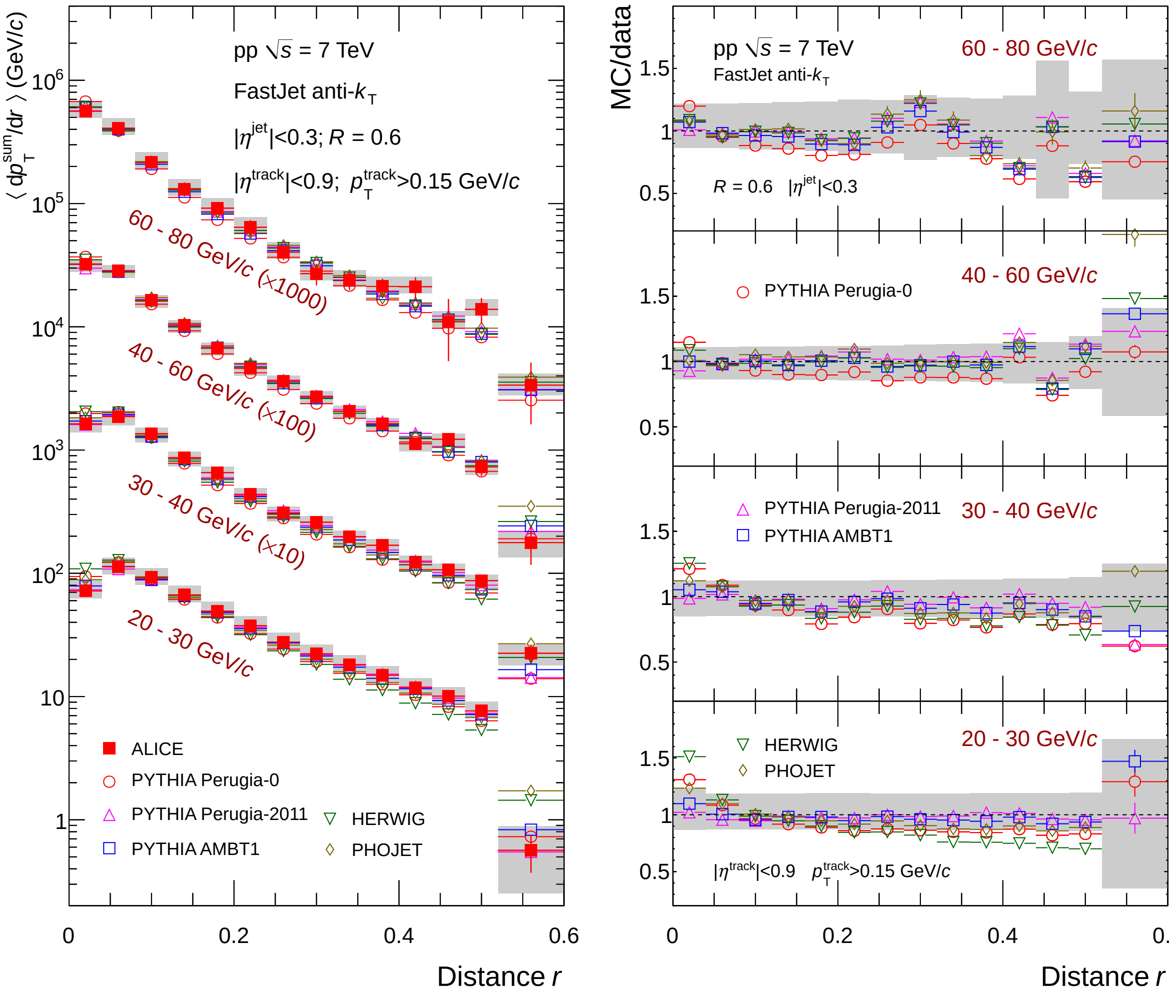

Fig. 10: (Color online) Same as Fig. 8 for a resolution parameter $R = 0.6$.

In the low momentum / high ξ^{ch} region, the measured yield is systematically larger than produced by the PYTHIA and PHOJET simulations. To investigate the discrepancy at low particle momentum, data and simulations are also compared without subtraction of the UE (not shown). In this case, the excess of low momentum constituents in data over PYTHIA simulations is still significant, however reduced in magnitude and comparable to other measurements at higher constituent momenta [9]. It is thus concluded that in the PYTHIA tunes investigated in this work the UE contribution to the low momentum particle yield is overestimated relative to the contribution from hard parton fragmentation. The data at low p_T are best described by the HERWIG event generator, which hints to a sensitivity of the low momentum fragmentation to the details of the parton shower model in the simulations.

9 Summary and conclusion

In summary, we reported measurements of the inclusive charged particle jet cross section, jet fragmentation and jet shapes at midrapidity in pp collisions at $\sqrt{s}$ = 7 TeV using the ALICE detector at the LHC.

Jets were reconstructed with infrared and collinear safe jet finding algorithms, k_T, anti-k_T and a seedless infrared safe iterative cone based algorithm, SISCone. As the measured inclusive jet spectra did not show any significant dependence on the jet algorithm used, all observables discussed throughout the paper were based on jets reconstructed with the anti-k_T sequential recombination algorithm, commonly

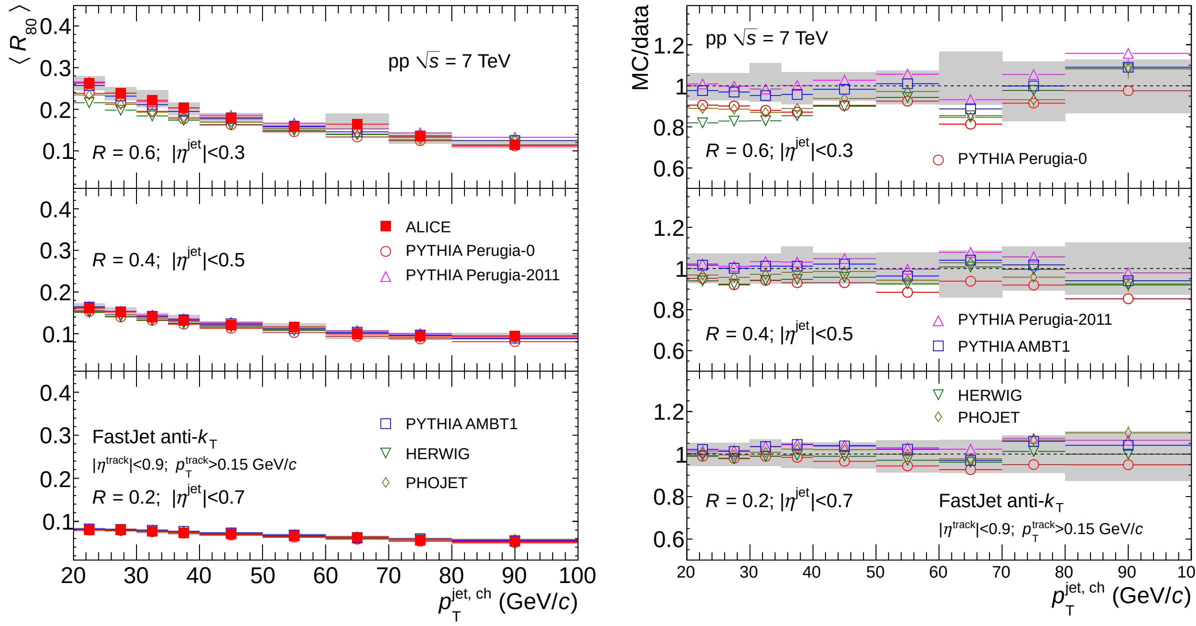

Fig. 11: (Color online) Left panel: Distributions of average radius '$\langle R_{80} \rangle$' containing 80% of the p_{T} with respect to the total reconstructed jet p_{T} as a function of jet p_{T} compared to MC models for pp collisions at $\sqrt{s}$ = 7 TeV for various jet resolution parameters (R = 0.6 (left top), R = 0.4 (left middle) and R = 0.2 (left bottom)). Right panel: Ratios MC/data. Shaded bands show quadratic sum of the statistical and systematic uncertainties of the data drawn at unity.

utilized in the LHC community. In order to gain as much information as possible , the anti-k_{T} algorithm was run with several resolution parameters R ranging from 0.2 to 0.6.

The inclusive charged jet cross section was measured in the $p_{\mathrm{T}}^{\mathrm{jet,ch}}$ interval from 20 to 100 GeV/c and found to be consistent with the ATLAS measurement at the same collision energy. The ratios of jet cross sections for resolution parameter R = 0.2 over R = 0.4 and 0.6, respectively, are found to increase with increasing p_{T} of jets, pointing toward an increasing collimation of particles in jets around the jet axis. This finding, expected by pQCD calculations, is corroborated by a detailed study of $\langle R_{80} \rangle$ variable defined as the average radius containing 80% of total charged jet p_{T}. The p_{T} density is found to be the largest near the jet axis and decreases radially away from the jet axis. This radial decrease is found to be larger for high p_{T} jets which are more collimated. The averaged charged particle multiplicity in jets ($\langle N_{\mathrm{ch}} \rangle$) increases with jet momentum and resolution parameter R. We studied charged particle fragmentation in leading charged jets. The scaled p_{T} spectra of charged particles associated with jets exhibit a pronounced maximum commonly referred to as 'hump-backed plateau' consistent with the suppression of low momentum particle production by QCD coherence. The area of the distribution increases with jet p_{T} and reflects the observed increase of $\langle N_{ch} \rangle$ discussed above. The observed behaviour is in qualitative agreement with MLLA [70] calculations and earlier measurements [21] in p$\bar{\mathrm{p}}$ collisions at the Tevatron ($\sqrt{s}$ = 1.8 TeV). The jet fragmentation distributions for the measured jet p_{T} ranges indicate a scaling of charged jet fragmentation with jet p_{T} for $z^{\mathrm{ch}} > 0.1$.

All measured observables were also compared to several MC generators (PYTHIA, PHOJET, HERWIG). None of the generators gives a perfect description of the measured charged jet cross section. PHOJET and most of the PYTHIA tunes used in this work overestimate the cross section. PYTHIA Perugia-2011 agrees reasonably well with the data for intermediate and high charged jet p_{T}, whereas HERWIG reproduces best the cross section at low jet p_{T}. The jet properties are reproduced rather well by the MC generators. The agreement of the calculations with the data for observables $\langle N_{\mathrm{ch}} \rangle$, $\langle R_{80} \rangle$, and radial p_{T} density is typically at the level of 5-10%. In case of the fragmentation functions, the data are better

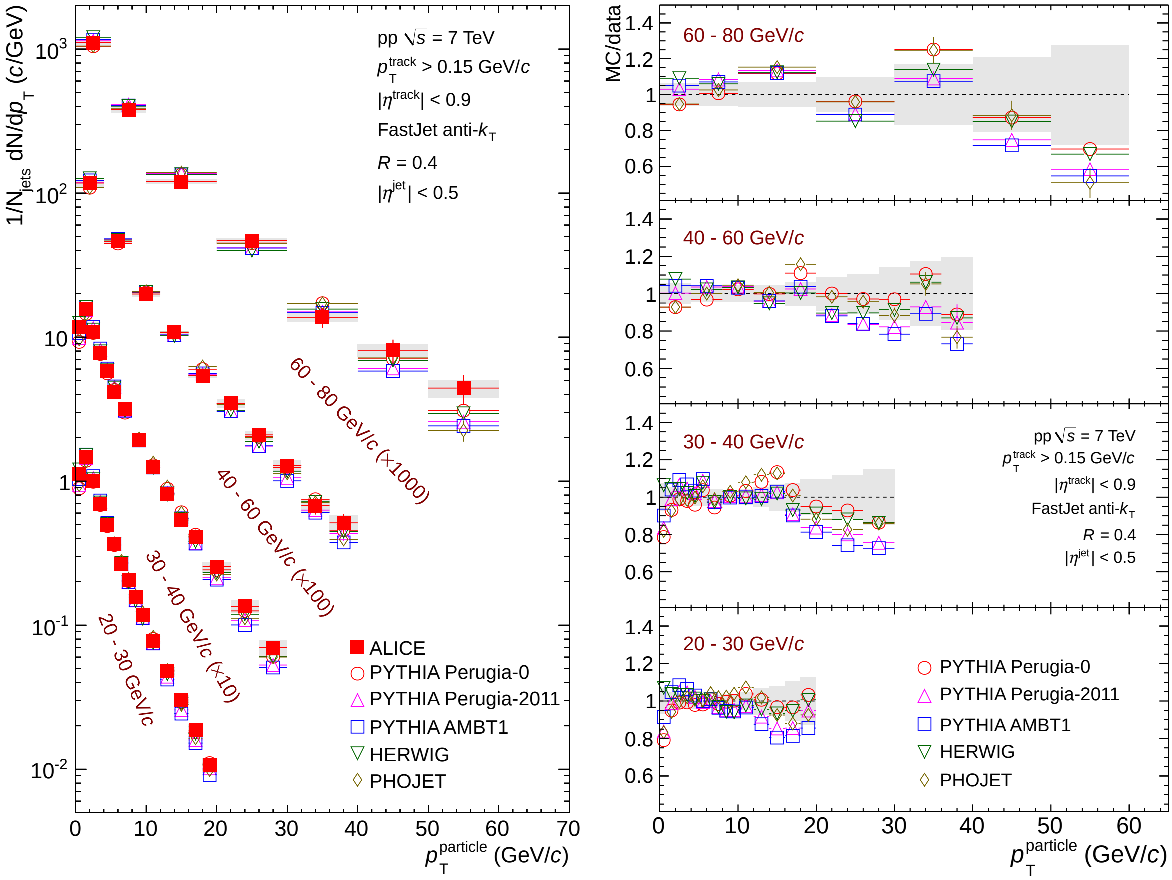

Fig. 12: (Color online) Left panel: Charged particle p_{T} spectra $\mathrm{d}N/\mathrm{d}p_{\mathrm{T}}$ in leading jets for different bins in jet transverse momentum, compared to simulations. For simulations and data, the UE contribution is subtracted. Right panel: Ratio of simulations to data. The shaded band indicates the quadratic sum of statistical and systematic uncertainties on the data.

described by the HERWIG event generator. The high momentum (low ξ^{ch}) region is relatively well described by the generators, while for the low momenta (high ξ^{ch}), the measured yield significantly exceeds PHOJET and PYTHIA predictions. We emphasize the relevance of this observation for the choice of a generator based pp reference for future measurements of jet fragmentation in nuclear collisions, where similar effects are predicted as a signature of parton energy loss in the hot and dense strongly-interacting medium.

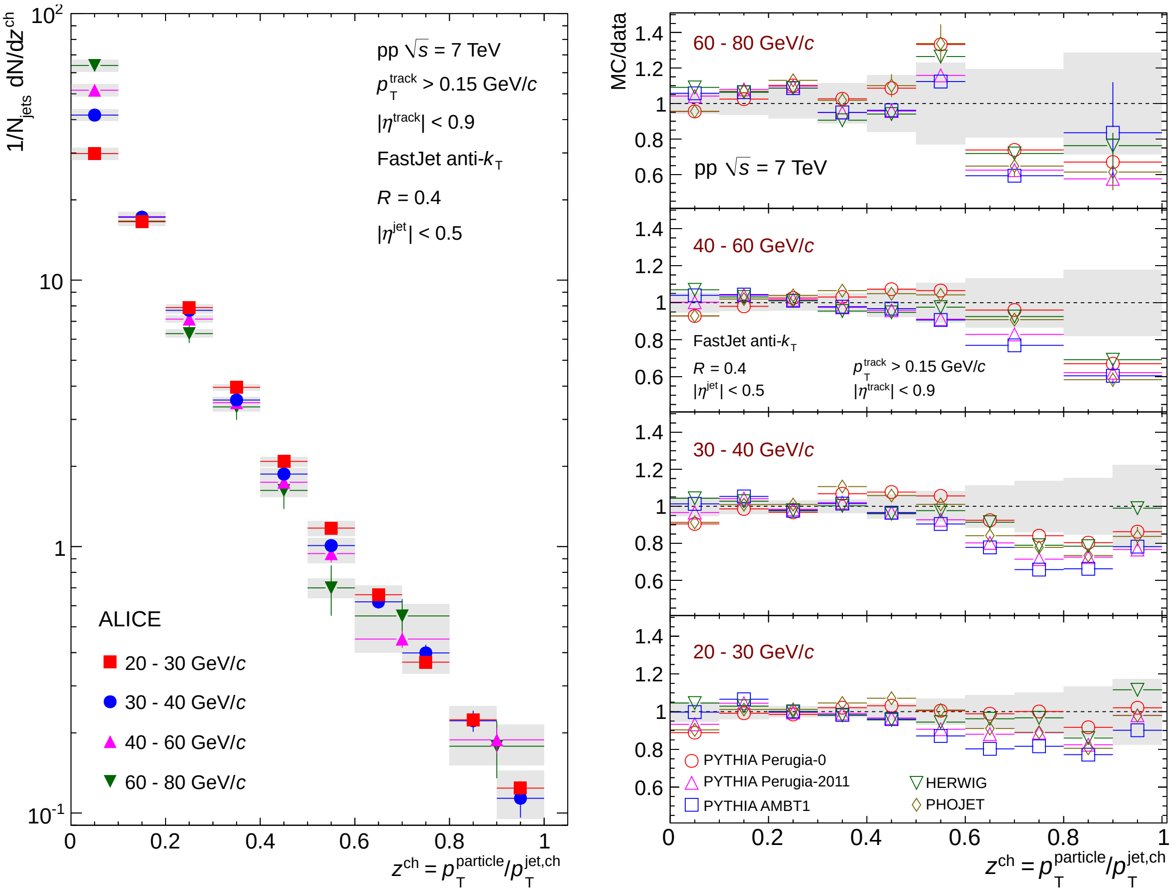

Fig. 13: (Color online) Left panel: Charged particle scaled p_{T} spectra $\mathrm{d}N/\mathrm{d}z^{\mathrm{ch}}$ in leading jets for different bins in jet transverse momentum. Right panel: Ratio of simulations to data. The shaded band indicates the quadratic sum of statistical and systematic uncertainties on the data. UE contributions are subtracted from both data and simulations.

]

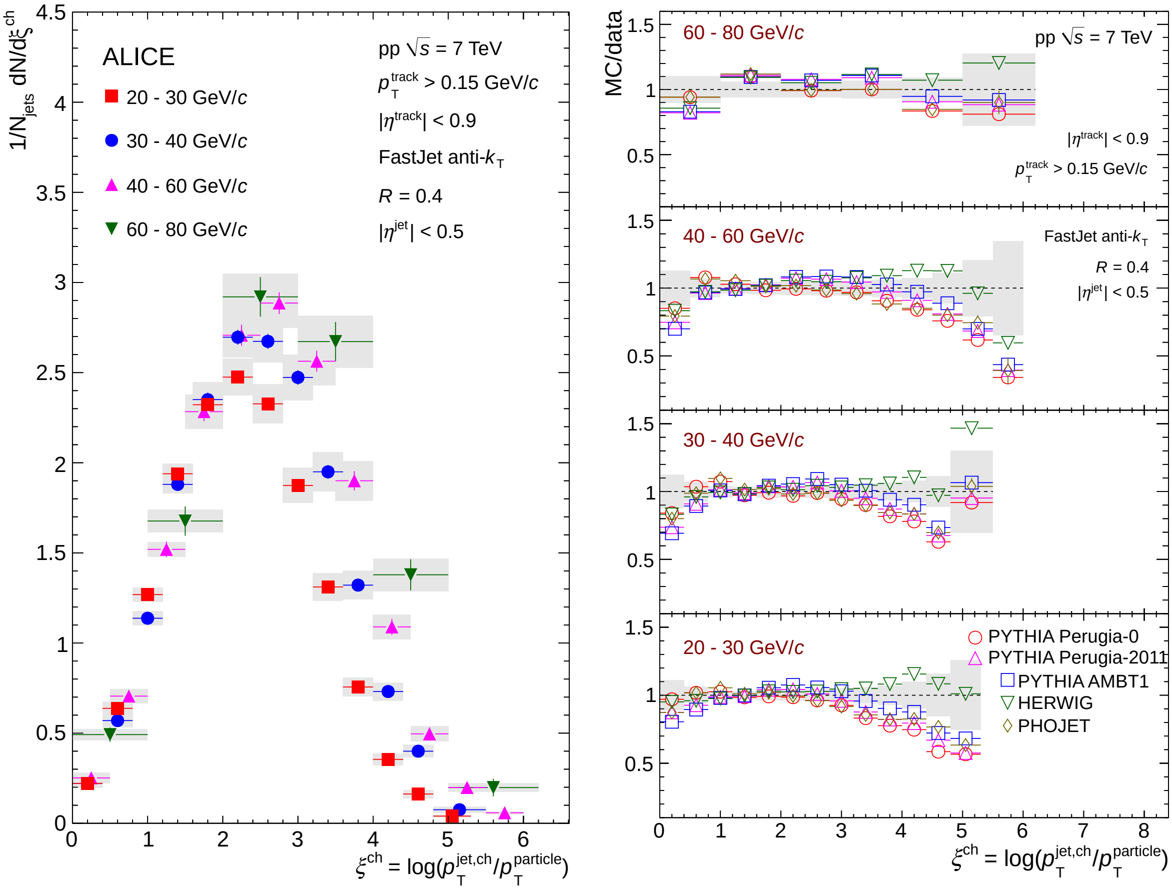

Fig. 14: (Color online) Left panel: Charged particle scaled p_{T} spectra $\mathrm{d}N/\mathrm{d}\xi^{\mathrm{ch}}$ in leading jets for different bins in jet transverse momentum. Right panel: Ratio of simulations to data. The shaded band indicates the quadratic sum of statistical and systematic uncertainties on the data. UE contributions are subtracted from both data and simulations.

Acknowledgements

The ALICE Collaboration would like to thank all its engineers and technicians for their invaluable contributions to the construction of the experiment and the CERN accelerator teams for the outstanding performance of the LHC complex. The ALICE Collaboration gratefully acknowledges the resources and support provided by all Grid centres and the Worldwide LHC Computing Grid (WLCG) collaboration. The ALICE Collaboration acknowledges the following funding agencies for their support in building and running the ALICE detector: State Committee of Science, World Federation of Scientists (WFS) and Swiss Fonds Kidagan, Armenia, Conselho Nacional de Desenvolvimento Científico e Tecnológico (CNPq), Financiadora de Estudos e Projetos (FINEP), Fundação de Amparo à Pesquisa do Estado de São Paulo (FAPESP); National Natural Science Foundation of China (NSFC), the Chinese Ministry of Education (CMOE) and the Ministry of Science and Technology of China (MSTC); Ministry of Education and Youth of the Czech Republic; Danish Natural Science Research Council, the Carlsberg Foundation and the Danish National Research Foundation; The European Research Council under the European Community's Seventh Framework Programme; Helsinki Institute of Physics and the Academy of Finland; French CNRS-IN2P3, the 'Region Pays de Loire', 'Region Alsace', 'Region Auvergne' and CEA, France; German BMBF and the Helmholtz Association; General Secretariat for Research and Technology, Ministry of Development, Greece; Hungarian OTKA and National Office for Research and Technology (NKTH); Department of Atomic Energy and Department of Science and Technology of the Government of India; Istituto Nazionale di Fisica Nucleare (INFN) and Centro Fermi - Museo Storico della Fisica e Centro Studi e Ricerche "Enrico Fermi", Italy; MEXT Grant-in-Aid for Specially Promoted Research, Japan; Joint Institute for Nuclear Research, Dubna; National Research Foundation of Korea (NRF); CONACYT, DGAPA, México, ALFA-EC and the EPLANET Program (European Particle Physics Latin American Network) Stichting voor Fundamenteel Onderzoek der Materie (FOM) and the Nederlandse Organisatie voor Wetenschappelijk Onderzoek (NWO), Netherlands; Research Council of Norway (NFR); Polish Ministry of Science and Higher Education; National Science Centre, Poland; Ministry of National Education/Institute for Atomic Physics and CNCS-UEFISCDI - Romania; Ministry of Education and Science of Russian Federation, Russian Academy of Sciences, Russian Federal Agency of Atomic Energy, Russian Federal Agency for Science and Innovations and The Russian Foundation for Basic Research; Ministry of Education of Slovakia; Department of Science and Technology, South Africa; CIEMAT, EELA, Ministerio de Economía y Competitividad (MINECO) of Spain, Xunta de Galicia (Consellería de Educación), CEADEN, Cubaenergía, Cuba, and IAEA (International Atomic Energy Agency); Swedish Research Council (VR) and Knut & Alice Wallenberg Foundation (KAW); Ukraine Ministry of Education and Science; United Kingdom Science and Technology Facilities Council (STFC); The United States Department of Energy, the United States National Science Foundation, the State of Texas, and the State of Ohio; Ministry of Science, Education and Sports of Croatia and Unity through Knowledge Fund, Croatia.

References

[1] D0 Collaboration, B. Abbott *et al.*, "The inclusive jet cross section in $\bar{p}p$ collisions at $\sqrt{s} = 1.8$ TeV," *Phys.Rev.Lett.* **82** (1999) 2451–2456, `arXiv:hep-ex/9807018 [hep-ex]`.

[2] D0 Collaboration, B. Abbott *et al.*, "The ratio of jet cross sections at $\sqrt{s} = 630$ GeV and 1800 GeV," *Phys.Rev.Lett.* **86** (2001) 2523–2528, `arXiv:hep-ex/0008072 [hep-ex]`.

[3] D0 Collaboration, V. Abazov *et al.*, "Measurement of the inclusive jet cross-section in $p\bar{p}$ collisions at $\sqrt{s} = 1.96$ TeV," *Phys.Rev.Lett.* **101** (2008) 062001, `arXiv:0802.2400 [hep-ex]`.

[4] CDF Collaboration, F. Abe *et al.*, "Inclusive jet cross-section in $\bar{p}p$ collisions at $\sqrt{s} = 1.8$ TeV," *Phys.Rev.Lett.* **68** (1992) 1104–1108.

[5] CDF Collaboration, F. Abe *et al.*, "Comparison of jet production in $\bar{p}p$ collisions at $\sqrt{s} = 546$ GeV and 1800 GeV," *Phys.Rev.Lett.* **70** (1993) 1376–1380.

[6] CDF Collaboration, F. Abe *et al.*, "Inclusive jet cross section in $\bar{p}p$ collisions at $\sqrt{s} = 1.8$ TeV," *Phys.Rev.Lett.* **77** (1996) 438–443, `arXiv:hep-ex/9601008 [hep-ex]`.

[7] CDF Collaboration, T. Affolder *et al.*, "Measurement of the inclusive jet cross section in $\bar{p}p$ collisions at $\sqrt{s} = 1.8$ TeV," *Phys.Rev.* **D64** (2001) 032001, `arXiv:hep-ph/0102074 [hep-ph]`.

[8] CDF Collaboration, A. Abulencia *et al.*, "Measurement of the inclusive jet cross section using the k(t) algorithm in p anti-p collisions at $\sqrt{s} = 1.96$-TeV.," *Phys.Rev.Lett.* **96** (2006) 122001, `arXiv:hep-ex/0512062 [hep-ex]`.

[9] ATLAS Collaboration, G. Aad *et al.*, "Properties of jets measured from tracks in proton-proton collisions at center-of-mass energy $\sqrt{s} = 7$ TeV with the ATLAS detector," *Phys.Rev.* **D84** (2011) 054001, `arXiv:1107.3311 [hep-ex]`.

[10] ATLAS Collaboration, G. Aad *et al.*, "Properties of jets measured from tracks in proton-proton collisions at center-of-mass energy $\sqrt{s} = 7$ TeV with the ATLAS detector," *Phys.Rev.* **D84** (2011) 054001, `arXiv:1107.3311 [hep-ex]`.

[11] CMS Collaboration, S. Chatrchyan *et al.*, "Measurement of the Inclusive Jet Cross Section in *pp* Collisions at $\sqrt{s} = 7$ TeV," *Phys.Rev.Lett.* **107** (2011) 132001, `arXiv:1106.0208 [hep-ex]`.

[12] CMS Collaboration, S. Chatrchyan *et al.*, "Measurements of differential jet cross sections in proton-proton collisions at $\sqrt{s} = 7$ TeV with the CMS detector," *Phys.Rev.* **D87** no. 11, (2013) 112002, `arXiv:1212.6660 [hep-ex]`.

[13] ALICE Collaboration, B. Abelev *et al.*, "Measurement of the inclusive differential jet cross section in *pp* collisions at $\sqrt{s} = 2.76$ TeV," *Phys.Lett.* **B722** (2013) 262–272, `arXiv:1301.3475 [nucl-ex]`.

[14] CDF Collaboration, F. Abe *et al.*, "A Measurement of jet shapes in $p\bar{p}$ collisions at $\sqrt{s} = 1.8$ TeV," *Phys.Rev.Lett.* **70** (1993) 713–717.

[15] CDF Collaboration, T. Affolder *et al.*, "Charged jet evolution and the underlying event in $p\bar{p}$ collisions at 1.8 TeV," *Phys.Rev.* **D65** (2002) 092002.

[16] CDF Collaboration, D. Acosta *et al.*, "Study of jet shapes in inclusive jet production in $p\bar{p}$ collisions at $\sqrt{s} = 1.96$ TeV," *Phys.Rev.* **D71** (2005) 112002, `arXiv:hep-ex/0505013 [hep-ex]`.

[17] D0 Collaboration, S. Abachi *et al.*, "Transverse energy distributions within jets in $p\bar{p}$ collisions at $\sqrt{s} = 1.8$ TeV," *Phys.Lett.* **B357** (1995) 500–508.

[18] ATLAS Collaboration, G. Aad *et al.*, "Study of Jet Shapes in Inclusive Jet Production in *pp* Collisions at $\sqrt{s} = 7$ TeV using the ATLAS Detector," *Phys.Rev.* **D83** (2011) 052003, `arXiv:1101.0070 [hep-ex]`.

[19] CMS Collaboration, S. Chatrchyan *et al.*, "Shape, Transverse Size, and Charged Hadron Multiplicity of Jets in pp Collisions at 7 TeV," *JHEP* **1206** (2012) 160, `arXiv:1204.3170 [hep-ex]`.

[20] CMS Collaboration, S. Chatrchyan *et al.*, "Modification of jet shapes in PbPb collisions at $\sqrt{s_{NN}} = 2.76$ TeV," *Phys.Lett.* **B730** (2014) 243–263, `arXiv:1310.0878 [nucl-ex]`.

[21] CDF Collaboration, D. Acosta *et al.*, “Momentum distribution of charged particles in jets in dijet events in $p\bar{p}$ collisions at $\sqrt{s} = 1.8$ TeV and comparisons to perturbative QCD predictions,” *Phys.Rev.* **D68** (2003) 012003.

[22] ATLAS Collaboration, G. Aad *et al.*, “Measurement of the jet fragmentation function and transverse profile in proton-proton collisions at a center-of-mass energy of 7 TeV with the ATLAS detector,” *Eur.Phys.J.* **C71** (2011) 1795, `arXiv:1109.5816 [hep-ex]`.

[23] ATLAS Collaboration, G. Aad *et al.*, “Measurement of inclusive jet charged particle fragmentation functions in Pb+Pb collisions at sqrt(s(nn)) = 2.76 TeV with the ATLAS detector,” *ATLAS-CONF-2012-115, ATLAS-COM-CONF-2012-159, https://cds.cern.ch/record/1472936* .

[24] CMS Collaboration, S. Chatrchyan *et al.*, “Measurement of jet fragmentation into charged particles in pp and PbPb collisions at $\sqrt{s_{NN}} = 2.76$ TeV,” *JHEP* **1210** (2012) 087, `arXiv:1205.5872 [nucl-ex]`.

[25] T. Sjostrand, S. Mrenna, and P. Z. Skands, “PYTHIA 6.4 Physics and Manual,” *JHEP* **0605** (2006) 026, `arXiv:hep-ph/0603175 [hep-ph]`.

[26] G. Marchesini, B. Webber, G. Abbiendi, I. Knowles, M. Seymour, *et al.*, “HERWIG: A Monte Carlo event generator for simulating hadron emission reactions with interfering gluons. Version 5.1 - April 1991,” *Comput.Phys.Commun.* **67** (1992) 465–508.

[27] G. Corcella, I. Knowles, G. Marchesini, S. Moretti, K. Odagiri, *et al.*, “HERWIG 6: An Event generator for hadron emission reactions with interfering gluons (including supersymmetric processes),” *JHEP* **0101** (2001) 010, `arXiv:hep-ph/0011363 [hep-ph]`.

[28] S. Roesler, R. Engel, and J. Ranft, “The Monte Carlo event generator DPMJET-III,” `arXiv:hep-ph/0012252 [hep-ph]`.

[29] ALICE Collaboration, B. Abelev *et al.*, “Measurement of charged jet suppression in Pb-Pb collisions at $\sqrt{s_{NN}}$ = 2.76 TeV,” *JHEP* **1403** (2014) 013, `arXiv:1311.0633 [nucl-ex]`.

[30] Particle Data Group, J. Beringer *et al.*, “Review of Particle Physics (RPP),” *Phys.Rev.* **D86** (2012) 010001. and 2013 partial update for the 2014 edition.

[31] K. C. Zapp, F. Krauss, and U. A. Wiedemann, “A perturbative framework for jet quenching,” *JHEP* **1303** (2013) 080, `arXiv:1212.1599 [hep-ph]`.

[32] S. Sapeta and U. A. Wiedemann, “Jet hadrochemistry as a characteristics of jet quenching,” *Eur.Phys.J.* **C55** (2008) 293–302, `arXiv:0707.3494 [hep-ph]`.

[33] R. Chatterjee, H. Holopainen, T. Renk, and K. J. Eskola, “Influence of initial state fluctuations on the production of thermal photons,” *Nucl.Phys.* **A904-905** (2013) 849c–852c, `arXiv:1210.3517 [hep-ph]`.

[34] ALICE Collaboration, K. Aamodt *et al.*, “The ALICE experiment at the CERN LHC,” *JINST* **3** (2008) S08002.

[35] J. Alme, Y. Andres, H. Appelshauser, S. Bablok, N. Bialas, *et al.*, “The ALICE TPC, a large 3-dimensional tracking device with fast readout for ultra-high multiplicity events,” *Nucl.Instrum.Meth.* **A622** (2010) 316–367, `arXiv:1001.1950 [physics.ins-det]`.

[36] ALICE Collaboration, K. Aamodt *et al.*, “Alignment of the ALICE Inner Tracking System with cosmic-ray tracks,” *JINST* **5** (2010) P03003, `arXiv:1001.0502 [physics.ins-det]`.

[37] ALICE Collaboration, P. Cortese *et al.*, "ALICE technical design report on forward detectors: FMD, T0 and V0," *CERN-LHCC-2004-025, https://cds.cern.ch/record/781854* (2004) .

[38] ALICE Collaboration, B. Abelev *et al.*, "Measurement of inelastic, single- and double-diffraction cross sections in proton–proton collisions at the LHC with ALICE," *Eur.Phys.J.* **C73** (2013) 2456, `arXiv:1208.4968 [hep-ex]`.

[39] M. Cacciari, G. P. Salam, and G. Soyez, "The Anti-k(t) jet clustering algorithm," *JHEP* **0804** (2008) 063, `arXiv:0802.1189 [hep-ph]`.

[40] S. Catani, Y. L. Dokshitzer, M. Seymour, and B. Webber, "Longitudinally invariant K_t clustering algorithms for hadron hadron collisions," *Nucl.Phys.* **B406** (1993) 187–224.

[41] S. D. Ellis and D. E. Soper, "Successive combination jet algorithm for hadron collisions," *Phys.Rev.* **D48** (1993) 3160–3166, `arXiv:hep-ph/9305266 [hep-ph]`.

[42] M. Cacciari and G. P. Salam, "Dispelling the N^3 myth for the k_t jet-finder," *Phys.Lett.* **B641** (2006) 57–61, `arXiv:hep-ph/0512210 [hep-ph]`.

[43] G. P. Salam and G. Soyez, "A Practical Seedless Infrared-Safe Cone jet algorithm," *JHEP* **0705** (2007) 086, `arXiv:0704.0292 [hep-ph]`.

[44] B. Ermolaev and V. S. Fadin, "Log - Log Asymptotic Form of Exclusive Cross-Sections in Quantum Chromodynamics," *JETP Lett.* **33** (1981) 269–272.

[45] A. H. Mueller, "On the Multiplicity of Hadrons in QCD Jets," *Phys.Lett.* **B104** (1981) 161–164.

[46] P. Z. Skands, "Tuning Monte Carlo Generators: The Perugia Tunes," *Phys.Rev.* **D82** (2010) 074018, `arXiv:1005.3457 [hep-ph]`.

[47] R. Brun, F. Carminati, and S. Giani, "GEANT Detector Description and Simulation Tool," *CERN-W5013, CERN-W-5013, https://cds.cern.ch/record/1082634* .

[48] T. Sjostrand and P. Z. Skands, "Transverse-momentum-ordered showers and interleaved multiple interactions," *Eur.Phys.J.* **C39** (2005) 129–154, `arXiv:hep-ph/0408302 [hep-ph]`.

[49] B. Andersson, G. Gustafson, and B. Soderberg, "A General Model for Jet Fragmentation," *Z.Phys.* **C20** (1983) 317.

[50] ATLAS Collaboration, "Charged particle multiplicities in p p interactions at $\sqrt{s}$ = 0.9 and 7 TeV in a diractive limited phase-space measured with the ATLAS detector at the LHC and new PYTHIA6 tune," *ATLAS-CONF-2010-031, ATLAS-COM-CONF-2010-031, https://cds.cern.ch/record/1277665* (2010) .

[51] CTEQ Collaboration, H. Lai *et al.*, "Global QCD analysis of parton structure of the nucleon: CTEQ5 parton distributions," *Eur.Phys.J.* **C12** (2000) 375–392, `arXiv:hep-ph/9903282 [hep-ph]`.

[52] A. Sherstnev and R. Thorne, "Parton Distributions for LO Generators," *Eur.Phys.J.* **C55** (2008) 553–575, `arXiv:0711.2473 [hep-ph]`.

[53] M. Gluck, E. Reya, and A. Vogt, "Dynamical parton distributions of the proton and small x physics," *Z.Phys.* **C67** (1995) 433–448.

[54] G. D'Agostini, "A Multidimensional unfolding method based on Bayes' theorem," *Nucl.Instrum.Meth.* **A362** (1995) 487–498.

[55] A. Hocker and V. Kartvelishvili, “SVD approach to data unfolding,” *Nucl.Instrum.Meth.* **A372** (1996) 469–481, `arXiv:hep-ph/9509307 [hep-ph]`.

[56] T. Adye, “Unfolding algorithms and tests using RooUnfold,” `arXiv:1105.1160 [physics.data-an]`. See also http://hepunx.rl.ac.uk/ adye/software/unfold/RooUnfold.html.

[57] CMS Collaboration, V. Khachatryan *et al.*, “Strange Particle Production in *pp* Collisions at $\sqrt{s} = 0.9$ and 7 TeV,” *JHEP* **1105** (2011) 064, `arXiv:1102.4282 [hep-ex]`.

[58] P. Skands *et al. https://mcplots.cern.ch* .

[59] ATLAS Collaboration, G. Aad *et al.*, “Measurement of underlying event characteristics using charged particles in pp collisions at $\sqrt{s} = 900 GeV$ and 7 TeV with the ATLAS detector,” *Phys.Rev.* **D83** (2011) 112001, `arXiv:1012.0791 [hep-ex]`.

[60] ATLAS Collaboration, G. Aad *et al.*, “Measurements of underlying-event properties using neutral and charged particles in *pp* collisions at 900 GeV and 7 TeV with the ATLAS detector at the LHC,” *Eur.Phys.J.* **C71** (2011) 1636, `arXiv:1103.1816 [hep-ex]`.

[61] CMS Collaboration, S. Chatrchyan *et al.*, “Measurement of the Underlying Event Activity at the LHC with $\sqrt{s} = 7$ TeV and Comparison with $\sqrt{s} = 0.9$ TeV,” *JHEP* **1109** (2011) 109, `arXiv:1107.0330 [hep-ex]`.

[62] ALICE Collaboration, B. Abelev *et al.*, “Underlying Event measurements in *pp* collisions at $\sqrt{s} = 0.9$ and 7 TeV with the ALICE experiment at the LHC,” *JHEP* **1207** (2012) 116, `arXiv:1112.2082 [hep-ex]`.

[63] ALICE Collaboration, B. Abelev *et al.*, “Centrality Dependence of Charged Particle Production at Large Transverse Momentum in Pb–Pb Collisions at $\sqrt{s_{\rm NN}} = 2.76$ TeV,” *Phys.Lett.* **B720** (2013) 52–62, `arXiv:1208.2711 [hep-ex]`.

[64] CDF Collaboration *CDF/ANAL/CDF/CDFR/7703* .

[65] ALICE Collaboration, B. Abelev *et al.*, “Measurement of inelastic, single- and double-diffraction cross sections in proton–proton collisions at the LHC with ALICE,” *Eur.Phys.J.* **C73** (2013) 2456, `arXiv:1208.4968 [hep-ex]`.

[66] ALICE Collaboration, K. Oyama, “Reference cross section measurements with ALICE in pp and Pb-Pb collisions at LHC,” `arXiv:1305.7044 [nucl-ex]`.

[67] C. Tsallis, “Possible Generalization of Boltzmann-Gibbs Statistics,” *J.Statist.Phys.* **52** (1988) 479–487.

[68] C. Tsallis, *Introduction to Nonextensive Statistical Mechanics*. Springer, 2009. For an updated bibliography on this subject see http://tsallis.cat.cbpf.br/biblio.htm.

[69] ALICE Collaboration, B. Abelev *et al.*, “Measurement of charged jet suppression in Pb-Pb collisions at $\sqrt{s_{NN}}$ = 2.76 TeV,” *JHEP* **1403** (2014) 013, `arXiv:1311.0633 [nucl-ex]`.

[70] Y. I. Azimov, Y. L. Dokshitzer, V. A. Khoze, and S. Troyan, “Humpbacked QCD Plateau in Hadron Spectra,” *Z.Phys.* **C31** (1986) 213.

A ALICE Collaboration

B. Abelev[71] , J. Adam[37] , D. Adamová[79] , M.M. Aggarwal[83] , G. Aglieri Rinella[34] , M. Agnello[107,90] ,
A. Agostinelli[26] , N. Agrawal[44] , Z. Ahammed[126] , N. Ahmad[18] , I. Ahmed[15] , S.U. Ahn[64] , S.A. Ahn[64] ,
I. Aimo[90,107] , S. Aiola[131] , M. Ajaz[15] , A. Akindinov[54] , S.N. Alam[126] , D. Aleksandrov[96] , B. Alessandro[107] ,
D. Alexandre[98] , A. Alici[101,12] , A. Alkin[3] , J. Alme[35] , T. Alt[39] , S. Altinpinar[17] , I. Altsybeev[125] ,
C. Alves Garcia Prado[115] , C. Andrei[74] , A. Andronic[93] , V. Anguelov[89] , J. Anielski[50] , T. Antičić[94] ,
F. Antinori[104] , P. Antonioli[101] , L. Aphecetche[109] , H. Appelshäuser[49] , S. Arcelli[26] , N. Armesto[16] ,
R. Arnaldi[107] , T. Aronsson[131] , I.C. Arsene[93,21] , M. Arslandok[49] , A. Augustinus[34] , R. Averbeck[93] ,
T.C. Awes[80] , M.D. Azmi[85,18] , M. Bach[39] , A. Badalà[103] , Y.W. Baek[66,40] , S. Bagnasco[107] , R. Bailhache[49] ,
R. Bala[86] , A. Baldisseri[14] , F. Baltasar Dos Santos Pedrosa[34] , R.C. Baral[57] , R. Barbera[27] , F. Barile[31] ,
G.G. Barnaföldi[130] , L.S. Barnby[98] , V. Barret[66] , J. Bartke[112] , M. Basile[26] , N. Bastid[66] , S. Basu[126] ,
B. Bathen[50] , G. Batigne[109] , A. Batista Camejo[66] , B. Batyunya[62] , P.C. Batzing[21] , C. Baumann[49] ,
I.G. Bearden[76] , H. Beck[49] , C. Bedda[90] , N.K. Behera[44] , I. Belikov[51] , F. Bellini[26] , R. Bellwied[117] ,
E. Belmont-Moreno[60] , R. Belmont III[129] , V. Belyaev[72] , G. Bencedi[130] , S. Beole[25] , I. Berceanu[74] ,
A. Bercuci[74] , Y. Berdnikov[ii,81] , D. Berenyi[130] , M.E. Berger[88] , R.A. Bertens[53] , D. Berzano[25] , L. Betev[34] ,
A. Bhasin[86] , I.R. Bhat[86] , A.K. Bhati[83] , B. Bhattacharjee[41] , J. Bhom[122] , L. Bianchi[25] , N. Bianchi[68] ,
C. Bianchin[53] , J. Bielčík[37] , J. Bielčíková[79] , A. Bilandzic[76] , S. Bjelogrlic[53] , F. Blanco[10] , D. Blau[96] ,
C. Blume[49] , F. Bock[89,70] , A. Bogdanov[72] , H. Bøggild[76] , M. Bogolyubsky[108] , F.V. Böhmer[88] , L. Boldizsár[130] ,
M. Bombara[38] , J. Book[49] , H. Borel[14] , A. Borissov[92,129] , M. Borri[78] , F. Bossú[61] , M. Botje[77] , E. Botta[25] ,
S. Böttger[48] , P. Braun-Munzinger[93] , M. Bregant[115] , T. Breitner[48] , T.A. Broker[49] , T.A. Browning[91] , M. Broz[37] ,
E. Bruna[107] , G.E. Bruno[31] , D. Budnikov[95] , H. Buesching[49] , S. Bufalino[107] , P. Buncic[34] , O. Busch[89] ,
Z. Buthelezi[61] , D. Caffarri[34,28] , X. Cai[7] , H. Caines[131] , L. Calero Diaz[68] , A. Caliva[53] , E. Calvo Villar[99] ,
P. Camerini[24] , F. Carena[34] , W. Carena[34] , J. Castillo Castellanos[14] , A.J. Castro[120] , E.A.R. Casula[23] ,
V. Catanescu[74] , C. Cavicchioli[34] , C. Ceballos Sanchez[9] , J. Cepila[37] , P. Cerello[107] , B. Chang[118] ,
S. Chapeland[34] , J.L. Charvet[14] , S. Chattopadhyay[126] , S. Chattopadhyay[97] , V. Chelnokov[3] , M. Cherney[82] ,
C. Cheshkov[124] , B. Cheynis[124] , V. Chibante Barroso[34] , D.D. Chinellato[116,117] , P. Chochula[34] , M. Chojnacki[76] ,
S. Choudhury[126] , P. Christakoglou[77] , C.H. Christensen[76] , P. Christiansen[32] , T. Chujo[122] , S.U. Chung[92] ,
C. Cicalo[102] , L. Cifarelli[12,26] , F. Cindolo[101] , J. Cleymans[85] , F. Colamaria[31] , D. Colella[31] , A. Collu[23] ,
M. Colocci[26] , G. Conesa Balbastre[67] , Z. Conesa del Valle[47] , M.E. Connors[131] , J.G. Contreras[37,11] ,
T.M. Cormier[129,80] , Y. Corrales Morales[25] , P. Cortese[30] , I. Cortés Maldonado[2] , M.R. Cosentino[115] , F. Costa[34] ,
P. Crochet[66] , R. Cruz Albino[11] , E. Cuautle[59] , L. Cunqueiro[34,68] , A. Dainese[104] , R. Dang[7] , A. Danu[58] ,
D. Das[97] , I. Das[47] , K. Das[97] , S. Das[4] , A. Dash[116] , S. Dash[44] , S. De[126] , H. Delagrange[109,i], A. Deloff[73] ,
E. Dénes[130] , G. D'Erasmo[31] , A. De Caro[29,12] , G. de Cataldo[100] , J. de Cuveland[39] , A. De Falco[23] ,
D. De Gruttola[12,29] , N. De Marco[107] , S. De Pasquale[29] , R. de Rooij[53] , M.A. Diaz Corchero[10] , T. Dietel[85,50] ,
P. Dillenseger[49] , R. Divià[34] , D. Di Bari[31] , S. Di Liberto[105] , A. Di Mauro[34] , P. Di Nezza[68] , Ø. Djuvsland[17] ,
A. Dobrin[53] , T. Dobrowolski[73] , D. Domenicis Gimenez[115] , B. Dönigus[49] , O. Dordic[21] , S. Dørheim[88] ,
A.K. Dubey[126] , A. Dubla[53] , L. Ducroux[124] , P. Dupieux[66] , A.K. Dutta Majumdar[97] , T. E. Hilden[42] ,
R.J. Ehlers[131] , D. Elia[100] , H. Engel[48] , B. Erazmus[109,34] , H.A. Erdal[35] , D. Eschweiler[39] , B. Espagnon[47] ,
M. Esposito[34] , M. Estienne[109] , S. Esumi[122] , D. Evans[98] , S. Evdokimov[108] , D. Fabris[104] , J. Faivre[67] ,
D. Falchieri[26] , A. Fantoni[68] , M. Fasel[89,70] , D. Fehlker[17] , L. Feldkamp[50] , D. Felea[58] , A. Feliciello[107] ,
G. Feofilov[125] , J. Ferencei[79] , A. Fernández Téllez[2] , E.G. Ferreiro[16] , A. Ferretti[25] , A. Festanti[28] , J. Figiel[112] ,
M.A.S. Figueredo[119] , S. Filchagin[95] , D. Finogeev[52] , F.M. Fionda[31] , E.M. Fiore[31] , E. Floratos[84] , M. Floris[34] ,
S. Foertsch[61] , P. Foka[93] , S. Fokin[96] , E. Fragiacomo[106] , A. Francescon[28,34] , U. Frankenfeld[93] , U. Fuchs[34] ,
C. Furget[67] , A. Furs[52] , M. Fusco Girard[29] , J.J. Gaardhøje[76] , M. Gagliardi[25] , A.M. Gago[99] , M. Gallio[25] ,
D.R. Gangadharan[70,19] , P. Ganoti[80,84] , C. Gao[7] , C. Garabatos[93] , E. Garcia-Solis[13] , C. Gargiulo[34] ,
I. Garishvili[71] , J. Gerhard[39] , M. Germain[109] , A. Gheata[34] , M. Gheata[34,58] , B. Ghidini[31] , P. Ghosh[126] ,
S.K. Ghosh[4] , P. Gianotti[68] , P. Giubellino[34] , E. Gladysz-Dziadus[112] , P. Glässel[89] , A. Gomez Ramirez[48] ,
P. González-Zamora[10] , S. Gorbunov[39] , L. Görlich[112] , S. Gotovac[111] , L.K. Graczykowski[128] , A. Grelli[53] ,
A. Grigoras[34] , C. Grigoras[34] , V. Grigoriev[72] , A. Grigoryan[1] , S. Grigoryan[62] , B. Grinyov[3] , N. Grion[106] ,
J.F. Grosse-Oetringhaus[34] , J.-Y. Grossiord[124] , R. Grosso[34] , F. Guber[52] , R. Guernane[67] , B. Guerzoni[26] ,
M. Guilbaud[124] , K. Gulbrandsen[76] , H. Gulkanyan[1] , M. Gumbo[85] , T. Gunji[121] , A. Gupta[86] , R. Gupta[86] ,
K. H. Khan[15] , R. Haake[50] , Ø. Haaland[17] , C. Hadjidakis[47] , M. Haiduc[58] , H. Hamagaki[121] , G. Hamar[130] ,
L.D. Hanratty[98] , A. Hansen[76] , J.W. Harris[131] , H. Hartmann[39] , A. Harton[13] , D. Hatzifotiadou[101] ,
S. Hayashi[121] , S.T. Heckel[49] , M. Heide[50] , H. Helstrup[35] , A. Herghelegiu[74] , G. Herrera Corral[11] , B.A. Hess[33] ,
K.F. Hetland[35] , B. Hippolyte[51] , J. Hladky[56] , P. Hristov[34] , M. Huang[17] , T.J. Humanic[19] , N. Hussain[41] ,
T. Hussain[18] , D. Hutter[39] , D.S. Hwang[20] , R. Ilkaev[95] , I. Ilkiv[73] , M. Inaba[122] , G.M. Innocenti[25] , C. Ionita[34] ,

M. Ippolitov[96] , M. Irfan[18] , M. Ivanov[93] , V. Ivanov[81] , A. Jachołkowski[27] , P.M. Jacobs[70] , C. Jahnke[115] , H.J. Jang[64] , M.A. Janik[128] , P.H.S.Y. Jayarathna[117] , C. Jena[28] , S. Jena[117] , R.T. Jimenez Bustamante[59] , P.G. Jones[98] , H. Jung[40] , A. Jusko[98] , V. Kadyshevskiy[62] , P. Kalinak[55] , A. Kalweit[34] , J. Kamin[49] , J.H. Kang[132] , V. Kaplin[72] , S. Kar[126] , A. Karasu Uysal[65] , O. Karavichev[52] , T. Karavicheva[52] , E. Karpechev[52] , U. Kebschull[48] , R. Keidel[133] , D.L.D. Keijdener[53] , M. Keil SVN[34] , M.M. Khan[iii,18] , P. Khan[97] , S.A. Khan[126] , A. Khanzadeev[81] , Y. Kharlov[108] , B. Kileng[35] , B. Kim[132] , D.W. Kim[40,64] , D.J. Kim[118] , J.S. Kim[40] , M. Kim[40] , M. Kim[132] , S. Kim[20] , T. Kim[132] , S. Kirsch[39] , I. Kisel[39] , S. Kiselev[54] , A. Kisiel[128] , G. Kiss[130] , J.L. Klay[6] , J. Klein[89] , C. Klein-Bösing[50] , A. Kluge[34] , M.L. Knichel[93] , A.G. Knospe[113] , C. Kobdaj[110,34] , M. Kofarago[34] , M.K. Köhler[93] , T. Kollegger[39] , A. Kolojvari[125] , V. Kondratiev[125] , N. Kondratyeva[72] , A. Konevskikh[52] , V. Kovalenko[125] , M. Kowalski[112] , S. Kox[67] , G. Koyithatta Meethaleveedu[44] , J. Kral[118] , I. Králik[55] , A. Kravčáková[38] , M. Krelina[37] , M. Kretz[39] , M. Krivda[55,98] , F. Krizek[79] , E. Kryshen[34] , M. Krzewicki[93,39] , V. Kučera[79] , Y. Kucheriaev[96,i], T. Kugathasan[34] , C. Kuhn[51] , P.G. Kuijer[77] , I. Kulakov[49] , J. Kumar[44] , P. Kurashvili[73] , A. Kurepin[52] , A.B. Kurepin[52] , A. Kuryakin[95] , S. Kushpil[79] , M.J. Kweon[89,46] , Y. Kwon[132] , P. Ladron de Guevara[59] , C. Lagana Fernandes[115] , I. Lakomov[47] , R. Langoy[127] , C. Lara[48] , A. Lardeux[109] , A. Lattuca[25] , S.L. La Pointe[107] , P. La Rocca[27] , R. Lea[24] , L. Leardini[89] , G.R. Lee[98] , I. Legrand[34] , J. Lehnert[49] , R.C. Lemmon[78] , V. Lenti[100] , E. Leogrande[53] , M. Leoncino[25] , I. León Monzón[114] , P. Lévai[130] , S. Li[7,66] , J. Lien[127] , R. Lietava[98] , S. Lindal[21] , V. Lindenstruth[39] , C. Lippmann[93] , M.A. Lisa[19] , H.M. Ljunggren[32] , D.F. Lodato[53] , P.I. Loenne[17] , V.R. Loggins[129] , V. Loginov[72] , D. Lohner[89] , C. Loizides[70] , X. Lopez[66] , E. López Torres[9] , X.-G. Lu[89] , P. Luettig[49] , M. Lunardon[28] , G. Luparello[53,24] , R. Ma[131] , A. Maevskaya[52] , M. Mager[34] , D.P. Mahapatra[57] , S.M. Mahmood[21] , A. Maire[51,89] , R.D. Majka[131] , M. Malaev[81] , I. Maldonado Cervantes[59] , L. Malinina[iv,62] , D. Mal'Kevich[54] , P. Malzacher[93] , A. Mamonov[95] , L. Manceau[107] , V. Manko[96] , F. Manso[66] , V. Manzari[100] , M. Marchisone[66,25] , J. Mareš[56] , G.V. Margagliotti[24] , A. Margotti[101] , A. Marín[93] , C. Markert[34,113] , M. Marquard[49] , I. Martashvili[120] , N.A. Martin[93] , P. Martinengo[34] , M.I. Martínez[2] , G. Martínez García[109] , J. Martin Blanco[109] , Y. Martynov[3] , A. Mas[109] , S. Masciocchi[93] , M. Masera[25] , A. Masoni[102] , L. Massacrier[109] , A. Mastroserio[31] , A. Matyja[112] , C. Mayer[112] , J. Mazer[120] , M.A. Mazzoni[105] , D. Mcdonald[117] , F. Meddi[22] , A. Menchaca-Rocha[60] , E. Meninno[29] , J. Mercado Pérez[89] , M. Meres[36] , Y. Miake[122] , K. Mikhaylov[54,62] , L. Milano[34] , J. Milosevic[v,21] , A. Mischke[53] , A.N. Mishra[45] , D. Miśkowiec[93] , J. Mitra[126] , C.M. Mitu[58] , J. Mlynarz[129] , N. Mohammadi[53] , B. Mohanty[126,75] , L. Molnar[51] , L. Montaño Zetina[11] , E. Montes[10] , M. Morando[28] , D.A. Moreira De Godoy[109,115] , S. Moretto[28] , A. Morreale[109] , A. Morsch[34] , V. Muccifora[68] , E. Mudnic[111] , D. Mühlheim[50] , S. Muhuri[126] , M. Mukherjee[126] , H. Müller[34] , M.G. Munhoz[115] , S. Murray[85] , L. Musa[34] , J. Musinsky[55] , B.K. Nandi[44] , R. Nania[101] , E. Nappi[100] , C. Nattrass[120] , K. Nayak[75] , T.K. Nayak[126] , S. Nazarenko[95] , A. Nedosekin[54] , M. Nicassio[93] , M. Niculescu[34,58] , J. Niedziela[34] , B.S. Nielsen[76] , S. Nikolaev[96] , S. Nikulin[96] , V. Nikulin[81] , B.S. Nilsen[82] , F. Noferini[12,101] , P. Nomokonov[62] , G. Nooren[53] , J. Norman[119] , A. Nyanin[96] , J. Nystrand[17] , H. Oeschler[89] , S. Oh[131] , S.K. Oh[vi,63,40] , A. Okatan[65] , T. Okubo[43] , L. Olah[130] , J. Oleniacz[128] , A.C. Oliveira Da Silva[115] , J. Onderwaater[93] , C. Oppedisano[107] , A. Ortiz Velasquez[32,59] , A. Oskarsson[32] , J. Otwinowski[112,93] , K. Oyama[89] , M. Ozdemir[49] , P. Sahoo[45] , Y. Pachmayer[89] , M. Pachr[37] , P. Pagano[29] , G. Paić[59] , C. Pajares[16] , S.K. Pal[126] , A. Palmeri[103] , D. Pant[44] , V. Papikyan[1] , G.S. Pappalardo[103] , P. Pareek[45] , W.J. Park[93] , S. Parmar[83] , A. Passfeld[50] , D.I. Patalakha[108] , V. Paticchio[100] , B. Paul[97] , T. Pawlak[128] , T. Peitzmann[53] , H. Pereira Da Costa[14] , E. Pereira De Oliveira Filho[115] , D. Peresunko[96] , C.E. Pérez Lara[77] , A. Pesci[101] , V. Peskov[49] , Y. Pestov[5] , V. Petráček[37] , M. Petran[37] , M. Petris[74] , M. Petrovici[74] , C. Petta[27] , S. Piano[106] , M. Pikna[36] , P. Pillot[109] , O. Pinazza[101,34] , L. Pinsky[117] , D.B. Piyarathna[117] , M. Płoskoń[70] , M. Planinic[94,123] , J. Pluta[128] , S. Pochybova[130] , P.L.M. Podesta-Lerma[114] , M.G. Poghosyan[82,34] , E.H.O. Pohjoisaho[42] , B. Polichtchouk[108] , N. Poljak[123,94] , A. Pop[74] , S. Porteboeuf-Houssais[66] , J. Porter[70] , B. Potukuchi[86] , S.K. Prasad[129,4] , R. Preghenella[101,12] , F. Prino[107] , C.A. Pruneau[129] , I. Pshenichnov[52] , M. Puccio[107] , G. Puddu[23] , P. Pujahari[129] , V. Punin[95] , J. Putschke[129] , H. Qvigstad[21] , A. Rachevski[106] , S. Raha[4] , S. Rajput[86] , J. Rak[118] , A. Rakotozafindrabe[14] , L. Ramello[30] , R. Raniwala[87] , S. Raniwala[87] , S.S. Räsänen[42] , B.T. Rascanu[49] , D. Rathee[83] , A.W. Rauf[15] , V. Razazi[23] , K.F. Read[120] , J.S. Real[67] , K. Redlich[vii,73] , R.J. Reed[131,129] , A. Rehman[17] , P. Reichelt[49] , M. Reicher[53] , F. Reidt[89,34] , R. Renfordt[49] , A.R. Reolon[68] , A. Reshetin[52] , F. Rettig[39] , J.-P. Revol[34] , K. Reygers[89] , V. Riabov[81] , R.A. Ricci[69] , T. Richert[32] , M. Richter[21] , P. Riedler[34] , W. Riegler[34] , F. Riggi[27] , A. Rivetti[107] , E. Rocco[53] , M. Rodríguez Cahuantzi[2] , A. Rodriguez Manso[77] , K. Røed[21] , E. Rogochaya[62] , S. Rohni[86] , D. Rohr[39] , D. Röhrich[17] , R. Romita[78,119] , F. Ronchetti[68] , L. Ronflette[109] , P. Rosnet[66] , A. Rossi[34] , F. Roukoutakis[84] , A. Roy[45] , C. Roy[51] , P. Roy[97] , A.J. Rubio Montero[10] , R. Rui[24] , R. Russo[25] , E. Ryabinkin[96] , Y. Ryabov[81] , A. Rybicki[112] , S. Sadovsky[108] , K. Šafařík[34] , B. Sahlmuller[49] , R. Sahoo[45] , S. Sahoo[57] , P.K. Sahu[57] , J. Saini[126] , S. Sakai[68] , C.A. Salgado[16] , J. Salzwedel[19] , S. Sambyal[86] , V. Samsonov[81] , X. Sanchez Castro[51] , F.J. Sánchez Rodríguez[114] , L. Šándor[55] ,

A. Sandoval[60] , M. Sano[122] , G. Santagati[27] , D. Sarkar[126] , E. Scapparone[101] , F. Scarlassara[28] , R.P. Scharenberg[91] , C. Schiaua[74] , R. Schicker[89] , C. Schmidt[93] , H.R. Schmidt[33] , S. Schuchmann[49] , J. Schukraft[34] , M. Schulc[37] , T. Schuster[131] , Y. Schutz[34,109] , K. Schwarz[93] , K. Schweda[93] , G. Scioli[26] , E. Scomparin[107] , R. Scott[120] , G. Segato[28] , J.E. Seger[82] , Y. Sekiguchi[121] , I. Selyuzhenkov[93] , K. Senosi[61] , J. Seo[92] , E. Serradilla[10,60] , A. Sevcenco[58] , A. Shabetai[109] , G. Shabratova[62] , R. Shahoyan[34] , A. Shangaraev[108] , A. Sharma[86] , N. Sharma[120] , S. Sharma[86] , K. Shigaki[43] , K. Shtejer[9,25] , Y. Sibiriak[96] , S. Siddhanta[102] , T. Siemiarczuk[73] , D. Silvermyr[80] , C. Silvestre[67] , G. Simatovic[123] , R. Singaraju[126] , R. Singh[86] , S. Singha[75,126] , V. Singhal[126] , B.C. Sinha[126] , T. Sinha[97] , B. Sitar[36] , M. Sitta[30] , T.B. Skaali[21] , K. Skjerdal[17] , M. Slupecki[118] , N. Smirnov[131] , R.J.M. Snellings[53] , C. Søgaard[32] , R. Soltz[71] , J. Song[92] , M. Song[132] , F. Soramel[28] , S. Sorensen[120] , M. Spacek[37] , E. Spiriti[68] , I. Sputowska[112] , M. Spyropoulou-Stassinaki[84] , B.K. Srivastava[91] , J. Stachel[89] , I. Stan[58] , G. Stefanek[73] , M. Steinpreis[19] , E. Stenlund[32] , G. Steyn[61] , J.H. Stiller[89] , D. Stocco[109] , M. Stolpovskiy[108] , P. Strmen[36] , A.A.P. Suaide[115] , T. Sugitate[43] , C. Suire[47] , M. Suleymanov[15] , R. Sultanov[54] , M. Šumbera[79] , T.J.M. Symons[70] , A. Szabo[36] , A. Szanto de Toledo[115] , I. Szarka[36] , A. Szczepankiewicz[34] , M. Szymanski[128] , J. Takahashi[116] , M.A. Tangaro[31] , J.D. Tapia Takaki[viii,47] , A. Tarantola Peloni[49] , A. Tarazona Martinez[34] , M. Tariq[18] , M.G. Tarzila[74] , A. Tauro[34] , G. Tejeda Muñoz[2] , A. Telesca[34] , K. Terasaki[121] , C. Terrevoli[23] , J. Thäder[93] , D. Thomas[53] , R. Tieulent[124] , A.R. Timmins[117] , A. Toia[49,104] , V. Trubnikov[3] , W.H. Trzaska[118] , T. Tsuji[121] , A. Tumkin[95] , R. Turrisi[104] , T.S. Tveter[21] , K. Ullaland[17] , A. Uras[124] , G.L. Usai[23] , M. Vajzer[79] , M. Vala[55,62] , L. Valencia Palomo[66] , S. Vallero[25,89] , P. Vande Vyvre[34] , J. Van Der Maarel[53] , J.W. Van Hoorne[34] , M. van Leeuwen[53] , A. Vargas[2] , M. Vargyas[118] , R. Varma[44] , M. Vasileiou[84] , A. Vasiliev[96] , V. Vechernin[125] , M. Veldhoen[53] , A. Velure[17] , M. Venaruzzo[69,24] , E. Vercellin[25] , S. Vergara Limón[2] , R. Vernet[8] , M. Verweij[129] , L. Vickovic[111] , G. Viesti[28] , J. Viinikainen[118] , Z. Vilakazi[61] , O. Villalobos Baillie[98] , A. Vinogradov[96] , L. Vinogradov[125] , Y. Vinogradov[95] , T. Virgili[29] , V. Vislavicius[32] , Y.P. Viyogi[126] , A. Vodopyanov[62] , M.A. Völkl[89] , K. Voloshin[54] , S.A. Voloshin[129] , G. Volpe[34] , B. von Haller[34] , I. Vorobyev[125] , D. Vranic[34,93] , J. Vrláková[38] , B. Vulpescu[66] , A. Vyushin[95] , B. Wagner[17] , J. Wagner[93] , V. Wagner[37] , M. Wang[7,109] , Y. Wang[89] , D. Watanabe[122] , M. Weber[117,34] , S.G. Weber[93] , J.P. Wessels[50] , U. Westerhoff[50] , J. Wiechula[33] , J. Wikne[21] , M. Wilde[50] , G. Wilk[73] , J. Wilkinson[89] , M.C.S. Williams[101] , B. Windelband[89] , M. Winn[89] , C.G. Yaldo[129] , Y. Yamaguchi[121] , H. Yang[53] , P. Yang[7] , S. Yang[17] , S. Yano[43] , S. Yasnopolskiy[96] , J. Yi[92] , Z. Yin[7] , I.-K. Yoo[92] , I. Yushmanov[96] , A. Zaborowska[128] , V. Zaccolo[76] , A. Zaman[15] , C. Zampolli[101] , S. Zaporozhets[62] , A. Zarochentsev[125] , P. Závada[56] , N. Zaviyalov[95] , H. Zbroszczyk[128] , I.S. Zgura[58] , M. Zhalov[81] , H. Zhang[7] , X. Zhang[7,70] , Y. Zhang[7] , C. Zhao[21] , N. Zhigareva[54] , D. Zhou[7] , F. Zhou[7] , Y. Zhou[53] , Zhou, Zhuo[17] , H. Zhu[7] , J. Zhu[7,109] , X. Zhu[7] , A. Zichichi[12,26] , A. Zimmermann[89] , M.B. Zimmermann[50,34] , G. Zinovjev[3] , Y. Zoccarato[124] , M. Zyzak[49]

Affiliation notes

[i] Deceased
[ii] Also at: St. Petersburg State Polytechnical University
[iii] Also at: Department of Applied Physics, Aligarh Muslim University, Aligarh, India
[iv] Also at: M.V. Lomonosov Moscow State University, D.V. Skobeltsyn Institute of Nuclear Physics, Moscow, Russia
[v] Also at: University of Belgrade, Faculty of Physics and "Vinča" Institute of Nuclear Sciences, Belgrade, Serbia
[vi] Permanent Address: Permanent Address: Konkuk University, Seoul, Korea
[vii] Also at: Institute of Theoretical Physics, University of Wroclaw, Wroclaw, Poland
[viii] Also at: University of Kansas, Lawrence, KS, United States

Collaboration Institutes

[1] A.I. Alikhanyan National Science Laboratory (Yerevan Physics Institute) Foundation, Yerevan, Armenia
[2] Benemérita Universidad Autónoma de Puebla, Puebla, Mexico
[3] Bogolyubov Institute for Theoretical Physics, Kiev, Ukraine
[4] Bose Institute, Department of Physics and Centre for Astroparticle Physics and Space Science (CAPSS), Kolkata, India
[5] Budker Institute for Nuclear Physics, Novosibirsk, Russia
[6] California Polytechnic State University, San Luis Obispo, CA, United States
[7] Central China Normal University, Wuhan, China

[8] Centre de Calcul de l'IN2P3, Villeurbanne, France
[9] Centro de Aplicaciones Tecnológicas y Desarrollo Nuclear (CEADEN), Havana, Cuba
[10] Centro de Investigaciones Energéticas Medioambientales y Tecnológicas (CIEMAT), Madrid, Spain
[11] Centro de Investigación y de Estudios Avanzados (CINVESTAV), Mexico City and Mérida, Mexico
[12] Centro Fermi - Museo Storico della Fisica e Centro Studi e Ricerche "Enrico Fermi", Rome, Italy
[13] Chicago State University, Chicago, USA
[14] Commissariat à l'Energie Atomique, IRFU, Saclay, France
[15] COMSATS Institute of Information Technology (CIIT), Islamabad, Pakistan
[16] Departamento de Física de Partículas and IGFAE, Universidad de Santiago de Compostela, Santiago de Compostela, Spain
[17] Department of Physics and Technology, University of Bergen, Bergen, Norway
[18] Department of Physics, Aligarh Muslim University, Aligarh, India
[19] Department of Physics, Ohio State University, Columbus, OH, United States
[20] Department of Physics, Sejong University, Seoul, South Korea
[21] Department of Physics, University of Oslo, Oslo, Norway
[22] Dipartimento di Fisica dell'Università 'La Sapienza' and Sezione INFN Rome, Italy
[23] Dipartimento di Fisica dell'Università and Sezione INFN, Cagliari, Italy
[24] Dipartimento di Fisica dell'Università and Sezione INFN, Trieste, Italy
[25] Dipartimento di Fisica dell'Università and Sezione INFN, Turin, Italy
[26] Dipartimento di Fisica e Astronomia dell'Università and Sezione INFN, Bologna, Italy
[27] Dipartimento di Fisica e Astronomia dell'Università and Sezione INFN, Catania, Italy
[28] Dipartimento di Fisica e Astronomia dell'Università and Sezione INFN, Padova, Italy
[29] Dipartimento di Fisica 'E.R. Caianiello' dell'Università and Gruppo Collegato INFN, Salerno, Italy
[30] Dipartimento di Scienze e Innovazione Tecnologica dell'Università del Piemonte Orientale and Gruppo Collegato INFN, Alessandria, Italy
[31] Dipartimento Interateneo di Fisica 'M. Merlin' and Sezione INFN, Bari, Italy
[32] Division of Experimental High Energy Physics, University of Lund, Lund, Sweden
[33] Eberhard Karls Universität Tübingen, Tübingen, Germany
[34] European Organization for Nuclear Research (CERN), Geneva, Switzerland
[35] Faculty of Engineering, Bergen University College, Bergen, Norway
[36] Faculty of Mathematics, Physics and Informatics, Comenius University, Bratislava, Slovakia
[37] Faculty of Nuclear Sciences and Physical Engineering, Czech Technical University in Prague, Prague, Czech Republic
[38] Faculty of Science, P.J. Šafárik University, Košice, Slovakia
[39] Frankfurt Institute for Advanced Studies, Johann Wolfgang Goethe-Universität Frankfurt, Frankfurt, Germany
[40] Gangneung-Wonju National University, Gangneung, South Korea
[41] Gauhati University, Department of Physics, Guwahati, India
[42] Helsinki Institute of Physics (HIP), Helsinki, Finland
[43] Hiroshima University, Hiroshima, Japan
[44] Indian Institute of Technology Bombay (IIT), Mumbai, India
[45] Indian Institute of Technology Indore, Indore (IITI), India
[46] Inha University, Incheon, South Korea
[47] Institut de Physique Nucléaire d'Orsay (IPNO), Université Paris-Sud, CNRS-IN2P3, Orsay, France
[48] Institut für Informatik, Johann Wolfgang Goethe-Universität Frankfurt, Frankfurt, Germany
[49] Institut für Kernphysik, Johann Wolfgang Goethe-Universität Frankfurt, Frankfurt, Germany
[50] Institut für Kernphysik, Westfälische Wilhelms-Universität Münster, Münster, Germany
[51] Institut Pluridisciplinaire Hubert Curien (IPHC), Université de Strasbourg, CNRS-IN2P3, Strasbourg, France
[52] Institute for Nuclear Research, Academy of Sciences, Moscow, Russia
[53] Institute for Subatomic Physics of Utrecht University, Utrecht, Netherlands
[54] Institute for Theoretical and Experimental Physics, Moscow, Russia
[55] Institute of Experimental Physics, Slovak Academy of Sciences, Košice, Slovakia
[56] Institute of Physics, Academy of Sciences of the Czech Republic, Prague, Czech Republic
[57] Institute of Physics, Bhubaneswar, India
[58] Institute of Space Science (ISS), Bucharest, Romania

[59] Instituto de Ciencias Nucleares, Universidad Nacional Autónoma de México, Mexico City, Mexico
[60] Instituto de Física, Universidad Nacional Autónoma de México, Mexico City, Mexico
[61] iThemba LABS, National Research Foundation, Somerset West, South Africa
[62] Joint Institute for Nuclear Research (JINR), Dubna, Russia
[63] Konkuk University, Seoul, South Korea
[64] Korea Institute of Science and Technology Information, Daejeon, South Korea
[65] KTO Karatay University, Konya, Turkey
[66] Laboratoire de Physique Corpusculaire (LPC), Clermont Université, Université Blaise Pascal, CNRS–IN2P3, Clermont-Ferrand, France
[67] Laboratoire de Physique Subatomique et de Cosmologie, Université Grenoble-Alpes, CNRS-IN2P3, Grenoble, France
[68] Laboratori Nazionali di Frascati, INFN, Frascati, Italy
[69] Laboratori Nazionali di Legnaro, INFN, Legnaro, Italy
[70] Lawrence Berkeley National Laboratory, Berkeley, CA, United States
[71] Lawrence Livermore National Laboratory, Livermore, CA, United States
[72] Moscow Engineering Physics Institute, Moscow, Russia
[73] National Centre for Nuclear Studies, Warsaw, Poland
[74] National Institute for Physics and Nuclear Engineering, Bucharest, Romania
[75] National Institute of Science Education and Research, Bhubaneswar, India
[76] Niels Bohr Institute, University of Copenhagen, Copenhagen, Denmark
[77] Nikhef, National Institute for Subatomic Physics, Amsterdam, Netherlands
[78] Nuclear Physics Group, STFC Daresbury Laboratory, Daresbury, United Kingdom
[79] Nuclear Physics Institute, Academy of Sciences of the Czech Republic, Řež u Prahy, Czech Republic
[80] Oak Ridge National Laboratory, Oak Ridge, TN, United States
[81] Petersburg Nuclear Physics Institute, Gatchina, Russia
[82] Physics Department, Creighton University, Omaha, NE, United States
[83] Physics Department, Panjab University, Chandigarh, India
[84] Physics Department, University of Athens, Athens, Greece
[85] Physics Department, University of Cape Town, Cape Town, South Africa
[86] Physics Department, University of Jammu, Jammu, India
[87] Physics Department, University of Rajasthan, Jaipur, India
[88] Physik Department, Technische Universität München, Munich, Germany
[89] Physikalisches Institut, Ruprecht-Karls-Universität Heidelberg, Heidelberg, Germany
[90] Politecnico di Torino, Turin, Italy
[91] Purdue University, West Lafayette, IN, United States
[92] Pusan National University, Pusan, South Korea
[93] Research Division and ExtreMe Matter Institute EMMI, GSI Helmholtzzentrum für Schwerionenforschung, Darmstadt, Germany
[94] Rudjer Bošković Institute, Zagreb, Croatia
[95] Russian Federal Nuclear Center (VNIIEF), Sarov, Russia
[96] Russian Research Centre Kurchatov Institute, Moscow, Russia
[97] Saha Institute of Nuclear Physics, Kolkata, India
[98] School of Physics and Astronomy, University of Birmingham, Birmingham, United Kingdom
[99] Sección Física, Departamento de Ciencias, Pontificia Universidad Católica del Perú, Lima, Peru
[100] Sezione INFN, Bari, Italy
[101] Sezione INFN, Bologna, Italy
[102] Sezione INFN, Cagliari, Italy
[103] Sezione INFN, Catania, Italy
[104] Sezione INFN, Padova, Italy
[105] Sezione INFN, Rome, Italy
[106] Sezione INFN, Trieste, Italy
[107] Sezione INFN, Turin, Italy
[108] SSC IHEP of NRC Kurchatov institute, Protvino, Russia
[109] SUBATECH, Ecole des Mines de Nantes, Université de Nantes, CNRS-IN2P3, Nantes, France
[110] Suranaree University of Technology, Nakhon Ratchasima, Thailand
[111] Technical University of Split FESB, Split, Croatia

[112] The Henryk Niewodniczanski Institute of Nuclear Physics, Polish Academy of Sciences, Cracow, Poland
[113] The University of Texas at Austin, Physics Department, Austin, TX, USA
[114] Universidad Autónoma de Sinaloa, Culiacán, Mexico
[115] Universidade de São Paulo (USP), São Paulo, Brazil
[116] Universidade Estadual de Campinas (UNICAMP), Campinas, Brazil
[117] University of Houston, Houston, TX, United States
[118] University of Jyväskylä, Jyväskylä, Finland
[119] University of Liverpool, Liverpool, United Kingdom
[120] University of Tennessee, Knoxville, TN, United States
[121] University of Tokyo, Tokyo, Japan
[122] University of Tsukuba, Tsukuba, Japan
[123] University of Zagreb, Zagreb, Croatia
[124] Université de Lyon, Université Lyon 1, CNRS/IN2P3, IPN-Lyon, Villeurbanne, France
[125] V. Fock Institute for Physics, St. Petersburg State University, St. Petersburg, Russia
[126] Variable Energy Cyclotron Centre, Kolkata, India
[127] Vestfold University College, Tonsberg, Norway
[128] Warsaw University of Technology, Warsaw, Poland
[129] Wayne State University, Detroit, MI, United States
[130] Wigner Research Centre for Physics, Hungarian Academy of Sciences, Budapest, Hungary
[131] Yale University, New Haven, CT, United States
[132] Yonsei University, Seoul, South Korea
[133] Zentrum für Technologietransfer und Telekommunikation (ZTT), Fachhochschule Worms, Worms, Germany

References

[1] ATLAS and CMS Collaboration, “Birth of a Higgs boson,” CERN Cour. **53N4** (2013) 21.

[2] Peter W. Higgs. Broken symmetries and the masses of gauge bosons. *Phys. Rev. Lett.*, 13:508–509, Oct 1964.

[3] P. W. Anderson. Plasmons, gauge invariance, and mass. *Phys. Rev.*, 130:439–442, Apr 1963.

[4] F. Englert and R. Brout. Broken symmetry and the mass of gauge vector mesons. *Phys. Rev. Lett.*, 13:321–323, Aug 1964.

[5] G. S. Guralnik, C. R. Hagen, and T. W. B. Kibble. Global conservation laws and massless particles. *Phys. Rev. Lett.*, 13:585–587, Nov 1964.

[6] P.A.R. Ade et al. Planck 2013 results. I. Overview of products and scientific results. 2013.

[7] A. Einstein, “Concerning an heuristic point of view toward the emission and transformation of light,” Annalen Phys. **17** (1905) 132.

[8] E. Fermi, “Trends to a Theory of beta Radiation. (In Italian),” Nuovo Cim. **11** (1934) 1.

[9] F.J. Hasert et al. Observation of Neutrino Like Interactions Without Muon Or Electron in the Gargamelle Neutrino Experiment. *Phys.Lett.*, B46:138–140, 1973.

[10] A. Astbury, Phys. Bull. **34** (1983) 434.

[11] G. Arnison *et al.* [UA1 Collaboration], “Experimental Observation of Isolated Large Transverse Energy Electrons with Associated Missing Energy at s**(1/2) = 540-GeV,” Phys. Lett. B **122** (1983) 103.

[12] G. Arnison *et al.* [UA1 Collaboration], “Experimental Observation of Lepton Pairs of Invariant Mass Around 95-GeV/c**2 at the CERN SPS Collider,” Phys. Lett. B **126** (1983) 398.

[13] M. Banner *et al.* [UA2 Collaboration], “Observation of Single Isolated Electrons of High Transverse Momentum in Events with Missing Transverse Energy at the CERN anti-p p Collider,” Phys. Lett. B **122** (1983) 476.

[14] P. Bagnaia *et al.* [UA2 Collaboration], “Evidence for Z0 —> e+ e- at the CERN anti-p p Collider,” Phys. Lett. B **129** (1983) 130.

[15] Serguei Chatrchyan et al. "Measurement of the ratio of the inclusive 3-jet cross section to the inclusive 2-jet cross section in pp collisions at $\sqrt{s} = 7$ TeV and first determination of the strong coupling constant in the TeV range". *Eur.Phys.J.*, C73:2604, 2013.

[16] Kokkas P. PDF and alphaS constraints from jet measurements at CMS. *PoS*, EPS-HEP:436, 2013.

[17] R. Brandelik *et al.* [TASSO Collaboration], "Evidence for Planar Events in e+ e- Annihilation at High-Energies," Phys. Lett. B **86** (1979) 243.

[18] B. H. Wiik, "First Results from PETRA," Conf. Proc. C **7906181** (1979) 113.

[19] C. Berger *et al.* [PLUTO Collaboration], "Jet Analysis of the Υ (9.46) Decay Into Charged Hadrons," Phys. Lett. B **82** (1979) 449.

[20] Alison Lister. Measurement of b^- quark Jet Shapes at CDF. 2006.

[21] Hung-Liang Lai, Marco Guzzi, Joey Huston, Zhao Li, Pavel M. Nadolsky, et al. New parton distributions for collider physics. *Phys.Rev.*, D82:074024, 2010.

[22] G. Dissertori, I.G. Knowles, and M. Schmelling. *Quantum Chromodynamics: High Energy Experiments and Theory*. International Series of Monographs on Physics. OUP Oxford, 2009.

[23] Ulrich W. Heinz. Concepts of heavy ion physics. pages 165–238, 2004.

[24] INPAC. "QCD phase diagram: what happened if the matter were extremely compressed?" `http://inpac.physics.sjtu.edu.cn/en/content.aspx?info_lb=289&flag=225`

[25] C. A. Salgado, J. Alvarez-Muniz, F. Arleo, N. Armesto, M. Botje, M. Cacciari, J. Campbell and C. Carli *et al.*, "Proton-Nucleus Collisions at the LHC: Scientific Opportunities and Requirements," J. Phys. G **39** (2012) 015010 [arXiv:1105.3919 [hep-ph]].

[26] E. Iancu, "QCD in heavy ion collisions," arXiv:1205.0579 [hep-ph].

[27] J. M. Burward-Hoy [PHENIX Collaboration], "Source parameters from identified hadron spectra and NBT radii for Au - Au collisions at s(NN)**(1/2) = 200-GeV in PHENIX," Nucl. Phys. A **715** (2003) 498 [nucl-ex/0210001].

[28] S. V. Afanasiev, T. Anticic, B. Baatar, D. Barna, J. Bartke, R. A. Barton, M. Behler and L. Betev *et al.*, "Recent results on spectra and yields from NA49," Nucl. Phys. A **715** (2003) 161 [nucl-ex/0208014].

[29] J. Rafelski and B. Muller, "Strangeness Production in the Quark - Gluon Plasma," Phys. Rev. Lett. **48** (1982) 1066 [Erratum-ibid. **56** (1986) 2334].

[30] T. Matsui and H. Satz, "J/ψ Suppression by Quark-Gluon Plasma Formation," Phys. Lett. B **178** (1986) 416.

[31] A. Mocsy and P. Petreczky, "Quarkonium melting above deconfinement," J. Phys. G **35** (2008) 104154.

[32] J. Adams *et al.* [STAR Collaboration], “Evidence from d + Au measurements for final state suppression of high p(T) hadrons in Au+Au collisions at RHIC,” Phys. Rev. Lett. **91** (2003) 072304 [nucl-ex/0306024].

[33] B. B. Abelev *et al.* [ALICE Collaboration], “Transverse momentum dependence of inclusive primary charged-particle production in p-Pb collisions at $\sqrt{s_{\mathrm{NN}}} = 5.02$ TeV,” Eur. Phys. J. C **74** (2014) 9, 3054 [arXiv:1405.2737 [nucl-ex]].

[34] S. Chatrchyan *et al.* [CMS Collaboration], “Study of high-pT charged particle suppression in PbPb compared to *pp* collisions at $\sqrt{s_{NN}} = 2.76$ TeV,” Eur. Phys. J. C **72** (2012) 1945 [arXiv:1202.2554 [nucl-ex]].

[35] E. Appelt [CMS Collaboration], “Jet and charged hadron nuclear modification factors in pPb collisions with CMS,” Nucl. Phys. A (2014).

[36] S. Chatrchyan *et al.* [CMS Collaboration], “Measurement of jet fragmentation in PbPb and pp collisions at sqrt(s[NN]) = 2.76 TeV,” Phys. Rev. C **90** (2014) 024908 [arXiv:1406.0932 [nucl-ex]].

[37] CMS results from QM2012 conference. `http://cms.web.cern.ch/news/new-cms-heavy-ion-results-quark-matter-2012-conference`. Visited 21.11.2014.

[38] B. Abelev *et al.* [ALICE Collaboration], “Measurement of charged jet suppression in Pb-Pb collisions at $\sqrt{s_{NN}} = 2.76$ TeV,” JHEP **1403** (2014) 013 [arXiv:1311.0633 [nucl-ex]].

[39] D.V. Perepelitsa*et al.* [ATLAS Collaboration], “Centrality and rapidity dependence of inclusive jet production in $\sqrt{s_{\mathrm{NN}}} = 5.02$ TeV p+Pb collisions with the ATLAS detector,” Nuclear Physics A (2014), `http://dx.doi.org/10.1016/j.nuclphysa.2014.10.031`.

[40] CMS Collaboration [CMS Collaboration], “Charged particle nuclear modification factor and pseudorapidity asymmetry in pPb collisions at sqrt(sNN)=5.02 TeV with CMS,” CMS-PAS-HIN-12-017.

[41] ATLAS Collaboration [ATLAS Collaboration], “Charged hadron production in p+Pb collisions at $\sqrt{s_{\mathrm{NN}}} = 5.02$ TeV measured at high transverse momentum by the ATLAS experiment,” ATLAS-CONF-2014-029

[42] CMS Collaboration [CMS Collaboration], “Measurement of inclusive jet nuclear modification factor in pPb collisions at sqrtsNN=5.02 TeV with CMS,” CMS-PAS-HIN-14-001.

[43] G. Roland, K. Safarik and P. Steinberg, “Heavy-ion collisions at the LHC,” Prog. Part. Nucl. Phys. **77** (2014) 70.

[44] CERN. Cern accelerators. `http://maalpu.org/lhc/LHC.main.htm`. Visited 17.3.2014.

[45] T. Muta. *Foundations of Quantum Chromodynamics: An Introduction to Perturbative Methods in Gauge Theories.* World Scientific lecture notes in physics. World Scientific, 2010.

[46] M. Cacciari, G. P. Salam and G. Soyez, "FastJet User Manual," Eur. Phys. J. C **72** (2012) 1896 [arXiv:1111.6097 [hep-ph]].

[47] M. Cacciari and G. P. Salam, "Dispelling the N^3 myth for the k_t jet-finder," Phys. Lett. B **641** (2006) 57 [hep-ph/0512210].

[48] `http://www.hep.phy.cam.ac.uk/drw/pix/opalpix.html~` Visited 10.3.2014.

[49] G. P. Salam and G. Soyez, "A Practical Seedless Infrared-Safe Cone jet algorithm," JHEP **0705** (2007) 086 [arXiv:0704.0292 [hep-ph]].

[50] S. Catani, Y. L. Dokshitzer, M. H. Seymour and B. R. Webber, "Longitudinally invariant K_t clustering algorithms for hadron hadron collisions," Nucl. Phys. B **406** (1993) 187.

[51] S. D. Ellis and D. E. Soper, "Successive combination jet algorithm for hadron collisions," Phys. Rev. D **48** (1993) 3160 [hep-ph/9305266].

[52] M. Cacciari, G. P. Salam and G. Soyez, "The anti-k_t jet clustering algorithm," JHEP **0804** (2008) 063 [arXiv:0802.1189 [hep-ph]].

[53] T. Adye, RooUnfold: ROOT Unfolding Framework `http://hepunx.rl.ac.uk/~adye/software/unfold/RooUnfold.html`. Visited 3.7.2014.

[54] T. Adye, "Unfolding algorithms and tests using RooUnfold," Proceedings of the PHYSTAT 2011 Workshop, CERN, Geneva, Switzerland, January 2011, CERN-2011-006, pp 313-318 [arXiv:1105.1160 [physics.data-an]].

[55] G. D'Agostini, "A Multidimensional unfolding method based on Bayes' theorem," Nucl. Instrum. Meth. A **362** (1995) 487.

[56] A. Hocker and V. Kartvelishvili, "SVD approach to data unfolding," Nucl. Instrum. Meth. A **372** (1996) 469 [hep-ph/9509307].

[57] B. Abelev *et al.* [ALICE Collaboration], "Measurement of inelastic, single- and double-diffraction cross sections in proton–proton collisions at the LHC with ALICE," Eur. Phys. J. C **73** (2013) 2456 [arXiv:1208.4968 [hep-ex]].

[58] Fields R. Hard scattering. `http://www.phys.ufl.edu/~rfield/cdf/chgjet/hard_scat.html`. Visited 23.6.2014.

[59] B. Abelev *et al.* [ALICE Collaboration], "Underlying Event measurements in pp collisions at $\sqrt{s} = 0.9$ and 7 TeV with the ALICE experiment at the LHC," JHEP **1207** (2012) 116 [arXiv:1112.2082 [hep-ex]].

[60] P. Z. Skands, "Tuning Monte Carlo Generators: The Perugia Tunes," Phys. Rev. D **82** (2010) 074018 [arXiv:1005.3457 [hep-ph]].

[61] G. Aad *et al.* [ATLAS Collaboration], "Charged-particle multiplicities in pp interactions measured with the ATLAS detector at the LHC," New J. Phys. **13** (2011) 053033 [arXiv:1012.5104 [hep-ex]].

[62] K. Aamodt *et al.* [ALICE Collaboration], "Charged-particle multiplicity measurement in proton-proton collisions at $\sqrt{s} = 7$ TeV with ALICE at LHC," Eur. Phys. J. C **68** (2010) 345 [arXiv:1004.3514 [hep-ex]].

[63] G. Aad *et al.* [ATLAS Collaboration], "Measurement of underlying event characteristics using charged particles in pp collisions at $\sqrt{s} = 900GeV$ and 7 TeV with the ATLAS detector," Phys. Rev. D **83** (2011) 112001 [arXiv:1012.0791 [hep-ex]].

[64] G. Corcella, I. G. Knowles, G. Marchesini, S. Moretti, K. Odagiri, P. Richardson, M. H. Seymour and B. R. Webber, "HERWIG 6: An Event generator for hadron emission reactions with interfering gluons (including supersymmetric processes)," JHEP **0101** (2001) 010 [hep-ph/0011363].

[65] G. Corcella, I. G. Knowles, G. Marchesini, S. Moretti, K. Odagiri, P. Richardson, M. H. Seymour and B. R. Webber, "HERWIG 6.5 release note," hep-ph/0210213.

[66] P. Nason, "A New method for combining NLO QCD with shower Monte Carlo algorithms," JHEP **0411** (2004) 040 [hep-ph/0409146].

[67] S. Frixione, P. Nason and C. Oleari, "Matching NLO QCD computations with Parton Shower simulations: the POWHEG method," JHEP **0711** (2007) 070 [arXiv:0709.2092 [hep-ph]].

[68] S. Alioli, P. Nason, C. Oleari and E. Re, "A general framework for implementing NLO calculations in shower Monte Carlo programs: the POWHEG BOX," JHEP **1006** (2010) 043 [arXiv:1002.2581 [hep-ph]].

[69] S. Alioli, K. Hamilton, P. Nason, C. Oleari and E. Re, "Jet pair production in POWHEG," JHEP **1104** (2011) 081 [arXiv:1012.3380 [hep-ph]].

[70] P. M. Nadolsky, H. -L. Lai, Q. -H. Cao, J. Huston, J. Pumplin, D. Stump, W. -K. Tung and C. -P. Yuan, "Implications of CTEQ global analysis for collider observables," Phys. Rev. D **78** (2008) 013004 [arXiv:0802.0007 [hep-ph]].

[71] K. J. Eskola, H. Paukkunen and C. A. Salgado, "EPS09: A New Generation of NLO and LO Nuclear Parton Distribution Functions," JHEP **0904** (2009) 065 [arXiv:0902.4154 [hep-ph]].

[72] M. Hirai, S. Kumano and T. -H. Nagai, "Determination of nuclear parton distribution functions and their uncertainties in next-to-leading order," Phys. Rev. C **76** (2007) 065207 [arXiv:0709.3038 [hep-ph]].

[73] [ATLAS Collaboration], "Measurement of differential cross section and fragmentation of jets from tracks in proton-proton collisions at center-of-mass energy $\sqrt{s} = 7$ TeV with the ATLAS detector," Phys. Rev. D **84** (2011) 054001.

[74] K. J. Eskola, R. Vogt and X. N. Wang, "Nuclear overlap functions," Int. J. Mod. Phys. A **10** (1995) 3087.

[75] R. Haake [ALICE Collaboration], "Charged Jets in Minimum Bias p-Pb Collisions at $\sqrt{s_{NN}} = 5.02$ TeV with ALICE," PoS EPS **-HEP2013** (2013) 176.

[76] O. Busch, "Charged Particle Momentum Distribution in Jets," `https://aliceinfo.cern.ch/Notes/node/40`.

[77] S. K. Prasad, "Study of jet properties in pp collisions at 7 TeV," `https://aliceinfo.cern.ch/Notes/node/205`.

[78] Private discussion with P. Nason, October 2013.

[79] C. Tsallis, "Possible Generalization of Boltzmann-Gibbs Statistics," J. Statist. Phys. **52** (1988) 479.

[80] C. Tsallis and Z. G. Arenas, "Nonextensive statistical mechanics and high energy physics," EPJ Web Conf. **71** (2014) 00132.